EPFL

Development of free-boundary equilibrium and transport solvers for simulation and real-time interpretation of tokamak experiments

Francesco CARPANESE

■ École
polytechnique
fédérale
de Lausanne

2021

"Bah..."
— F.Carpanese commenting his results

To my wife Elena

Abstract

To exploit fusion as a source of energy, a hot and dense confined plasma is needed. This is achieved in tokamaks by actively controlling the plasma state meaning in particular shape, position and internal kinetic profiles. This thesis addresses two topics: the development of a tokamak simulator to design and test real-time controllers; the reconstruction of the plasma state from diagnostic measurements.

A flexible control oriented simulator is needed to design the feedforward trace of the current evolution in the external conductors and to test/design/verify the controllers that maintain the desired shape, position and vertical stability. A fully Matlab-based suite of routines called "LIUQE-suite", sharing the same optimized low level routines, has been developed at SPC-EPFL addressing multiple problems related to the free-boundary equilibrium. It covers the full range of free-boundary magnetic equilibrium codes from computing the coil currents for a sequence of desired plasma equilibria (FBT code), simulating the plasma magnetic evolution coupled to controller dynamics (FGE code), performing magnetic equilibrium reconstruction (MER) from synthetic/experimental data both in post discharge and for real-time analysis (LIUQE code).

In this thesis, two new codes have been added to this code suite. FGS (Forward Grad-Shafranov Static) which solves the forward static free-boundary equilibrium problem. FGE (Forward Grad-Shafranov Evolutive) which solves the dynamics of conductor current evolution, coupled to the resistive plasma current decay on subsequent states of free-boundary equilibria. Both codes use the Jacobian Free Newton Krylov (JFNK) method, which combines the stability property of the Newton-like algorithm without requiring the explicit Jacobian of the problem. This enables the implementation of a monolithic approach to solve the coupled system of equation and avoids iterative coupling between the free-boundary solution and 0D current diffusion equation (CDE). A particular form of the CDE, derived in this thesis, allows to avoid the expensive computation of the geometrical coefficients in the coupling. A linearized state-space version of FGE is presented, consistently including deformable plasmas and plasma current resistive diffusion. A novel contribution of this thesis is also the derivation of an analytic Jacobian for the free-boundary forward equilibrium problem discretized in space with finite differences, which can enable the implementation of a standard Newton method. FGS was used to investigate the impact of some simplification hypotheses in the LIUQE algorithm, related to the functional dependencies of the synthetic diagnostics on the plasma flux map,

Abstract

finding a small impact to the resulting magnetic equilibrium reconstruction (MER), confirming the robustness of LIUQE code. A proof of principle application of Bayesian analysis to obtain uncertainty quantification for MER is shown. To validate the implementation of FGE, the growth rates of vertical displacement events (VDE) for several TCV plasmas were compared to the rigid displacement RZIP model. After coupling the real vertical stability and position controller of TCV, the request of the central solenoid in the simulation was compared to the experiment, in order to verify the correctness of the CDE implemented. Good agreement was found in all cases, enabling in future a confident use of FGS and FGE for the development of TCV controllers.

Kinetic equilibrium reconstruction (KER) is the consistent reconstruction of the plasma flux surface shapes and internal kinetic profiles combining external magnetic measurements, internal kinetic measurements and/or transport modelling, under the constraint of MHD force balance. KER originated from improving the magnetic equilibrium reconstruction (MER), where only external magnetic measurements are considered, and is becoming a standard post-discharge analysis in many tokamaks as a starting point for stability threshold evaluation and gyrokinetic transport analysis, which are highly sensitive to internal profile features. It is also an important step to compare our understanding of the discharge time evolution combining "all" the diagnostics available, hence also known as integrated data analysis. The real-time KER is much more difficult, and yet compulsory, to inform the controllers and safely achieve burning plasmas close to their maximum performances. The difficulties rely both on the limited set of available real-time diagnostics and on the computational time requirements. This thesis makes significant advances in both off-line and real-time kinetic equilibrium reconstructions.

The KER is formulated, implemented and compared against MER, both in post-discharge and real-time, for several TCV discharges with different physical characteristics. As a result of the limited set of diagnostics, in particular the lack of direct measurements of the internal plasma current density, together with an inaccurate estimate of the ion temperature T_i and effective charge Z_{eff}, the final reconstruction is affected by significant uncertainties. Hence, KER in TCV will need further improvements to obtain an accurate reconstruction in particular of the safety factor profile. On the other hand, the possibility for routine use of KER analysis enabled by this thesis provides insights on which diagnostics and physics to be first improved and/or verified. Moreover the rigorous derivation of KER interpreted as a dynamic state and parameter identification from a forward predictive model contributes to the general understanding of the problem, identifying the limitation of the derivation hypotheses.

Keywords: Tokamak, TCV, vertical stability control, magnetic equilibrium reconstruction, kinetic equilibrium reconstruction, real-time, free-boundary equilibrium, Grad-Shafranov, Jacobian free Newton krylov solver, LIUQE, FGE, FGS, Bayesian parameter estimation, Bayesian equilibrium reconstruction, inverse problem, reconstruction problem, Tokamak simulator, non-linear least-squares optimization, Newton method, analytic Jacobian, LIUQE-suite, meq

Sinossi

Per sfruttare la fusione termonucleare come fonte di energia è necessario confinare un plasma denso ed estremamente caldo ottenuto nei tokamak controllando attivamente la forma, la posizione e i profili cinetici interni al plasma. In questa tesi si affrontano due temi principali: lo sviluppo di un simulatore per il design e la verifica dei controllori utilizzati in tempo reale; la ricostruzione dello stato del plasma utilizzando le misure disponibili.

Un simulatore flessibile orientato al controllo è necessario per preparare i riferimenti di corrente per i conduttori attivi del tokamak a per progettare e verificare i controllori che mantengono la forma, la posizione e la stabilità verticale del plasma. Un insieme di programmi completamente basato sul linguaggio Matlab chiamata "LIUQE-suite", condividendo le funzionalità di base principali, è stato sviluppato al centro di ricerca SPC-EPFL. È dedicato alla soluzioni di problemi legati all'equilibrio di plasmi deformabilii (free-boundary equilibrium). Comprende l'intera gamma di codici che si occupano del calcolo delle correnti dei conduttori per ottenere un plasma desiderato (codice FBT), simulare l'evoluzione magnetica del plasma accopiata ai controllori (codice FGE), calcolare la ricostruzione di equilibrio magnetico sia durante che dopo l'esperimento (codice LIUQE).

In questa tesi sono stati sviluppati due nuovi codici. FGS (Forward Grad-Shafranov Static), che si occupa di risolvere il problema di equilibrio statico per plasma deformabile. FGE (Forward Grad Shafranov Evolutive) che si occupa di risolvere la dinamica di evoluzione delle correnti nei conduttori, accopiata al decadimento resistivo della corrente di plasma, attraverso stati succesivi di equilibrio MHD. Entrambi i codici fanno uso dell'algoritmo Jacobian Free Newton Krylov (JFNK), che combina le proprietà di stabilità di un algorimo di tipo Newton, senza richiedere di calcolare esplicitamente lo Jacobiano del problema. Questo permette l'utilizzo di un approccio monolitico nella soluzione dei problemi senza dover far ricorso a techniche di accoppiamento basato su iterazioni del solutore di equilibrio e del modello di diffusione della corrente. Una particolare espressione per l'equazione di diffusione della corrente è stata derivata in questa tesi che potenzialmente permette di evitare il calcolo dei coefficienti geometrici durante l'accoppiamento, che sono particolarmente costosi in termini di tempo computazionale. Inoltre, viene derivata una linearizazzione di FGE nello spazio degli stati che include consistentemente il modello di plasma deformabile e di diffusione resistiva della corrente. Un ulteriore risultato di questa tesi è la derivazione di uno Jacobiano analitico per il problema di equilibrio per plasmi deformabili, specifico per la discretizzazione con differenze

finite, che permetterebbe l'implementazione di un methodo di algoritmo di Newton standard per la soluzione del problema.

Il codice FGS è stato utilizzato per studiare l'impatto di alcune ipotesi semplificative del codice LIUQE, legate alla dipendenza della diagnostiche sintetiche dalla mappa di flusso del plasma, trovando un impatto molto piccolo sulla soluzione finiale della ricostruzione di equilibrio magnetico MER, cofermando cosí la robustezza del codice LIUQE. Viene anche presentata una dimostrazione dell'applicazione di analisi Bayesiana per ottenere la stima di incertezza per il problema MER. Per validare l'implementazione di FGE, il tasso di crescita della instabilità verticale per diversi plasmi di TCV è stata confrontata con simulazioni di plasma rigido con il modello RZIP. Dopo aver accopiato il controllore di stabilità veriticale e di posizione utilizzato durante l'esperimento TCV, la traccia della richiesta del controllore al solenoide centrale di una risimulazione di un esperimento è stata confrontata con la ricostruzione di equilibrio dei dati reali, per validare il modello di diffusione di corrente implementato in FGE. In tutti i casi studiati si è trovato un buon accordo tra il codice e l'esperimento permettendo cosí in un prossimo futuro di utilizzare il codice per lo sviluppo dei controllori real-time di TCV.

La tecnica della ricostruzione di equilibrio cinetico (kinetic equilibrium reconstruction, KER) è la ricostruzione autoconsistente delle superfici magnetiche del plasma e dei profili cinetici combinando le misure disponibili e/o la modelizzazione teorica del trasporto, soddisfando la condizione di equilibrium di forze del modello MHD. KER è nato come un miglioramento della ricostruzione di equilibrio magnetico (magnetic equilibrium reconstruction MER), dove vengono utilizzate solamente le misure magnetiche esterne al tokamak. KER sta diventando progressivamente una tra le techniche di analisi dati standard in molti tokamak, come punto di partenza per il calcolo delle soglie di stabilità e per modelizzazione di trasporto con codici girocinetici. Queste ultime applicazioni sono particolarmente sensibili ai profili cinetici interni del plasma. Inoltre, KER contribuisce a migliorare la comprensione delle esperimento combinando la maggior parte possibile delle diagnostiche disponibili, da cui deriva il nome, *analisi integrata dei dati* con cui a volte ci si riferisce. Eseguire KER in tempo reale durante un esperimento comporta diverse complicazioni, ma è necessario per dare informazioni ai controllori grazie ai quali si può ottenere attivamente lo stato del plasma, in particolare per plasmi termonucleari (burning plasma) in modo stabile e vicino ai limiti massimi di operazione. Le difficoltà sono legate sia ad un ridotto insieme di diagnostiche disponibili durante l'esperimento, sia agli stringenti limiti di tempo di calcolo. Questa tesi apporta progressi significativi allo sviluppo ed utilizzo di KER, sia durante l'esperimento che nella successiva analisi dei dati.

La tecnica di KER in questa tesi viene formulata rigorosamente, implementata e confrontata con MER, sia in real-time che successivamente all'esperimento, per diversi experiementi di TCV con caratteristiche fisiche differenti. La disponibilità limitata di diagnostiche, in particolare la mancanza di una misura diretta della distribuzione di densità di corrente interna al plasma, insieme alla poco accurata stima della temperatura ionica T_i e della carica efficace

Z_{eff}, portano a forti incertezze nella ricostruzione finale. Pertanto, KER come attualmente implementato per TCV, necessita di ulteriori miglioramenti in particolar modo per ottenere una ricostruzione accurata del profilo del fattore di sicurezza (safaty factor) nel plasma. D'altro canto, la possibilità di far utilizzo di KER in modo semi-automatico ottenuta con questa tesi da la possibilità di identificare quali diagnostiche e quali modellizzazioni è necessario migliorare con priorità. Inoltre, la rigorosa derivazione di KER presentata in questa tesi, interpretando il problema come la ricostruzione dinamica dello stato e dei parametri di plasma dal problema predittivo corrispondente, contribuisce ad una migliore comprensione di KER, identificando le limitazioni delle ipotesi presenti nelle varie implementazioni.

Contents

Contents

1 Introduction

In the last decade (2010-2020) the global warming and the green house effects have become a popular worldwide topics of discussion, driving the attention of the media with an increasing interest of youngest generation. Nuclear fusion could become the holy grail of energy sources. Its main advantages are: carbon free, unlimited fuel mostly taken from the ocean and not localized in few regions of the planet, no long-lived radioactive waste, limited risk of proliferation, no risk of melt-down of the reactor. This process, which takes place in stars and heats them up, is difficult to handle on earth due to the extreme temperature conditions required. After more than 80 years of research, even if several physics aspects are not fully understood, it became mainly a technological issue. It is the conviction of the author of this thesis that human kind will be able to exploit this source of energy one day. The history will tell if this will happen in this century or waiting for new technological discoveries will be needed. Moreover in the next 20 years the results of the ITER experiment, which is supposed to start its first operation at the end of 2025 in Cadarache (France), will be a major turning point to understand how soon a test power plant can be operating.

1.1 Fusion energy and plasma physics

Nuclear fusion is the process in which two or more nuclei are combined to form one or more atomic nuclei of different elements together with other subatomic particles. This is an exothermic reaction when the incoming nuclei are lighter than iron-56 and is the process which allows the formation of new elements in stars. For the reaction to occur the original nuclei, composed by neutrons and protons, must reach a proximity such that the so-called nuclear "strong force" prevails on the repulsion between protons given by the Coulomb force between particles of the same charge. This condition can be achieved only if the incoming nuclei have a velocity (kinetic energy) high enough to counteract the Coulomb repulsion. The kinetic energy manifests itself on the macroscopic scale as the temperature of the medium. Any gas, in a temperature range of 10000K, undergoes a phase transition where a large fraction of the atoms (potentially all of them depending on the temperature) gets ionized. The electrons get detached from the nuclei and free to move independently. When the kinetic energy of

the charged particle exceeds the potential energy of their electrostatic particle-particle attraction/repulsion collective effects, mediated by long range electrostatic interactions, dominate over single particle interaction. When this occurs, the matter reaches the state of "plasma". Most of the observed matter in the universe is found in plasma state both in high density, like the stars, and low density conditions as the interstellar plasma.

The plasma is therefore the natural state to reach conditions such that many nuclei can undergo fusion reactions. A useful consequence of this state is that, since the plasma is composed of charged particles, its behavior can be influenced by external electromagnetic fields thanks to the Lorentz's force $\boldsymbol{F} = q(\boldsymbol{E} + \boldsymbol{v} \times \boldsymbol{B})$, where q is the charge of a single particle composing the plasma, $\boldsymbol{v}$ is the velocity and $\boldsymbol{B}, \boldsymbol{E}$ are the magnetic and electric fields generated either externally or by the charged particles of the plasma themselves. As a consequence of the Lorentz force, the particles will mainly follow the magnetic field lines, allowing to design magnetic field configurations able to confine the plasma. This is the underlying principle of the so called "magnetically confined fusion". A toroidally symmetric (donut shape) magnetic field configuration is the backbone of the device called "tokamak" [Wesson and Campbell 2011] exploited in this thesis.

1.1.1 Conditions for fusion reaction and plasma confinement

Exploiting nuclear fusion as a commercial source of energy requires a large fraction of plasma particles to achieve the physical condition for the reactions to occur, therefore the plasma must become sufficiently dense and hot. Out of the possible fusion reactions, the one with the highest probability at lowest temperature is the reaction between the two isotopes of Hydrogen, the Deuterium ($_1^2D$) and Tritium ($_1^3T$),

$$_1^2D + _1^3T \rightarrow _2^4H_e(3.5\text{MeV}) + n(14.1\text{MeV}). \tag{1.1}$$

Unfortunately a large instantaneous fusion reaction rate is not sufficient for continuous energy generation. The energy released by the fusion reaction must be confined inside the plasma for a long enough time to allow heating other "colder" particles and bringing them to fusion condition. This concept is expressed by the energy confinement time (τ_E) defined as the ratio between the plasma total energy and power losses. The condition at which the plasma ignites, hence when a chain of fusion reactions is sustained by the energy released by fusion reactions themselves, is expressed by the Lawson's criterion [Lawson 1955] in terms of the "triple" product $nT_e\tau_E$ where n and T are the density and temperature of the plasma.

$$nT_e\tau_E \geq 3 \times 10^{21} m^{-3}[keV\,s] \tag{1.2}$$

Given the optimal T fixed by the D-T reaction cross-section $T \sim 20keV$, a minimum requirement for the product $n\tau_E$ is obtained. This requirement can be achieved both by increasing the density or the confinement time τ_E, which leads to the two paradigms of nuclear fusion research: the "inertial" confinement fusion and the "magnetically confined fusion" respec-

tively. The first aims to achieve high density, but small confinement time, by compressing small capsules containing the isotopes ($^2_1 D$) and ($^3_1 T$) shooting lasers to the target. The most advanced experiment in this respect is the NIF [Patel et al. 2020] facilities in Livermore (USA), The second approach aims instead to use a low density plasma, much less dense than the atmosphere on earth, but higher τ_E. The confinement, as anticipated, is obtained by properly designing the shape of the magnetic fields generated both externally with solenoids and by the current flowing in the plasma.

After the first linear devices developed in the 1940s, two main toroidal devices have emerged which are shown in figs. 1.1 and 1.2. In the stellarator concept, invented by Lyman Spitzer of Princeton University in 1951 [Bishop 1958], the magnetic field confining the plasma is fully generated by external coils. It has the advantages to not give rise to disruptive plasma instabilities, due to almost null net plasma current flowing in the toroidal direction, and to naturally allow for stationary operation that would be desirable for a future power plant. However so far the stellarator concept has not achieved the same performance, in terms of Lawson criterion, as the tokamak concept explained in the following. Notably the recent experiment Wendelstein 7-X (W7X) [Wolf et al. 2019] is providing significant advancements thanks to the optimized magnetic field configuration developed. The tokamak concept, invented by the Soviet Physicists Igor Tamm and Andrei Sakharov in early 1950s, is a toroidally symmetric device where the total magnetic field is generated both by the plasma current and by external magnetic fields. So far it has reached the best performance in terms of triple product but it suffers from disruptive instabilities, mainly due to the presence of the large total toroidal plasma current itself.

Tokamaks and stellarators have both achieved the reactor relevant target temperatures and densities independently, but not at the same time with a sufficient τ_E, hence the Lawson's criterion has not been met yet. The worldwide effort culminated in the results achieved in 1997 [Keilhacker et al. 1999] by the Joint European Torus, with the production of 16 MW of fusion power. Even though the plasma transport physics is not yet fully understood, it is known to improve with the dimension of the machine. This motivated the design of the new experiment ITER as a joint effort of seven members: China, European Union with Switzerland, India, Japan, Russia, South Korea and the United States. The goal is to exceed the break-even condition, $Q = P_{fus}/P_{aux}$=1, where P_{fus} is the fusion power and P_{aux} the auxiliary heating provided externally, and to produce ten times more fusion power than what is required externally to heat up the plasma ($Q = 10$). This will be the step in between an experimental facility and being able to design a power plant scale device.

The ITER experimental results will be a major turning point for the fusion research and if successful a big step in the history of human kind.
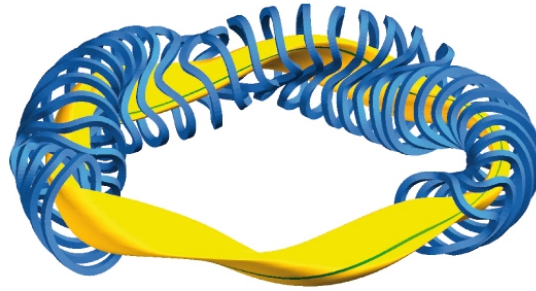
Figure 1.1 – W7-X schematic drawing. External coils in blue and plasma in yellow.
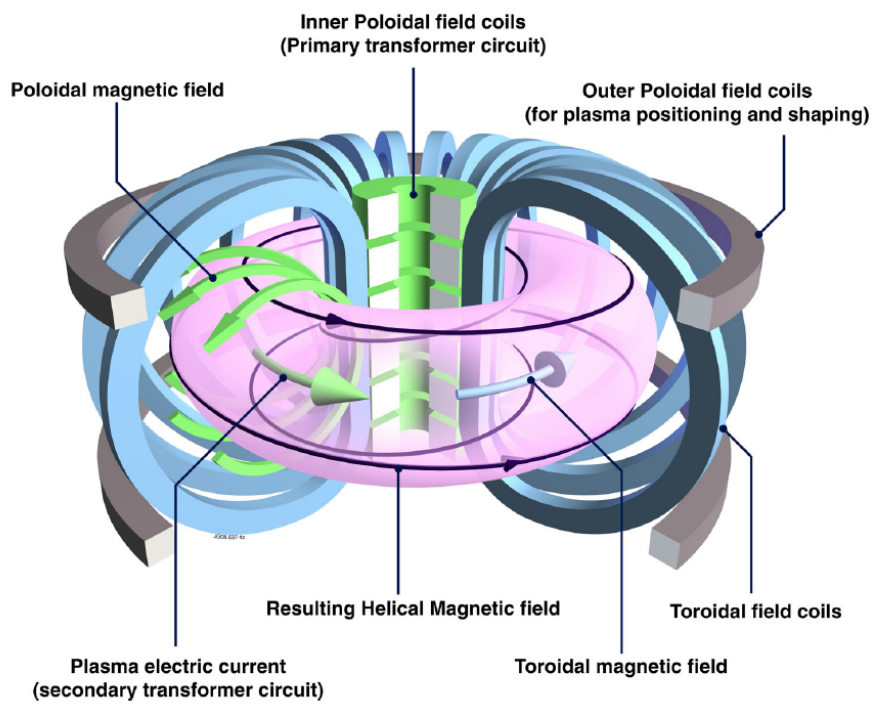
Figure 1.2 – Tokamak schematic drawing.

1.2 The Tokamak device

The tokamak will be the only device analysed in this thesis since most part of the results presented have been obtained with TCV (Tokamak a configuration Variable [Coda et al. 2019]) at the SPC (Swiss Plasma Center).

1.2.1 Magnetic field and coil systems

The skeleton of the tokamak is a toroidally symmetric (donut shape) device composed by three main sets of coils as shown in figure 1.2. The main magnetic field is the one in the toroidal direction (around the torus) generated by a set of identical toroidal field coils (in blue). The plasma charged particle, as a first order motion, will gyrate around the magnetic field lines (black lines) performing simple revolutions around the torus. Unfortunately a pure toroidal magnetic field is not sufficient to confine the plasma, since gradient and curvature of the toroidal magnetic field generate a radial drift motion for the particle. A second component, orthogonal to the toroidal field, called "poloidal field", is needed. This component is generated mainly by the toroidal plasma current induced by the primary transformer circuit, called also Ohmic coil (OH), and partially by the poloidal field coils (gray) controlled externally, together with eventual external current drive systems.

The Ohmic coil, inducing current in the plasma, helps heating the plasma by resistive heating. A continuous increase of the current in the Ohmic coils is needed in order to sustain the natural resistive decay of the plasma current due to Coulomb collisions of plasma particles. This is one of the intrinsic limitations of the tokamak device since OH coil current cannot ramp-up indefinitely, hence the tokamak operates with repeated pulses unless other non-inductive means of driving the plasma current are exploited.

The shape of the plasma is defined by the surfaces (magenta surface) on which the magnetic field lines lay (black helical lines wounding the surface). Taking a section of the torus with a vertical plane, the projection of the magnetic field lines on the plane generates the red contour line in figure 1.3. The surfaces are typically composed by nested flux surfaces up to the so called Last Closed Flux Surface (LCFS) which ultimately defines the outermost shape of the plasma. In a tokamak, in general, the LCFS terminates on the divertor region prolonging into two legs up to the strike points. The strike points end on the divertor plates where most of the exhausted heat of the plasma is released. The shape of the LCFS as well as the location of the strike points are controlled by the poloidal field coils.

1.2.2 Auxiliary heating and current drive systems

In order to sustain the tokamak operation two requirements are needed: generate the plasma current which together with the external coils provide the magnetic field topology confining the plasma; heat and fuel the plasma. The plasma current naturally decays if not sustained

externally, and becomes a source of heat. However, the resistivity scales as $\eta \sim T_e^{-3/2}$, where T_e is the electron temperature. Opposite to metals and other materials, the hotter is the plasma the smaller the resistivity. This is beneficial for driving the plasma current but limits the maximum achievable heating. Auxiliary devices have been developed to both heat and drive plasma current. These are based on two main concepts: injection of fast particles which release their energy inside the plasma and injection of electromagnetic waves which resonate with plasma characteristic frequencies releasing their energy.

In Neutral Beam Injection (NBI) heating and current drive (NBCD), highly energetic neutral particles are injected into the plasma. Since the particles are neutral, they can penetrate the confining magnetic field till they get ionized inside the plasma, where they release their energy. Depending on the injection aiming direction, the total amount of current drive can change. Moreover the NBI is an important source of rotation for the plasma.

Injecting an electromagnetic wave inside the plasma contributes to heat the plasma and can drive current. Depending on the frequency, the wave can interact more with electrons or with ions. The ion cyclotron resonance heating (ICRH) is a low radio frequency (30MHz to 55MHz), it couples mainly with the ions and requires an antenna in the proximity of the plasma region. The Electron Cyclotron Resonance Heating (ECRH) and Electron Cyclotron Current Drive (ECCD) heats the electrons with high-frequency waves (100 GHz to 170 GHz) which resonate with the electron cyclotron motion around the field lines. The ECRH and ECCD can deliver current and heat in a very localized and controllable region of the plasma and therefore they are used in order to control a certain class of plasma instabilities. The Lower Hybrid Resonance Heating (LHRH) and current drive (LHCD) use an intermediate frequency to heat the plasma and drive current.

All the systems have advantages and disadvantages. For example the ECRH has a simple design and the wave can be generated away from the tokamak and carried to the device through wave guides. However, the ECCD efficiency is lower than LHCD. A combination of the systems is therefore needed to operate a tokamak. For example the design of ITER includes NBI, ICRH and ECH where each of them will have different roles. Together with the external magnetic field coils, they constitute the actuators to control the experiment.

1.2.3 Tokamak parameters and plasma scenarios

The performances of the plasma in a tokamak are measured by a number of global and local parameters. The total plasma current I_p is defined by the flux of the toroidal component of the plasma current density in the poloidal cross section. I_p, after an initial ramp-up phase, is maintained stationary and then ramped-down at the end of the experiment. The normalized pressure factor β is the ratio between the volume averaged thermal pressure and the averaged

magnetic field pressure:

$$\beta = \frac{<p>}{B_0^2/2\mu_0},\qquad(1.3)$$

where B_0 is the magnitude of the vacuum magnetic field at the device major radius R_0. β is an important figure of merit since the goal of fusion energy is to achieve the highest fusion power, which is proportional to p, when the maximum B_0 is set by the mechanical limit of the materials and feasibility of high B_0, and is the "cost" for confining.

Increasing p and I_p leads the plasma to an unstable state as briefly discussed in the next section. The parameter

$$\beta_N = \frac{\beta[\%]}{I[MA]\,a[m]\,B_0[T]}\qquad(1.4)$$

allows to express the proximity to the tokamak stability limit [Troyon et al. 1984].

Apart from the global quantities, many spatial dependent quantities play a role both for the stability and the global performances of the plasma. The magnetic topology of the plasma is characterized by nested flux surfaces up to the LCFS as shown in fig. 1.3. By defining a radial coordinate which labels these surfaces we can define 1-dimensional radial profiles from the plasma axis towards the edge. Some quantities are constant on these 2D toroidally symmetric surfaces while for others an average on the surface can provide 1D profiles.

The ion and electron temperatures T_e, T_i and densities n_e, n_i are almost constant on flux surfaces, and directly define the total plasma pressure hence β. These are usually called kinetic profiles.

The distribution of the plasma current density contributes both to the plasma transport and stability. Strictly related to this quantity is the "safety factor" q. The magnetic field lines wrap around the flux surfaces as shown by the black lines in fig. 1.2 generating a spiral. q is the ratio of the number of times a particular magnetic field line travels around the toroidal direction "long way" (toroidally) to the "short way" (poloidally), i.e. a measure of the helicity of the spiral. Since the magnetic field lines are generated both by the plasma and the external currents, q is a result of the plasma state and external actuators. Many types of plasma instabilities are related to the value of q, hence the name "safety factor".

The shape of the kinetic and plasma current density profiles define different plasma operation regimes. For example the High confinement mode (H-mode), the standard operating mode for ITER, presents a characteristic very steep pressure gradient in the proximity of the plasma edge, which affects also the distribution of the plasma current.

An accurate identification of the kinetic and plasma current density profiles is therefore important both for plasma operation and post-discharge analysis and will be one of the topic of this thesis.

1.2.4   Plasma MHD instabilities during operation

Unstable states lead to degradation of performances and in the worst case to an abrupt interruption of confinement releasing a large amount of energy to the tokamak structure. This event is called disruption and in large devices, such as ITER, can limit the lifetime of the machine. The triggering phenomena and onset thresholds for these instabilities have not been completely understood for all of them. Plasma operation stays away from operational regions where these are expected to occur and/or mitigate/suppress their effects when required.

We list in the following some of these instabilities in order of appearance from the outside of the plasma toward the plasma axis. We consider only macroscopic instabilities, described by the Magneto-Hydrodynamics MHD [Freidberg 2014], of first concern during tokamak operation [Hender et al. 2007].

- Vertical displacement event (VDE): The plasma force balance equilibrium obtained with the magnetic field is globally unstable. The plasma drifts away from the original position with a mainly rigid displacement. This instability is ubiquitous during plasma operation and needs to be actively controlled exploiting external coils. In this thesis we will develop a code to simulate the initial phase of this instability [Hender et al. 2007] and to help designing real-time controllers.

- β limit/Resistive wall Mode (RWM): Increasing the plasma pressure and current leads the plasma to unstable conditions occurring as a helical deformation of the plasma. This instability can be mitigated/suppressed by adding a conductive wall in the proximity of the LCFS. The closer the plasma to the wall the better the stabilization indicating the importance to fine control the plasma shape [Chu and Okabayashi 2010], but then RWM can occur, and closer wall is leading to higher growth rate.

- Edge Localized Modes (ELMs): These modes are an exclusive feature of H-mode plasma operation. The steep edge pressure gradient suddenly collapses releasing particles and plasma energy to the divertor plates. ELM-free regimes with H-mode performances have been studied in recent years and require specific design of the internal plasma profiles trajectories to reach the condition. A recent promising discovery is the possibility of achieving H-mode like performances remaining in L-mode with a plasma shape characterized by negative triangularity [Austin et al. 2019].

- Neoclassical tearing mode (NTM): When a finite resistance of the plasma is considered, the nested shape of the flux surfaces can break into local independent regions called islands. This occurs in regions of rational value of q. An accurate knowledge of the location in space of these regions allows to steer the external source of heating and current drive to suppress these instabilities which deteriorates the plasma performances [Zohm et al. 1999].

- Sawtooth: a periodic sudden relaxation of the core pressure appearing when the safety factor drops below 1. Though they might be beneficial to remove ashes from the plasma
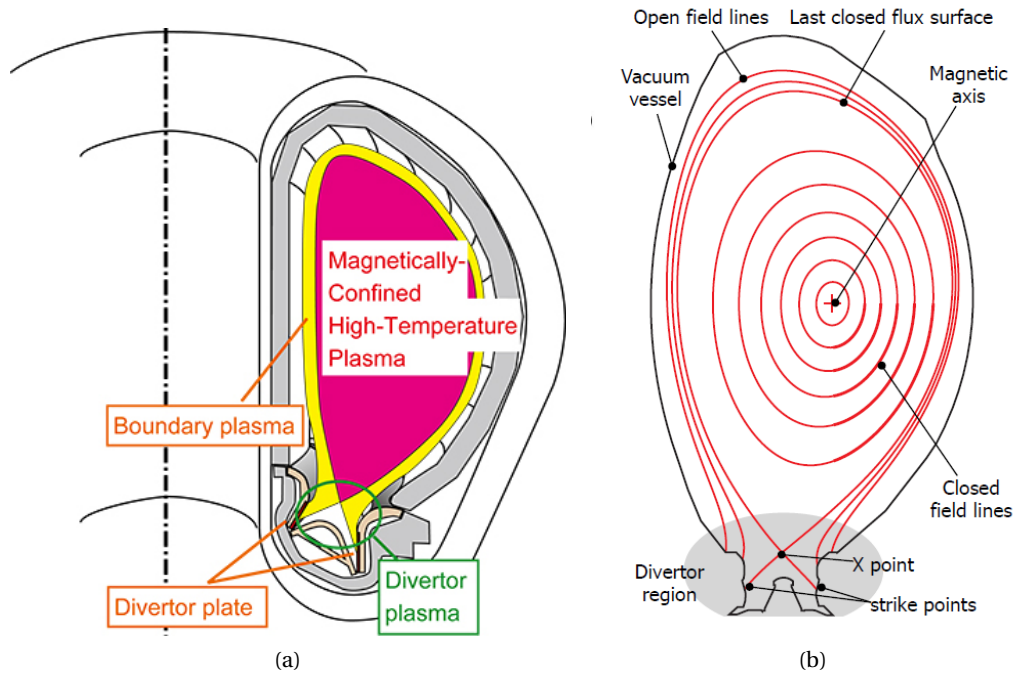
Figure 1.3 – Tokamak poloidal cross section [Teplukhina 2018]

core they can trigger NTMs. The control of current density affects their behavior [Chapman 2010].

The triggering and evolution of these MHD instabilities are all affected by the plasma shape and internal profiles. An accurate reconstruction during plasma operation is therefore important as input to the real-time controllers.

1.3 Tokamak operation overview

While the target that needs to be achieved to exploit nuclear fusion as a source of energy is clear and summarized by the Lawson's criterion, plasma physics sets many requirements/constraints/limits for the tokamak operation. Achieving the desired target respecting all of them robustly and repeatedly is necessarily not only for the present and future experiments but even more so for the future power plants. The tokamak operation can be summarized by the schematic picture in figure 1.4. The picture does not want to be exhaustive but only to show the main aspects that will be addressed in this thesis.

Operation requests

We start from the requests which are the target for the operation aimed for. We divide them between "normal operation" and "off-normal events".

The first normal operation request is to safely initialize the plasma, ramp-up the plasma current, achieve and maintain the stationary operation point and ramp-down the plasma current. During all these phases the control of plasma shape and strike point locations are required. TCV in this respect is a unique tokamak in terms of plasma shape flexibility. At the stationary operating point, both some global plasma parameters and specific kinetic and current density profiles are needed to enter the desired plasma scenario.

The "off-normal" events are for example the instabilities presented in the previous section which require active control during plasma operation and are influenced by plasma shape and internal kinetic profiles.

Actuators

The operation requests are converted into requests for the available actuators. Those are primarily the currents in the coils and the heating, fueling and current drive systems described in previous section.

Diagnostics

The actuators drive the experiment and the diagnostics measure its performances. These are composed both of magnetic diagnostics placed externally to the plasma volume and diagnostics able to measure the internal kinetic and current density profiles. The set of TCV diagnostics will be specified later in this thesis. Only a subset of the diagnostics provides data with a time resolution suited for real-time application.

State reconstruction

The raw signals of the diagnostics need to be interpreted to extract the plasma parameters of interest. For example from the measurements of the external magnetic fields, assuming the plasma in an equilibrium state, one can infer the flux surface shapes. This allows to map the kinetic measurements into 1D radial profiles from the plasma axis to the edge. The reconstruction of shape and profiles, known in control theory as parameter and state reconstruction, is crucial both during real-time operation and for the post-discharge analysis.

Control

Given the observed plasma state, the control block aims to change the requests of the actuators in order to achieve a different target. This can be done both from one experiment to the next or in real-time. Controlling the plasma is required both to achieve a normal operation condition and to avoid/mitigate/correct off-normal events. However, a large number of control targets need to be satisfied with a relatively small number of actuators, which therefore need to be shared among the tasks with a careful prioritization [Blanken et al. 2019], [Vu et al. 2019].
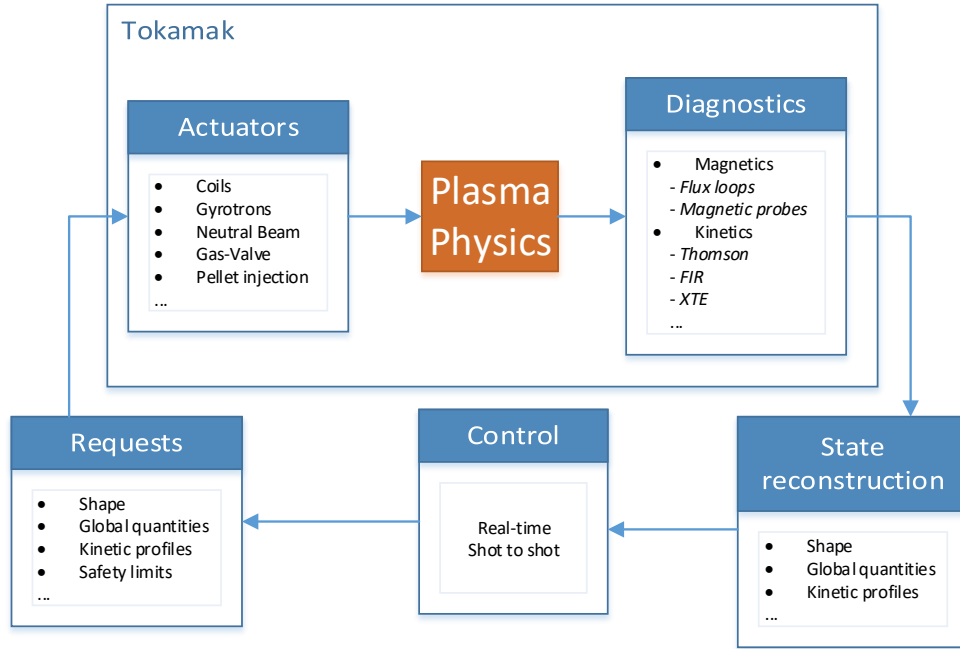
Figure 1.4 – Operation phases in tokamak experiment

1.4 Motivation for this thesis

The tokamak is a complex device where many different components have to work together in order to achieve the target operation condition being constrained by the plasma physics and avoiding development of detrimental instabilities. This thesis focuses on two fundamental aspects of the tokamak operation represented by the "plasma physics" block, developing a simulator, and "state reconstruction" block in fig. 1.4.

Predictive simulator for plasma shape, conductor current evolution and plasma current resistive diffusion

Starting from the low level routines developed for the code LIUQE [Moret et al. 2015], a simulator is developed to describe the evolution of the plasma shape coupled to the evolution of the currents in the coils and passive conductors, including the dynamics of the vertical displacement event in its early phase and including a simplified dynamics for the resistive decay of the plasma current. The purpose was to extend the suite of codes available at our institution to help the design of real-time controllers for vertical stabilization, position, shape and total plasma current control, which is the very basic aspect of tokamak operation. Similar codes already existed before this thesis. In the simulator presented in this thesis some novel numerical algorithms have been explored which allowed flexibility to address many different problems within the same framework and to quickly test new physics modules.

11

Real-time and post-discharge consistent reconstruction of plasma shape and kinetic profiles

Obtaining an accurate reconstruction of the plasma state from the available diagnostics is necessarily to interpret the experimental results, design new experiments and to provide, in real-time, the observed inputs for the controllers in order to drive the actuators and obtain the desired performances and avoid/correct off-normal events. The shape of the internal flux surfaces of the plasma is intrinsically related to the kinetic plasma profiles and, at the same time, the evolution of these profiles depends on the plasma shape. However a consistent reconstruction of these two aspects, the plasma shape and the kinetic profiles, merging together information from first principle models and available diagnostics, is still an open field of research leading to the so called kinetic equilibrium reconstruction or integrated data analysis. In this thesis we develop and test new tools and models to perform kinetic equilibrium reconstruction both for the post-discharge analysis and real-time reconstruction for TCV experiment.

1.5   Thesis outline

The first chapter is dedicated to a brief introduction to plasma physics, thermonuclear fusion and the tokamak device. The focus is put on the different experimental operation phases in order to provide the motivation of the thesis to study both the simulation and reconstruction of the plasma state.

The thesis content is divided into two parts. The first part aims to formulate the analytic problems addressed in this thesis while the second presents their numerical implementation and applications.

Part I

- In Chapter 2 the forward/predictive problems are presented. Within the MHD model we focus on the coupled dynamics of the free-boundary plasma equilibrium, the evolution of the current in tokamak external conductors and the evolution of the flux surface averaged plasma current density and kinetic profiles.

- A reconstruction problem aims to find the best estimate of plasma state and parameters combining noisy/redundant measurements and uncertain first-principle models. In Chapter 3 the reconstruction/interpretative problems is derived from their equivalent forward/predictive models, by making assumptions on the measurement and model uncertainties and adopting a statistical interpretation. We derive first the reconstruction problem for the plasma shape, pressure and current profiles from the external magnetic measurements constrained by the MHD free-boundary equilibrium, obtaining the magnetic equilibrium reconstruction (MER) problem. After discussing MER limitations, the Kinetic Equilibrium Reconstruction (KER) problem is obtained where

models for the free-boundary equilibrium and kinetic profiles evolution are treated consistently together with external magnetic and internal kinetic measurements. A reduced formulation suited for the set of TCV diagnostics is provided. KER can be performed relatively routinely in many institutions with different approaches but often considered as a simple integration of existing tools. This thesis contributes to interpret KER as a unique framework for all reconstruction problems providing a detailed description of assumptions and limitation during the derivation.

Part II

- In Chapter 4 we present the new forward/predictive codes developed in this thesis based on the low-level routines of the free-boundary equilibrium reconstruction code LIUQE. They include: a forward static free-boundary equilibrium code (Forward Grad-Shafranov Static "FGS"); a forward free-boundary equilibrium code coupled to the dynamics of active and passive conductors and including 0D equation for the resistive evolution of the total plasma current (Free-boundary Grad-Shafranov Evolutive "FGE"); a linearization of FGE on trajectories of solutions of the free-boundary equilibrium, providing also its state space representation. The use of the Jacobian Free Newton Krylov Solver (JFNK) algorithm to solve all the formulated problems, the monolithic coupling of the current diffusion equation with the free-boundary equilibrium evolution and the derivation of the linearized problem including both a free-boundary equilibrium and the current diffusion are novel contributions of this thesis. The Vertical displacement event growth rate of FGE is benchmarked with rigid displacement RZIP model. The current diffusion equation is validated against experiment after coupling FGE with the TCV real-time controller. The code is now used to improve and design vertical stability and shape controllers. A magnetic equilibrium reconstruction code is implemented starting from FGS. This allows to investigate limitations/simplifications of the equilibrium reconstruction code LIUQE. A novel contribution of this thesis is the numerical demonstration of the difference between the proper solution of the non-linear least-squares magnetic equilibrium problem and the "quasi-linear" approach adopted in LIUQE, in presence of noisy measurements. This is detailed in Appendices E and F. Furthermore, a preliminary example of magnetic equilibrium reconstruction considered as a Bayesian parameter estimation is provided, based on the FGS code, and compared with the standard least-squares approach previously discussed. It shows how uncertainty quantification can be computed for the equilibrium reconstruction problem. FGS is used to generate synthetic data for an ITER standard H-mode equilibrium with realistic kinetic profiles to compare different reconstruction solutions.

- In Chapter 5, the implementation of kinetic equilibrium reconstruction developed during this thesis for post-discharge analysis in TCV is presented. This couples the free-boundary equilibrium reconstruction code LIUQE [Moret et al. 2015], the transport code ASTRA [Pereverzev and Yushmanov 2002], the ray-tracing code Toray-GA [Matsuda

1989], the kinetic and magnetic measurements. We investigate the sensitivity of the equilibrium reconstruction to internal plasma profiles on a database of TCV discharges with different physical content and the comparison between MER and KER for few discharges with significant plasma profile features generated by external heating and current drive and plasma transport.

- In Chapter 6 we present the implementation and first time application of kinetic equilibrium reconstruction in real-time during tokamak operation, including consistently a magnetic equilibrium reconstruction code LIUQE, a transport code RAPTOR [Felici et al. 2018] and magnetic and kinetic measurements. The results have been published in [Carpanese et al. 2020].

- In Chapter 7 summary and outlooks are provided.

- In Appendix A we briefly discuss the Kalman Filter technique to perform state and parameter estimation combining dynamic models with available measurements.

- In Appendix B the estimate of the effective charge from the flux surface averaged plasma current diffusion is described as implemented in the kinetic equilibrium reconstruction post-discharge analysis.

- In Appendix C the formulation of an analytic gradient for the free-boundary equilibrium problem with finite difference spatial discretization is derived. This derivation is a novel contribution of this thesis.

- In Appendix D we describe the Jacobian Free Newton Krylov (JFNK) to solve root-finding type problems.

- In Appendix E we discuss analytically the difference between the solution of linear and "quasi-linear" least-squares optimization problems.

- In Appendix F we discuss the application of the Lagrange's multipliers to show the difference between the solution of linear and "quasi-linear" least-squares optimization problem with equality constraint, in order to explain analytically the difference between the solution of the LIUQE reconstruction code and magnetic equilibrium reconstruction performed with the FGS code developed in this thesis.

- In Appendix G the derivation of the integral current diffusion equation as implemented in FGE is provided. Also this derivation is a novel contribution of this thesis.

Other work carried out during this thesis

During the thesis the author participated to other scientific works not mentioned in the chapters which are listed here for completeness.

- Contribution to several weekly code camps to provide TCV magnetic data, first into the EU-ITM data structure contributing to [Pinches et al. 2021], and then to the IMAS/IDS framework [Pinches et al. 2017], within the EUROfusion Project on Code Development for Integrated Modelling (WPCD) contributing to [Pinches et al. 2021]. This work included the porting of the LIUQE code to read IMAS/ITM data structure.

- First benchmark of LIUQE against EFIT equilibrium reconstruction code for ITER H-mode discharge synthetic data [F.Carpanese 2017] which led to start a more extended benchmark (2020) to assess its potential use during ITER operation.

- During a visit at ITER and in collaboration with ITER-IO (2020), LIUQE equilibrium reconstruction code was interfaced with ITER Plasma Control System Simulation Plant-form (PCSSP) [Walker et al. 2014].

- Main supervisor of the Master Thesis of Lucas Marietan [Marietan], where the routines to perform post-discharge kinetic equilibrium reconstruction analysis developed in this thesis have been used to quantitatively compare kinetic and magnetic equilibrium reconstruction for TCV.

Formulation of the problems Part I

2 Forward/predictive problems

In this chapter we derive the formulation of the forward/predictive models addressed in this thesis.

We start by revising the transport in tokamak on resistive time scale ordering. Then in section 2.2 and 2.3, from the static free-boundary MHD equilibrium, we couple it to the evolutionary equations for the current in the active and passive structures. We derive in section 2.4 a 0D current diffusion equation, integrating the flux surface averaged poloidal flux evolution, and we briefly discuss the heat and particle flux surface averaged transport equations.

2.1 Diffusion and transport in tokamaks with resistive time scale ordering

Citing directly from [Fasoli et al. 2016]: "Magnetic-fusion plasmas are complex self-organized systems with an extremely wide range of spatial and temporal scales, from the electron-orbit scales ($\sim 10^{-11} s$, $\sim 10^{-5} m$) to the diffusion time of electrical current through the plasma ($\sim 10^2$ s) and the distance along the magnetic field between two solid surfaces in the region that determines the plasma–wall interactions ($\sim 100 m$). The most straightforward way for describing plasmas would be the microscopic particle approach: solving the equations of motion for the many individual particles that form the plasma in externally imposed electromagnetic fields and in the fields that the particles themselves generate. However, this is computationally impossible to apply to realistic magnetic-fusion plasmas, which typically contain 10^{22}–10^{23} particles".

Every plasma model of practical use is therefore targeted to a small spatial and time scale range and aims to address specific aspects of the plasma physics. In this thesis we are interested to investigate the basic aspects of the tokamak operation, in particular:

1. Macroscopic force balance equilibrium between the plasma pressure and the electromagnetic forces.

2. The radial (across flux surface) diffusion of kinetic and plasma current profiles.

3. The evolution of plasma through subsequent states of equilibrium due to the evolution of both external current in conductors and plasma profiles.

We are interested both in developing predictive capabilities (problems described in this chapter) and to reconstruct these plasma states from available measurements in post-discharge analysis and during the experiment (problems described in next chapters).

These aspects are found in spatial scales of the order of fraction of the plasma minor radius a, comparable to fraction of the size of the vacuum chamber of the device ($a \sim 25$cm in TCV), where the kinetic profiles are described. For the time scales we will make a distinction which will be clearer in the following.

The time and spatial scale of these aspects fit the Magnetic Hydro Dynamic model under the resistive time scale ordering. This is derived and described rigorously in many textbooks and manuals [Jardin 2010; Pereverzev and Yushmanov 2002; Blum and Le Foll 1984; Hinton and Hazeltine 1976]. We discuss here only the key aspects and hypotheses leading to a system of equations describing the phenomena of interest.

In the spatial scale of interest, the fluid can be described by the scalar pressure two-fluid MHD system of equations.

$$n_i m_i \left(\frac{\partial \boldsymbol{u}}{\partial t} + \boldsymbol{u} \cdot \nabla \boldsymbol{u} \right) + \nabla p = \boldsymbol{j} \times \boldsymbol{B} \tag{2.1}$$

$$\frac{\partial n_i}{\partial t} + \nabla \cdot (n_i \boldsymbol{u}) = S_{n,i} \tag{2.2}$$

$$\frac{\partial n_e}{\partial t} + \nabla \cdot (n_e \boldsymbol{u}) = S_{n,e} \tag{2.3}$$

$$\frac{3}{2} \frac{\partial p_i}{\partial t} + \nabla \cdot \left[\boldsymbol{q}_i + \frac{3}{2} p_i \boldsymbol{u} \right] = -p_e \nabla \cdot \boldsymbol{u} + \boldsymbol{j} \cdot \boldsymbol{R} + Q_{\Delta_{ie}} + S_{ii} \tag{2.4}$$

$$\frac{3}{2} \frac{\partial p_e}{\partial t} + \nabla \cdot \left[\boldsymbol{q}_e + \frac{3}{2} p_e \boldsymbol{u} \right] = -p_e \nabla \cdot \boldsymbol{u} + \boldsymbol{j} \cdot \boldsymbol{R} + Q_{\Delta_{ei}} + S_{ee} \tag{2.5}$$

$$\frac{\partial \boldsymbol{B}}{\partial t} = -\nabla \times \boldsymbol{E} \tag{2.6}$$

$$\boldsymbol{E} + \boldsymbol{u} \times \boldsymbol{B} = \boldsymbol{R} \tag{2.7}$$

$$\boldsymbol{j} = n_i z_i \boldsymbol{u}_i + n_e z_e \boldsymbol{u}_e \tag{2.8}$$

In the system we defined with n_i the density of the ions, n_e the density of the electrons and z_i, z_e their respective charges. We consider for the moment only the presence of electron and ions with a single charge and the quasi neutrality condition reads $n = n_e = n_i$. The mass bulk fluid velocity $\boldsymbol{u} = (m_e n_e \boldsymbol{u}_e + m_i n_i \boldsymbol{u}_i)/(m_e n_e + m_i n_i) \sim \boldsymbol{u}_i$, is approximately equal to the ion bulk velocity $\boldsymbol{u}_i$ since $m_i \gg m_e$. We indicate with $p = p_e + p_i$ the total plasma pressure, with S_{n_e} and S_{n_i} the sources of particles, with q_i and q_e the heat fluxes, with $Q_{\Delta_{ei}}$ and $Q_{\Delta_{ie}}$ the

exchange of heat between species and with S_{ii} and S_{ee} the sources of heat, for the electron and ion species respectively. The Q_Δ represents the collisional exchange of energy between particles and $\boldsymbol{R}$ the collision exchange of momentum which, in its most simple expression, can be represented by the scalar Ohm's law $\boldsymbol{R} = \frac{1}{\eta}\boldsymbol{j}$, where η is the plasma resistivity.

We can recognize in order, the total momentum balance equation eq. (2.1), the particle density conservation for the species eq. (2.2) and eq. (2.3), the heat diffusion equations for the species eq. (2.4) and eq. (2.5), the Faraday's law eq. (2.6) and generalized Ohm's law eq. (2.7). The system of equations still needs a closure to relate the fluxes and cross exchange sources/sinks to the kinetic quantities. These are given in the many references [Jardin 2010; Pereverzev and Yushmanov 2002; Blum and Le Foll 1984] and we will provide only some specific cases when needed in the next sections.

There are two important time scales in the system of equations eq. (2.1) and eq. (2.7). We define first the Alfven velocity,

$$V_A = \frac{B}{\sqrt{\mu_0 n_i m_i}} \tag{2.9}$$

which represents the travelling velocity of typical oscillation of ions (hence the bulk mass of the plasma) and magnetic fields. The Alfven time τ_A is the characteristic time of propagation of the previously described waves in the system,

$$\tau_A = \frac{a}{V_A}, \tag{2.10}$$

where a is the minor radius of the plasma approximately equal to the radial dimension of the vacuum chamber. The resistive time scale,

$$\tau_R = \frac{\mu_0 a^2}{\eta} \tag{2.11}$$

is the characteristic time of momentum transport due to particle collisions. The ratio of the two time scales defines the Lundquist non dimensional parameter $S \equiv \frac{\tau_R}{\tau_A}$. This number for modern fusion experiment is typically $S \sim 10^6 - 10^{12}$, meaning that the propagation of the ions/magnetic field oscillations in the system is much faster than the momentum diffusion from collisions.

We are now interested in phenomena of the order of the resistive time $t \sim \tau_R \sim S\tau_A$. We can use $\epsilon = S^{-1}$ as a small parameter to perform the ordering expansion. We consider first all the sources of dissipation to be small,

$$\eta \sim \boldsymbol{R} \sim S_n \sim S_e \sim \boldsymbol{q}\epsilon \ll 1. \tag{2.12}$$

Moreover, we look for solutions in which all the time derivatives and velocities are of order ϵ,

$$\frac{\partial}{\partial t} \sim \boldsymbol{u} \sim \epsilon \ll 1, \tag{2.13}$$

and also the electric field is considered to have the same order $\boldsymbol{E} \sim \epsilon$.

If we apply this scaling to the system of equations eq. (2.1) to eq. (2.7), all the equations remain unchanged, only picking up an ϵ factor in front, except the momentum balance equation,

$$\epsilon^2 n m_i \left(\frac{\partial \boldsymbol{u}}{\partial t} + \boldsymbol{u} \cdot \nabla \boldsymbol{u} \right) + \nabla p = \boldsymbol{j} \times \boldsymbol{B}. \tag{2.14}$$

The derivation is found in [Jardin 2010]. In the limit $\epsilon - > 0$, we can neglect the inertial $n m_i$ term and obtain the force balance equation $\nabla p = \boldsymbol{j} \times \boldsymbol{B}$, the ideal massless MHD force balance, also called the "plasma equilibrium equation".

Some important remarks on the obtained set of equations.

- Having removed from the system the inertial terms has the consequence to remove all the wave behavior of the system, in particular all the instabilities. The remaining system indeed is represented only by diffusion equations, hence parabolic type equations, with the force balance as a constraint.

- If we did not consider a scaling assumption for the time derivatives and velocity, we would have obtained the ideal MHD system of equations. The instabilities of the ideal MHD are of major concern for tokamak operation when the pressure and current overcome a certain threshold. These instabilities are removed with the resistive time scale ordering.

- The velocity of the plasma $\boldsymbol{u}$ is not removed from the system, since it is still present in the equations except the force balance equation. The plasma therefore can still move, but only through equilibrium states, meaning through states which respect the force balance equation.

- The force balance equation is not in its final used in this thesis. Exploiting the toroidal symmetry of the tokamak device, one can reduce its dimensionality. This will lead to the Grad-Shafranov equation discussed in the next section. The solution of the force balance equation is represented by nested surfaces at constant poloidal flux and constant pressure, where the magnetic field lines lie. We will define a coordinate system moving with the flux surfaces. This way we will allow the plasma to move, and the transport equation to be represented, only through states respecting the force balance equation under plasma toroidal symmetry assumption.

- The transport of heat and particles is very fast along the magnetic field lines but much slower across them, since the particles are at first approximation forced to gyrate about the magnetic field lines. In the resistive time scale limit, we are only interested in the

transport orthogonal to magnetic field lines. We will therefore use a flux surface average of the transport equations to describe the dynamics across flux surfaces.

In summary, from the two fluids MHD model, applying the resistive time scale ordering, one obtains a system of equations suited to describe the transport across flux surfaces, where all the fast dynamics including the ideal MHD instabilities have been removed.

The system of equations however is not sufficient to describe all the dynamics targeted in this thesis. There are indeed phenomena, described in the following, which appear in a time range between the Alfven time scale τ_A and the resistive time scale τ_R, which are important for the tokamak operation and are still compatible with the actuators response.

Vertical Displacement Event (VDE)

When we add the circuit equations describing the dynamics of the currents in the active and passive conductors around the plasma, the Vertical Displacement Event (VDE) instability arises. This instability, at least in its early phase, can be described by subsequent equilibria with plasma drifting vertically towards the wall. A vertical stability controller acting on a set of poloidal field coils is needed during tokamak operation. The resulting system of equations, coupled to the conductor dynamics, will be described in the following section. The time scale of this instability in TCV is of the order of ms or fraction of ms, while the typical diffusion time scale for the heat/particle flux and current diffusion ranges from $5-200ms$.

For completeness, we specify that coupling the two-fluid MHD under resistive time scale ordering, which led to neglect the plasma inertia, with the evolutionary equations for the current in the active and passive conductors allows to describe the VDE only during its initial phase. When the plasma, after displacing, approaches the wall a large increase of so-called "halo currents" [Hender et al. 2007], currents flowing partially in a small region outside the LCFS and partially in the vessel, provides an important contribution to the magnetic force of the structures. We will not consider this aspect in this thesis. Moreover in a later phase of the instability, when the plasma shrinks, non-toroidally symmetric instabilities prevail, which cannot be described by the model under resistive time scale assumptions [Strauss 2015, 2018; Pfefferlé et al. 2018; Artola et al. 2018; Sovinec and Bunkers 2019].

In this thesis however, we only aim to use a model to design the controllers to keep the plasma in a desired equilibrium condition and not to recover from a later phase of the instability. The system of equations under resistive time scale ordering coupled to the dynamics of the conductors contains therefore enough physics content for our purpose.

Other plasma events with $\tau_A \ll \tau \ll \tau_R$

We have listed in the introduction some MHD instabilities that appear during tokamak operation which can have intermediate time scales between the τ_A and τ_R. These are the sawtooth

crash of the central current profile, the localized modes with a fast pressure pedestal drop at the plasma edge, and the opening up of a magnetic island between nested flux surfaces. These instabilities might not necessarily lead to a disruption but can be detrimental for the plasma performances, in particular magnetic islands. These need dedicated modelling to be able to simulate the dynamics and are not represented by the system of equations described before. We will not aim in this thesis to simulate them in their dynamics however when performing reconstruction/interpretative problem (described in the next chapter) we will eventually consider their macroscopic effects on the plasma profiles.

2.2 MHD static equilibrium problem

The static free boundary equilibrium problem looks for the magnetic field which satisfies the MHD force balance equation together with the Maxwell's equations both under static condition $\frac{d}{dt} = 0$. The system of equations reads,

$$
\begin{cases}
\boldsymbol{j} \times \boldsymbol{B} = \nabla p \\
\nabla \times \boldsymbol{B} = \mu_0 \boldsymbol{j} \\
\nabla \cdot \boldsymbol{B} = 0
\end{cases}
\tag{2.15}
$$

where $\boldsymbol{j}$ is composed of the contribution of both the plasma current density $\boldsymbol{j}_{pl}$ and currents external to the plasma $\boldsymbol{j}_e$ but present in the domain of validity of the system, for example the currents belonging to conductors (coils and passive structures). We consider a cylindrical coordinate system $\{R, \phi, Z\}$ were ϕ is the toroidal angle. When a toroidally symmetric solution is sought, the magnetic field $\boldsymbol{B}$ can be expressed with the use of two scalar potentials $\{\psi, T\}$ as

$$
\boldsymbol{B} = \underbrace{\frac{1}{2\pi} \nabla \psi \times \nabla \phi}_{\boldsymbol{B}_p} + \underbrace{T \nabla \phi}_{\boldsymbol{B}_\phi},
\tag{2.16}
$$

where $\boldsymbol{B}_\phi$ represents the toroidal magnetic field and $\boldsymbol{B}_p$ the poloidal magnetic field. The choice of the coordinate system corresponds to COCOS=17 as described in [Sauter and Medvedev 2013]. Notice that $\boldsymbol{B}_p$ lies on a plane $\perp \nabla \phi$ called the poloidal plane which corresponds to the (R, Z) plane. $\psi = \psi(R, Z)$ is related to the poloidal flux of $\boldsymbol{B}_p$ and $T(R, Z) = RB_\phi$. For example, if one considers a disk centered at the center of symmetry of the coordinate system, of radius R_i, placed orthogonal to Z direction at the height Z_i, then $\psi(R_i, Z_i) = \int \boldsymbol{B}(R, Z_i)_p \cdot \boldsymbol{e}_z 2\pi R dR$. This is the case for the flux loop measuring the poloidal flux around the tokamak vessel. A property of the system eq. (2.15) is that, inside the plasma, nested surfaces at constant value of ψ are formed. Moreover, these surfaces are also surfaces of constant pressure hence $p = p(\psi(R, Z))$ and also $T = T(\psi(R, Z))$. Making use of eq. (2.16) and the properties just cited, the system of equations (2.15) becomes the well known Grad-Shafranov equation [Grad and

Rubin 1958],

$$\Delta^*\psi = -2\pi\mu_0 R(j_{pl,\phi} + j_{e,\phi}) = -4\pi^2\left(\mu_0 R^2 \frac{dp}{d\psi} + T\frac{dT}{d\psi}\right) - 2\pi\mu_0 R j_{e,\phi}, \qquad (2.17)$$

where $j_{pl,\phi}(R,Z)$ is the toroidal component of the plasma current density, $p = p(\psi)$ is the total plasma pressure, $j_{e,\phi}$ the external (to the plasma) toroidal current density belonging to the currents flowing in the active coils circuits j_a or in the passive conductors j_v such as the vacuum vessel. The location in the poloidal plane of these currents is shown in fig.2.1a for the case of TCV tokamak. In eq. (2.17) we introduced the so-called Grad-Shafranov operator,

$$\Delta^* = R\frac{\partial}{\partial R}\left(R\frac{\partial}{\partial R}\right) + \frac{\partial^2}{\partial Z^2}. \qquad (2.18)$$

The toroidal symmetry hypothesis will be always valid in this document. Hence the toroidal component j_ϕ of any current density, either from the plasma or external conductor, is the only component which provides contribution to the poloidal flux ψ. The label ϕ will be therefore dropped in the rest of the document from any current density distribution component j_i meaning with that $j_i = j_{i,\phi}$ unless differently specified.

It is useful to specify in table 2.1 the sub-domains of (R,Z) poloidal plane that are used in this work. These are shown in fig. 2.1 for the TCV tokamak. With the symbol Ω_* we refer to the

Ω	(R,Z) plane
Ω_c	Computational domain
Ω_{pl}	Plasma region where $j_{pl} \neq 0$
Ω_v	Vessel region
$\Omega_{vac} = (\Omega_c \cap \Omega_{pl})^c$	Vacuum region inside computational domain
Ω_a	Active coil region

Table 2.1

open set, i.e. excluding its boundary $\partial\Omega_*$. The computational domain Ω_c, where the solution of the Grad-Shafranov equation is sought, can be any subset of the poloidal plane. In fig. 2.1a, Ω_c is represented with a rectangular box enclosed within $\partial\Omega_c$ (blue continuous curve). This particular choice of the shape for $\partial\Omega_c$ will simplify the numerical finite difference formulation in sec. 4.2. The plasma region Ω_{pl} is contained within the so-called "last closed flux surface" (LCFS) represented with the continuous red line in fig. 2.1a and 2.1b. As suggested by the name, the LCFS is the outermost closed surface of the nested flux surfaces at constant ψ. There are two possible conditions in a tokamak that can define the LCFS. If the plasma touches the limiter (black continuous line) then the LCFS is given by the isoflux line at the flux value of the contact point. In this case we refer to a so-called "limited" plasma. In the second case, the one represented in figs. 2.1a and 2.1b, the boundary of the plasma region $\partial\Omega_{pl}$ is defined by the isoflux line at the value of the poloidal flux of the X point (red cross in fig. 2.1a), which is a saddle point of the flux map $\psi(R,Z)$. The vessel region Ω_v (gray region) might
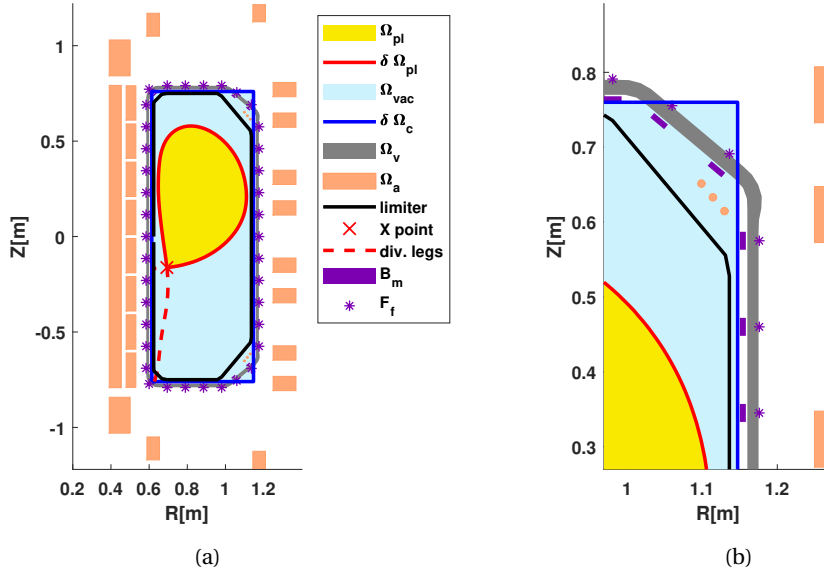
Figure 2.1 – Example of domains in poloidal plane of TCV: Plasma domain Ω_{pl} (yellow region), delimited by the plasma boundary $\partial\Omega_{pl}$ (red continuous line); the X point is represented with a red cross and the divertor legs with dashed red lines; the computational domain is contained inside the computational domain boundary $\partial\Omega_c$ (dark blue line) and is composed by the union of the plasma domain Ω_{pl} and the vacuum region Ω_{vac} in light blue; the vessel region Ω_v (gray) intersects Ω_c in the upper and lower right corner; locations of the active coil filaments in pink; limiter displayed with black continuous line, violet region for magnetic probes location B_m and violet stars for flux loops F_f .

be partially inside and partially outside Ω_c as seen from the more detailed representation in fig. 2.1b. The active coils Ω_a(pink regions) can be located both inside and outside the vessel, but always separated from the plasma which will remain inside the region delimited by the physical structure called limiter (black continuous line). For example in TCV the coils inside the vessel which are visible in fig. 2.1b (small pink circles inside Ω_c) are used for the vertical stabilization of the plasma since their fast response is less screened by the vessel induction. Therefore we will assume for this case $\Omega_v \cap \Omega_c \neq \emptyset$, $\Omega_a \cap \Omega_c \neq \emptyset$ but $\Omega_v \not\subset \Omega_c$ and $\Omega_a \not\subset \Omega_c$. In fig. 2.1 the position of the magnetic field probes B_m(small violet regions near the vessel), measuring locally the component of the magnetic field orthogonal to the probe, and the flux loop diagnostics F_f(violet stars), measuring the poloidal flux $\psi(R, Z)$, are shown. The flux loops are circular conductors centered around the vertical axis of the tokamak at various R,Z locations and placed perpendicular to the Z direction.

In order to solve eq. (2.17), the functions $p'(\psi)$ and $TT'(\psi)$ together with the boundary conditions at the computational boundary $\partial\Omega_c$ need to be specified. The boundary condition at $\partial\Omega_c$ are given by,

$$\psi(R, Z) = \sum_{i=[pl,a,v]} \int_{\Omega_i} G(R, Z; R', Z') j_i(R', Z') dR' dZ' \quad \text{with} \quad (R, Z) \in \partial\Omega_c. \qquad (2.19)$$

The integral in eq. (2.19), which in principle is extended to the whole poloidal plane Ω for (R', Z'), is effectively evaluated only in the region where $j_i \neq 0$ equivalent to $\Omega_a \cup \Omega_v \cup \Omega_{pl}$ and we call $G(R, Z; R', Z')$ the Green's function that provides the contribution of the toroidal current density $j_i(R', Z')$ to the flux $\psi(R, Z)$. In eq. (2.19) j_i can belong either to the plasma j_{pl} (always inside Ω_c) or to the external current density j_e (inside or outside Ω_c) composed by active coil j_a (poloidal field coils and OH coils) and passive structure currents such as the vessel j_v. For the external current $\boldsymbol{I}_e$, instead of continuous distribution in the poloidal plane, we will always consider sets of filamentary currents $\boldsymbol{I} = \{j(R_j, Z_j)\}$ located at the positions $\{(R_j, Z_j)\}$ with point-wise sections in the poloidal plane, calling $\boldsymbol{I}_a$ the active coil current filaments and $\boldsymbol{I}_v$ the vessel ones and packing them together in $\boldsymbol{I}_e = \{\boldsymbol{I}_a, \boldsymbol{I}_v\}$. This is equivalent to consider j_i as a Dirac distribution $I_i \delta(R - R_i, Z - Z_i)$, where (R_i, Z_i) is the location of the filament i. This way the contribution of the filamentary current i to the poloidal flux at a given location in the poloidal plane (R_k, Z_k) from eq. (2.19), is simply given by $\psi_i(R_k, Z_k) = g(R_k, Z_k; R_i, Z_i) I_i$.

We notice that another possible boundary condition is to set $\lim_{\{R,Z\}\to\infty} \psi = 0$, which requires to consider a much bigger computational domain.

We now define with $\psi_A = \psi(R_A, Z_A)$ the value of the poloidal flux at plasma axis as an extremum point of the poloidal flux map $\psi(R, Z)$ (either a maximum or a minimum depending on the sign of the plasma current). The point in the poloidal plane $\{R_A, Z_A\}$ represents the center of the plasma. With $\psi_B = \psi(R_B, Z_B)$ we define the value of the flux at the plasma boundary. The point (R_B, Z_B) in case of limited plasma is given by the value of the flux at the plasma/limiter contact point, and in case of a diverted plasma by the value of the flux at the X point, which is a saddle point in the poloidal flux map $\psi(R, Z)$. We define the normalized

poloidal flux as

$$\hat{\psi} = \frac{\psi(R, Z) - \psi_A}{\psi_B - \psi_A} \tag{2.20}$$

Given the $\hat{\psi}$ definition we note that $p'(\psi) = p'(\hat{\psi})/(\psi_B - \psi_A)$, and similarly $TT'(\psi) = TT'(\hat{\psi})/(\psi_B - \psi_A)$

2.2.1 Free boundary equilibrium

We can finally formulate the forward static free boundary equilibrium problem.
Given: $p'(\hat{\psi})$, $TT'(\hat{\psi})$, the active coil $\boldsymbol{I}_a$ and vessel coil $\boldsymbol{I}_v$ currents
Find: $\psi(R, Z)$ in Ω_c, solving eq. (2.17) with boundary conditions in eq. (2.19).

The main difficulty in solving this non-linear 2nd order elliptic PDE is to find the plasma domain Ω_{pl} entering in the surface integral in eq. (2.19). This is not given a priori as input in the free-boundary equilibrium problem and requires to find the value ψ_B of the flux at the plasma boundary. Indeed, this particular non linearity is why the problem is called "free-boundary" as opposed to "fixed boundary" where the plasma boundary $\partial\Omega_{pl}$ is known. We consider the $p'(\psi)$ and $TT'(\psi)$ defined only within Ω_{pl} and j_{pl} is considered null outside this region.

$$j_{pl}(\psi(R, Z), p'(\hat{\psi}), TT'(\hat{\psi})) = \begin{cases} \frac{2\pi}{\psi_B - \psi_A}\left(R\frac{dp}{d\hat{\psi}} + \frac{1}{\mu_0 R} T\frac{dT}{d\hat{\psi}} \right) & \text{for} \quad (R, Z) \in \Omega_{pl} \\ 0 & \text{for} \quad (R, Z) \in (\Omega_c \cap \Omega_{pl})^c \end{cases} \tag{2.21}$$

The plasma region Ω_{pl}, as a property of ideal MHD system of equations, is always a closed flux surface defined by the isoflux line at ψ_B. In real plasma there is a small region outside the LCFS, called the scrape of layer, where a small non null toroidal plasma current is present, but we do not consider it in this work.

It is convenient to express the free-boundary equilibrium forward problem as a root finding problem. We will be able to represent all the problems formulated in this part of the thesis in this form such that a single technique will be applied for their numerical solution. We define the unknown $x \equiv \psi(R, Z)$ and the inputs $\nu \equiv \{p'(\hat{\psi}), TT'(\hat{\psi}), \boldsymbol{I}_a, \boldsymbol{I}_v\}$. Bringing the RHS of eq. (2.17) and 2.19 to the LHS, we can define the nonlinear operator $F = F(x; \nu)$ as,

$$F(x; \nu) = \begin{cases} \Delta^*\psi + 2\pi\mu_0 R(j_{pl} + j_e) & \text{in} \quad \Omega_c \\ \psi(R, Z) - \sum_{i=[pl,a,s]} \int_{\Omega_i} G(R, Z; R', Z') j_{\varphi,i}(R', Z') dR' dZ' & \text{in} \quad \partial\Omega_c \end{cases} \tag{2.22}$$

The static free boundary forward equilibrium problem can be now expressed as a root finding problem.
Given: $\nu = \{p'(\hat{\psi}), TT'(\hat{\psi}), \boldsymbol{I}_a, \boldsymbol{I}_v\}$
Find: $x = \psi(R, Z)$ such that $F(x; \nu) = 0$ in Ω_c, with j_{pl} defined in eq. (2.21).

We stress the fact that finding Ω_{pl} in order to compute j_{pl} defined in eq. (2.21) is part of the solution of the problem. Because of the non-linearity of finding a saddle point from a 2D map $\psi(R, Z)$, it is not possible to write the analytical gradient of the operator $\nabla_x F(x; v)$ in continuous (R, Z) space representation for diverted plasma. This will be discussed extensively in the second part of the thesis when the problem will be addressed numerically.

2.2.2 Fixed boundary equilibrium

To complete the overview of the forward problems described in this chapter related to the Grad-Shafranov equation we summarize in the following the formulation of the problem in case $\partial\Omega_{pl}$ is given, which is typically addressed as the "fixed boundary equilibrium problem". In this case the problem becomes,

Given: $\{p'(\hat{\psi}), TT'(\hat{\psi})\}$ and $\partial\Omega_{pl}$

Find: $\hat{\psi}(R, Z)$ such that,

$$\begin{cases} \Delta^* \hat{\psi} = -\left(\frac{2\pi}{\psi_B - \psi_A}\right)^2 \left(\mu_0 R^2 \frac{dp}{d\hat{\psi}} + T \frac{dT}{d\hat{\psi}}\right) & \text{for} \quad (R, Z) \in \Omega_{pl} \\ \hat{\psi}(R, Z) = 1 & \text{for} \quad (R, Z) \in \partial\Omega_{pl} \end{cases} \tag{2.23}$$

The problem eq. (2.23) is much easier to solve than eq. (3.9) since one does not need to find the domain Ω_{pl} which is the most difficult non linearity of the free boundary case. One can specify an additional constraint, which is typically set to be the total plasma current I_p, since one can rescale the sources and $\psi_B - \psi_A$ to yield a self-similar equation.

Some analytic solutions exist for simple plasma profiles both for fixed-boundary and free-boundary case [Cerfon and Freidberg 2010; Guazzotto and Freidberg 2007].

2.2.3 Flux surface coordinate system and related quantities

In this section we will define several quantities that can be computed from the solution of the equilibrium equation that will appear in several formulation in the remainder of this thesis.

First of all we notice that, since the plasma at equilibrium forms nested flux surfaces at constant ψ, if we label each flux surface with the corresponding value of the flux we obtain a monotonic increasing/decreasing (depending on the convention) range of ψ from ψ_A to ψ_B. Therefore, within the plasma, the value of ψ at a given flux surface can be used as radial coordinate from the plasma axis to the boundary.

In principle every quantity which is constant on a given flux surface and monotonic from the plasma axis to the boundary could be used as a radial coordinate. We define two of them in the following. The volume enclosed by a constant flux surface is given by,

$$V(\psi^*) = \int\int_{\Omega_{\psi^*}} 2\pi R dR dZ = \int_0^{2\pi} \int_{\psi_A}^{\psi^*} \int_0^{l_{p,tot}(\psi^*)} R d\phi \frac{d\psi}{|\nabla\psi|} dl_p = \int_{\psi_A}^{\psi^*} d\psi \oint \frac{dl_p}{B_p} \tag{2.24}$$

in particular dl_p is an infinitesimal length in the poloidal plane along the flux surface, $B_p = \frac{1}{2\pi}\frac{|\nabla\psi|}{R}$ is the modulus of the poloidal magnetic field as it can be seen from eq. (2.16) and Ω_ψ is the subset of the volume in physical space enclosed by the flux surface at $\psi = \psi^*$ constant. To derive equation eq. (2.24) we use the coordinate system transformation from (R, ϕ, Z) to (ψ, l_p, ϕ) using ψ as a radial coordinate as anticipated and l_p the length of the cross section contour of the flux surface in the poloidal plane. The volume $V(\psi)$ is a flux surface quantity and can be used as a radial coordinate. Also, note that

$$\frac{dV}{d\psi} = 2\pi \oint R \frac{dl_p}{|\nabla\psi|} = \oint \frac{dl_p}{B_p} \tag{2.25}$$

We can define similarly the area of the cross section of a given flux surface at $\psi = \psi^*$ as

$$A(\psi^*) = \int_{\Omega_{\psi^*}} dRdZ = \int_{\psi_A}^{\psi^*} d\psi \oint \frac{dl_p}{2\pi R B_p}. \tag{2.26}$$

We have in particular the following Jacobians for coordinate transformation,

$$dA = \frac{d\psi}{|\nabla\psi|} dl_p$$

$$dV = Rd\phi \frac{d\psi}{|\nabla\psi|} dl_p.$$

It is important to notice that in case of a diverted plasma in presence of an X point, which by definition has $\nabla\psi = 0$, these Jacobians diverge hence care must be taken in choosing a non degenerate coordinate system when computing integrals which include the separatrix.

We call toroidal flux $\Phi(\psi^*)$ the flux of the toroidal magnetic field in the poloidal cross section of a flux surface at $\psi = \psi^*$,

$$\Phi(\psi^*) = \int_{\Omega_{\psi^*}} \boldsymbol{B}_\phi \cdot d\boldsymbol{A} = \int_{\Omega_{\psi^*}} \frac{T}{R^2} dRdZ = \int_{\psi_A}^{\psi^*} \oint \frac{T(\psi)}{R^2} \frac{d\psi}{|\nabla\psi|} dl_p \tag{2.27}$$

Since the toroidal magnetic field in a tokamak is mainly produced by the external toroidal field coils which provide a field of magnitude $B_0 \sim \frac{1}{R}$, the toroidal flux ϕ is monotonously increasing from the plasma axis to the plasma boundary and can be used as a radial coordinate.

With I_p we indicate the total flux of the toroidal plasma current density inside the poloidal cross section of a flux surface at $\psi = \psi^*$

$$I_p(\psi^*) = \int_{\Omega_{\psi^*}} \boldsymbol{j}_{pl} \cdot d\boldsymbol{A} = \int_{\Omega_{\psi^*}} j_{pl} dA = \frac{1}{2\pi} \int_{\psi_A}^{\psi^*} d\psi \oint \frac{j_{pl}}{R} \frac{dl_p}{B_p} \tag{2.28}$$

We also use the fact that $d\boldsymbol{A} = dA\hat{e}_\phi$, having defined the unity vector $\hat{e}_\phi = R\nabla\varphi$ and $|\nabla\phi| = \frac{1}{R}$.

Not that $I_p(\psi)$ is not in general a good flux surface label since it may not be monotonic in special cases.

We summarize in the following the radial coordinates which will appear in the following formulations together with their range of value that they can assume within the LCFS:

$$\hat{\psi} = \frac{\psi - \psi_A}{\psi_B - \psi_A} [0,1] \qquad\qquad \rho_{\hat{\psi}} = \rho_{pol} = \sqrt{\psi_N} [0,1]$$

$$\hat{\Phi} = \frac{\Phi}{\Phi_B} [0,1] \qquad\qquad \hat{\rho} = \rho_{\Phi_N} = \rho_{tor,N} = \sqrt{\hat{\Phi}} [0,1]$$

$$\rho_{vol} = \sqrt{\frac{V(\rho)}{V(\rho_B)}} [0,1] \qquad\qquad \rho_\Phi = \rho_{tor} = \sqrt{\frac{\Phi}{\pi B_0}} [0, \sqrt{\Phi_B/\pi B_0}].$$

We tried to use the most common names and symbols in literature for each quantity. We notice that ψ is defined also outside the LCFS, hence it is possible to find $\hat{\psi} > 1$ in literature when for example displaying some kinetic profiles. However in this thesis we will restrict to $\hat{\psi} \le 1$. We stress that $\hat{\rho}$, which will be the main radial coordinate for the current diffusion equation in the next section, is computed from the normalized toroidal flux $\hat{\Phi}$ and not from the poloidal flux. Moreover, B_0 is defined as the vacuum toroidal magnetic field, meaning the toroidal magnetic field generated by external conductors, at R_0 fixed location, which is typically chosen to be the geometrical center of the vacuum vessel.

We remind here some useful relations between the quantities that will be convenient in the following derivations. We notice again that these definitions assume $COCOS = 17$ [Sauter and Medvedev 2013].

$$\frac{d\psi}{d\Phi} \equiv \iota \equiv \frac{1}{q} \qquad\qquad\qquad \frac{d\hat{\psi}}{d\psi} = \frac{1}{\psi_B - \psi_A} \qquad\qquad (2.29)$$

$$\frac{d\Phi}{d\hat{\rho}} = 2\Phi_B \hat{\rho} \qquad\qquad\qquad \frac{d\hat{\rho}}{d\hat{\psi}} = \frac{\psi_B - \psi_A}{2\Phi\hat{\rho}\iota} \qquad\qquad (2.30)$$

$$\frac{d\hat{\rho}}{d\hat{\Phi}} = \frac{1}{2}\frac{1}{\sqrt{\hat{\Phi}}} \qquad\qquad \frac{d\psi}{d\hat{\rho}} = \frac{d\psi}{d\hat{\rho}}\frac{d\Phi}{d\hat{\rho}} = 2\iota\Phi_B\hat{\rho} \qquad\qquad (2.31)$$

In particular we stress the definition of the quantity q,

$$\frac{d\psi}{d\Phi} \equiv \iota \equiv \frac{1}{q} \qquad\qquad (2.32)$$

usually called "safety factor", which can be shown to be related the number of toroidal turns to complete one poloidal revolution of a given magnetic field line lying on a given flux surface. The q profile is related to the onset of different plasma instabilities, and has become a crucial parameter to estimate and control during plasma operation. One of the purpose of the kinetic equilibrium reconstruction that will be explained in the following is to improve the estimation of this quantity from the available measurements. We now define an averaging operator which will be crucial in the following derivations for transport equations. The intuition to introduce

this operator is that the transport along the magnetic field lines, which lays on a given flux surface, has strongly different properties with respect to the transport across them. One can study the two of them independently, at least in the resistive time scales of interest.

The flux surface average for quantity Q on a given flux surface ψ^* is defined as,

$$\langle Q \rangle(\psi^*) = \frac{\partial}{\partial V} \int_{\Omega_{\psi^*}} Q \, dV = \frac{\partial \psi}{\partial V} \frac{\partial}{\partial \psi} \int_{\psi_A}^{\psi^*} \int_0^{2\pi} \oint Q \frac{R \, dl_p}{|\nabla \psi|} d\psi \, d\phi = \oint Q \frac{dl_p}{B_p} \Big/ \oint \frac{dl_p}{B_p} \tag{2.33}$$

We stress that in order to apply this operator to a given quantity $Q(R, Z)$ it is necessary to know the full poloidal distribution of $\psi(R, Z)$ in order to obtain the flux surface geometry and compute the average.

We define as in [Fable et al. 2013a],

$$g_0 = \langle |\nabla V| \rangle \tag{2.34}$$

$$g_1 = \langle < (\nabla V)^2 \rangle \tag{2.35}$$

$$g_2 = \langle \frac{|\nabla V|^2}{R^2} \rangle \tag{2.36}$$

$$g_3 = \langle \frac{1}{R^2} \rangle \tag{2.37}$$

which we will always refer to as geometrical quantities.

2.2.4 Alternative specification of free functions for equilibrium problem

Thanks to the quantities defined in the previous section, one can rewrite the Grad-Shafranov equation eq. (2.17) by specifying different input functions instead of $p'(\hat{\psi})$ and $TT'(\hat{\psi})$.

We define $j_{\parallel}$ as,

$$j_{\parallel} \equiv \frac{< \boldsymbol{j}_{pl} \cdot B >}{B_0} = \frac{1}{8\pi^2 B_0} \frac{1}{\mu_0 \Phi_B} \frac{T^2}{V'_{\hat{\rho}}} \frac{\partial}{\partial \hat{\rho}} \left[\frac{g_2 g_3}{\hat{\rho}} \frac{\partial \psi}{\partial \hat{\rho}} \right] \tag{2.38}$$

and j_{tor} as,

$$j_{tor} \equiv R_0 < \frac{j_{pl,\phi}}{R} >= 2\pi R_0 \frac{1}{16\pi^3 \mu_0 \Phi_B} \frac{1}{V'_{\hat{\rho}}} \frac{\partial}{\partial \hat{\rho}} \left(T \frac{g_2 g_3}{\hat{\rho}} \frac{\partial \psi}{\partial \hat{\rho}} \right) \tag{2.39}$$

where in particular $V'_{\hat{\rho}} = \frac{dV}{d\hat{\rho}}$ and Φ_B is the toroidal flux enclosed by the LCFS. The derivation of the quantities eq. (2.38) and eq. (2.39) can be found in [Felici et al. 2011].

By taking the flux surface average of the Grad-Shafranov equation one can also find the relation

between $j_\parallel$, j_{tor}, q and the previously used free functions $\frac{dp}{d\hat{\psi}}$ and $T\frac{dT}{d\hat{\psi}}$. The relations are,

$$j_\parallel = -\frac{2\pi T}{\mu_0 B_0}\frac{1}{\psi_B - \psi_A}\left\{\mu_0\frac{dp}{d\hat{\psi}} + T\frac{dT}{d\hat{\psi}}\left[g_3 + \frac{g_2}{4\pi^2 T^2 (V_{\hat{\rho}}')^2}\left(\frac{d\psi}{d\hat{\rho}}\right)^2\right]\right\}, \qquad (2.40)$$

$$j_{tor} = \frac{R_0\pi}{\psi_B - \psi_A}\left(\frac{dp}{d\hat{\psi}} + g_3\frac{1}{\mu_0}T\frac{dT}{d\hat{\psi}}\right), \qquad (2.41)$$

$$q = T\frac{dV}{d\psi}g_3. \qquad (2.42)$$

From the relations eq. (2.40) to eq. (2.42) one can see that different combination of quantities can be used to specify the RHS of the Grad-Shafranov equation. One simply needs to invert the relations to find $\frac{dp}{d\hat{\psi}}$ and $T\frac{dT}{d\hat{\psi}}$ and replace them in eq. (2.17).

However to make use of any quantity among $j_\parallel$, j_{tor}, q implies to compute the geometrical quantities g_2, g_3 from $\psi(R,Z)$ which have divergent behavior in case of diverted plasma and add an extra non-linearity to the problem. In the following of the thesis we will stick therefore with the formulation of the Grad-Shafranov equation usig p' and TT' as free functions. However $j_\parallel$, j_{tor} and q definitions will be important when coupling the free boundary equilibrium problem to the current diffusion equation explained in the following sections.

2.3 Circuit equation for evolution of conductor currents

The Grad-Shafranov equation described in previous section represents a force balance equation in the direction $\perp \boldsymbol{B}$ under the hypothesis of toroidal symmetry. Given a set of external toroidal currents $j_a(R,Z)$, $j_v(R,Z)$ distribution in the poloidal plane, it finds the solution of the plasma current distribution such that the plasma is an equilibrium state and the pressure gradient force is balanced by the $\boldsymbol{j} \times \boldsymbol{B}$ force. The equilibrium condition is reached in the MHD timescale that can be estimated by the Alfven frequency which is much faster than the usual time scale of the evolution of the external currents in active and passive conductors. In this section we will provide the equation for the evolution of the current in the external conductors, and we will assume that the plasma evolves through a sequence of MHD equilibria represented by the Grad-Shafranov equation. Notice that the phenomena of interest are found at intermediate time scaled between the Alfven and resistive/transport time scale, this means that we can use the GS equation (massless approximation) but assume the profiles p', TT' are static for one GS solution.

The evolution of the toroidal currents in a filament of an active conductor is described by Ohm/Faraday's law,

$$\frac{d\psi}{dt} = V - RI, \qquad (2.43)$$

where the resistive decay of the current, described by the Ohm's law RI, is sustained by the externally applied voltages V (only for the active coils) and the back-EMF $\frac{d\psi}{dt}$ produced by

the variation of the magnetic flux. The magnetic flux is the flux of the poloidal magnetic field when considering only toroidal current filaments and it is generated by all toroidal currents present in whole domain including the currents of the filament itself.

Formally, if we define with $\psi_t = \psi(R_t, Z_t)$ the poloidal flux enclosed by the toroidal filament t where (R_t, Z_t) is the coordinate in the poloidal plane of the location of the toroidal filament t

$$\psi(R_t, Z_t) = \sum_{k=[pl,a,v]} \int_{\Omega_k} G(R_t, Z_t; R', Z') j_k(R', Z') dR' dZ'. \tag{2.44}$$

In a tokamak typically the active conductors, which are used to generate the magnetic field to keep the plasma in equilibrium, are connected in circuits. In particular, a single active conductor that we will call "coil" and label with c, is made of several toroidal wires represented by filamentary windings connected in series that we label with w. The active coils are then connected in series to form what we call an "active circuit" which we will label with a.

We now define $\psi_{i,j,k} = \psi(R_{i,j,k}, Z_{i,j,k})$ with $i \in [1, .., N_{j,k}^w]$ where $N_{j,k}^w$ is the total number of windings of the coil j belonging to the active circuit k, $j \in [1, ..., N_k^c]$ where N_k^c is the total number of coils belonging to the circuit k, and finally $k \in [1, ..., N_a]$ with N_a the total number of active circuits. Hence from eq. (2.43), for all the individual windings belonging to all active circuits we have obtained the following system of equations:

$$\frac{d\psi_{i,j,k}}{dt} = V_{i,j,k} - R_{i,j,k} I_{i,j,k}. \tag{2.45}$$

We can now use Kirchkoff's for series connection to group some of the equations in eq. (2.45). We define $V_{a,k} = \sum_{j=1}^{N_k^c} \sum_{i=1}^{N_{j,k}^w} V_{i,j,k}$ the effective voltage applied to the active circuit k with $k \in [1, ..., N_a]$ and $R_{a,k} = \sum_{j=1}^{N_k^c} \sum_{i=1}^{N_{j,k}^w} R_{i,j,k}$ the effective resistance of the active circuit k with again $k \in [1, ..., N_a]$. Thanks to the property of series connection $I_{i,j,k} = I_{l,m,k} \forall i, l \in [1, .., N_{j,k}^w]$ and $\forall j, m \in [1, ..., N_k^c]$. We define therefore the current flowing in the active circuit k as $I_{a,k}$ equal to any of the current of a given filament i of a given coil j belonging to the active circuit k. We now perform the sum $\sum_{j=1}^{N_k^c} \sum_{i=1}^{N_{j,k}^w}$ on eq. (2.45) to obtain,

$$\frac{d\boldsymbol{\psi}_a}{dt} = \boldsymbol{V}_a - \mathbb{R}_{aa} \boldsymbol{I}_a \tag{2.46}$$

where $\boldsymbol{V}_a = \{V_{a,k}\}$, $\boldsymbol{I}_a = \{I_{a,k}\}$, $\boldsymbol{\psi}_a = \{\psi_{a,k}\}$ with $k \in [1, ..., N_a]$, and $\mathbb{R}_{aa}$ being a diagonal matrix containing the $R_{a,k}$.

We can now further simplify the expression by grouping together expression related to the active circuits and the passive structure. In this part I of the thesis we wanted to provide the formulation of the problem in continuous space form. However we will make an exception for the case of the current in the passive structure since this will greatly simplify the notation and the generalization to a continuous distribution of passive current $j_v(R, Z)$ is trivial. We label the current in the passive conductors with v since in a tokamak they are mainly present in the

vessel. We consider $j_v(R, V) = \{I_{v,i}\delta(R_i - R, Z_i - Z)\}$ with $i = [1, ..., N_v]$ and N_v being the total number of toroidal filaments considered. We use the notation $\delta(R_i - R, Z_i - Z)$ to indicate the Dirac distribution. While the filaments in an active conductors are typically physically connected as described above, and represent real wires of a coil, the filaments in the passive conductor are only an artificial discretization of the current distribution. They have to be considered independent, hence not connected if not differently specified, and N_v can be chosen arbitrarily to have a more or less fine discretization of $j_v(R, Z)$. We call $\boldsymbol{\psi}_v = \{\psi(R_i, Z_i)\}$ and $\boldsymbol{I}_v = \{I_{v,i}\}$ with $i = [1, ..., N_v]$. Finally we group $\boldsymbol{\psi}_e = \{\boldsymbol{\psi}_a, \boldsymbol{\psi}_v\}$, $\boldsymbol{I}_e = \{I_a, I_v\}$ to obtain,

$$\frac{d\boldsymbol{\psi}_e}{dt} = \boldsymbol{V}_e - \mathbb{R}_{ee}\boldsymbol{I}_e \tag{2.47}$$

where,

$$\boldsymbol{V}_e = \begin{bmatrix} V_a \\ \mathbb{0}^{N_v,1} \end{bmatrix} \tag{2.48}$$

$$\mathbb{R}_{ee} = \begin{bmatrix} \mathbb{R}_{aa} & \mathbb{0}^{N_v,N_a} \\ \mathbb{0}^{N_a,N_v} & \mathbb{R}_{vv} \end{bmatrix} \tag{2.49}$$

and we indicate with $\mathbb{0}^{x,y}$ a matrix of zeros of dimension $x \times y$. We stress the fact that the passive conductors do not have any externally applied voltages, hence the corresponding part of $\boldsymbol{V}_e$ is set to 0.

Since both the active and passive conductors are described with filamentary currents of type $j(R, Z) = \sum_i I_i \delta(R - R_i, Z - Z_i)$, one can insert this relation in eq. (2.44). Taking as an example the passive structure, $j_v(R, Z) = \sum_{i=1}^{N_v} I_{v,i}\delta(R - R_i, Z - Z_i)$, the contribution of all filaments of the passive structure to the poloidal flux at a location (R, Z) is given simply by,

$$\psi(R, Z) = \sum_{i=1}^{N_v} G(R, Z; R_i, Z_i)I_{v,i} = \boldsymbol{M}^T \boldsymbol{I}_v \tag{2.50}$$

where the vector $\boldsymbol{M}$ is simply the collection of the Green's functions, $M_i = g(R, Z, R_i, Z_i)$. Guided by the relation in eq. (2.50), we define $(\boldsymbol{\psi}_x)_{I_y}$, with $x, y \in \{a, v\}$, the contribution to the effective flux $\boldsymbol{\psi}_x$ from current I_y. For example $(\boldsymbol{\psi}_a)_{I_v}$ is the contribution to the effective flux of the active circuit a from the vessel filaments $\boldsymbol{I}_v$. In particular from the definitions eq. (2.44) and eq. (2.50) the following linear relations can be obtained,

$$(\boldsymbol{\psi}_a)_{I_a} = \mathbb{M}_{aa}\boldsymbol{I}_a \qquad\qquad (\boldsymbol{\psi}_a)_{I_v} = \mathbb{M}_{av}\boldsymbol{I}_v$$

$$(\boldsymbol{\psi}_v)_{I_a} = \mathbb{M}_{va}\boldsymbol{I}_a \qquad\qquad (\boldsymbol{\psi}_v)_{I_v} = \mathbb{M}_{vv}\boldsymbol{I}_v$$

We stress the fact that the two attached labels as aa in $\mathbb{M}_{aa}$, are not the indices of the matrix but $\mathbb{M}_{aa}$ is the full name given to the matrix. The matrices $\mathbb{M}_{xx}$ contains the needed collection

of sums of Green's functions. We also define,

$$\mathbb{M}_{ee} = \begin{bmatrix} \mathbb{M}_{aa} & \mathbb{M}_{av} \\ \mathbb{M}_{va} & \mathbb{M}_{vv} \end{bmatrix} \tag{2.51}$$

such that $(\boldsymbol{\psi}_e)_{I_e} = \mathbb{M}_{ee}\boldsymbol{I}_e$. Finally the contribution of the plasma current density j_{pl} to the k component of $\boldsymbol{\psi}_e$, called $(\boldsymbol{\psi}_{e,k})_{j_{pl}}$ is given by,

$$(\boldsymbol{\psi}_{e,k})_{j_{pl}} = \sum_{j=1}^{N_k^c} \sum_{i=1}^{N_{j,k}^w} \int_{\Omega_{pl}} g(R_{i,j,k}, Z_{i,j,k}; R', Z') j_{pl}(R', Z') dR' dZ' \tag{2.52}$$

such that $\boldsymbol{\psi}_e = (\boldsymbol{\psi}_e)_{I_e} + (\boldsymbol{\psi}_e)_{j_{pl}}$, where $(\boldsymbol{\psi}_e)_{pl} = \{(\boldsymbol{\psi}_{e,k})_{pl}\}$ for $k = [1, ..., N_a + N_v]$.

2.3.1 Coupling with free boundary equilibrium

The formulation of the problem coupling the dynamics of the currents in the passive/active conductors with a plasma described by subsequent states of equilibrium can be now formulated.

Given: $p'(\hat{\psi}, t)$, $TT'(\hat{\psi}, t)$,$\boldsymbol{V}_e(t)$ + initial condition
Find: $j_{pl}(R, Z; t)$, $\psi(R, Z; t)$ in $\Omega_c \cup \partial\Omega_c$ and $\boldsymbol{\psi}_e(t)$, $\boldsymbol{I}_e(t)$ such that,

$$\begin{cases} \dfrac{d\boldsymbol{\psi}_e}{dt} & = \boldsymbol{V}_e - \mathbb{R}_{ee}\boldsymbol{I}_e \\ \boldsymbol{\psi}_e & = \mathbb{M}_{ee}\boldsymbol{I}_e + (\boldsymbol{\psi}_e)_{j_{pl}} \\ \Delta^*\psi & = -2\pi\mu_0 R(j_{pl} + j_e) & \text{in} \quad \Omega_c \\ \psi(R, Z) & = \sum_{i=[pl,a,s]} \int_{\Omega_i} G(R, Z; R', Z') j_{\varphi,i}(R', Z') dR' dZ' & \text{in} \quad \partial\Omega_c \\ j_{pl} & = \dfrac{2\pi}{\psi_B - \psi_A}\left(R\dfrac{dp}{d\hat{\psi}} + \dfrac{1}{\mu_0 R} T\dfrac{dT}{d\hat{\psi}}\right) & \text{in} \quad \Omega_{pl} \\ j_{pl} & = 0 & \text{in} \quad (\Omega_c \cap \Omega_{pl})^c \end{cases} \tag{2.53}$$

Looking at the system of eq. (2.53) one can understand the coupling between the plasma dynamics and evolution of the currents in the conductors. A displacement of the plasma, which modifies Ω_{pl}, or a modification of the plasma current distribution $j_{pl}(R, Z; t)$ produces a modification of the flux $\boldsymbol{\psi}_e$, which induces a back EMF to the active/passive conductors through the Faraday's law in the first equation. At the same time, a modification of the $\boldsymbol{I}_e$ requires the plasma to change its current distribution $j_{pl}(R, Z; t)$ in order to find a new equilibrium condition which must respect the Grad-Shafranov equation.

We would like to make some remarks.

- As already discussed in the introduction part, the obtained system of equations contains the dynamics for vertical displacement events. A controller acting on the input voltages V_a is needed to stabilize the system. One of the purpose of simulators based on eq. (2.53)

is indeed to design and test these controllers, together with the controllers to obtain a desired plasma shape.

- $I_p(t)$ is effectively given trough the profiles of p' and TT', but it could be given as an input parameter instead, provided that the profiles are re-scaled.

The problem is a DAE (Differential Algebraic) problem of the type,

$$\begin{cases} \frac{dx}{dt} = Ry + A \\ \beta(y, x) = 0 \end{cases} \tag{2.54}$$

and, being first order in time, it requires an initial condition. We will discuss this in detail in the second part of the thesis when addressing the numerical discretization of the problem.

2.4 Current diffusion equation

In the previous sections we described the coupling between the slow evolution of the currents in the external conductors and the force balance equation to keep the plasma into an equilibrium state. Now we will discuss physical models for the evolution of the plasma profiles $p'(\hat{\psi}, t)$ and $TT'(\psi, t)$. We notice that this will not contradict the static assumption to derive the Grad-Shafranov equation. Indeed, the Grad-Shafranov equation provides the state of equilibrium for the $\perp B$ force balance equation, which is reached on the Alfven time scale τ_A. We are interested in describing the evolution of plasma profiles due to the diffusion across the flux surfaces which are much slower than τ_A. The plasma will therefore evolve through subsequent states of equilibrium for the $\perp B$ force balance equation. In this section we will discuss a model which describes the evolution of the parallel current $j_\parallel$. In the next section, a transport model for the evolution of the temperature profiles is presented. Both $j_\parallel$ and T_e, T_i will contribute to the evolution of $p'(\hat{\psi}, t)$ and $TT'(\hat{\psi}, t)$ as clear from the relation in sec. 2.2.4.

We assume the validity of the Ohm's law in the parallel to **B** direction and consider the resulting flux surface averaged equation:

$$j_\parallel = \sigma_\parallel E_\parallel + \frac{< j_{bs} \cdot B >}{B_0} + \frac{< j_{cd} \cdot B >}{B_0} \tag{2.55}$$

where $E_\parallel$ is the parallel electric field, $\sigma_\parallel$ is the conductivity (the inverse of the resistivity) and j_{bs} and j_{cd} are the non-inductive bootstrap and auxiliary current densities. All the quantities with the label $\parallel$ in eq. (2.55) are defined as for example $j_\parallel = < \boldsymbol{j} \cdot B > / B_0$. The $j_\parallel$ and $E_\parallel$ terms can be rewritten as function of ψ and its time derivative to obtain the flux diffusion equation, which we will also refer to as the current diffusion equation in this dissertation. The derivation of the equation can be found in literature [Pereverzev and Yushmanov 2002; Blum et al. 2012; Felici 2011; Jardin 2010].

The current diffusion equation reads:

$$\sigma_{\parallel}\underbrace{\left(\frac{\hat{\rho}^2 \dot{\Phi}_B}{V_{\hat{\rho}}'} \frac{\partial \psi}{\partial \hat{\rho}} - \frac{2\Phi_B}{V_{\hat{\rho}}'} \hat{\rho} \frac{\partial \psi}{\partial t} \bigg|_{\hat{\rho}} \right)}_{<\boldsymbol{j}_{\Omega} \cdot B>} = \underbrace{\frac{T^2}{8\pi\mu_0 \Phi_B V_{\hat{\rho}}'} \frac{\partial}{\partial \hat{\rho}} \left(\frac{g_2 g_3}{\hat{\rho}} \frac{\partial \psi}{\partial \hat{\rho}} \right)}_{<\boldsymbol{j} \cdot B>} - <\boldsymbol{j}_{ni} \cdot B> \qquad (2.56)$$

where the following relations holds,

$$\lim_{\hat{\rho} \to 1} \frac{T}{16\pi^3 \mu_0 \Phi_B} \frac{g_2 g_3}{\hat{\rho}} \frac{\partial \psi}{\partial \hat{\rho}} = I_p \qquad (2.57)$$

$$\frac{\partial \psi}{\partial \hat{\rho}} \bigg|_{\hat{\rho}=0} = 0, \qquad (2.58)$$

which also represents the usual boundary conditions to solve eq. (2.56). The condition on I_p is considered in the limit sense since in case of diverted plasma some geometrical terms diverge but their combination has a finite limit.

The current diffusion equation can be considered as the diffusion equation of the poloidal flux ψ across surface of constant Φ. In other words, in a plasma with finite parallel resistance, surfaces at constant Φ move differently to surfaces at constant ψ. This is the intuition of the two time derivative terms in the LHS of eq. (2.56).

Another intuitive interpretation of eq. (2.56) considers the flux surface averaged current $< \boldsymbol{j} \cdot B >$ as composed by an inductive contribution $< \boldsymbol{j}_{\Omega} \cdot B >= \sigma_{\parallel} E_{\parallel}$, which is mainly (but not completely) due to the induced electric field generated by the external coils in the central solenoid of the tokamak, and a non-inductive part which can be either self-generated by the plasma j_{bs} or due to external non inductive sources such as the current by ECRH sources or neutral beam injection.

In order to solve the current diffusion equation to obtain $\psi(\hat{\rho}, t)$ one needs to provide the inputs $\sigma_{\parallel}(\hat{\rho}, t)$, $< \boldsymbol{j}_{ni} \cdot B >$ and quantities that are computed from the solution of the free-boundary equilibrium $\dot{\Phi}_B(t)$, $V'(\hat{\rho}, t)$, $g_2(\hat{\rho}, t)$ and $g_3(\hat{\rho}, t)$.

The eq. (2.56) admits a stationary-state solution. When all the sources and geometrical quantities do not vary in time, $\dot{\Phi}_B = 0$ and the total plasma current I_p is fixed, there exists a solution where $\frac{\partial}{\partial \hat{\rho}} \frac{\partial \psi}{\partial t} = 0$. This condition means that the time derivative of the poloidal flux $V_{ss} = \frac{\partial \psi}{\partial t}$ has a constant stationary state value V_{ss} over $\hat{\rho}$. During normal tokamak operation, when a stationary phase is reached and the current density profile has relaxed to the stationary condition, the V_{ss} has to be supplied mainly by the Central solenoid coil in order to keep a constant plasma current and overcome the resistive decay. The stationary state operation with inductive current is the normal operation mode in present experiments. We notice that a stationary condition is not a steady-state condition where all the time derivatives would vanish. A steady-state condition could be achieved instead if the resistive decay of the plasma current would be fully sustained by the external sources j_{cd} and/or the bootstrap current

j_{bs}, resulting in $\frac{d\psi}{dt}$. This scenario would be desirable to exploit the tokamak as a continuous source of energy and it has been reached in TCV with ECCD [Sauter et al. 2001] and 100% bootstrap current [Coda et al. 2008]. However the externally driven current systems are not sufficiently efficient and high I_p scenarios with high percentage of bootstrap current are under investigation. One of the goal of ITER is to prove the possibility of sustaining a tokamak plasma in steady-state condition with no current driven inductively.

In this thesis we will make use of an integral version of eq. (2.56). We provide here the final expression and the derivation is given in appendix G. We define the integral operator,

$$\Gamma(A) = \frac{T_B}{2\pi} \int \frac{A}{T^2} dV \tag{2.59}$$

and apply it to eq. (2.56), to obtain:

$$-(A_{1,1} + A_2) = I_p - \Gamma(<j_{ni} \cdot B>) \tag{2.60}$$

with,

$$A_2 = -\frac{T_B(\psi_B - \psi_A)}{2\pi} \int_0^1 \frac{\sigma_\parallel}{T^2} \frac{\partial \Phi}{\partial t}\bigg|_{\hat{\psi}} d\hat{\psi} \tag{2.61}$$

$$A_{1,1} = \frac{T_B \Phi_B}{2\pi} \int_0^1 \frac{\sigma_\parallel}{T^2} \frac{\partial \psi}{\partial t}\bigg|_{\hat{\psi}} d\hat{\Phi}. \tag{2.62}$$

The integral 0D eq. (2.60) is useful when one is not interested in simulating and predicting the evolution of the current density profile of the plasma but just to take into account the global decay of the total plasma current I_p due to plasma resistivity. However, it is of notable interest that the expressions eq. (2.61),eq. (2.62) do not contain the flux-surface averaged geometrical quantities (g_2, g_3) that were originally present in eq. (2.56). While we chose here to integrate over the entire plasma domain, yielding a 0D equation, in principle we could also integrate in different several sub-domains up to $0 < \hat{\psi} < 1$, respectively $0 < \hat{\Phi} < 1$. This potentially allows to solve a full 1D CDE that does not require evaluation of flux-surface averaged geometrical quantities. This will be discussed in more detail in section 4.3

2.4.1 Coupling free boundary equilibrium and conductor currents evolution

Coupling the current diffusion equation with the free boundary equilibrium problem allows to remove the free parameters $TT'(\hat{\psi}, t)$ from the set of forward inputs needed to solve the Grad-Shafranov equation. There can be many formulation of the problem depending on which inputs are used in the RHS of the Grad-Shafranov equation. We provide here only one among them with the purpose of clarifying the relation between the different physical models.

Given: $p'(\hat{\psi}, t)$, $V_e(t)$, $\sigma_\parallel(\hat{\psi}, t)$, $j_{cd}(\hat{\psi}, t)$, $j_{bs}(\hat{\psi}, t)$ + initial condition ψ_e^0, $\psi^0(\rho)$
Find: $j_{pl}(R, Z; t)$, $\psi(R, Z; t)$ in $\Omega_c \cup \partial\Omega_c$, $\boldsymbol{\psi}_e(t)$, $I_e(t)$, $\psi(\hat{\rho}, t) \in [0, 1]$, $TT'(\hat{\psi}, t)$, $I_p(t)$ and all the other quantities appearing in the system, such that

$$\begin{cases}
\frac{d\boldsymbol{\psi}_e}{dt} = \boldsymbol{V}_e - \mathbb{R}_{ee}\boldsymbol{I}_e \\[4pt]
\boldsymbol{\psi}_e = \mathbb{M}_{ee}\boldsymbol{I}_e + (\boldsymbol{\psi}_e)_{jpl} \\[4pt]
\Delta^*\psi = -2\pi\mu_0 R(j_{pl} + j_e) & (R,Z) \in \Omega_c \\[4pt]
\psi(R,Z) = \sum_{i=[pl,a,s]} \int_{\Omega_i} G(R,Z;R',Z')\,j_{\varphi,i}(R',Z')\,dR'\,dZ' & (R,Z) \in \partial\Omega_c \\[4pt]
j_{pl} = \frac{2\pi}{\psi_B - \psi_A}\left(R\frac{dp}{d\hat{\psi}} + \frac{1}{\mu_0 R} T\frac{dT}{d\hat{\psi}}\right) & (R,Z) \in \Omega_{pl} \\[4pt]
j_{pl} = 0 & (R,Z) \in (\Omega_c \cap \Omega_{pl})^c \\[4pt]
\sigma_\parallel \left(\frac{\hat{\rho}^2 \dot{\Phi}_B}{V'_{\hat{\rho}}}\frac{\partial\psi}{\partial\hat{\rho}} - \frac{2\Phi_B}{V'_{\hat{\rho}}}\hat{\rho}\frac{\partial\psi}{\partial t}\Big|_{\hat{\rho}}\right) = \frac{T^2}{8\pi\mu_0\Phi_B V'_{\hat{\rho}}}\frac{\partial}{\partial\hat{\rho}}\left(\frac{g_2 g_3}{\hat{\rho}}\frac{\partial\psi}{\partial\hat{\rho}}\right) - B_0(j_{bs} + j_{cd}) & \hat{\rho} \in (0,1) \\[4pt]
\frac{T}{16\pi^3\mu_0\Phi_B}\frac{g_2 g_3}{\hat{\rho}}\frac{\partial\psi}{\partial\hat{\rho}} = I_p & \hat{\rho} \to 1 \\[4pt]
\frac{\partial\psi}{\partial\hat{\rho}} = 0 & \hat{\rho} = 0 \\[4pt]
T\frac{dT}{d\hat{\psi}} = \frac{\mu 0}{g_3}\left(j_{tor}\frac{\psi_B - \psi_A}{R_0\pi} - \frac{dp}{d\hat{\psi}}\right) & \hat{\psi} \in [0,1]
\end{cases}$$

$$(2.63)$$

We would like to stress some features of the obtained eq. (2.63).

- $I_p(t)$ is not a feedforward input for the system, but it has to be found as part of the solution. The total plasma current without any external drive would decay as a consequence of the resistivity in the Ohm's law (current diffusion equation). In this system it is maintained through both the non-inductive sources j_{bs}, j_{cd} and the electric field produced by the central solenoid. The voltages applied to the active coils will produce a variation in time of the poloidal flux. The plasma will respond to this variation and will feel a $\frac{\partial\psi}{\partial t}\Big|_{\hat{\rho}}$. This will drive inductive current in the plasma. As a consequence of that, the system eq. (2.63), differently to eq. (2.53), allows to design and test controllers for the central solenoid to control the total $I_p(t)$.

- From the current diffusion equation one can compute $\psi(\hat{\rho}, t)$, this can be used to compute $j_{tor}(\hat{\psi}, t)$ from the formula eq. (2.41), which is then used in the system to compute $TT'(\hat{\psi}, t)$. The current diffusion equation is used therefore effectively to specify one of the free function which enter in the RHS of the Grad-Shafranov equation.

- Having coupled the dynamics of the conductor, this system of equations contains the Vertical Displacement Events and needs active stabilization, with the addition that a dedicated controller for the central solenoid is needed to control the total plasma current.

2.5   Heat and particles diffusion equations

The derivation of the flux surface averaged heat and particles diffusion equation can be found in [Teplukhina et al. 2017; Pereverzev and Yushmanov 2002; Blum and Le Foll 1984; Hinton

and Hazeltine 1976]. We provide here their final form for convenience. The energy flux for various species "s" (electrons, ions, impurities) reads,

$$\frac{3}{2}\frac{1}{(V'_{\hat\rho})^{5/3}}\left(\left.\frac{\partial}{\partial t}\right|_{\hat\rho} - \frac{\dot\Phi_B}{2\Phi_b}\frac{\partial}{\partial\hat\rho}\hat\rho\right)[(V'_{\hat\rho})^{5/3} n_s T_s] = \frac{1}{V'_{\hat\rho}}\frac{\partial}{\partial\hat\rho}\left[\frac{g_1}{V'_{\hat\rho}} n_s \chi_s \frac{\partial T_s}{\partial\hat\rho} + \frac{5}{2} T_s \Gamma_s g_0\right] + P_s \qquad (2.64)$$

where $\chi_s(\hat\rho, t)$ is the thermal diffusivity, Γ_s is the convective flux defined below and $P_s(\rho, t)$ represents the power density as a sum of the various sources and sinks.

Similarly the particle transport,

$$\frac{1}{V'_{\hat\rho}}\left(\left.\frac{\partial}{\partial t}\right|_{\hat\rho} - \frac{\dot\Phi_B}{2\Phi_b}\frac{\partial}{\partial\hat\rho}\hat\rho\right)[V'_{\hat\rho} n_s] = -V'_{\hat\rho}\frac{\partial}{\partial\hat\rho}\Gamma_s + S_s \qquad (2.65)$$

where the particle flux is defined as,

$$\Gamma_s = -\frac{g_1}{V'_{\hat\rho}} D_s \frac{\partial n_s}{\partial\hat\rho} + g_0 V_s n_s, \qquad (2.66)$$

with D_s corresponding to the particle diffusivity, V_s the pinch velocities and S_s a combination of various sources and sinks of particles.

When these transport equations are added to eq. (2.63), the pressure plasma profile is fully specified hence the p' is no longer a free parameter to be given as a feed-forward input. We do not discuss here the case in presence of fast ions. This way a predictive simulation of the flux surface averaged MHD system of equations on resistive time-scales can be obtained.

2.6   Summary

When the resistive time scale ordering is applied to the two fluids MHD model, a system of equations suited to describe the radial transport of heat and particles through states of magnetic force balance equilibria is obtained, removing all the fast MHD instabilities and under toroidal symmetric assumptions. This will be the basis for the reconstruction/inverse problems described in the following chapters. When this system is coupled to the dynamics of the active and passive conductors, the Vertical Displacement Event instability appears. This second set of equations will be implemented in a predictive simulator to design the vertical stability and shape controller for tokamak operation.

3 Reconstruction/interpretative/inverse problems

In this chapter we will introduce the reconstruction/interpretative/inverse problems where the knowledge of some measurements is used to infer the parameters and/or the state of the plasma. In control theory this is typically called a state and parameter identification problem. In statistics this is called inference of parameters or inverse problem. We will use the name "reconstruction" in the following.

The problem of how to combine uncertain measurements with models to provide the best estimate of the parameters and state and how to define a measure to compare different estimates is discussed in terms of a statistical interpretation comparing the Frequentist approach to the Bayesian one. The result is the derivation of the least-squares optimization technique which will be the basis for all the inverse problems discussed in this thesis.

After that we will provide the formulation of the Magnetic Equilibrium Reconstruction (MER) problem including some reduced formulation to simplify its implementation. We will stress in particular the limits which advocate for the implementation of the Kinetic Equilibrium Reconstruction (KER).

After a short literature investigation on the available techniques to perform KER, based on the minimum least squares problem, we define some assumptions to derive the formulation implemented in TCV. We discuss in details the set of diagnostics available in TCV and the forward models needed to complete the formulation. We provide, at the end of the chapter, two reduced formulations of the problem which will be implemented and discussed in part II of this thesis.

3.1 Statistical interpretation

In the previous chapter we derived several "forward" models. A forward model is a relation of the type $x = f(\theta)$, where given the parameter θ on can predict the state x. More generally it can be given as a non-linear relation $f(x,\theta) = 0$ that can be inverted to find x. From the state and the parameter one can compute the "simulated measurements" $y = g(x,\theta)$, which are

obtained typically as a post processing from the knowledge of the state x and parameters θ.

For example taking the case of the free boundary equilibrium problem eq. (3.9), $\theta = \{p'(\hat{\psi}), TT'(\hat{\psi}), \boldsymbol{I}_a, \boldsymbol{I}_v\}$, $x = \psi(R, Z)$ and $y = \psi(R_i, Z_i)$ could be the estimate of the poloidal flux at the location of the flux loops.

We call a reconstruction/inverse/identification problem (several names have been used in literature to indicate the same family of problems) when the parameters θ are unknowns but measurements $\tilde{y}$ are available for the simulated measurements. The goal is to infer the parameters θ and state x such that the forward model $x = f(\theta)$ is satisfied and the simulated measurements $y = g(\theta, x)$ match in some sense the measurements $\tilde{y}$ (we will be more specific in the following).

It is important to notice that the difference between the state x and parameters θ is arbitrary. Indeed, provided that one can always compute the forward model, replacing x everywhere one could obtain a formulation depending only on θ, in particular $y = g(f(\theta), \theta) = g(\theta)$. In this chapter while deriving the Frequentist and Bayesian approaches, we will always consider only the θ dependence to simplify the notation, except when we will present the case of the magnetic equilibrium reconstruction, where a particular form of g will make it clearer to split and consider x and θ independently.

To introduce the problem let us consider the ideal case where a number of perfect (noiseless, infinite precision) measurements $\tilde{y}$ are available, and the physics is perfectly described, hence there exists θ such that $\tilde{y} = g(\theta)$. In this case, provided that g can be inverted, simply $\theta = g^{-1}(\tilde{y})$.

However when dealing with real experiments, things are more complicated,

- Measurements have uncertainties, coming both from limited resolution and noise.

- The forward model might not perfectly describe the physics of the phenomenon addressed, hence there is no θ such that $\tilde{y} = g(\theta)$.

- Different types of diagnostics can provide measurements of the same physical quantity/state x at different levels of uncertainties.

- Different forward models relying on different sets of parameters might provide estimates of the same state x.

- The forward model generally might not have a unique solution.

On top of the complications mentioned above for the uncertainty of the measurements and models, another important issue is, given that the goal of a reconstruction problem is finding the best estimate of θ and x, how "best" is defined? In other words, one needs to provide a measure of the quality of the reconstructed state and parameters which in principle allows to compare between different estimates.

To make progress, one needs to take assumptions on the type of uncertainties of the models and measurements. For the models, we will consider that the uncertainty can be expressed as extra parameters ϵ to be estimated. Suppose that the parameter θ, for example the conductivity $\sigma_{\parallel} = \theta + \epsilon$ in the current diffusion equation eq. (2.56), is known up to a certain additive uncertainty ϵ, then ϵ becomes an extra free parameter to be inferred.

For the measurements, there are two types of uncertainties. The first is the resolution of the diagnostic which has to be considered as a fixed lower bound interval within which the measurements cannot be distinguished. The second is the uncertainty due to noise of the measurements. Under these conditions, the measurement $\tilde{y}$ could be considered as drawn from a probability distribution $P(y)$. Different types of measurement uncertainties can be described in this framework. For example the resolution of the diagnostic can be described by a uniform distribution on the interval given by the precision of the diagnostic. A white noise is instead described by the Gaussian (Normal) distribution with given standard deviation. Systematic errors, if known, should be removed directly from the measurements. Otherwise they can be treated as additive disturbance, where the shift is an extra free parameter to be inferred.

Applying a statistical interpretation to the parameter and the measurement uncertainties allows to treat all the complications mentioned above in a consistent framework and provides the definition of measures to compare different methods of estimating the parameters θ as well as providing the information on the quality of these estimations. However, this requires to make assumptions on the uncertainties of the model and the measurements.

Next, we will discuss two possible interpretations in statistic: the frequentist and the Bayesian approaches [Hogg et al. 2005].

3.1.1 Frequentist approach

In the frequentist interpretation of the inverse(reconstruction) problem, the measurements $\tilde{y}$ are considered to be the sample of a random process taken from a repeatable experiment that can be described by a conditional probability distribution function $p(\tilde{y}|\theta)$ called likelihood. For example white noise is described by a $p(\tilde{y}|\theta)$ being a Normal distribution with a given mean and standard deviation.

The frequentist approach looks for an estimator $\hat{\theta}(\tilde{y})$ for the fixed but unknown parameter θ. It is important to notice that, in this approach, θ is not a random variable, but it is unique and fixed, while $\tilde{y}$ is a random variable and therefore also $\hat{\theta}(\tilde{y})$ is a random variable. There is not a unique approach to choose the best estimator $\hat{\theta}$. However a common approach, the so called maximum likelihood, is to consider $\hat{\theta} = \mathrm{argmax}_{\theta}\, p(\tilde{y}|\theta)$. The relation tells that the best estimator $\hat{\theta}(\tilde{y})$ is the θ which maximizes the probability of obtaining the measurement $\tilde{y}$ conditioned to the fact of considering the parameter θ represented by the conditioned probability distribution function $p(\tilde{y}|\theta)$.

To clarify the concept lets make an important example which will be the basis for the derivation of the reconstruction problem in the remainder of this chapter. Assume we have the forward model $y = g(\theta)$ which has no uncertainty. We consider the case of additive white noise, hence $\tilde{y} = g(\theta) + \epsilon$ with $\epsilon \sim N(0, \sigma)$ and N indicating a Gaussian probability distribution with 0 mean and a given standard deviation σ that represents the uncertainty of the measurements. One can notice that in the likelihood function $p(\tilde{y}|\theta)$ the forward model $g(\theta)$ appears. The maximum likelihood estimator $\hat{\theta}(\tilde{y})$ can be demonstrated to be $\hat{\theta}(\tilde{y}) = \text{argmin}_\theta ||\tilde{y} - g(\theta)||_\sigma^2$, where we indicated with $||\tilde{y} - g(\theta)||_\sigma^2$ the 2-norm weighted by the standard deviation of the measurements.

In case we also want to estimate the state x of the system together with the parameters θ the problem can be formulated as follows:
Given: $\tilde{y}$, and the knowledge of the forward models f and g
Find: x^* and θ^*

$$\{x^*, \theta^*\} = \underset{x, \theta}{\text{argmin}} ||\tilde{y} - y||_\sigma^2 \tag{3.1}$$

such that

$$\begin{cases} x = f(\theta) \\ y = g(x, \theta) \end{cases} \tag{3.2}$$

The problem is classified as non-linear least-squares optimization with non-linear equality constraints represented by the forward function $f(x)$ and the simulated measurements forward model $g(x, \theta)$.

We would like to make some remarks on the problem obtained in eq. (3.2),

- The problem eq. (3.2) is the formulation of the inverse/reconstruction problem that we seek. Starting from a forward model it estimates the state x and parameter θ from the knowledge of some measurements $\tilde{y}$. This will be the basis for all the formulation of all the reconstruction problems in this thesis.

- In order to solve the obtained MLS problem with equality constraints, one can adopt Lagrange's multipliers technique. This is discussed for the case of linear and "quasi-linear" forward model $g(x, \theta)$ in Appendices E and F. We do not discuss in this thesis the case of inequality constraints which would require to satisfy the Karush–Kuhn–Tucker (KKT) conditions [Kuhn and Tucker 1951].

- All different diagnostics, eventually also measuring the same quantity, can be included in eq. (3.2) by adding them to the cost function. The information on the uncertainty of each diagnostic is independently provided by the factor σ, weighting each least squares term. In the framework of eq. (3.2), the uncertainty of the measurement is modelled as white noise with standard deviation σ.

- Due to the possible non-linearity of the forward model, the inverse problem might result

to be ill-posed: no solution might match the data (existence), many solutions might match the data (uniqueness), ill-conditioning/instability small change in data might lead to large changes in the estimator $\hat{\theta}$. To recover from these issues two techniques are used either to reduce the number of free parameters or to add a regularization term to the cost functions. We will see in the following that this issue will appear when discussing the magnetic equilibrium reconstruction and it will be one of the motivation to develop the kinetic equilibrium reconstruction.

- To provide some insight on the quality of the state x and parameters θ obtained in eq. (3.2), one can study its variance with respect to the input measurements. The strategy is to sample the distribution of the measurements noise and recover the conditional distribution $P(\theta^*|\bar{y})$. Since computing θ^* requires to solve the optimization problem, this procedure is very expensive, and technique such as Markov Chain Monte Carlo MCMC are used to build $P(\theta^*|\bar{y})$ with the minimum amount of forward solution of the problem. This technique allows to compute some confidence bar for the obtained θ^* and it is used in frequentist analysis with maximum likelihood estimator to provide information on the propagation of the errors from the measurement to the final reconstructed parameter.

- The last remark on the problem eq. (3.2) is related to the case that the forward model includes time evolutive problems of ODE type. In that case the optimal parameter $\theta^*(t)$ must be the one minimizing the cost function at every time slices, in particular one needs to consider the correlation between different time slices: a variation of the parameter at the time instant t will have a deterministic effect on the estimate of the state $x(t + dt)$, hence on the cost function at $t + dt$. Therefore, supposing that the forward model needs a number N_p of parameters and a numerical scheme is sought to solve N_t number of time steps, then the number of total parameters that all together enter in the optimization problem is $N_p \times N_t$. The number of free parameters therefore increases rapidly when time evolving problems are considered. A typical simplification adopted is to remove correlation between timeslices above a certain threshold up to the limit of considering every time slice as independent. This will be the case for the inverse problems that we will adopt in this thesis. Otherwise there exists techniques estimating the parameters recursively, using the information already obtained from the previous time slice.

3.1.2 Bayesian approach

The Bayesian interpretation is different from the frequentist one. In Bayesian approach one does not look for the unique true parameter θ and instead accepts that the knowledge one can have on θ will always have a certain degree of uncertainty. The Bayesian analysis provides the technique to reduce the degree of uncertainty on a prior belief on the parameter θ, represented by a probability distribution $P(\theta)$, with the information contained in the measurements. The goal of the Bayesian analysis is not to find θ, but rather to find the conditional probability

$P(\theta|\tilde{y})$, which is the probability density function of the parameter θ to be θ given a set of measurements $\tilde{y}$, which have a degree of uncertainty for θ smaller than the prior belief on θ represented by $P(\theta)$, measured for example by the standard deviation of $P(\theta|\tilde{y})$.

The Bayesian approach uses the Bayes theorem to compute $P(\theta|\tilde{y})$,

$$P(\theta|\tilde{y}) = \frac{P(\tilde{y}|\theta)P(\theta)}{P(\tilde{y})} \tag{3.3}$$

where in particular $P(\tilde{y}|\theta)$ is called the "likelihood", $P(\theta)$ is called the "prior", $P(\tilde{y})$ the "evidence" and $P(\theta|\tilde{y})$ the "posterior".

The prior $P(\theta)$ reflects our prior belief on the parameter θ. A typical case is that, for physical reasons, we know a range of values that the parameter can assume. For example if the parameter is a temperature, it must be positive and below a maximum limit. If no other information are available, one can choose the prior to be a uniform distribution in the range of validity of the parameter.

The likelihood, as it was the case for the frequentist analysis, provides the degree of uncertainty of the measurements. Statistical noise and/or measurement resolution are modelled with choice of the likelihood. For example suppose to model additive white noise on the measurements, as for the case of the frequentist analysis, and assume there are no uncertainties on the forward model $y = g(\theta)$, we can assume,

$$P(\tilde{y}|\theta) = \frac{1}{\sigma\sqrt{2\pi}} exp\left(-\frac{(\tilde{y} - g(\theta))^2}{2\sigma^2}\right) \tag{3.4}$$

This tells us that, if we had θ, then it is certain to have value $y = g(\theta)$, but the probability of observing $\tilde{y}$ is given by eq. (3.4) since measurement has additive white noise described by normal distribution with σ standard deviation. It is important to notice that it is in the likelihood that the forward model $g(\theta)$ appears as for the case of the frequentist analysis.

The evidence $P(\tilde{y}) = \int P(\tilde{y}|\theta)P(\theta)d\theta$ in eq. (3.3) can be considered simply as a normalization constant to make the posterior a proper probability distribution function integrating to 1.

We would like to make some remarks on the Bayesian approach,

- It provides a formal procedure to combine several diagnostics with different uncertainties and computes how these propagates to the uncertainty of the final estimate $p(\theta|\tilde{y})$. This allows to understand which measurements are most relevant for the final estimation.

- From the knowledge $p(\theta|\tilde{y})$, the degree of uncertainty of the estimated parameter can be computed considering moments of the posterior distribution. This provides information on the quality of the inferred parameters and allows also to compare different forward models.

- In addition to the definition of the likelihood, as in the frequentist analysis, one needs to provide the prior $P(\theta)$. This is one of the criticisms that frequentist approach moves to Bayesian analysis since the choice of $P(\theta)$ affects the final result and its choice is quite arbitrarily based on the prior belief of the user on the parameter. To avoid having bias on the estimation of the parameter from the prior, $P(\theta)$ is usually considered as a broad distribution function, for example a uniform distribution within a wide range.

- A point estimation of the parameter θ can be provided in the Bayesian approach considering for example the maximum of the posterior (MAP) distribution function $\hat{\theta} = \text{argmax}_\theta P(\theta|\tilde{y})$.

- In order to use the Bayes theorem to obtain the posterior distribution, one needs to sample from it. Since this involves computing the forward model $g(\theta)$, which is contained in the likelihood function, this becomes rapidly expensive with the increase of the number of parameters. Instead therefore of sampling uniformly θ, Markovian Chain Monte Carlo techniques [Von Toussaint 2011] are used to reduce the number of samples for getting a good estimate of the probability distribution, by sampling mainly on the regions of high probability. The MLS problem obtained with frequentist analysis instead can be formulated as a unique root-finding problem which is much less expensive to solve.

- In case of time dependent forward models, assumptions can be taken on the correlation of subsequent states in order to estimate recursively the posterior without sampling on all the previous time slices. The most famous of this recursive Bayesian filter/estimator is the Kalman Filter which is widely used in control field for parameters and state estimation [Särkkä 2013], which are discussed in Appendix A.

3.1.3 Summary

We discussed in this introduction the formulation for the inverse/reconstruction problem, which addresses the case of estimating the parameters θ of a forward model $y = g(\theta)$, when some measurements $\tilde{y}$ are available. The uncertainties on the measurements are described by a user-define likelihood probability distribution function $P(\tilde{y}|\theta)$, which given a certain parameter θ provides the probability of experiencing $\tilde{y}$. There are two statistical interpretation to make use of the hypothesis on the measurement uncertainties to estimate θ.

In the frequentist approach, one looks for the unique true parameter θ and its estimator $\hat{\theta}(\tilde{y})$ is usually considered as the one maximizing the likelihood $\hat{\theta} = \text{argmax}_\theta P(\tilde{y}|\theta)$. When only the additive white noise is considered as uncertainty for the measurements, represented by a normal distribution with $N(0, \sigma)$ with zero mean and standard deviation σ, this provides the weighted minimum least squares (MLS) estimator $\hat{\theta}(\tilde{y}) = \text{argmin}_\theta ||\tilde{y} - g(\theta)||_\sigma^2$. The MLS is the basis for all the inverse problem formulation in the following of this thesis.

In Bayesian approach, instead of trying to infer the unique true parameter θ, the aim is to

find the conditional probability density $P(\theta|\tilde{y})$, called posterior, providing the probability of the parameter to be θ given the measured $\tilde{y}$. It assumes a likelihood $P(\tilde{y}|\theta)$ to estimate the measurements uncertainties as for the case of the frequentist analysis but it also assumes the prior $P(\theta)$ probability distribution which models the prior belief on the parameter θ. The posterior $P(\theta|\tilde{y})$ is obtained with the help of the Bayes theorem. With the Bayesian approach a point estimation for the parameter θ from the posterior $P(\theta|\tilde{y})$ can be obtained by looking for the maximum of the posterior (MAP) distribution $\theta^* = \mathrm{argmax}_\theta P(\theta|\tilde{y})$, similarly to the maximum likelihood principle but with a completely different meaning.

Several pros and cons have been discussed about the two approaches, we mention just the main ones. The costly part of the inverse problem is generally to compute the operator $f(\theta)$. The MLS provides a unique root-finding type problem to be solved which could find also real-time application and it will be the basis for the magnetic equilibrium reconstruction and kinetic equilibrium reconstruction problems. The Bayesian approach instead requires to sample from the posterior distribution, hence to compute many times the operator $g(\theta)$, which we remind requires also to compute $f(\theta)$, making it usually very expensive. Techniques to estimate this posterior distribution function recursively are available for time dependent problems such as Kalman Filter [Welch et al. 1995], Unscented Kalman Filter [Knudsen and Leth 2018], which finds many application also in real-time. This approach provides the correct framework to propagate the measured uncertainties to the θ estimate and gives a measure of the quality of the reconstruction.

We conclude this summary by providing in table 3.1 a list of I/O for Frequentist and Bayesian approach.

	Frequentist	Bayesian
Find	Estimator $\hat{\theta}$	Posterior $P(\theta|\tilde{y})$
Given	$P(\tilde{y}|\theta)$	$P(\tilde{y}|\theta)$, $P(\theta)$
Point estimate	Max likelihood	Max posterior (MAP)
	$\hat{\theta} = \mathrm{argmax}_\theta P(\tilde{y}|\theta)$	$\theta = \mathrm{argmax}_\theta P(\theta|\tilde{y})$
	(For additive white noise -> MLS)	
Error propagation	Variance of $\hat{\theta}$	Momenta of $P(\theta|\tilde{y})$

Table 3.1 – Frequentiest vs Bayesian parameter estimation.

It is important to mention that fusion community is largely using these approaches for data analysis. The Bayesian error estimation is gaining interest [Fischer et al. 2010], [Fischer et al. 2016], [Mazon et al. 2020] together with the increasing application of machine learning techniques.

3.2 Magnetic Equilibrium Reconstruction(MER)

In the previous section, we saw how to derive a reconstruction problem from its forward counterpart, in particular in eq. (3.2) we interpreted the minimum least-squares (MLS) problem in

a frequentist statistical framework. In this section, starting from the forward free-boundary equilibrium eq. (2.22), we will derive the magnetic equilibrium reconstruction (MER) as an MLS problem. We first describe the set of external magnetic diagnostics available in TCV and then we formulate the reconstruction problem where the internal plasma profiles represent the parameters to be inferred and the Grad-Shafranov equation non-linear constraint to be respected. We finally describe an important simplification, which is usually adopted by many codes addressing this problem, including our equilibrium reconstruction code LIUQE.

The solution of the free boundary equilibrium is a fundamental analysis for both the post-discharge analysis and the tokamak operation. It provides the shape of the plasma and the magnetic surfaces geometry which are the starting point for several further analyses. However the internal plasma profiles $\frac{dp}{d\psi}$ and $T\frac{dT}{d\psi}$ which enter in the RHS of the Grad-Shafranov equation are not known a priori, hence the problem is to infer them from available measurements. The Magnetic Equilibrium Reconstruction (MER) takes its name because it considers only external magnetic measurements, which are directly related to $\psi(R, Z)$.

We follow the notation in [Moret et al. 2015]. The unknown parameters $p'(\psi)$ and $TT'(\psi)$ are first expanded into a linear combination of known basis functions $g_i(\hat{\psi})$ with $i = [1, ..., N_g]$ where N_g is the total number of basis function

$$j_{pl}(R, Z) = 2\pi\left(Rp' + \frac{TT'}{\mu_0 R}\right) = \sum_{i=1}^{N_g} \frac{a_i R^{\nu_i}}{\psi_B - \psi_A} g_i(\hat{\psi}(R, Z)), \qquad (3.5)$$

where $\nu_i = 1$ for terms contributing to p' and $\nu_i = -1$ for terms contributing to TT', and $\boldsymbol{a} = \{a_i\}$ with $i = [1, ..., N_g]$ are the basis function coefficients, which will become the new parameters to be inferred with the reconstruction problem. In principle different sets of basis $\boldsymbol{g}(\hat{\psi})$ can be used to express p' and TT', however to simplify the notation we assume to use the same functional form of basis functions for the two profiles. We stress the fact that one needs to specify only the 1D functional form $\boldsymbol{g} = \boldsymbol{g}(\hat{\psi})$ function of only $\hat{\psi}$. In eq. (3.5) the (R, Z) dependence is then given automatically by the definition $\hat{\psi}(R, Z) = (\psi(R, Z) - \psi_A)/(\psi_B - \psi_A)$. The $\frac{1}{\psi_B - \psi_A}$ comes from the chain rule $\frac{dp}{d\psi} = \frac{1}{\psi_B - \psi_A}\frac{dp}{d\psi_N}$. Remembering the relation between toroidal current density and poloidal magnetic flux at the poloidal point (R_f, Z_f),

$$\psi(R_f, Z_f) = \sum_{k=[pl,a,v]} \int_{\Omega_k} G(R_f, Z_f; R', Z') j_k(R', Z') dR' dZ', \qquad (3.6)$$

making use of eq. (3.5), one can write,

$$\psi(R_f, Z_f) = \mathbb{M}_{fe} \boldsymbol{I}_e + \sum_{i=1}^{N_g} a_i K_i \qquad (3.7)$$

where $\mathbb{M}_{fe}$, similarly to the definition $\mathbb{M}_{ee}$ eq. (2.51), is the matrix containing the mutual inductance between the location of the external current filaments $\boldsymbol{I}_e$ and the location (R_f, Z_f) such that $\mathbb{M}_{fe} \boldsymbol{I}_e$ is the contribution to the poloidal flux $\psi(R_f, Z_f)$ of the external current $\boldsymbol{I}_e$.

Moreover we have,

$$K_i = \int_{\Omega_{pl}} \frac{G(R_f, Z_f; R', Z')R^{\nu_i}}{\psi_B - \psi_A} g_i(\hat{\psi}(R', Z')) \, dA \qquad (3.8)$$

In this relation one should not confuse the Green's function $G(R_f, Z_f; R', Z')R^{\nu_i}$, with the basis functions to represent the $p'(\hat{\psi})$ and $TT'(\psi)$ profiles $g_i(\hat{\psi}(R', Z'))$. We stress one needs to know $\psi(R, Z)$ in order to find Ω_{pl} and ψ_A, ψ_B to compute $\hat{\psi}(R', Z')$.

If we call state $x = \psi(R, Z)$ and parameters $\boldsymbol{\theta} = \{\boldsymbol{I}_e, \boldsymbol{a}\}$ from eq. (3.7), a "quasi-linear" relation $\psi(R_f, Z_f) = \mathbb{A}(x)\boldsymbol{\theta}$ is found. The term "quasi-linear" might be improper, we use it in this thesis to refer to the case where the relation for ψ is linear in θ but the matrix A depends on the state x. Since $\boldsymbol{B}_p = 1/2\pi \nabla\psi \times \nabla\phi$, also for the components of the poloidal magnetic field the relation is "quasi-linear". The same can be shown for I_p which is the surface integral of eq. (3.5). Under the hypothesis of small diamagnetic flux, meaning that the contribution to the toroidal flux Φ_B enclosed by the LCFS is mainly composed by the contribution of the vacuum toroidal field, a "quasi-linear" relation is found also for Φ_B. Further details can be found in [Moret et al. 2015].

We can call simulated measurements all these quantities $\boldsymbol{y}$ which can be computed from the "quasi-linear" forward model $\mathbb{A}(x)\boldsymbol{\theta}$, from the knowledge of the state x and parameters $\boldsymbol{\theta}$, to conform to the notation used in eq. (3.2) to present the MLS problem.

$\tilde{\boldsymbol{F}}_f$,	Poloidal flux from flux loops
$\tilde{\boldsymbol{B}}_m$	Poloidal B component from magnetic probes
$\tilde{\boldsymbol{I}}_v$,	Current of the vessel filaments
$\tilde{\boldsymbol{I}}_a$,	Active coils
$\tilde{\Phi}_p$	Toroidal flux from diamagnetic flux loop
$\tilde{I}_p$	Total toroidal plasma current

Table 3.2 – The symbol ~ is used to indicate measurements from real diagnostic.

We now discuss the set of external magnetic measurements typically available in a tokamak, taking TCV as an example. With the tilde symbol ~ we will always refer to a measured value coming from a real diagnostic. The available measurements in TCV, which are common in essential all tokamaks, are listed in table 3.2, and their location displayed in fig. 2.1. They are composed by a set of 38 magnetic probes $\tilde{\boldsymbol{B}}_m$, shown in fig. 2.1a with the purple rectangle, measuring the poloidal component of the magnetic field at (R_m, Z_m) in the poloidal plane with $m = [1, ..., N_m]$ and N_m being the total number of probes, with acquisition frequency of 10 kHz for equilibrium reconstruction and 500kHz for MHD analysis. A set of 38 flux loops $\tilde{\boldsymbol{F}}_f$, shown fig. 2.1a with the purple crosses, measuring the poloidal flux $\psi(R_f, Z_f)$ at (R_f, Z_f) with $f = [1, ..., N_f]$ and N_f being the total number of loops, with an acquisition frequency of $2kHz$. The diamagnetic flux loop (DML) measuring the contribution of the plasma to the flux of the total toroidal magnetic field Φ_t in the area enclosed by the loop. Due to the absence of a Rogowski coil in TCV, no direct measurement of I_p is available. An estimate is computed using

Stokes theorem on the Ampere's law, $\mu_0 I_p = \oint_{\partial\Omega_{B_m}} \boldsymbol{B} \cdot d\boldsymbol{l}$, where $\partial\Omega_{B_m}$ is a contour passing through the (R_m, Z_m) position of magnetic probes and therefore effectively obtained from $\tilde{\boldsymbol{B}}_m$ measurements. A direct measurements of the $\tilde{\boldsymbol{I}}_a$ is available while $\tilde{\boldsymbol{I}}_v$ are estimated from the loop voltage measured by the flux loops close to the vessel, combining Faraday's law with an effective Ohm's law of type $I_v \propto \frac{1}{R}\frac{d\psi}{dt}$, R being an effective resistance of the vessel. More details are found in [Moret et al. 1998].

We can now finally formulate the MER problem as an inverse problem of the type derived in eq. (3.2). Let us call $\tilde{\boldsymbol{M}}$ the set of all measured inputs, $\tilde{\boldsymbol{M}} = \{\tilde{\boldsymbol{B}}_m, \ \tilde{\boldsymbol{F}}_f, \ \tilde{\boldsymbol{I}}_v, \ \tilde{\boldsymbol{I}}_a, \tilde{F}_t, \tilde{I}_p\}$. All measurements $\tilde{M}_i$ are considered to be affected by white noise with standard deviation δ_{M_i}. We call $\boldsymbol{\theta} = \{\boldsymbol{I}_e, \boldsymbol{a}\}$ the parameters and $x = \psi(R, Z)$ the state.
Given: $\tilde{\boldsymbol{M}}$ and a set of basis functions $\{g_i(\psi_N)\}$
Find: $x^* = \psi(R, Z)$ in $\Omega_c \cup \partial\Omega_c$ and $\boldsymbol{\theta}^*$

$$\{x^*, \boldsymbol{\theta}^*\} = \underset{x, \boldsymbol{\theta}}{\mathrm{argmin}} ||\tilde{\boldsymbol{M}} - \mathbb{A}(x)\boldsymbol{\theta}||_w^2$$

such that
$$\begin{cases} \Delta^* \psi = -2\pi\mu_0(j_{pl} + j_e) & \text{in} \quad \Omega_c \\ \psi(R, Z) = \sum_{i=[pl,a,s]} \int_{\Omega_i} G_i(R, Z; R', Z') j_{\varphi,i}(R', Z') dR' dZ' & \text{in} \quad \partial\Omega_c \\ j_{pl} = \sum_{i=1}^{N_g} a_i R^{\nu_i} g_i(\hat{\psi}(R, Z)) & \text{in} \quad \Omega_{pl} \\ j_{pl} = 0 & \text{in} \quad (\Omega_{pl} \cap \Omega_c)^c \end{cases} \tag{3.9}$$

We would like to make some remarks on eq. (3.9).

- The problem was obtained following the MLS problem derived in eq. (3.2) where the forward model $f(x, \theta)$ is given by the Grad-Shafranov equation, the forward observer $g(x, \theta)$ by the "quasi-linear" operator $\mathbb{A}(x)$, the state is the poloidal flux $x = \psi(R, Z)$ and the parameters are $\boldsymbol{\theta} = \{I_e, \boldsymbol{a}\}$.

- In eq. (3.9) the least squares is weighted depending on the uncertainties $w_i = \delta_{\tilde{M}_i}$, where $\delta_{\tilde{M}_i}$ is the uncertainty of $\tilde{M}_i$ measurements. In a statistical interpretation the measurements are considered to have only additive white noise.

- We split the domain of j_{pl} into plasma and non-plasma region to emphasize the free boundary nature of the problem.

- The problem eq. (3.9) is classified as a non linear least-squares optimization problem with equality constraints and can be solved using the Lagrange multipliers technique as explained in Appendix F and G.

- The problem is static since it is formulated for each time slice independently. In order to estimate the vessel currents I_v, a simple static Ohm's law $I_v \propto \frac{1}{R}\frac{d\psi}{dt}$ is used, by grouping the coils around the flux loop measurements. One could imagine otherwise to formulate a reconstruction as in eq. (3.9) but using as forward model the coupled system of equations of the free boundary equilibrium and the conductor evolution eq. (2.63). This

would turn the problem into a dynamic state and parameters reconstruction and would provide better time evolution of the current in the conductors.

3.2.1 MER reduced problem

To simplify the optimization problem instead of looking for $\{x^*, \boldsymbol{\theta}^*\} = \underset{x, \boldsymbol{\theta}}{\operatorname{argmin}} ||\tilde{\boldsymbol{M}} - \mathbb{A}(x)\boldsymbol{\theta}||_w^2$ one can consider variation only in the parameters $\boldsymbol{\theta}$ and not on the states x, hence replacing the optimization part of eq. (3.9) with $\{x^*, \boldsymbol{\theta}^*\} = \underset{\boldsymbol{\theta}}{\operatorname{argmin}} ||\tilde{\boldsymbol{M}} - \mathbb{A}(x)\boldsymbol{\theta}||_w^2$ (notice that the argmin is computed letting only $\boldsymbol{\theta}$ to vary). What remains is a linear-squares problem which has the following solution $\boldsymbol{\theta} = (\mathbb{A}^T(\boldsymbol{x})\mathbb{A}(\boldsymbol{x}))^{-1}\mathbb{A}^T(\boldsymbol{x}) \cdot \tilde{\boldsymbol{M}}$. Replacing this solution in eq. (3.9), from an optimization problem, one obtains a more simple non-linear root finding problem.

$$
\begin{cases}
\boldsymbol{\theta} = (\mathbb{A}^T(\boldsymbol{x})\mathbb{A}(\boldsymbol{x}))^{-1}\mathbb{A}^T(\boldsymbol{x}) \cdot \tilde{\boldsymbol{M}} & \\
\Delta^*\psi = -2\pi\mu_0(j_{pl} + j_e) & \text{in} \quad \Omega_c \\
\psi(R, Z) = \sum_{i=[pl,a,s]} \int_{\Omega_i} G_i(R, Z; R', Z') j_{\varphi,i}(R', Z') dR' dZ' & \text{in} \quad \partial\Omega_c \\
j_{pl} = \sum_{i=1}^{N_g} a_i R^{v_i} g_i(\hat{\psi}(R, Z)) & \text{in} \quad \Omega_{pl} \\
j_{pl} = 0 & \text{in} \quad (\Omega_{pl} \cap \Omega_c)^c
\end{cases}
\tag{3.10}
$$

The eq. (3.10) is the problem implemented in LIUQE [Moret et al. 2015]. The differences between the solution of the original problem eq. (3.9) and the simplified one eq. (3.10) are explained analytically in Appendices E, F. In the part II of the thesis we will investigate the difference numerically for some TCV cases. However we can anticipate that the simplification is equivalent to consider $\nabla_x \mathbb{A}(x) = 0$ and since the external magnetic measurements are not very sensitive to variations of the plasma flux inside the plasma, $x = \psi(R, Z)$, this simplified solution will not make a significant difference on the final result.

3.2.2 Critical aspects of MER and motivation for KER

A critical aspect in MER is the ill-conditioning of the problem in eq. (3.9): a not very accurate reconstruction of the plasma profiles can be obtained since the external magnetic measurements are not very sensitive to internal profile feature. One needs to either include regularization terms in the cost function or reducing the number of basis functions. However, as a result, the reconstructed $p(\rho)$ and $j(\rho)$ profiles, which are directly related to $p'(\hat{\psi})$ and $TT'(\hat{\psi})$ from eq. (2.40), can be strongly affected by the adopted regularization technique rather than real physical features. In many plasma scenarios like H-mode, flat profile due to internal mode, hollow current density profiles, transport barrier, ..., these features are essential components to regulate the plasma performances and therefore it would be important to properly take them into account in the equilibrium reconstruction.

The third important aspect is that, among all the available magnetic measurements $\tilde{\boldsymbol{M}}$, only the toroidal flux $\tilde{\Phi}_t$ from the DML is directly related to only one of the two free functions, p' and TT', making this measurement essential for disentangling the degeneracy between

Rp' and TT'/R in the RHS of GS equation. Important quantities like the total stored plasma energy, i.e. the integral of the pressure over the plasma volume, are strongly sensitive to this measurement. Unfortunately this measurement is difficult to calibrate, since the plasma component of the toroidal flux is orders of magnitude smaller than the vacuum one. It may cause errors in reconstruction unless the measurement is very precisely calibrated.

We will see in the next section that KER aims to solve these issues by providing direct constraints on $p'(\rho, t)$ and $TT'(\rho, t)$ from available kinetic measurements and/or first principle based modeling.

3.3 Kinetic Equilibrium Reconstruction(KER) in TCV

After having discussed some of the critical aspects of magnetic equilibrium reconstruction in the previous section, we introduce in this section the formulation of Kinetic Equilibrium Reconstruction (KER) performed in TCV. Since a general consensus on the definition of KER has not been achieved in the fusion community, we build our definition incrementally from the magnetic equilibrium reconstruction problem. We first state a list of assumptions on which we will base our formulation and discuss the specific set of measurements available in TCV and the required additional modeling. Following the frequentist approach we obtain a first formulation of the problem as a least-squares non-linear optimization problem with non-linear equality constraints, as done for the magnetic equilibrium reconstruction. As for the case of the Magnetic Equilibrium Reconstruction, we will adopt some simplifications obtaining two possible simplified formulations that will be implemented in the part II of this thesis. The purpose of this simplification is only to facilitate the numerical implementation of the problem. Limitations and consequences of the assumptions taken will be discussed in details.

3.3.1 Definition and literature investigation

The reconstruction problem is always a combination of forward model and measurements. A first definition of Kinetic Equilibrium reconstruction is to interpret it as performing a Magnetic Equilibrium Reconstruction providing direct constraints on internal plasma profiles from modeling and/or available measurements.

A relatively large set of diagnostics is available to measure internal plasma features. We provide here a non-exhaustive list restricted to the most established diagnostics available. We will restrict for simplicity to diagnostics providing measurements which appear directly or indirectly in the forward model as in sec. 2. The electron temperature T_e can be measured by Thomson Scattering (TS) [Peacock et al. 1969], soft X-ray [von Goeler et al. 1974] emission originate by electrons in thermal range, Electron Cyclotron Emission (ECE) diagnostics [Bornatici et al. 1983]. The electron density n_e is measured mainly by TS and microwave reflectometry [Undertaking 1992]. The ion temperature T_i is measured by Charge eXchange Recombination

Spectroscopy [Isler 1994]. The magnetic or magnetic field pitch angle can be measured inside the plasma by Motional Stark Effect (MSE) [Rice et al. 1997], imaging motional stark effect [Thorman et al. 2018], or polarimetry . These last one can be related directly to the plasma current density j. Direct measurements of the plasma shape can be made using visible light or filter emission, and bolometers can be used to measure the plasma radiation and to compute the total power balance. The pros of using constraints from measurements are simply that they provide the real physical value of a given quantity in a given time instant and location. However, measurements have limitations in both availability and resolution. For example the MSE diagnostic, while being the only one together with polarimetry to be able to provide information on the internal distribution of the plasma current, it is often difficult to calibrate in particular for metal wall machine [Makowski et al. 2008]. The limitations become more stringent when the reconstruction is performed in real-time during an experiment.

From the forward modeling side, we have already discussed in sec. 2 a system of equations, the flux surface averaged transport problem, which can provide first-principle based estimates of plasma kinetic profiles. The pros of using constraints from modelling are that these quantities are available in principle at any time and space resolution provided to be able to solve the set of equations describing the forward model. The cons are that the quality of the predictive/forward estimation depends on the assumptions made to derive the forward model and to the knowledge/uncertainty of the model. For example, solving the energy equation for the ion temperature requires to provide the transport coefficients χ_i which is not a well known quantity.

As we have seen there are multiple diagnostics, sometimes redundant, and several models that can provide information of the same physical quantity. A question rises then, what to use to define the KER and provide constraints to the equilibrium profiles? The answer is trivial only in the extreme cases. If there is a diagnostic which is much more precise. For example the Thomson scattering diagnostic has proved to be a very reliable and precise measurements for T_e and n_e in different operation in TCV condition and it is always taken into account whenever available. If, on the contrary, no measurements are available for a given quantity, then one can only use estimation from modelling. In TCV, for example, there are no measurements for the internal distribution of the current density profile, hence it is necessary to use the CDE equation eq. (2.56) to provide constraints on the current density profile.

However, when performing Kinetic Equilibrium Reconstruction, one is almost never in one of the two extreme cases and information from both the diagnostic and modelling have to be used. It should be clear that from the first definition of KER, based on simply improving the limitations of MER providing internal constraints to the profiles, the target moves to a more complex interpretation where quantities related to the plasma equilibrium problem have to be considered at the same level as the kinetic ones. This way the border between the Kinetic Equilibrium Reconstruction and what we could call in general Integrated Data Analysis becomes less defined.

We discussed in detail in sec. 3.1 how from a forward model, making assumptions on the type of uncertainties of the measurements and models, one can derive a reconstruction problem that combines the available measurements and modelling. We have seen in particular how to make use of the frequentist approach to derive the minimum least-squares problem for the magnetic equilibrium reconstruction and the differences with the Bayesian approach.

In the following we will derive the formulation of KER implemented in TCV replicating the steps done for the MER eq. (3.9), obtaining a minimum least-squares MLS problem, where the forward model will be the coupled equilibrium and transport system of equations and the measurements a combination of kinetic and magnetic measurements.

3.3.2 Problem derivation hypothesis

The derivation of the problem proposed in the following is general for every tokamak, however some choices of the derivation are due to the specific set of diagnostics available in TCV. This however could be easily generalized to account for different set of diagnostics. We will take the following working assumptions,

1. The 1.5D equilibrium and transport model is considered for the forward model.

2. Only the best available estimate for each quantity is retained (modelling or measurement), hence most of the time a single source for each physical quantity is used.

3. Least-squares approach: any available measurement enters in a least-square type cost function weighted by its uncertainty. Any unknown parameter, if not estimated by a predictive model, is considered as a free parameter to be found in order to minimize the cost function.

4. No modelling errors: Uncertainties on the estimation of the forward model only come from uncertain inputs.

5. Error propagation analysis will not be considered.

A last remark, which is trivial but it is worth to specify in this context, is that whenever a given quantity appears in different places in a system of equations, this must be assumed the same value everywhere to be an exact solution of the problem. In other words, the values used in the models must be consistent across different equations.

Given the least squares approach, the hypothesis 2 is not restrictive and can be relaxed, since many different measurements, eventually redundant, can enter together in the cost function, without changing the formulation. We imposed strongly only to derive the specific TCV formulation, since for most of the kinetic quantities there is no redundancy on the measurements or, better, one of the estimate is clearly more accurate than the others. The working hypothesis 4 could be relaxed by considering the model uncertainty as extra parameters to be found. Also

the hypothesis 5 could be relaxed, by remembering that the quality of the reconstructed state and parameters in a frequentist approach are estimated by evaluating the sensitivity of the estimator.

Given the working assumptions we now focus on TCV by starting to provide details on assumption 2, discussing first the available set of diagnostics considered and then the additional modeling needed in order to complete the formulation.

Set of kinetic diagnostics

A detailed description of the diagnostics available in TCV is listed in [Coda et al. 2017]. As for the case of the magnetic measurements in the MER problem, we will indicate with the $\sim$ a quantity measured by a diagnostic and in bold-tilde a collection of measurements acquired at different time instants and space locations. For example $\tilde{\boldsymbol{A}} = \{A(R_i, Z_i, t_k)\}$ with $i = [1, .., N_p]$ and $t = [1, .., N_t]$ is a collection of $N_p \times N_t$ of the quantity at (R_i, Z_i) positions in the poloidal plane and t_k time instants.

Additionally to all the magnetic measurements used for the MER we will consider the following list of kinetic measurements:

- $\tilde{\boldsymbol{T}}_e$: The Thomson scattering system is the main diagnostic for the measurement of the spatial profiles of the electron temperature and density on TCV. The profiles are measured along a laser beam passing the plasma in vertical direction at R=0.9m (mid radius of the TCV vessel). At present, there are 109 observation positions covering the region from Z=-69cm to Z=+55cm with a spatial integration length that depends on the channel location. The acquisition frequency is $20 Hz$ or $60 Hz$, which does not allow to follow the diffusion time scale for the electron temperature in TCV. A description of the spatial resolution and the position of all the observation positions is given in [Arnichand et al. 2019].

- $\tilde{\boldsymbol{n}}_e$: Together with the Thomson scattering diagnostic, a 14-channel Mach-Zehnder type interferometer is used to measure the line-integrated density along parallel chords in the vertical direction. The system comprises a FIR (FarInfraRed with CH2F2 difluoromethane gas) laser, pumped by a CO2 laser, and emitting a continuous wave at 184.3 μm , and a multi-element detector unit (InSb hot-electron bolometer) with an acquisition frequency of $20 kHz$ available also during real-time operation [Barry 1999].

- $\tilde{\boldsymbol{T}}_i$: The Charge eXchange Recombination Spectroscopy [Marini 2017] coupled with the diagnostic neutral beam injection provides information on the ion temperature with 10-50 Hz acquisition frequency. However this diagnostic is not used by default during operation and not available for real-time purposes.

We summarize the measurements and their diagnostic in the following table 3.3.

Symbol	Name	Source
$\tilde{\boldsymbol{B}}_m$	Poloidal B component	Magnetic probes
$\tilde{\boldsymbol{F}}_f,$	Poloidal flux	Flux loops
$\tilde{\boldsymbol{I}}_a,$	Active coil currents	
$\tilde{\boldsymbol{I}}_v,$	Vessel filament currents	V measurements + model resistance
$(\tilde{F}_t)$	Plasma toroidal flux	diamagnetic flux loop (DML)
$\tilde{I}_p,$	Plasma current	Ampére's law on $\boldsymbol{B}_m$
$\tilde{\boldsymbol{n}}_e,$	Electron density	Thomson scattering / FIR
$\tilde{\boldsymbol{T}}_e,$	Electron temperature	Thomson scattering
$(\tilde{\boldsymbol{T}}_i)$	Ion temperature	Charge Exchange

Table 3.3 – Summary of measurements used for Kinetic Equilibrium Reconstruction in TCV and related sources. With the symbols in parenthesis we indicate the measurements which are not always available/used in post-discharge analysis of a specific experiments.

Modeling

- p: The flux surface averaged total plasma pressure $p(\rho, t)$ is modeled as

$$p(\rho, t) = n_e T_e + n_i T_i + \frac{(p_{B,\parallel} + p_{B,\perp})}{2} + p_{fast} \tag{3.11}$$

where in particular $p_{B,\parallel}$ and $p_{B,\parallel}$ are the parallel and perpendicular pressure provided by the neutral beam heating system. p_{fast} is the contribution of the pressure provided by the fast ions hence from the ions in the tails of the energy distribution, but not belonging to the beam, for example the alpha particles generated by the fusion reaction. In TCV and experimental devices p_{fast} is negligible but we report it here for completeness. In eq. (3.11) we give the expression as implemented in the ASTRA code [Pereverzev and Yushmanov 2002] which will be used in the implementation of KER in the following chapters. To estimate the contribution of the beam, a model to describe the slowing down of the fast ions from the injection into the system, solving the particle trajectories, is needed. We refer to [Polevoi et al. 1997] for details. In particular n_e, T_e, and sometimes T_i, have direct measurements.

- n_i: From the definition of the effective charge Z_{eff} and the hypothesis of quasi neutrality,

$$Z_{eff} = \frac{\sum_{j=\{i,c\}} Z_j^2 n_j}{\sum_{j=\{i,c\}} Z_j n_j} \qquad \sum_{j=\{e,i,c\}} Z_j n_j = 0,$$

assuming carbon to be the only impurity species, Z_{eff} being constant in the plasma volume and performing the flux surface average we obtain

$$n_i(\rho) = n_e(\rho) \frac{Z_c - Z_{eff}}{Z_c - 1}. \tag{3.12}$$

The bulk ion density n_i in TCV is typically represented by Deuterium $Z_i = 1$. We remind

that for carbon, which is the main impurity for TCV, $Z_c = 6$, and that $Z_e = -1$.

In case a fast ion population n_B contribution is given from the beam, this is subtracted from the bulk ions n_i, and Z_{eff} has to be considered as a given parameter or a free parameter to be found with the optimization problem. A possible way to estimate Z_{eff} from the stationary state current diffusion equation is provided in appendix B.

- T_i: There are several options for this quantity, depending on the diagnostics and discharge condition. The CXRS measurements is not always available. Several modelling options are considered.

    1. $T_i(\rho, t)$ as one of the free parameter to be found with the MLS problem.

    2. The flux surface averaged diffusion for T_i was already discussed in eq. (2.64) The transport coefficient $\chi_i(\rho, t)$ is considered either a free parameter to be found by the optimization or given by neoclassical estimation [Angioni and Sauter 2000b], [Angioni and Sauter 2000a]. Eventually a scaling factor is multiplied to χ_i, tuned to match the CXRS measurements in available experiment. We refer to ASTRA manual sec. 3.9 for specifications of the boundary condition, sources and sinks. In particular the function to compute the contribution of the fast ions is given in [Polevoi et al. 1997].

    3. Another option is to consider $T_i(\rho, t) = \alpha T_e(\rho, t)$. The parameter α can be considered as a given parameter or a free parameter to be found with the optimization problem. Another possibility is to specify a given total plasma stored energy $W_{MHD} = \frac{3}{2} \int p \, dV$. Recalling eq. (3.11), this becomes

    $$\alpha = \frac{\frac{3}{2} W_{MHD} - \int (n_e T_e + p_b + p_f) dV}{\int n_i T_e dV}, \tag{3.13}$$

    where we indicated the contribution to the pressure of the neutral beam. In this case W_{MHD} becomes the new parameter to be specified a priori or to be found with the optimization problem.

- $j_\parallel / j_{tor}$: Since no diagnostics to measure these quantities are available at present in TCV, we will make use of the current diffusion equation already explained in detail in sec. 2.4.

- $P_\perp$, $P_\parallel$, P_i: The contribution of the fast particles to the total pressure and eventually to the heat source for the T_i diffusion equation, are computed from analytical approximation [Polevoi et al. 1997].

As clear from the measurements and modelling description, one can choose among several options, in particular to estimate T_i, that would lead to a different formulation of the problem. The choice is based on the availability and the quality of the measurements, as also stated in working assumption 2.

3.3.3 Problem formulation

We can finally provide the formulation for the KER problem. Only the case where T_i is estimated from transport diffusion modelling is provided as an example. The other formulations can be easily derived from that. In the derivation we will not make the distinction between state and free parameters to simplify the notation, considering that for each set of parameters the forward model can be solved.

In particular we define the free parameters $\boldsymbol{P} = \{\, \boldsymbol{I}_a, \boldsymbol{I}_v, T_e(\rho), n_e(\rho) \,\}$ and the set of measurements $\tilde{\boldsymbol{M}} = \{\tilde{\boldsymbol{B}}_m, \tilde{\boldsymbol{F}}_f, \tilde{I}_p, \tilde{F}_t, \tilde{\boldsymbol{I}}_v, \tilde{\boldsymbol{I}}_a, \tilde{\boldsymbol{T}}_e, \tilde{\boldsymbol{n}}_e \,\}$.

The formulation of the problem becomes:
Given: $\tilde{\boldsymbol{M}}$, inputs $\chi_i(\rho, t)$, $Z_{eff}(t)$, $n_B(\rho, t)$, the sources $j_{cd}(\rho, t)$, $P_i(\rho, t)$ and the initial condition for the diffusion equation $T_{i,0}(\rho)$, $\psi_0(\rho)$ and all the other terms appearing in the equation
Find: $\boldsymbol{P}^*$ and all the quantities appearing in the system of equations

$$\boldsymbol{P}^* = \underset{\boldsymbol{P}}{\mathrm{argmin}} ||\tilde{\boldsymbol{M}} - \boldsymbol{M}(\boldsymbol{P})||_w^2$$
such that
$$
\begin{cases}
\Delta^* \psi = -2\pi\mu_0(j_{pl} + j_e) & \text{in} \quad \Omega_c \\
\psi(R, Z) = \sum_{i=[pl,a,s]} \int_{\Omega_i} G_i(R, Z; R', Z') j_{\varphi,i}(R', Z') dR' dZ' & \text{in} \quad \partial\Omega_c \\
\frac{3}{2} \frac{1}{(V'_{\hat{\rho}})^{5/3}} \left(\frac{\partial}{\partial t}\Big|_{\hat{\rho}} - \frac{\dot{\Phi}_B}{2\Phi_b} \frac{\partial}{\partial\hat{\rho}}\hat{\rho} \right)[(V'_{\hat{\rho}})^{5/3} n_i T_i] = \frac{1}{V'_{\hat{\rho}}} \frac{\partial}{\partial\hat{\rho}} \left[\frac{g_1}{V'_{\hat{\rho}}} n_i \chi_i \frac{\partial T_i}{\partial\hat{\rho}} + \frac{5}{2} T_i \Gamma_i g_0 \right] + P_i & \\
n_i(\rho) = n_e(\rho) \frac{Z_c - Z_{eff}}{Z_c - 1} - n_B. & \text{in} \quad \rho \in [0,1] \\
p(\rho, t) = n_e T_e + n_i T_i + \frac{p_{B,\|} + p_{B,\perp}}{2} + p_{fast} & \text{in} \quad \rho \in [0,1] \\
\sigma_\| \left(\frac{\partial\psi}{\partial t} - \frac{\hat{\rho}\dot{\Phi}_B}{2\Phi_B} \frac{\partial\psi}{\partial\hat{\rho}} \right) = \frac{T^2}{16\pi^2\mu_0\Phi_B^2\hat{\rho}} \frac{\partial}{\partial\hat{\rho}} \left(\frac{g_2 g_3}{\hat{\rho}} \frac{\partial\psi}{\partial\hat{\rho}} \right) - \frac{B_0}{2\Phi_B\hat{\rho}} V'_{\hat{\rho}} (j_{bs} + j_{cd}) & \text{in} \quad \rho \in [0,1] \\
\left(\frac{g_2}{4\pi^2\mu_0} \frac{1}{V'_{\hat{\rho}}} \frac{\partial\psi}{\partial\hat{\rho}} \right)\Big|_{\hat{\rho}_B} = I_p, \qquad \frac{\partial\psi}{\partial\hat{\rho}}\Big|_{\hat{\rho}=0} = 0, \qquad \psi(\rho, t = 0) = \psi_0 &
\end{cases}
$$
(3.14)

We would like to make some remarks on the formulated problem eq. (3.14).

- With the $*$ we indicate the solution of the formulated problem.

- In the present thesis we aim to discuss KER only for events occurring at the time scales of energy/particle confinement and of resistive diffusion. The system of equations eq. (3.14), while including dynamic models for the kinetic profiles, does not present any instability. One could include for example the evolution of the current in the coils and vessel in the forward model, provided that when solving the equation a sufficient time resolution is used and the vertical stability controller is coupled to the system of equation. This would allow for example to reconstruct the early phase of an eventual VDE event. The same thing applies to other type of instabilities. A model to describe the dynamics of the sawtooth crash [Biskamp and Drake 1994] can be included to reconstruct the evolution of the q profile on axis during these events eventually synchronizing the

crashes in the reconstruction with measurements from diagnostics with high acquisition frequency [Fischer et al. 2019], or simply to recover on average central q above 1.

- The problem is classified as a minimum least-squares (MLS) problem with non-linear equality constraints represented by the force balance equation (Grad-Shafranov), the current diffusion equation, the radial transport diffusion equation for $T_i(\rho, t)$ and the model for $n_i(\rho, t)$ and $p(\rho, t)$. The cost function is weighted by the measurements uncertainty. In frequentist interpretation this corresponds to assuming additive white noise to all measurements. The solution of the problem can be sought with the use of Lagrangian multipliers.

- The forward model for the observer $\boldsymbol{M}(\boldsymbol{P})$ is nonlinear. For a given set of parameters $\boldsymbol{P}$, it requires to solve the full system of equations representing the constraints. We have already seen in the Magnetic Equilibrium Reconstruction how from the solution of the Grad-Shafranov equation the forward estimate of the magnetic measurements are obtained. The extra kinetic ones $\tilde{\boldsymbol{T}}_e$, $\tilde{\boldsymbol{n}}_e$ are directly related to the new free parameters $T_e(\rho, t)$, $n_e(\rho, t)$.

- In eq. (3.14) the equilibrium and the transport problem are strongly coupled. For example, a variation of the free parameter n_e produces a modification of p hence a modification of the RHS of the Grad-Shafranov equation and ultimately a variation of the forward prediction of the magnetic measurements contained in $\boldsymbol{M}(\boldsymbol{P})$.

- The plasma current distribution $j_{pl}(\rho, t) = j_{pl}(\psi(R, Z), p'(\psi), TT'(\psi))$ is computed with eq. (2.21) after having found the Ω_{pl} from the flux map $\psi(R, Z)$. Thus, $p'(\hat{\psi})$ and $TT'(\hat{\psi})$ are no longer free parameters in this problem but are obtained from the modelling of $p(\rho, t)$ and the current diffusion equation, through the evaluation of $j_{tor}(\rho, t)$ eq. (2.38) and its relation with p' and TT' eq. (2.41). As discussed in sec. 2.2.4, different quantities can be chosen to relate the current diffusion results to the RHS of the Grad-Shafranov equation. However the solution of the system will not change for a different choice of the coupling profiles.

- The free parameters $n_e(\rho, t)$, $T_e(\rho, t)$ can be treated, similarly to what is done in the Magnetic Equilibrium Reconstruction, by expanding them into a linear combination of known basis functions, where the coefficients of the expansion become the new free parameters to be found.

- The problem formulated in eq. (3.14) respects all the working assumptions in sec. 3.3.2. In particular for each physical quantity, only its best known estimate, either from model or measurements, is used. For example for T_i one can substitute in the model the different forward models depending on the availability of the diagnostic for a given experiment.

- In case of uncertainty of the models, this can be added to the list of free parameters. For example suppose that the effective charge $Z_{eff} = Z_{eff,0} + a$ is known up to a constant a, this constant can become part of the free parameters to estimate.

- In eq. (3.14) the sources for the transport equation, the current drive j_{cd} and the energy released by the presence of the neutral beam P_i are assumed to be given. In general the models to compute them, a full-wave warm plasma model [Poli et al. 2001] and a kinetic model for the diffusion of the neutral particles [Pankin et al. 2004; Weiland et al. 2019], could be included in the system of equations to be solved.

- In eq. (3.14) $\chi_i(\rho, t)$, $Z_{eff}(t)$ are considered as given parameters, however in general these might not be known a priori. One could include them in the list of free-parameters to be found with the optimization problem. We also notice that in principle Z_{eff} might have a spatial dependence. One needs to remember that increasing the number of parameters without increasing the measurements or the constraints easily leads to an ill-posed problem.

- Differently to the magnetic equilibrium reconstruction, which considered a static problem, eq. (3.14) includes time evolutive dynamic models for the evolution of the ion temperature and current density profiles. As a consequence, all the free parameters and quantities entering in the equality constraints depend on time. As discussed when deriving the inverse problem within a statistical framework, this significantly enlarges the number of free parameters. Indeed correlation between two different time slices have to be taken into account, for example a variation of the electron density n_e at time t will have an impact on the pressure estimate at time $t + \Delta t$, hence will impact the cost function at $t + \Delta t$. Suppose that the system of equations is solved by discretizing it in N_t time steps and that the number of parameters for a given time step is N_θ, the total number of parameters that are let free to vary in order to minimize the cost function becomes $N_t \times N_\theta$. A solution to reduce the number of free parameters is to forget the correlation above a certain characteristic time scale, where the threshold can be obtained from the physical time scale of the evolutive equation in the system. In the implementation that we will consider of KER, we will almost always assume each time slice as independent. Another option could be to let the free parameters to vary only in few timeslices and interpolate between them. The choice of the time slice could be for example the sampling rate of the measurements. Another possible choice is to consider the system to be represented by a Markov process where the next state only depends on the actual state and inputs, but not on its previous history. This leads to formulation of recursive estimation of the parameters such as Bayesian filters techniques [Särkkä 2013].

- The last remark is about the error propagation analysis and how to estimate the quality of the reconstructed parameters. Given the frequentist interpretation of the problem, this could be achieved by studying the sensitivity of the reconstructed parameters to variations of the inputs measurements. This can also be done by solving the problem and sampling the measurements from a Gaussian distribution with the same standard deviation used in the cost function. However this is very expensive because it requires to solve the optimization problem for every sample.

3.3.4 Reduced formulations

In the previous section, after having described the diagnostic set of TCV, we derived a formulation for the Kinetic Equilibrium Reconstruction problem based on a minimum least-squares principles. However the non-linear nature of the problem together with the combination of dynamic and distributed models, makes the formulation eq. (3.14) difficult to address.

We discuss in this section two reductions of the problem that will simplify its implementation in part II of the thesis. The idea, as it was done for the MER, is to eliminate some non-linearities from the optimization problem in particular, splitting the optimization of the magnetic measurements from the optimization of the kinetic ones, and to turn them into a linear optimization problem. This way the solution of the optimization problem will be given by its normal equation. The problem will become therefore a root-finding problem similarly to what is done for the MER.

To derive the first reduced formulation we split the free-parameters into the magnetic $\boldsymbol{P}_m = \{\boldsymbol{I}_a, \boldsymbol{I}_v\}$ and the kinetic ones $\boldsymbol{P}_k = \{T_e(\rho, t), n_i(\rho, t), n_e(\rho, t)\}$. Similarly we split the measurements between magnetic ones $\tilde{\boldsymbol{M}}_{\boldsymbol{m}} = \{\tilde{\boldsymbol{B}}_m, \tilde{\boldsymbol{F}}_f, \tilde{I}_p, \tilde{\Phi}_t, \tilde{\boldsymbol{I}}_v, \tilde{\boldsymbol{I}}_a\}$ and kinetic ones $\tilde{\boldsymbol{M}}_{\boldsymbol{k}} = \{\tilde{\boldsymbol{T}}_e, \tilde{\boldsymbol{n}}_e\}$, and we do that also for the forward observer model $\boldsymbol{M}(\boldsymbol{P_k}, \boldsymbol{P_m}) = \{\boldsymbol{M}_k(\boldsymbol{P}_k), \boldsymbol{M}_m(\boldsymbol{P}_m)\}$. This way the cost function can also be split in the sum of two contributions $\chi^2 = \chi_m^2 + \chi_k^2$, where $\chi_m^2 = ||\tilde{\boldsymbol{M}}_m - \boldsymbol{M}_m(\boldsymbol{P}_m)||_{w_m}^2$ and $\chi_k^2 = ||\tilde{\boldsymbol{M}}_k - \boldsymbol{M}_k(\boldsymbol{P}_k)||_{w_k}^2$.

We now consider some simplification assumptions.

1. No non-linear dependence between the magnetic and the kinetic contribution in the cost function, hence $\nabla_{P_m}\boldsymbol{M}_k = 0$ and $\nabla_{P_k}\boldsymbol{M}_m = 0$. This way the original optimization problem can be split in two independent optimization problems,

$$\boldsymbol{P}_m = \operatorname*{argmin}_{\boldsymbol{P}_m} \chi_m^2 \tag{3.15}$$

$$\boldsymbol{P}_k = \operatorname*{argmin}_{\boldsymbol{P}_k} \chi_k^2 \tag{3.16}$$

2. Linear relation between free parameters and estimation of measurements from the forward models. This means for example $\boldsymbol{M}_k = \mathbb{B}\boldsymbol{P}_k$, for a given $\mathbb{B}$ matrix, such that the solution of the optimization problem eq. (3.16) becomes $P_k = (\mathbb{B}^T\mathbb{B})^{-1}\mathbb{B}^T\tilde{\boldsymbol{M}}_k$. For the case of the magnetic related problem, this becomes exactly the same problem as for the MER as discussed in section 3.2.1, except for the fact that only $\boldsymbol{I}_a, \boldsymbol{I}_v$ are considered as free parameters. For the kinetic problem, this will depend on the choice of the representation for $T_e(\rho, t), n_e(\rho, t)$. We choose a spline representation, such that the spline coefficients become the $\boldsymbol{P}_k$ free parameters and the relation between the spline coefficients and $\boldsymbol{M}_k$ is linear. However the mapping between the (R, Z) location of the measurements and ρ will depend on the $\psi(R, Z)$ solution, hence $\mathbb{B}(\psi(R, Z))$.

3. Time independence of the optimization problem for every time instant. This is a strong

assumption which reduces the problem to a series of independent linear optimization problem. This effectively breaks correlation between parameters at different time instant. This can play a role in the time evolving models present in the formulation. For example, the free parameters $T_e(\rho, t)$, solution of the optimization problem at time t, that enters in the computation of $\sigma_{\parallel}(\rho, t)$ at time t and will affect the solution of the current profile of the current diffusion equation at $t + \Delta t$, hence the $TT'(\rho, t + \delta T)$ and therefore the χ_m at $t + \Delta t$. This secondary effect is neglected in this simplified problem and T_e is taken such that it minimizes the cost function instantaneously at a given instant t.

With these hypothesis we can now formulate a new simplified problem starting from eq. (3.14)

Given: $\tilde{M}_m$, $\tilde{M}_k$ inputs $\chi_i(\rho, t)$, $Z_{eff}(t)$, $n_B(\rho, t)$, the sources $j_{cd}(\rho, t)$, $P_i(\rho, t)$ and the initial condition $T_0(\rho)$, $\psi_0(\rho)$

Find: $\boldsymbol{P}_k^*$, $\boldsymbol{P}_m^*$ and all the quantities appearing in the system of equations such that

$$
\begin{cases}
\boldsymbol{P}_m^* = (\mathbb{A}(\psi)^T \mathbb{A}(\psi))^{-1} \mathbb{A}(\psi)^T \tilde{\boldsymbol{M}}_m \\
\Delta^* \psi = -2\pi\mu_0 (j_{pl} + j_e) & \text{in} \quad \Omega_c \\
\psi(R, Z) = \sum_{i=[pl,a,s]} \int_{\Omega_i} G_i(R, Z; R', Z') j_{\varphi,i}(R', Z') dR' dZ' & \text{in} \quad \partial\Omega_c \\
\boldsymbol{P}_k^* = (\mathbb{B}(\psi)^T \mathbb{B}(\psi))^{-1} \mathbb{B}(\psi)^T \tilde{\boldsymbol{M}}_k \\
\frac{3}{2} \frac{1}{(V_{\hat{\rho}}')^{5/3}} \left(\frac{\partial}{\partial t}\Big|_{\hat{\rho}} - \frac{\dot{\Phi}_B}{2\Phi_b} \frac{\partial}{\partial\hat{\rho}} \hat{\rho} \right) [(V_{\hat{\rho}}')^{5/3} n_i T_i] = \frac{1}{V_{\hat{\rho}}'} \frac{\partial}{\partial\hat{\rho}} \left[\frac{g_1}{V_{\hat{\rho}}'} n_i \chi_i \frac{\partial T_i}{\partial\hat{\rho}} + \frac{5}{2} T_i \Gamma_i g_0 \right] + P_i \\
T_i(\rho = 1, t) = 0, \qquad \frac{\partial T_i}{\partial\rho}\Big|_{\rho=1} = 0, \qquad T(\rho, t = 0) = T_0 \\
n_i(\rho) = n_e(\rho) \frac{Z_c - Z_{eff}}{Z_c - 1} - n_B. & \text{in} \quad \rho \in [0, 1] \\
p(\rho, t) = n_e T_e + n_i T_i + \frac{p_{B,\parallel} + p_{B,\perp}}{2} + p_{fast} & \text{in} \quad \rho \in [0, 1] \\
\sigma_{\parallel} \left(\frac{\partial\psi}{\partial t} - \frac{\hat{\rho}\dot{\Phi}_B}{2\Phi_B} \frac{\partial\psi}{\partial\hat{\rho}} \right) = \frac{T^2}{16\pi^2\mu_0\Phi_B^2\hat{\rho}} \frac{\partial}{\partial\hat{\rho}} \left(\frac{g_2 g_3}{\hat{\rho}} \frac{\partial\psi}{\partial\hat{\rho}} \right) - \frac{B_0}{2\Phi_B\hat{\rho}} V_{\hat{\rho}}'(j_{bs} + j_{cd}) & \text{in} \quad \rho \in [0, 1] \\
\left(\frac{g_2}{4\pi^2\mu_0} \frac{1}{V_{\hat{\rho}}'} \frac{\partial\psi}{\partial\hat{\rho}} \right)\Big|_{\hat{\rho}_B} = I_{pl}(t), \qquad \frac{\partial\psi}{\partial\hat{\rho}}\Big|_{\hat{\rho}=0} = 0, \qquad \psi(\rho, t = 0) = \psi_0
\end{cases}
$$

$$(3.17)$$

We would like to make some remarks first on the consequences to the simplification assumptions taken,

- The linear dependence assumption allowed to turn the problem into a root finding making it easier to solve.

- The solution of eq. (3.17) is not a solution of eq. (3.14). With the first assumption we effectively removed a non linear dependence between the kinetic and the magnetic part of the system of equations. It is possible therefore that a solution of eq. (3.17) indicated with the suffix 0 will have a smaller $\chi_{k,0}^2$ than the corresponding part of the cost function

in eq. (3.14), but globally $\chi_{k,0}^2 + \chi_{m,0}^2 > \chi^2$ where χ^2 is the total one of eq. (3.14) problem. This problem can be interpreted as an overfitting issue. To explain further, consider the case of fitting n_e: for the same number of basis functions as in eq. (3.14) to represent $n_e(\rho, t)$ in eq. (3.17), when the cost function is split, there will be effectively a lower number of measurements to fit, the magnetic ones being not present in χ_k.

- Due to the simplification assumption 1, the magnetic measurements are effectively used only to estimate I_a and I_v, since $\boldsymbol{P}_m = \{\boldsymbol{I}_a, \boldsymbol{I}_v\}$. This is a very poor usage of their information content. The plasma profiles p' and TT' indeed are fully specified from the modelling and the kinetic measurements, through p and j_{tor} from the current diffusion, however the magnetic measurements are known to retain at least information on the global scaling of the internal plasma profile and of some integrated quantities, such as the total stored energy.

- Due to the simplification assumption 2, the Φ_t measurement is effectively not used since in eq. (3.17) it has a null linear variation with respect to $\boldsymbol{I}_a$, $\boldsymbol{I}_v$. This quantity indeed depends linearly only on TT', which is directly provided by the kinetic modeling in eq. (3.17). The information content of this quantity, which is very important in MER to disentangle the contribution of p' and TT' to the RHS of the Grad-Shafranov equation, is lost in the simplified problem eq. (3.17). This might be either an advantage or a disadvantage in terms of the resulting fit depending on the case. If the estimation of the kinetic profiles from the kinetic measurements and model is reliable removing the dependencies on the DML measurement, which is always difficult to calibrate, would be positive. But if instead the kinetic profile estimation is not accurate, for example because the T_i estimation is not accurate, it would neglect the information of a crucial measurement.

In order to partially address these issues, we would like to present also a second simplified formulation starting from eq. (3.14) and eq. (3.17). The simplification assumptions, in particular 1, which lead to eq. (3.17) had the effect of braking some non-linearities between the equilibrium part of the modelling and the transport one. In the following we would like obtain a trade-off of partially retaining these non-linearities but keeping a linear optimization problem, hence a root finding problem to simplify its implementation in part II. We will maintain the time-independence as in the 3rd simplification hypothesis.

We start from the equations related to the kinetic modeling, considering for the moment that all the quantities dependent on the magnetic equilibrium are known without uncertainties, where we included also explicitly the formula to compute p' and TT' from the pressure and

current density modelling.

$$
\left\{
\begin{aligned}
&\boldsymbol{P}_k = (\mathbb{B}(\psi)^T \mathbb{B}(\psi))^{-1} \mathbb{B}(\psi)^T \tilde{\boldsymbol{M}}_k \\
&\tfrac{3}{2}(V')^{-5/3}\left(\tfrac{\partial}{\partial t} - \tfrac{\dot{B}_0}{2B_0}\tfrac{\partial}{\partial \rho}\right)\left[(V')^{5/3} n_i T_i\right] - \tfrac{1}{V'}\tfrac{\partial}{\partial \rho}\left[V' G_1 n_i \chi_i \left(1 + 2\left(\tfrac{\rho}{\rho_B}\right)^2\right)\tfrac{\partial T_i}{\partial \rho}\right] = P_i && \text{in} \quad \rho \in [0,1] \\
&T_i(\rho = 1, t) = 0, \qquad \left.\tfrac{\partial T_i}{\partial \rho}\right|_{\rho=1} = 0, \qquad T(\rho, t=0) = T_0 \\
&n_i(\rho) = n_e(\rho)\tfrac{Z_c - Z_{eff}}{Z_c - 1} - n_B. && \text{in} \quad \rho \in [0,1] \\
&p(\rho, t) = n_e T_e + n_i T_i + \tfrac{p_{B,\parallel} + p_{B,\perp}}{2} + p_{fast} && \text{in} \quad \rho \in [0,1] \\
&\sigma_\parallel \left(\tfrac{\partial \psi}{\partial t} - \tfrac{\hat{\rho}\dot{\Phi}_B}{2\Phi_B}\tfrac{\partial \psi}{\partial \hat{\rho}}\right) = \tfrac{T^2}{16\pi^2 \mu_0 \Phi_B^2 \hat{\rho}}\tfrac{\partial}{\partial \hat{\rho}}\left(\tfrac{g_2 g_3}{\hat{\rho}}\tfrac{\partial \psi}{\partial \hat{\rho}}\right) - \tfrac{B_0}{2\Phi_B \hat{\rho}}V'_{\hat{\rho}}(j_{bs} + j_{cd}) && \text{in} \quad \rho \in [0,1] \\
&\left(\tfrac{g_2}{4\pi^2\mu_0}\tfrac{1}{V'_{\hat{\rho}}}\tfrac{\partial \psi}{\partial \hat{\rho}}\right)\big|_{\hat{\rho}_B} = I_{pl}(t), \qquad \tfrac{\partial \psi}{\partial \hat{\rho}}\big|_{\hat{\rho}=0} = 0, \qquad \psi(\rho, t=0) = \psi_0 \\
&j_{tor}(\hat{\rho}, t) = 2\pi R_0 \tfrac{1}{16\pi^3 \mu_0 \Phi_b}\tfrac{1}{V'_{\hat{\rho}}}\tfrac{\partial}{\partial \hat{\rho}}\left(T\tfrac{g_2 g_3}{\hat{\rho}}\tfrac{\partial \psi}{\partial \hat{\rho}}\right) && \text{in} \quad \rho \in [0,1] \\
&TT'(\hat{\rho}, t) = \tfrac{\mu_0}{g_3}\left(\tfrac{1}{R_0 \pi}j_{tor} - p'\right) && \text{in} \quad \rho \in [0,1]
\end{aligned}
\right.
$$

$$(3.18)$$

We can interpret eq. (3.18) as synthetic diagnostic/estimator, hence an independent reconstruction problem, for the quantities $\tilde{p}'(\rho, t)$ and $\tilde{T}T'(\rho, t)$. Given our working assumption 4 of no modelling errors, the uncertainty on $\tilde{p}'$ and $\tilde{T}T'$ can be estimated performing an error propagation analysis starting from the uncertainties of the kinetic measurements in eq. (3.18). We can now, similarly of what is done in MER, extend the set of free parameters for the magnetic problem to be $\boldsymbol{P}_m = \{I_a, I_v, p'(\rho, t), TT'(\rho, t)\}$, and include $\tilde{p}'(\rho, t)$ and $\tilde{T}T'(\rho, t)$ as measurements with their uncertainties in χ_m^2 as $||\tilde{p}' - p||^2_{w_{p'}} + ||\tilde{T}T' - TT'||^2_{w_{TT'}}$. As for the MER, $p'(\rho, t)$ and $TT'(\rho, t)$ are expanded into a series of basis functions, the coefficients of the expansion will become the free parameters and the forward model for the observer remains linear. It is important to notice that one could pass directly the estimate of $p(\rho, t)$ and $j_{tor}(\rho, t)$ to the cost function χ_m while keeping a linear forward observer model with respect to the $\boldsymbol{P}_m = \{I_a, I_v, p'(\rho, t), TT'(\rho, t)\}$, through eq. (2.41).

The new formulation for the kinetic equilibrium reconstruction becomes
Defining: $\tilde{\boldsymbol{M}}_m = \{\tilde{\boldsymbol{B}}_m, \tilde{\boldsymbol{F}}_f, \tilde{I}_p, \tilde{\Phi}_t, \tilde{\boldsymbol{I}}_v, \tilde{\boldsymbol{I}}_a, \tilde{p}'(\rho, t), \tilde{T}T'(\rho, t)\}$, $\tilde{\boldsymbol{M}}_k = \{\tilde{\boldsymbol{T}}_e, \tilde{\boldsymbol{n}}_e\}$
Given:The magnetic measurements $\{\tilde{\boldsymbol{B}}_m, \tilde{\boldsymbol{F}}_f, \tilde{I}_p, \tilde{\Phi}_t, \tilde{\boldsymbol{I}}_v, \tilde{\boldsymbol{I}}_a\}$, kinetic measurements $\tilde{\boldsymbol{M}}_k = \{\tilde{\boldsymbol{T}}_e, \tilde{\boldsymbol{n}}_e\}$ and the $\chi_i(\rho, t)$, $Z_{eff}(t)$, the sources j_{cd}, P_i, the initial condition $T_{i,0}$ and $\psi_0(\rho)$. Notice that $\tilde{p}'(\rho, t)$, $\tilde{T}T'(\rho, t)$ are not given inputs even if they appear in $\tilde{\boldsymbol{M}}_m$.
Find: $\boldsymbol{P}_m = \{I_a, I_v, p(\rho, t), TT'(\rho, t)\}$ and $\boldsymbol{P}_k = \{T_e(\rho, t), n_e(\rho, t)\}$
such that

$$
\left\{
\begin{aligned}
&\boldsymbol{P}_m = (\mathbb{A}(\psi)^T \mathbb{A}(\psi))^{-1} \mathbb{A}(\psi)^T \tilde{\boldsymbol{M}}_m \\
&\Delta^* \psi = -2\pi\mu_0(j_{pl} + j_e) && \text{in} \quad \Omega_c \\
&\psi(R, Z) = \sum_{i=[pl,a,s]} \int_{\Omega_i} G_i(R, Z; R', Z') j_{\varphi,i}(R', Z') dR' dZ' && \text{in} \quad \partial\Omega_c \\
&\{\tilde{p}'(\rho, t), \tilde{T}T'(\rho, t)\} = \text{Kin}\big(\psi(R, Z), \tilde{\boldsymbol{M}}_k, \chi_i(\rho, t), Z_{eff}(t), I_p(t), j_{cd}(\rho, t), P_i(\rho, t), T_{i,0}, \psi_0\big)
\end{aligned}
\right.
$$

$$(3.19)$$

We would like now to make some remarks for the problem formulated in eq. (3.19).

- Notice that in eq. (3.19) $\tilde{\boldsymbol{M}}_m$ has a different definition with respect to eq. (3.17) and eq. (3.14).

- The "Kin" operator in eq. (3.19), represents the solution of the problem eq. (3.18) to estimate the $\tilde{p}'$ and $\tilde{T}T'$ from the kinetic measurements, the pressure and the current diffusion modelling.

- As for the case of eq. (3.17), the solution eq. (3.19) is not a solution of the original problem eq. (3.14). In fact in eq. (3.19) we are still neglecting the coupling between the magnetic parameters and the kinetic cost function $\nabla_{P_m}\chi_k = 0$ and vice versa $\nabla_{P_k}\chi_m = 0$. The problem of overfitting the cost function is also present in eq. (3.19) as it was in eq. (3.17).

- In eq. (3.19) there is a better usage of the information content of the magnetic measurements since they are used together with the kinetic modeling to estimate the internal plasma profiles p' and TT'. This was one of the issues in eq. (3.17). Moreover, adding $p'(\rho, t)$ and $TT'(\rho, t)$ allows to make use of all the magnetic measurements including Φ_t which has a linear dependence on only the free parameter TT' in eq. (3.19).

- The problem formulated in eq. (3.19) does not violate the principle of consistent models within a system of equations. For example, $\tilde{j}_{tor}$ appearing in eq. (3.19) can also be computed from $p'(\rho, t), TT'(\rho, t)$ and the flux map $\psi(R, Z, t)$ in the Grad-Shafranov with eq. (2.42) that we will call $\hat{j}_{tor}$ in this context. When the problem eq. (3.19) is solved in general $\tilde{j}_{tor} \neq \hat{j}_{tor}$. However the two quantities have a different interpretation in the problem formulated in eq. (3.19). The $\hat{j}_{tor}$ has to be considered as the reconstructed quantity, the one provided as an output of KER, since it combines the information of the magnetic and indirectly the kinetic measurements through $\tilde{p}'(\rho, t), \tilde{T}T'(\rho, t)$. The $\tilde{j}_{tor}$ instead has to be considered only as an estimate of the quantity j_{tor} affected by uncertainties coming from the error propagation of the uncertainties in the kinetic measurements, at the same level as the other measurements entering in χ_m. Of course, if magnetic measurements and kinetic measurements are consistent then $\tilde{j}_{tor} \sim \hat{j}_{tor}$.

- The choice of introducing $\tilde{p}'(\rho, t), \tilde{T}T'(\rho, t)$ can be seen as an improvement to prevent the overfitting problem that might arise from having neglected some non-linearities in the cost function. One could indeed almost perfectly match the kinetic measurements in χ_k by choosing a high number of basis functions to represent $T_e(\rho, t)$, $n_e(\rho, t)$, causing the problem of fitting also the noise present in the measurements. This will produce a poor quality $\tilde{j}_{tor}$ and therefore $\tilde{p}'(\rho, t), \tilde{T}T'(\rho, t)$ which will not be consistent with the magnetic measurements which will re-scale p' and TT' resulting in a sensibly different $\hat{j}_{tor}$. This "feedback" was not present in the formulation eq. (3.17) and it is just a tentative way to recover part of the non-linear interaction between equilibrium and kinetic modelling that has been broken by previous simplifying assumptions.

- It is important to notice that similar variation of this formulation can be obtained. For example, one can consider j_{tor} to be strictly given from the current diffusion equation, and let only the parameter for p' to be varied and TT' computed from eq. (2.40). This would cover the case when more confidence is given to the current diffusion equation and less to the transport modelling, which is in general affected by poor knowledge of T_i. The resulting problem would still be "quasi-linear" in the free parameter p', but the evaluation of some geometrical flux surface integral such as $< \frac{1}{R^2} >$ would be required.

3.4 Summary and outlook

In this chapter we discussed the formulation of the inverse/reconstruction problems which aims to estimate some unknowns parameters combining first principle modelling and available measurements.

First, in section 3.1, we discussed how to pass from a forward/predictive problem to the reconstruction problem by making assumptions on the type of uncertainties of the measurements and models and use a statistical framework. We discussed the differences between the frequentist approach, which led to the minimum least-squares fitting problem, and the Bayesian approach. We showed that interpreting the problem with a statistical framework allows to derive measures of the quality of the reconstructed parameters and provides technique to deal with the error propagation analysis. The minimum least-square fitting problem is the building block for the formulation of reconstruction problems in 3.2 and 3.3.

Then, in section 3.2, we discussed the formulation of the Magnetic Equilibrium Reconstruction (MER) problem, which aims to find a free boundary equilibrium solution that best matches in least-squares sense a set of external magnetic measurements. We defined the set of external magnetic measurements available in TCV, which are common to most tokamaks, and the relation with the solution of the free boundary problem. We formulated the MER problem as a "quasi-linear" least-squares optimization problem with equality constraints and provided a simplified version to facilitate numerical implementation, which is widely used in fusion community. We discussed in 3.2.2 some critical aspects of MER, in particular due to the fact that the external magnetic measurements are little sensitive to internal modifications of the plasma state which results in a poor identification of the plasma pressure and current density profiles.

Then in section 3.3 we discussed the formulation of the Kinetic Equilibrium Reconstruction, which at first aims to improve the reconstruction of the internal plasma profiles. While for MER the fusion community has reached a consensus or at least a standard practice, the definition of KER is still debated due to the large set of diagnostics and models that can provide information to the internal plasma state, which are briefly listed at the beginning of the chapter. We derived our definition based on few working assumptions focused on the diagnostic set of TCV based on the minimum least-squares principle as it was done for the MER. Since in the formulated problem, a current diffusion model and T_i diffusion model is coupled to the free-boundary

equilibrium, differently to the MER, the KER is a dynamic state and parameter reconstruction. However, only resistive time scales have been considered hence instabilities are excluded from the reconstruction. KER presents a strong non-linear coupling between the equilibrium and the transport. We discussed therefore two possible simplifications based on breaking some non-linearities between the equilibrium and transport, considering only linear solution of the optimization problem and neglecting correlation of parameters between time instants. We discussed in details the consequences of the simplifications. All the proposed simplifications have been considered only to simplify the numerical implementation in part II of the thesis, however given the level of today's knowledge on methods to solve the forward problem and the available computational power it would not be unrealistic to tackle the original complete formulation.

As a last remark, for ITER high power operation, a kinetic equilibrium reconstruction approach is foreseen as demonstrated by the increasing attention on the topic in recent conferences [Mazon et al. 2020]. This will benefit also thanks to the effort in developing a unified and standardized data structure called IDS/IMAS [Pinches et al. 2017] which will allow to share analysis tools between different tokamaks.

There are various approaches to perform KER in literature that will be explained in 5. In this chapter we attempted to provide a formal derivation of the problem starting from its equivalent forward one, specifically for the set of TCV measurements, highlighting the simplification assumptions, in particular how breaking non-linearity between the equilibrium and transport might generate inconsistencies in the system, identifying the critical issues.

Implementation & Analysis Part II

4 New free-boundary forward static/ evolutive / and inverse solver

A new suite of codes is presented in this chapter:

- "FGS" (Forward Grad-Shafranov Static) solving the forward static free-boundary equilibrium problem eq. (2.22).

- "FGE" (Forward Grad-Shafranov Evolutive) solving the free-boundary equilibrium coupled to the evolution of the coils in conductors and the current diffusion equation in a 0D integral form eq. (2.63).

- A linearization of FGE including its state space representation.

- Preliminary implementation of the inverse magnetic equilibrium reconstruction problem with generic non-linear least-squares solver and a Bayesian approach to perform uncertainty quantification.

First, in section 4.1, the historical motivation for the project and similar examples available in literature are summarized.

Then, in section 4.2 and 4.3, the details of the numerical implementation will be presented. The strategy will be to formulate all the problems as discrete root finding problems of the type find x such that $F(x) = 0$ and use a single numerical scheme, the Jacobian Free Newton Krylov (JFNK), to solve them all.

In section 4.4 we present some first validation of the time evolutive code FGE. These include vertical stabilization cases with the real-time control system of TCV, validation of current diffusion equation implemented with experimental data and benchmark of the linearized code with respect to the linear rigid plasma displacement RZIP model for vertical stability controller design.

In section 4.5.1 FGS is applied to MER problem, removing some of the limitations of the equilibrium reconstruction code LIUQE and investigating their importance. This will give more

insights on the accuracy of the LIUQE code which is now considered as a potential candidate for the real-time equilibrium reconstruction in ITER. We will also consider a preliminary use of the code FGS to perform equilibrium reconstruction based on a Bayesian approach and compare the result with the frequentist approach, which leads to the non-linear least-squares problem.

In section 4.6, we will develop magnetic equilibrium reconstruction tools, together with LIUQE, to investigate numerically how they would perform for the future tokamak ITER during a stationary phase of an H-mode 15MA scenario. This aims in particular to address the effects of the internal features of the plasma profiles, present "by design" during the operation phase as necessary ingredient to achieve the desired performance. These results will show the limitation of the magnetic equilibrium reconstruction whenever a precise identification of the internal plasma profiles and internal plasma geometry is sought and motivate the development of techniques to perform kinetic equilibrium reconstruction discussed in the next chapters of this thesis.

At the end of this chapter we will list the many potential applications which can be addressed thanks to the new suite of codes developed in this thesis.

4.1 Historical motivation and literature investigation

The code LIUQE [Hofmann 1988] was developed starting in 1980s at SPC (at that time CRPP) to perform magnetic equilibrium reconstruction both in post-discharge analysis and real-time, in the highly shaped TCV tokamak. More recently [Moret et al. 2015], it was rewritten in Matlab [MATLAB 2017] with a library of C compiled low-level routines to perform the most computationally expensive sub-parts contained in the free-boundary equilibrium problem. This allows to compromise between the flexibility, thanks to the Matlab high-level programming language, and the computational time, thanks to the compiled C functions. The library includes in particular the identification of the plasma domain, the solution of the Laplace-like operator in the Grad Shafranov equation, the computation of the boundary conditions for the Poisson problem and the post-processing of the integrated and profile quantities from the $\psi(R, Z)$ solution. With this solution, LIUQE achieves real-time performances for TCV without the need for parallelization.

The first aim of the project is therefore to investigate whether we can use the same optimized library to obtain fast predictive solvers for shot preparation and controller design. The first code developed, FGS, solves the forward static free-boundary equilibrium problem in section 2.2.1, given the current in the conductors I_a, I_v and the description of the plasma profiles p', TT'. The numerical scheme solving the free-boundary static equilibrium problem based on Picard iteration implemented in LIUQE is numerically unstable [Lackner 1976]. The stabilization solution adopted in LIUQE, based on the magnetic measurements, can hence not be used in forward codes. This motivated the implementation of a more stable scheme, called Jacobian Free Newton Krylov (JFNK) solver. The scheme combines the stability properties of the

Newton iterations without the need to compute the Jacobian, which is unknown analytically for the free-boundary equilibrium [Heumann et al. 2015] due in particular to the non-linearity of finding the plasma boundary. Advantages and disadvantages of the numerical scheme are discussed in Appendix D.

The literature of codes solving the free-boundary equilibrium problem is wide and will be discussed later in this section. Developing FGS was just the starting block for several applications. It was first used to solve the magnetic equilibrium reconstruction (MER) problem in section 3.2 to investigate the impact of some simplifications in the LIUQE algorithm: remove the stabilization algorithm leading to a vertically shifted solution, extend the possibility of including measurements non-linearly dependent on the free parameters. We also realized that the algorithm implemented in LIUQE to solve the constrained least-squares optimization in MER can not converge to the minimum of the cost function, as it neglects the variation with respect to the flux map. This last point is discussed extensively in Appendices E and F. This is common to many equilibrium reconstruction codes such as EFIT[Lao et al. 1990], EQUAL [Zwingmann 2003], and CLISTE [McCarthy et al. 1999], as noticed also in [Faugeras 2020]. With the MER implemented with FGS, based on a Levenberg-Marquardt algorithm [Van Tol 1963], we can check the magnitude of this difference.

Uncertainty quantification is useful whenever MER or KER are used as inputs for further analysis such as gyrokinetic transport investigations [Zakharov et al. 2008; White 2019]. The Bayesian approach, discussed in section 3.1, provides the framework to correctly propagate the measurements and model uncertainties to the MER result, and is getting progressively more attention in fusion community [Fischer et al. 2010], [Fischer et al. 2019], [Mazon et al. 2020]. FGS is used to perform Bayesian analysis on magnetic equilibrium reconstruction in section 4.5.2, making use of the Markov Chain Monte Carlo [Gamerman and Lopes 2006] sampling routines available in the statistical Matlab package. Few similar examples are present in literature. Within the generic framework MINERVA [Svensson et al. 2010], which allows to perform Bayesian inference for several different problems, magnetic equilibrium reconstruction code have been included [Hole et al. 2010b], in particular one of the first code performing this analysis BEAST [Von Nessi et al. 2013]. Differently to previous works, we assume the free-boundary equilibrium model to be strictly respected, instead of appearing in the prior distribution function as a weak constrain. This allows us to make a direct comparison between the frequentist approach, which leads to the least-squares optimization problem solved in LIUQE and FGS with Levenberg-Marquardt algorithm, and the Bayesian approach.

After developing FGS, we coupled the free-boundary equilibrium solution with the dynamic evolution of the current in the passive and active conductor together with 0D model for the resistive decay of the total plasma current, obtaining the FGE code described in section 4.3. The aim is to obtain a simulator, which can simulate the dynamics of the early phases of vertical displacement events, to be used for designing the vertical stability, position and shape controllers. The research in developing a predictive code for the plasma dynamics described in section 2, which couples the evolution of the kinetic profiles on resistive time-scales to the

free-boundary equilibrium and the evolution of the external conductor coils was particularly active in the '80s as summarized in [Blum and Le Foll 1984]. We cite here only a few of the codes which have been used in the recent years, similar to FGE approach. We focus only on codes addressing the free-boundary problem.

- **NICE/FEEQS.M** [Faugeras 2020]: NICE was developed by INRIA to unify and update three former codes CEDRES++ [Heumann et al. 2015], EQUINOX [Blum et al. 2012] and VacTH[Faugeras et al. 2014]. It solves several problems related to free-boundary plasma equilibrium in tokamak including forward and inverse, static and dynamic evolution coupled to the conductor currents evolution. The main strength is that a single finite element (FEM) framework is used for all the declination of the problem, solved with a Newton method, for the forward models, and sequential quadratic programming for the inverse solution. This was enabled by the derivation of an analytic gradient for the FEM discretization presented in [Heumann et al. 2015]. The same numerical methods were implemented also in FEEQS.M [Blum et al. 2019], a Matlab version of NICE to test different problems and numerical algorithms. The codes, in its forward predictive usage, still lacks the implementation of the transport modelling to evolve the plasma current and kinetic profiles consistently with the equilibrium, which will come in future development according to [Faugeras 2020]. NICE and FEEQS.M are used regularly for WEST operation and are coupled to IMAS [Pinches et al. 2017] environment to enable porting to other devices.

- **CREATE-NL** [Albanese et al. 2015]: The code developed by CREATE solves the forward coupled dynamics of the free-boundary plasma equilibrium and the conductors currents. It is a Matlab based code designed mainly for control purposes, implementing FEM discretization and a Newton method. The Jacobian is approximated numerically with finite differences, but the a priori knowledge of the sparsity pattern is used to reduce the computational cost. It has been used extensively to study the vertical stability, position and shape control in many present and future tokamaks, such as DEMO [Maviglia et al. 2018], DTT [Ambrosino et al. 2017], EAST [Castaldo et al. 2018], ITER [Parail et al. 2013], . It provides a linearized version of the code for faster simulation, and the evolution of the kinetic profiles, including the current diffusion equation. It can be coupled with an iterative scheme, exchanging I/O information with a transport code during a single simulation time step. It does not include yet the possibility of performing inverse reconstruction problem or inverse static coil current fitting problem.

- **DINA** [Khayrutdinov and Lukash 1993]: It allows the simulation of the free-boundary equilibrium coupled to the evolution of the currents in the coils and the flux surface averaged transport equation for the current, heat and particle transport. It has been used in full-discharge simulation, scenario development and vertical displacement event analysis of many different tokamaks [Sugihara et al. 2004; Leuer et al. 2003], including the ITER operation design [Kim et al. 2009]. The coupling between the equilibrium and transport is based on an iterative scheme. The code uses a particular solution to solve

the free-boundary equilibrium based on the inverse variable technique [Degtyarev and Drozdov 1985]. The resulting flux aligned grid allows to quickly compute the flux surface averaged geometrical coefficients, which are needed in the transport equation and numerically expensive to compute in a Cartesian grid. The DINA code was more recently wrapped into a Simulink block to enable a more flexible development of controllers resulting in DINA-CH [Lister et al. 2005], which for example was validated against VDEs in the TCV tokamak [Lukash et al. 2003; Khayrutdinov et al. 2001].

- **TSC** [Jardin et al. 1986]: The code simulates the evolution of the free-boundary equilibrium coupled to the flux surfaced averaged transport equations. It has been used in the design and VDE simulation of several tokamaks [Nakamura et al. 2010; Sayer et al. 1993; Takei et al. 2003; Jardin et al. 2000], including TCV design [Marcus et al. 1985] and now used at EAST [Bo et al. 2018] as simulation suite for plasma control developments. The peculiarity of the code is that, instead of solving the force balance GS equation at each time step, it evolves a velocity field through a modified equation of motion which, by ad-hoc choice of the transport coefficients, is forced to remain very close to the equilibrium solution. This solution is convenient in coupling the free-boundary equilibrium with a transport simulation since it avoids the need of matching the plasma region and the vacuum region.

- **ASTRA-SPIDER** [Fable et al. 2013a]: The coupling between the transport code ASTRA [Pereverzev and Yushmanov 2002] and the free-boundary equilibrium code SPIDER [Ivanov et al. 2005], developed mainly at IPP-Garching, allows to simulate the evolution of the plasma equilibrium together with the currents in conductors and the transport equations of current, heat and particles. It was wrapped into Simulink resulting in the flight-simulator FENIX [Janky et al. 2019; Treutterer et al. 2019], based on the PCSSP platform developed for ITER (Plasma Control System Simulation Platform PCSSP [Walker et al. 2014]). This has allowed to simulate the ASDEX Upgrade plasma discharges before the operation [Janky et al. 2019]. An iterative coupling between the free-boundary equilibrium solver and the transport equation is applied [Fable et al. 2013b] which relies on the computation of the geometrical coefficients by the free-boundary equilibrium code SPIDER [Ivanov et al. 2005].

- **TokSys** [Humphreys et al. 2007]: Is the flight-simulator environment developed for DIII-D, and used extensively also at [Walker et al. 2015; Bao et al. 2020] EAST, KSTAR and MAST, wrapping the different models for the equilibrium evolution with Simulink. Its original implementation was at the basis of the development of PCSSP for ITER. TokSys embeds, in a Simulink wrapper, DINA as a core component. This is proprietary software and not freely available.

The different codes mentioned have different level of plasma physics complexity, computational cost and numerical solutions, even though they all share the coupling between a free-boundary equilibrium and a transport equation. Each of them are more suited for specific

applications, ranging from magnetic control design to full discharge simulation and scenario development, as well as flight simulator for experiment preparation. Some specific features of FGE are:

- No iterative coupling between the GS, the CDE and the evolution of the coil currents. The problem is formulated as a monolithic system of equations thanks to the flexibility of JFNK solver.

- 0D current diffusion equation derived in section G, obtained from the integration of 1D CDE. This novel contribution of this thesis provides a rigorous link between the 1D current diffusion equation used in transport codes and a 0D version used when solving the free-boundary equilibrium problem. As we will discuss later, this formulation can potentially be used to couple the 1D CDE to a free-boundary code avoiding the calculation computing the geometrical coefficients g_i eq. (2.34) to eq. (2.37), which requires to identify the plasma flux surfaces via a cpu-expensive contour finding algorithm.

In section 4.3.1 we provide also a linearization of FGE on subsequent states of equilibrium problem based on [Walker and Humphreys 2006], to allow fast simulation of the system around linearization points. We also derive a state space representation, using as state variables the current in the conductors I_e, and the total plasma current I_p, in order to conform to the RZIP model [Wainwright et al. 1997] to enable linear controller developments. Differently to previous linearization in literature, we consider deformable plasma and the consistent linearization of the current diffusion equation.

In summary, the newly developed FGS and FGE, together with the previously available LIUQE and FBT, compose the suite of codes named "**LIUQE-suite**". The most common usage and I/Os are listed in table 4.1. The suite aims to cover the full pipeline of tokamak operation: the computation of the feedforward traces to be used to run a tokamak experiment with FBT; the simulation of the equilibrium and conductor coils evolution for controller design with FGE; the reconstruction of the plasma state from synthetic data simulation and real measurements with LIUQE. Some of its peculiar features are:

- Finite difference discretization on square structured grid which allows fast solution of the GS operator (DFT method [Wendroff et al. 1976]).

- Grid only in regions containing the tokamak vacuum chamber, giving a much smaller numerical problem than including large vacuum regions outside the tokamak.

- Conductor equations solved as filamentary (discrete) structures leading to few equations for conductors.

- Real-time implementation of LIUQE in Simulink and routine use in real-time on TCV.

Name	Problem solved	Inputs	Outputs	Type	Application
LIUQE [Moret et al. 2015]	Mag. equil. reconstruction	Mag. measurements	$I_a, I_v, p', TT', \psi(R,Z)$	static	post-discharge real-time analysis
FBT [Hofmann 1988]	I_a for given plasma shape	p', TT', plasma shape	$I_a, \psi(R,Z)$	static	feedforward $I_a(t)$ TCV operation
FGS	Forward equilibrium	p', TT', I_a, I_v	$\psi(R,Z)$	static	building block for inverse and evolutive solvers developed in this thesis
FGE	Coupled equilibrium + external active/passive conductor circuit equation + resistive current diffusion evolution	$\beta_p(t), l_i(t), V_a(t)$	$I_a(t), I_v(t), \psi(R,Z,t)$	dynamic	simulator for vertical and shape control design

Table 4.1 – Free-boundary related codes in meq (matlab equilibrium) suite, most common usage and I/Os

4.2   Forward free-boundary Grad-Shafranov Static (FGS)

In this section we present the discrete implementation of the static free-boundary equilibrium forward problem eq. (2.22). This results in the code FGS (Free-boundary Grad-Shafranov Static). The purpose is first to discretize the problem in space by means of finite difference and then derive a root finding type problem *find x such that $F(x) = 0$*. Since in this section we discuss only the static solution of the free-boundary equilibrium problem, all the quantities are considered at the same time instant. We do not write explicitly t in this section to simplify the notation, while instead it will be important to specify it when dealing with the time evolutive problem in the next section. Since the new developed suite of codes use most of the low level routines of the LIUQE code [Moret et al. 2015], most of the numerical discretization techniques are common and we tried also to conform the notation.

As for the case of the continuous problem formulation in fig. 2.1a, we start by defining the discrete version of the domains, listed in table. 4.2 and displayed in fig.4.1a and fig. 4.1b. The computational domain Ω_c is discretized into a rectangular grid uniformly spaced in R and Z, with spacing ΔR, ΔZ respectively. The choice of a rectangular grid is made to simplify the finite difference discretization of the spatial differential operator at the boundary. We call Y (green dots in fig. 4.1) the set of pairs of coordinates $\{R_i, Z_i\}$ identifying the point i in the poloidal plane with $Y = \{\{R_i, Z_i\} \subset \Omega_c\}$, without the boundary $\delta\Omega_c$. We define a discrete version of the computational boundary $\delta\Omega_c$ calling it $O = \{\{R_i, Z_i\} \subset \delta\Omega_c\}$ (blue dots in fig. 4.1). We call $X = Y \cup O$. The X grid has a total number of points $n_{R,x} \times n_{Z,x}$, where $n_{R,x}$ and $n_{Z,x}$ are the number of discrete points in R and Z direction respectively. Finally we call $P \subset Y$ the discrete region where $j_{pl} \neq 0$, and δP its boundary. We will better define this region after having discussed the discrete representation of j_{pl} in eq. (4.2). For the moment we anticipate that δP(green line in 4.1a) is not a discretization of $\delta\Omega_p$ (red line in 4.1a), hence in particular $P \not\subset \delta\Omega_p$.

Taking the poloidal flux $\psi(R, Z)$ as an example for all the scalar fields defined in the poloidal plane, we will refer to ψ_x as $\psi(R_i, Z_i) \;\forall \{R_i, Z_i\} \in X$, and equivalently to ψ_y for $\psi_y = \psi(R_i, Z_i)$ $\forall \{R_i, Z_i\} \in Y$ and finally to ψ_o as $\psi_o = \psi(R_i, Z_i) \;\forall \{R_i, Z_i\} \in O$.

Y	discretized Ω_c
O	discretized $\delta\Omega_c$
$X = Y \cup O$	discretized $\Omega_c \cup \delta\Omega_c$
P	discretized plasma region where $j_{pl} \neq 0$
δP	continuous boundary of P (It can differ from a discretization of $\delta\Omega_{pl}$)

Table 4.2

The finding of the plasma boundary from the knowledge of ψ_y is explained in details in section 2.4 of [Moret et al. 2015]. We provide here only a simplified description. In case of a diverted plasma, from ψ_y one needs first to identify the coordinate (R_X, Z_X) of the saddle point (called X point) and its poloidal flux value $\psi(R_X, Z_X)$ which is usually called $\psi_b = \psi(R_X, Z_X)$ to indicate the flux at the plasma boundary. The capital X in this case must not be confused with
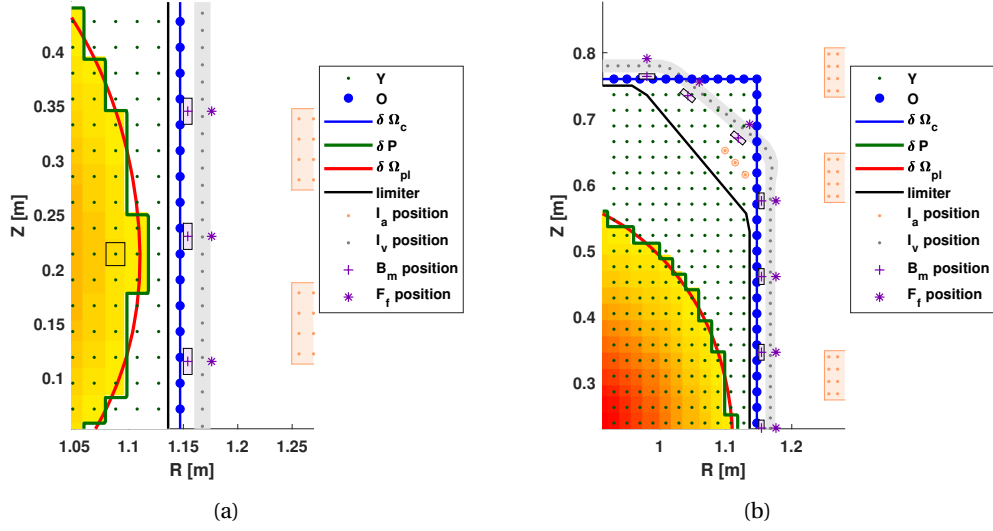
(a)

(b)

Figure 4.1 – Discrete domains for TCV: discrete inner computational grid Y (green small dots) excluding computational boundary O; discrete computational boundary O (blue dots), and continuous computational boundary $\delta\Omega_c$ (blue line); discrete plasma current j_{pl} represented with rectangular patches from yellow to red, color scaled to represent j_{pl} intensity, and one of these rectangular regions is highlighted in black in figure (a); discrete plasma region P where $j_{pl} \neq 0$ delimited by δP (green line); space plasma boundary $\delta\Omega_p$ represented here with red line for comparison with fig. 2.1a; limiter (black line), location of active coil filaments (pink dots), location of vessel current filaments (gray small dots), location of B_m probes (violet crosses) and location of flux loop diagnostics F_f (violet stars).

the label for the discretized computational grid X. The X point location (R_X, Z_X), from ψ_y as well, is essentially never one of point of the Y grid, hence it needs to be found by interpolation. The same applies also for ψ_b. The isoflux lines, from the flux value at the plasma axis to the flux value at the plasma boundary ψ_b, describe closed nested regions in the poloidal plane. To identify P one needs therefore to extract $\{R_i, Z_i\} \in Y$ in the closed region inside the isoflux line at ψ_b value, which is shown with the red line in fig. 4.1 and corresponds to $\delta\Omega_{pl}$ in the continuous space representation. We introduce here the numerical choice that the plasma j_{pl} is represented by piecewise constant rectangles of dimension ΔR and ΔZ equal to the spacing of the Y grid, centered in the Y grid point locations. These rectangles can be seen clearly in figure 4.1b, where the j_{pl} is represented with the yellow to red patches, to indicate its intensity. One of this rectangle box has been highlighted in black in 4.1a to help the visualization. P is the region where the discrete piecewise constant j_{pl} are different from 0, hence the boundary of this region called δP (green line in fig. 4.1a and 4.1b) follows this rectangular representation. This explains why $\delta P \not\subset \delta\Omega_{pl}$ which is clear by comparing green and red lines in fig. 4.1. In our codes we assume at this stage that the plasma current is contained inside δP, hence we do not consider currents in the scrape off layer.

Supposing for the moment to know P, we rewrite the relation between the plasma toroidal current density $j_{pl}(R, Z)$ and the free functions $p'(\psi(R, Z))$ and $TT'(\psi(R, Z))$, making use of a basis functions $\{g_g(\psi(R, Z)\}$ expansion:

$$j_{pl}(R_i, Z_i) = 2\pi \left(R p'(\psi) + \frac{T(\psi)}{\mu_0 R} T'(\psi) \right) = \sum_{g=1}^{N_g} \frac{a_g R^{\nu_g}}{\psi_B - \psi_A} g_g(\hat{\psi}(R_i, Z_i)) \ \ \forall \{R_i, Z_i\} \in P. \tag{4.1}$$

The expansion eq. (4.1) is identical to the one presented for the magnetic equilibrium reconstruction problem eq. (3.5) in sec. 3.2. A polynomial set of basis functions is typically used [Moret et al. 2015]. In eq. (4.1) we call $\boldsymbol{a} = \{a_1, ..., a_{N_g}\}$ the basis functions coefficients and define the exponent ν_g as $\nu_g = 1$ for the basis functions related to p' and $\nu_g = -1$ for the basis functions related to TT'. One can compute j_{pl} in the discrete grid Y as,

$$j_{pl}(Y) = \begin{cases} \sum_{g=1}^{N_g} \frac{a_g R^{\nu_g}}{\psi_B - \psi_A} g_g(\hat{\psi}(R_i, Z_i)) & \forall \{R_i, Z_i\} \in P \\ 0 & \forall \{R_i, Z_i\} \in (P)^c \end{cases} \tag{4.2}$$

As already stated, we will always consider the plasma current density as represented by piecewise rectangles centered around $\{R_i, Z_i\} \in Y$ with magnitude $j_{pl}(R_i, Z_i)$. We define $I_y = j_{pl}(Y)\Delta R\Delta Z$ such that the total plasma toroidal current I_p takes the following form,

$$I_p \equiv \int_{\Omega_{pl}} j_{pl} dRdZ = \sum_i I_{y,i} = \sum_i j_{pl}(R_i, Z_i)\Delta R\Delta Z \ \ \forall \{R_i, Z_i\} \in Y. \tag{4.3}$$

It is important to notice that $\boldsymbol{I_y}$ can be considered a nonlinear function of $(\psi_x, \boldsymbol{a})$, for a given set of basis functions, such that $I_y = I_y(\psi_x, \boldsymbol{a})$. In fact, in order to compute $\boldsymbol{I_y}$, given ψ_x and $\boldsymbol{a}$, one needs first to identify the plasma domain P and then use eq. (4.2). As discussed earlier the subscript y in $I_y = \{j_{pl}(R_i, Z_i)\Delta R\Delta Z \ \ \forall \{R_i, Z_i\} \in Y\}$ is to indicate that the quantity I_y is a

collection of values computed on the grid Y.

The next step, to formulate the discretization of the free-boundary equilibrium problem, is to discretize the differential operator Δ^* in the Grad-Shafranov equation eq. (2.17), as in the LIUQE code [Moret et al. 2015]. We use a 2nd order finite difference centered scheme defined as

$$(\Delta^*\psi)\bigg|_{(R_i,Z_j)} = (\Delta Z^2)^{-1}(\psi_{R_i,Z_{j+1}} + \psi_{R_i,Z_{j-1}} + a_i\psi_{R_{i+1},Z_j} + b_i\psi_{R_{i-1},Z_j} - c_i\psi_{R_i,Z_j}) \qquad (4.4)$$

for $(R_i, Z_j) \in Y$, with the following definition,

$$a_i = \left(\frac{\Delta Z}{\Delta R}\right)^2 \frac{R_i}{R_i + \Delta R/2}$$
$$b_i = \left(\frac{\Delta Z}{\Delta R}\right)^2 \frac{R_i}{R_i - \Delta R/2}$$
$$c_i = 2 + a_i + b_i.$$

The discrete version of the operator Δ^* is therefore a linear operator D applied to quantities defined on the grid X with results in the grid Y. We recall that Y is identical to X, without the boundary points O. To compute the operator D at the outermost location in the Y grid, since the operator uses the neighboring points of a given location, the value of the flux at O are needed. (centered finite difference scheme, hence the boundary points are excluded). From the definition eq. (4.4) we can express the action of D on ψ_x as a matrix vector multiplication $D\psi_x$.

The last equation needed before providing the discrete formulation of the problem requires to express the relation for the boundary condition eq. (2.19) in its discrete form. We have already seen in eq. (3.7), the relation between $\psi(R_b, Z_b)$ at a generic location $\{R_b, Z_b\}$, the external currents $\boldsymbol{I}_e$ and the plasma current density $j_{pl}(R, Z)\forall(R, Z) \in \Omega_c$. If we define the matrix $\mathbb{M}_{boy}$ as the collection of the Green's mutual inductance from the grid Y to the boundary points O,

$$\mathbb{M}_{boy;i,j} = G(R_i, Z_i; R_j, Z_j)\forall(R_i, Z_i) \in O \land \forall(R_j, Z_j) \in Y \qquad (4.5)$$

we can write:

$$\psi_o = \mathbb{M}_{boa}\boldsymbol{I}_a + \mathbb{M}_{bov}\boldsymbol{I}_v + \mathbb{M}_{boy}\boldsymbol{I}_y \qquad (4.6)$$

where $\psi_o = \psi(R_i, Z_i)\forall \{R_i, Z_i\} \in O$. We notice in particular that $\mathbb{M}_{boa}$, and $\mathbb{M}_{bov}$, equivalently to $\mathbb{M}_{fe}$ defined in eq. (3.7), take into account the series connection between the filaments composing the $\boldsymbol{I}_a$ and shown in 4.1a in pink dots, and the parallel connection between the filaments of the vessel $\boldsymbol{I}_v$ shown in gray dots. Moreover since we choose the representation of $j_{pl}(R, Z)$ as piecewise constant rectangles in the Y grid, the integral eq. (3.7), which allows to

compute the contribution of the plasma current density to poloidal flux at a given location, becomes just a matrix vector multiplication $\mathbb{M}_{boy}\boldsymbol{I}_y$. This multiplication is very expensive, of the order of $O(N^3)$ machine operation where N is the size of Y grid. It can be avoided by solving an homogeneous Laplace like problem for the GS operator and exploiting the Gauss theorem as explained in [Lackner 1976], reducing the cost to $O(N\ln N) + O(N^2)$. This is implemented in our code, however to simplify the reading we keep the relation eq. (4.6) in this formulation.

We can finally formulate the forward free boundary static equilibrium problem in its discrete form:

Given: $\{\boldsymbol{a}, \boldsymbol{I}_a, \boldsymbol{I}_\nu\}$ and the basis functions $\{g_i(\psi_N)\}$ functional forms with $i = [1, ..., N_g]$
Find: ψ_x on the discrete grid X (equivalently find ψ_y on the grid Y and ψ_o on O)
which solves the following system of equations:

$$
\begin{cases}
D\psi_x = -2\pi \frac{\mu_0 R_y}{\Delta R \Delta Z} \boldsymbol{I}_y(\boldsymbol{a}, \psi_x) - 2\pi \mu_0 R_y \boldsymbol{I}_e & \text{in } Y \\
\psi_o = \mathbb{M}_{boe} I_e + \mathbb{M}_{boy} I_y(\boldsymbol{a}, \psi_x) & \text{in } O
\end{cases}
\tag{4.7}
$$

remembering that $I_y(a_g, \psi_x)$ is a nonlinear operator which requires to find the discrete plasma boundary P from ψ_x and then compute I_y from eq. (4.2). R_y is the radial coordinate in poloidal plane computed at the Y location. We note in particular that there are N_x unknowns, $\psi_x = \{\psi_y, \psi_o\}$, and N_x equations.

We now make two small modifications to the problem which will reflect the actual implementation of the code and will simplify the description of the time evolving solver in the next section, in particular when also the current diffusion equation will be coupled to the system. First we defined $D_{\psi_o}^{-1}$ as the inverse of the linear operator D, such that given the boundary condition ψ_o and applied to the RHS of the Grad-Shafranov equation (first equation in eq. (4.7)) it allows to obtain ψ_x. This is equivalent to solving numerically the Laplace like operator appearing in the Grad-Shafranov equation. In the actual implementation of the code, we do not invert D explicitly and, whenever needed, we solve the corresponding linear problem efficiently by Fourier decomposition of structured rectangular grids as in our case. However to simplify the notation it is convenient to introduce $D_{\psi_o}^{-1}$, but the reader should remember that this in practice means solving the corresponding linear problem.

Secondly we generalize the problem and instead of providing the $\frac{dp}{d\psi}(\hat{\psi})$ and $T(\psi_N)\frac{dT}{d\psi}(\hat{\psi})$ through the specification of $\boldsymbol{a}$ basis function coefficients, we provide N_c number of constraints of physical quantities that can be computed out of the knowledge of ψ_x and all the other quantities appearing in eq. (4.7). These can be scalar values such as the total stored energy W_k, the internal inductance l_i, the safety factor at the axis q_A, the total plasma current I_p. In general also profiles, such as $q(\rho)$ profile, can be accepted since once discretized into N_p points on a ρ grid, it becomes N_p new constraints. Some of the constraints can be eventually a subset of the basis function coefficients $\boldsymbol{a}$. We pack all the constraints in $\boldsymbol{c}$, for example $\boldsymbol{c} = \{\beta_p, l_i, I_p\}$. N_c equality equations, the definition relation of how to compute the constraints from the knowledge of other quantities appearing in the system, are added to the system. The

goal is to always have the same number of unknowns and equations, hence a correct number of basis functions need to be considered depending on how many constraints are provided.

We provide now the formulation of the static free-boundary equilibrium problem with generic constraints in a root-finding form of type find x such that $F(x) = 0$. Once having defined the operator $F(x)$, we can use any suitable algorithm available to find its root.

Given: $\boldsymbol{v} = \{\boldsymbol{I}_a, \boldsymbol{I}_v, \boldsymbol{c}\}$, with $\boldsymbol{c} = \{c_i\}$ constraints and the basis functions $\{g_i(\psi_N)\}$ functional forms, with $i = [1, ..., N_c]$ both for the basis functions and the constraints.
Find: $\boldsymbol{x} = \{\boldsymbol{I}_y, \boldsymbol{a}\}$, and the basis functions coefficients $\boldsymbol{a}$ of p' and TT' expansion.
Such that $F(\boldsymbol{x}; \boldsymbol{v}) = \boldsymbol{0}$, where $\boldsymbol{0}$ is a vector of 0 of dimension equal to the number of unknowns, $F(\boldsymbol{x}, \boldsymbol{v})$ is defined as

$$F(x; v) = \begin{cases} \boldsymbol{I}_y - \tilde{I}_y(\boldsymbol{I}_y, \boldsymbol{a}, \boldsymbol{I}_e) \\ \text{Constraints}(\boldsymbol{x}, \boldsymbol{v})_{N_c} \end{cases} \tag{4.8}$$

and $\tilde{I}_y$ is obtained by computing subsequently the following set of equations given $\{\boldsymbol{I}_y, \boldsymbol{I}_e, \boldsymbol{a}, \boldsymbol{g}(\psi_N)\}$

$$\psi_o = \mathbb{M}_{boe} I_e + \mathbb{M}_{boy} I_y \qquad \qquad \text{in } O \qquad (4.9)$$

$$\psi_y = D_{\psi_o}^{-1}\left(-2\pi \frac{\mu_0 R_y}{\Delta R \Delta Z} \boldsymbol{I}_y - 2\pi \mu_0 R_y \boldsymbol{I}_e\right) \qquad \text{in } Y \qquad (4.10)$$

$$\text{find } \{P, \psi_A, \psi_B\} \text{ from } \psi_x \qquad \qquad (4.11)$$

$$\tilde{I}_y = \begin{cases} \sum_{g=1}^{N_g} \frac{a_g R^{v_g}}{\psi_B - \psi_A} g_g(\hat{\psi}(R_i, Z_i)) & \forall \{R_i, Z_i\} \in P \\ 0 & \forall \{R_i, Z_i\} \in (P)^c \end{cases} \tag{4.12}$$

We give a quick explanation on how to use the operator F to help visualize the algorithm. Suppose that some $\boldsymbol{v} = \{\boldsymbol{I}_a, \boldsymbol{I}_v, \boldsymbol{c}, \{g_i(\psi_N)\}\}$ and some values of $\boldsymbol{x} = \{\boldsymbol{I}_y, \boldsymbol{a}\}$ are given which are not the solution of the problem, hence $F(x; v) \neq 0$. To compute $F(x; v)$, one takes $\boldsymbol{x} = \{\boldsymbol{I}_y, \boldsymbol{a}\}$ and computes in order eq. (4.9) to eq. (4.12) to get $\tilde{I}_y$. After that one can compute eq. (4.8). Only if $F(x; v) = 0$ then $\boldsymbol{x} = \{\boldsymbol{I}_y, \boldsymbol{a}\}$ is a solution of the problem. Since the problem is strongly non-linear, it might have many solutions [Turnbull 1984], the hope is that they are distinct enough. We recall that the operator $D_{\psi_o}^{-1}$ depends on the flux at the computational boundary ψ_o. In order to find the solution of the problem we make use of the Jacobian Free Newton Krylov solver as explained in Appendix D.

Some features of the problem formulation eq. (4.8) are:

- The handling of the constraints is very general. One can change between them by simply replacing the constraint equality equation which provides a lot of flexibility to the code.

- The unknowns of the problem are in terms of the plasma current I_y, which will make it easier to couple to the evolutionary equation for the current in the coils discussed in the next section.

- Using as unknown I_y instead of for example ψ_x involves to solve the linear problem corresponding to $D_{\psi_o}^{-1}$ in order to compute $\tilde{I}_y$, but this can be done efficiently without loosing too much performance.

- Expressing the problem as a root finding problem, having defined $F(x)$, makes it easy to compute a numerical linearization of the system with respect to the unknowns and the inputs.

The application of FGS for the forward and magnetic equilibrium reconstruction problems are presented in section 4.5.

4.3 Forward free-boundary Grad-Shafranov Evolutive (FGE) code details

From the previous formulation of static problem, it is easier to explain the implementation of the coupling with the circuit equation for the evolution of the current in the conductors and the 0D currents diffusion equations obtained in eq. (2.60) and derived in Appendix G. The complete problem in its continuous form has been derived in eq. (2.63).

The spatial discretization of the problem has already been discussed in the previous section. For the time discretization we choose to implement a first order Euler implicit scheme. An explicit time stepping scheme was found to be numerically unstable for discrete time steps of the order of the growth rate of the VDE instability, which we aim to resolve. On top of the physical instability contained in the system, the Euler explicit scheme was found to be numerically unstable and required to use small Δt becoming too expensive. Every time derivative $\frac{dA}{dt}$ is approximated with 1st forward finite difference $\frac{dA}{dt} = \frac{A(t+dt)-A(t)}{\Delta t}$. We will define once again the problem in terms of a root finding problem. This time we will make the distinction in the inputs between the feedforward inputs v and the controller action u, since the system will optionally be coupled to feedback controller to stabilize the plasma vertical instability. We will call with the apex t the quantities evaluated at time t and with $t+1$ the quantities at $t + dt$. Since the scheme is first order in time only these two labels will appear.

We define the unknowns $x^{t+1} = \{I_y^{t+1}, I_e^{t+1}, a^{t+1}\}$, the controller action $u^t = V_a^t$, and the feedforward inputs $v^{t+1} = \{c^{t+1}, \sigma_\parallel^{t+1}(\rho), I_{ni}^{*,t+1}, \psi_e^t, \psi_A^t, \psi_B^t, \Phi^t(\hat{\psi})\}$. The quantities at t, meaning $\psi_e^t, \psi_A^t, \psi_B^t, \Phi^t$, come from the previous time step iteration but, considering only the problem of single Euler time step as in this case, they are effectively inputs. That is why we pack them

in $\boldsymbol{v}$. We define the operator $F(\boldsymbol{x}^{t+1}, \boldsymbol{v}^{t+1}, \boldsymbol{u}^{t+1})$ as follows

$$
F(\boldsymbol{x}, \boldsymbol{u}, \boldsymbol{v}) = \begin{cases} \frac{\psi_e^{t+1}-\psi_e^t}{\Delta t} - V_a^t + R_e I_e^{t+1} \\ \psi_e^{t+1} - M_{ee}I_e^{t+1} - M_{ey}I_y^{t+1} \\ I_y^{t+1} - \tilde{I}_y(I_y^{t+1}, I_e^{t+1}, \boldsymbol{a}^{t+1}) \\ \text{Constraints}(\boldsymbol{x}^{t+1}, \boldsymbol{u}^{t+1}, \boldsymbol{v}^{t+1}, c^{t+1}) \\ A_{1,1}^{t+1} + A_2^{t+1} + I_p^{t+1} - I_{ni}^{*,t+1} \end{cases} \tag{4.13}
$$

Where $A_{1,1}^{t+1}$, A_2^{t+1}

$$
A_{1,1}^{t+1} = \frac{T_B^{t+1}\Phi_B^{t+1}}{2\pi} \int_0^1 \frac{\sigma_\parallel^{t+1}}{T_{t+1}^2(\hat{\psi})} \left[\hat{\psi}\left(\frac{\psi_B^{t+1}-\psi_B^t}{\Delta t} - \frac{\psi_A^{t+1}-\psi_A^t}{\Delta t} \right) + \frac{\psi_A^{t+1}-\psi_A^t}{\Delta t} \right] d\hat{\Phi}^{t+1}(\hat{\psi}) \tag{4.14}
$$

$$
A_2^{t+1} = -(\tilde{\psi}_B^{t+1} - \tilde{\psi}_A^{t+1})\frac{T_B^{t+1}}{2\pi} \int_0^1 \frac{\sigma_\parallel^{t+1}}{\tilde{T}_{t+1}^2(\hat{\psi})} \frac{\tilde{\Phi}^{t+1}(\hat{\psi}) - \Phi^t(\hat{\psi})}{\Delta t} d\hat{\psi} \tag{4.15}
$$

We would like to make some remarks for the system of equations eq. (4.13).

- The controller actions V_a^t are computed at the time instant t, since the physical controller can only know the state of the system at t, when applied to a real tokamak in real time.

- The number of feed-forward constraints are 1 less than the dimension of the basis functions since the current diffusion equation acts as an additional constraint. If the CDE equation is not included in the system, the number of constraints must equal the number of basis functions.

- In case of three basis functions and CDE equation, typical constraints are integral quantities such as β_p and l_i.

- $\tilde{I}_y$ is computed from $\{I_y^{t+1}, I_e^{t+1}, \boldsymbol{a}^{t+1}\}$ by evaluating in order eq. (4.9) to eq. (4.12) as for the case of the static solver.

- The choice of the code is to use a fixed in time $\hat{\psi}$ grid.

- All the quantities appearing in eq. (4.14) and eq. (4.15), which are not given as forward inputs, can be computed from the knowledge of the unknowns $\boldsymbol{x}^{t+1} = \{I_y^{t+1}, I_e^{t+1}, \boldsymbol{a}^{t+1}\}$. In particular, given the basis function coefficients and the ψ_x map obtained when computing I_y with eq. (4.9) to eq. (4.12), one can compute the value of the toroidal flux enclosed in a given ψ_N surface, $\Phi(\hat{\psi})$, from $T(\hat{\psi}(R, Z))$.

- The formulation of the 0D CDE written above differs from what is typically done e.g. in rigid plasma models [Coutlis et al. 1999; Walker and Humphreys 2006], where the plasma is treated as a rigid conductor and a plasma circuit equation is formulated assuming a

fixed shape of the current distribution. The formulation above is derived as the integral of the 1D poloidal flux diffusion equation and contains no further approximations or assumptions.

- Thanks to the formulation of the 0D diffusion equation as in eq. (4.14) and eq. (4.15) one does not need to compute the geometrical quantities g_2 and g_3, which would involve the computation of the flux surface average which is computationally expensive. Also, as discussed in section 2.4, it should be possible in principle to write a discretized 1D CDE based on this formulation, that also does not require evaluation of geometrical quantities. This formulation was not yet attempted in this work, but would be interesting to attempt in the future.

The root-finding problem is now stated as usual, given $\boldsymbol{u}^t$ and $\boldsymbol{v}^{t+1}$, find x^{t+1}, such that $F(\boldsymbol{x}^{t+1}, \boldsymbol{u}^{t+1}, \boldsymbol{v}^{t+1}) = 0$. Also in this case the same JFNK is used to solve the problem.

4.3.1   Linearization of time evolutive system on approximate solution of the free-boundary equilibrium (Grad-Shafranov)

In this section we discuss the linearization of the system of equations for the quasi-stationary evolution of the free-boundary equilibrium, conductor current evolution and poloidal flux diffusion on trajectories of solutions of the free-boundary static equilibrium. We choose to provide the formulation for the problem already discretized in space for simplicity of the notation.

We only provide the formulation for the case of a current diffusion equation strictly valid only during a stationary state phase discussed in Appendix G.

$$
\begin{cases}
\frac{d\psi_e}{dt} = V - R_e I_e \\
\psi_e = M_{ee} I_e + M_{ey} I_y \\
\frac{d(\psi_A + \psi_B)}{dt} = 2\frac{I_{ni}^* - I_p}{\frac{T_B}{2\pi}\int_0^{\Phi_B}\frac{\sigma_\parallel}{T^2}d\Phi} \\
F(I_y, a; I_e, c) = 0 \\
y = P_P(I_y, a, I_e)
\end{cases}
\tag{4.16}
$$

The operator $F(I_y, a_g; I_e, c)$ represents the operator of the static free-boundary Grad-Shafranov equation with constraints as defined in eq. (4.8) corresponding to the one solved by the FGS code. We notice in particular that for the operator F, the I_y, a_g are the unknowns while I_e, c are inputs. This is the most computationally expensive part of the system of equation due to the several non linearities already explained in previous sections. The goal of this section is to find a linearization of this operator to obtain a fast simulator and the possibility of using a linear model for control design.

In the system of equations eq. (4.16) the unknowns are $\{I_y, a, I_e\}$. The forward inputs are $\{V_a, c\}$ and $\{I_{ni}, \sigma_\parallel\}$ for the current diffusion equation. In the system of equations eq. (4.31) we called $y = P_P(I_y, a, I_e)$ all the quantities that can be computed from the knowledge of the solution of the system of equations, as a post processing. These are sometimes referred to as simulated measurements. For example, all the quantities appearing in the current diffusion equation, ($T^2(\Phi, t)$, Φ_B ...) , together with all the synthetic diagnostics, for example the magnetic field at the B_m location the flux loops F_f, are included in y.

The number of constraints N_c equals the number of basis function coefficients N_a. The typical input constraints are in this case $\boldsymbol{c} = \{l_i, \beta_p, \psi_A + \psi_B\}$. Since $\psi_A + \psi_B$ appears explicitly in the time evolution of the CDE equation, it is convenient to use it directly as a constraint for the free-boundary equilibrium in the operator F. The linearization presented in the following will still be valid also in case the CDE equation is not included in the system of equation and $I_p(t)$ is provided as an input to the system. In this second case $\boldsymbol{c} = \{l_i, \beta_p, I_p\}$.

If we call $x = \{I_y, a, c, I_e\}$, we consider,

$$
\begin{cases}
I_y = I_y^0 + \delta I_y \\
a = a^0 + \delta a \\
c = c^0 + \delta c \\
I_e = I_e^0 + \delta I_e
\end{cases}
\tag{4.17}
$$

We choose the linearization original point to be a solution of the operator $F(I_y^0, a^0; c^0, I_e^0) = 0$ and we aim to find perturbations $\{\delta I_y, \delta a, \delta c, \delta I_e\}$ such that $F(I_y^0 + \delta I_y, a^0 + \delta a; c^0 + \delta c, I_e^0 + \delta I_e) = 0$ at first order. To do that formally we perform a Taylor expansion of the operator $F(x)$ up to the first order,

$$
F(x^0 + \delta x) = F(x^0) + \nabla_x F|_{x^0} \delta x + O(\delta x^2) = \nabla_x F|_{x^0} \delta x + O(\delta x^2).
\tag{4.18}
$$

Neglecting $O(\delta x^2)$ terms and using $F(x^0) = 0$, we look for those δx^* such that

$$
\nabla_x F|_{x^0} \delta x^* = 0.
\tag{4.19}
$$

It is now convenient to separate in eq. (4.18) the quantities $\{I_y, a, I_e\}$ from the constraints c to write,

$$
\begin{bmatrix} \nabla_{I_e} F & \nabla_{I_y} F & \nabla_a F \end{bmatrix}
\begin{bmatrix} \delta I_e \\ \delta I_y \\ \delta a \end{bmatrix}
= -\nabla_c F \cdot \delta c.
\tag{4.20}
$$

We notice that all the gradients are evaluated at the linearization point x^0, but in order to simplify the notation we avoid to specify it everywhere. This will be important however when discussing in the following the linearization of the system on time varying trajectories of $x^0 = x^0(t)$, but for the moment we will consider only a fixed in time linearization point x^0.

Similarly to what is done for the operator we can perform a Taylor expansion for all the post processing quantities,

$$y(x_0 + \delta x) \approx y(x^0) + \nabla_x P_P \cdot \delta x. \tag{4.21}$$

It is important to note that for practical reason, all the quantities composing the post processing quantities y are evaluated when evaluating the operator F, hence P_P for most of the quantities coincides with a sub-part of the operator F. Therefore most of $\nabla_x P_P$ is directly computed while computing $\nabla_x F$, which considerably saves computational time.

We note also that the obtained system of equations eq. (4.20) cannot be inverted since the matrix containing the gradient of the operator F in the RHS have dimensions $(N_y + N_a; N_y + N_a + N_e)$, hence it is not a full rank matrix. In order for the system to be invertible, one needs N_e extra equations. These are provided by the relation between the current and the fluxes in eq. (4.16). To show that we first define,

$$\psi_e^0 \equiv M_{ee} I_e^0 + M_{ey} I_y^0$$
$$\delta \psi_e \equiv \psi_e - \psi_e^0 = M_{ee} \delta I_e + M_{ey} \delta I_y$$

Putting everything together, we can write the final system of equations, including the linearization, which represents the time evolutive quasi-static problem linearized on trajectories of solutions of the Grad-Shafranov equation.

$$\begin{cases} \dfrac{d\psi_e}{dt} = V - R_e I_e \\ \dfrac{d\psi_A + \psi_B}{dt} = 2\dfrac{I_{ni}^* - I_p}{\frac{T_B}{2\pi}\int_0^{\Phi_B}\frac{\sigma_\parallel}{T^2}d\Phi} \\ y = y^0 + \nabla_x P \delta x \\ \underbrace{\begin{bmatrix} \nabla_{I_e} F & \nabla_{I_y} F & \nabla_a F \\ \mathbb{M}_{ee} & \mathbb{M}_{ey} & 0 \end{bmatrix}}_{\mathbb{M}_G(x^0)} \begin{bmatrix} \delta I_e \\ \delta I_y \\ \delta a \end{bmatrix} = \begin{bmatrix} -\nabla_c F \cdot \delta c \\ \delta \psi_e \end{bmatrix} \end{cases} \tag{4.22}$$

We would like to make some remarks on the system of equations obtained eq. (4.22).

- The free-boundary Grad-Shafranov equation is effectively a non-linear relation of $\{I_y, a\}$ as function of $\{I_e, c\}$. Thanks to the linearization performed we turned this relation into a linear problem to be solved, by inverting the matrix $\mathbb{M}_G$.

- The resulting matrix $\mathbb{M}_G(x^0)$ is a square matrix. The dependence on x^0 is due to the fact that the gradient of the operator F is evaluated at x^0.

- The hypothesis that x^0 is fixed in time was never used in the derivation. Hence the formulation eq. (4.22) is valid also considering time traces $x^0 = x^0(t)$. In general this would entail a time-varying $\mathbb{M}_G$, with linearizations of F around the time-varying trajectory

of $x_0(t)$. However, as was demonstrated in [Walker and Humphreys 2006], for flat-top stationary phases of a tokamak plasma discharge, during which I_y does not change in time, this linearization stays constant. This is due to the fact that, while I_e and ψ_e can change significantly with respect to the original linearization point, their changes are in directions that do not affect the value of $\mathbb{M}_G$.

- In case $\mathbb{M}_G$ does not change, then the matrix $\mathbb{M}_G(x^0(t^k))$ needs to be inverted only once, making the numerical solution of the system very fast with respect to the full non-linear one and suitable for real-time application. This would allow for example to design observers, for example for the current in the passive conductors, with techniques such as Kalman Filter or Unscented Kalman filter.

- It is also important to notice that one of the main problem with the solution of the free-boundary equilibrium, is that solving the operator F with Picard iterations is numerically unstable, which motivated the use of the Jacobian Free Newton Krylov solver. Since now a linear system replaces the solution of the Grad-Shafranov equation, this problem does not exist for the linearized system eq. (4.22).

- The formulation of eq. (4.22) is very general and one can easily substitute the Grad-Shafranov equation with another force balance equation with different formulation, for example considering the fixed-boundary equilibrium problem. One important case is to consider only rigid displacements of the plasma current distribution and eventually re-scaling of the total plasma current. In this case $I_y = I_y(R_A, Z_A, I_p; I_y^0)$, where the I_y^0 is the known plasma current density distribution which is rigidly displaced. To formulate the problem for rigid displacement is trivial from eq. (4.22). One only needs to exploit the chain rule $\nabla_{I_y} F \cdot \delta I_y = \nabla_{I_y} F \nabla_{R_A, Z_A, I_p} (I_y \cdot [\delta R_A, \delta Z_A, \delta I_p])$, where $\nabla_{R_A, Z_A, I_p} I_y$ can be calculated explicitly for rigid displacements as explained e.g. in [Walker and Humphreys 2006].

A simple Euler explicit scheme can be used for the time discretization.

$$
\begin{cases}
\frac{\psi_e^{t+1} - \psi_e^t}{\Delta t} = V^t - R_e I_e^t \\
\frac{\psi_A^{t+1} + \psi_B^{t+1} - \psi_A^t - \psi_B^t}{\Delta t} = 2 \frac{I_{ni}^{*,t} - I_p^t}{\frac{T_B^t}{2\pi} \int_0^{\Phi_B^t} \frac{\sigma_\parallel}{T^{2,t}} d\Phi} \\
y^t = y^0 + \nabla_x P \delta x^t \\
\mathbb{M}_G \begin{bmatrix} \delta I_e^t \\ \delta I_y^t \\ \delta a^t \end{bmatrix} = \begin{bmatrix} -\nabla_c F \cdot \delta c^t \\ \Delta \psi_e^t \end{bmatrix}
\end{cases}
\tag{4.23}
$$

This way the problem is fully explicit making the numerical implementation very fast to solve. With the stationary-state current diffusion equation, starting from eq. (4.23) one can put the system of equations into a state space form. This is discussed in the next section.

4.3.2   State-space representation of the linearized system

Starting from the results obtained in the previous section, we can re-cast eq. (4.22) into a state-space form, which is the usual form to study linear stabilization controllers. Moreover we choose as states $\{I_e, I_p\}$, hence the variables that will appear explicitly with a time derivative, in order to conform our linear system as much as possible to the RZIP model [Wainwright et al. 1997].

The RZIP code solves a linear system of equations as the linearized FGE presented in the previous section, but it assumes only rigid plasma displacements and a simplified equation for the total plasma current evolution. Our linear model should have a similar unstable dynamics for the VDE but allows at the same time to design plasma shape controllers. We follow the formulation in [Walker and Humphreys 2006], where it was demonstrated that the obtained formulation is also valid during stationary plasma states. Differently to [Walker and Humphreys 2006] however, we consider the case of deformable plasmas.

The final goal is to get the linearized system eq. (4.22) into the following form,

$$\begin{bmatrix} M_{ee} + M_{ey}\nabla_{I_e}GS^{I_y} & M_{ey}\nabla_{I_p}GS^{I_y} \\ \nabla_{I_e}GS^{\psi_{AB}} & \nabla_{I_p}GS^{\psi_{AB}} \end{bmatrix} \begin{bmatrix} \frac{d\delta I_e}{dt} \\ \frac{d\delta I_p}{dt} \end{bmatrix} = \begin{bmatrix} V - R_e(I_e + \delta I_e) \\ Q^0 + \nabla_{I_e}Q\delta I_e + \nabla_{I_p}Q\delta I_p + \nabla_{c_{in}}Q\delta_{c_{in}} \end{bmatrix}$$
$$+ \begin{bmatrix} -M_{ey}\nabla_{c_{cin}}GS^{I_y}\frac{dc_{in}}{dt} \\ -\nabla_{c_{cin}}GS^{\psi_{AB}}\frac{dc_{in}}{dt} \end{bmatrix}$$

where we indicate with GS^{I_y} and $GS^{\psi_{AB}}$, the solution of the free-boundary Grad-Shafranov problem for quantities I_y and $\psi_{AB} = \psi_A + \psi_B$ obtained with FGS given I_e and $c = \{I_p, l_i, \beta_p\}$, i.e the roots of the operator F eq. (4.8). We call the given input constraint $c_{in} = \{l_i, \beta_p\}$ to distinguish them from I_p, which is one of the state of the system evolved dynamically and not provided as an input for the system. In particular since I_p instead of $\psi_A + \psi_B$ is evolved as a state, to conform with RZIP, I_p enters as one of the constraints for the free-boundary Grad-Shafranov. With $\nabla_{I_e}GS^{I_y}$ we intend the gradient with respect to I_e of the solution of FGS for the quantity I_y about an initial solution $\{I_y^0, a^0; I_e^0, c^0\}$. With Q we refer to the RHS of the stationary state current diffusion equation specified later in eq. (4.39).

However, what we aim to achieve in this section is to express the previous linearized system in terms of the gradient of the operator of the free boundary Grad-Shafranov equation F eq. (4.8) and not in terms of the gradient of its roots, as for example in term $\nabla_{I_e}GS^{I_y}$. This will result in a much more computationally efficient solution, since for example estimating $\nabla_{I_e}GS^{I_y}$ with first order finite differences requires to solve, i.e. to find the roots, of the operator F a number of times equal to the dimension of I_e. Instead, to find the gradient of only the operator F with first order finite differences, and not the gradient of its solution, one needs only to evaluate the operator F a number of time equal to I_e dimension. Moreover, if the analytical expression for the gradient is available, the following formulation will be directly applicable.

We consider only the steady-state current diffusion equation. To simplify the notation, we

define

$$K(I_y, I_e, a, \sigma_\parallel) = \frac{T_B}{2\pi} \int_0^{\Phi_B} \frac{\sigma_\parallel}{T^2} d\Phi. \tag{4.24}$$

We split the F operator of the free-boundary equation into two parts as we already did when presenting the solver FGS eq. (4.8).

$$F(I_y, a; c, I_e) = \begin{cases} I_y - \tilde{I}_y(I_y, I_e, a) & = F_y(I_y, I_e, a) \\ \text{Constraints}(I_y, I_e, a, c) & = F_g(I_y, I_e, a, c) \end{cases} \tag{4.25}$$

$\tilde{I}_y(I_y, a, I_e)$ is a function which, from the inputs, performs the subsequent operations in order,

$$\psi_o = M_{boy} I_y + M_{boe} I_e \tag{4.26}$$

$$\psi_y = (D_{\psi_o}^{-1})\left(-\frac{2\pi\mu_0 R_y}{\Delta R \Delta Z} I_y - 2\pi\mu_0 I_e\right) \tag{4.27}$$

$$\text{find } P(\psi_y), \tilde{\psi}_A(\psi_y), \tilde{\psi}_B(\psi_y) \tag{4.28}$$

$$\tilde{I}_y = \begin{cases} \frac{\sum_g a_g g_g(\psi_y)}{\sum_Y \sum_g a_g g_g(\psi_y)} I_p & \text{in } P \\ 0 & \text{in } (P)^c \end{cases} \tag{4.29}$$

$$\tag{4.30}$$

that is why we write explicitly only the $\{I_y, I_e, a\}$ dependency. We call $\psi_{AB} = \psi_A + \psi_B$ and the resulting system of equations including the linearization of the free-boundary equilibrium is

$$\begin{cases} M_{ee}\frac{dI_e}{dt} + M_{ey}\frac{dI_y}{dt} = V - R_e I_e \\ \frac{1}{2}\frac{d(\psi_{AB})}{dt} K(I_y, I_e, a) = I_{ni}^* - I_p \\ y = y^0 + \nabla_x P \delta x \\ \begin{bmatrix} \nabla_{I_y} F_y & \nabla_a F_y & \nabla_{I_e} F_y & 0 \\ \nabla_{I_y} F_g & \nabla_a F_g & \nabla_{I_e} F_g & \nabla_c F_g \end{bmatrix} \begin{bmatrix} \delta I_y \\ \delta a \\ \delta I_e \\ \delta c \end{bmatrix} = 0 \end{cases} \tag{4.31}$$

Where we exploited the former knowledge that $\nabla_c F_y = 0$.

The goal is now to write the explicit (linear) relation $\delta I_y = \delta I_y(\delta c, \delta I_e)$ and $\delta a = \delta a(\delta c, \delta I_e)$ from the normal equations in terms of $\nabla_i F$, for appropriate i. From the second line of the gradient matrix we can explicitate δa,

$$\delta a = -\left(\nabla_a F_g\right)^{-1}\left(\nabla_{I_y} F_g \cdot \delta I_y + \nabla_{I_e} F_g \cdot \delta I_e + \nabla_c F_g \cdot \delta c\right). \tag{4.32}$$

Notice that we can invert $\left(\nabla_a F_g\right)^{-1}$, provided that the set of constraints c are not linearly dependent, since the number of constraints N_c are always equal to the number of basis functions, N_a, hence $\nabla_a F_g$ is a full rank matrix. Replacing δa from eq. (4.32) into the first line we get,

$$\underbrace{\left\{\nabla_{I_y} F_y + \nabla_a F_y\left[-\left(\nabla_a F_g\right)^{-1}\nabla_{I_y} F_g\right]\right\}}_{Z_1}\delta I_y+$$

$$+\underbrace{\nabla_a F_y\left[-\left(\nabla_a F_g\right)^{-1}\nabla_c F_g\right]}_{Z_2}\delta c+$$

$$+\underbrace{\left\{\nabla_{I_e} F_y + \nabla_a F_y\left[-\left(\nabla_a F_g\right)^{-1}\nabla_{I_e} F_g\right]\right\}}_{Z_3}\delta I_e$$

$$= 0$$

Therefore the relation sought becomes,

$$\delta I_y = -Z_1^{-1} Z_2 \delta c - Z_1^{-1} Z_3 \delta I_e = D_c^{I_y}\delta c + D_{I_e}^{I_y}\delta I_e \tag{4.33}$$

where, $-Z_1^{-1} Z_2 \equiv D_c^{I_y}$ and $D_{I_e}^{I_y} \equiv -Z_1^{-1} Z_3$. We can also use eq. (4.33), to eliminate the δI_y dependence in eq. (4.32). We define,

$$D_c^a \equiv -(\nabla_a F_g)^{-1}[(\nabla_{I_y} F_g)D_c^{I_y} + \nabla_c F_g] \tag{4.34}$$

$$D_{I_e}^a \equiv -(\nabla_a F_g)^{-1}[(\nabla_{I_y} F_g)D_{I_e}^{I_y} + \nabla_{I_e} F_g] \tag{4.35}$$

such that eq. (4.32) becomes,

$$\delta a = D_c^a\delta c + D_{I_e}^a\delta I_e. \tag{4.36}$$

It is important to notice that all the matrices encountered in this section are all dependent on the initial state x^0 since the different gradients of the operator are evaluated at x^0. So far the derivation in this section was correct also in case $x^0(t)$. However from now on we will enforce $\frac{dx^0}{dt} = 0$, so that $D_c^a, \dots$ matrices become time independent in order to extract them from the derivative sign. Again we refer to [Walker and Humphreys 2006] for the validity of this assumption. Moreover, with this assumption $\frac{dx}{dt} = \frac{d\delta x}{dt}$.

We will now choose our states $x_s = \{I_e, I_p\}$ and thanks to eq. (4.33) and eq. (4.36) we will be able to obtain the system of equations into a state-space form. If we introduce eq. (4.33) into

the first equation of eq. (4.16) we obtain.

$$(M_{ee} + M_{ey}D_{I_e}^{I_y})\frac{dI_e}{dt} + M_{ey}D_c^{I_y}\frac{dc}{dt} = V^t - R_e I_e \tag{4.37}$$

For comparison we notice that $M_{ey}D_{I_e}^{I_y} = X_{ee}$ in [Walker and Humphreys 2006]. We can bring the input c_{in} to the RHS side and keep the state I_p to the left.

$$(M_{ee} + M_{ey}D_{I_e}^{I_y})\frac{dI_e}{dt} + (M_{ey}D_c^{I_y})\frac{dI_p}{dt} = -R_e I_e - (M_{ey}D_c^{I_y})_{c_{in}}\frac{dc_{in}}{dt} + V^t \tag{4.38}$$

We now move to the linearization of the stationary state current diffusion equation. We call,

$$Q(I_p, I_e, a, I_{ni}^*, \sigma_\parallel, I_y) = 2\frac{I_{ni}^* - I_p}{K(I_y, I_e, a, \sigma_\parallel)} \tag{4.39}$$

and we Taylor expand up to the first order to compute $Q(I_p^0 + \delta I_p, I_e^0 + \delta I_e, a^0 + \delta a, I_{ni}^{*,0} + \delta I_{ni}^*, \sigma_\parallel^0 + \delta\sigma_\parallel, I_y^0 + \delta I_y)$,

$$Q \approx 2\frac{I_p^0 - I_{ni}^{*,0}}{K^0} + 2\frac{\delta I_p}{K^0} - 2\frac{\delta I_{ni}^*}{K^0} - 2\frac{I_p^0 - I_{ni}^{*,0}}{(K^0)^2}\nabla_{I_y, I_e, a, \sigma_\parallel}K\cdot[\delta I_y, \delta I_e, \delta a, \delta\sigma_\parallel]$$

We can now use the relation eq. (4.36) and eq. (4.33) to eliminate the δI_y, δa dependencies. We define,

$$D_{k,c}^Q \equiv (\nabla_{I_y}K)D_c^{I_y} + (\nabla_a K)D_c^a \tag{4.40}$$

$$D_{k,I_e}^Q \equiv (\nabla_{I_y}K)D_{I_e}^{I_y} + (\nabla_a K)D_{I_e}^a + \nabla_{I_e}K \tag{4.41}$$

such that,

$$
Q \approx \underbrace{\left(\frac{2}{K^0} - 2\frac{(I_p^0 - I_{ni}^{*,0})}{(K^0)^2}(D_{k,c}^Q)_{I_p}\right)}_{D_{I_p}^Q}\delta I_p + \underbrace{\left(-2\frac{(I_p^0 - I_{ni}^{*,0})}{(K^0)^2}D_{k,I_e}^Q\right)}_{D_{I_e}^Q}\delta I_e
$$
$$
+ \underbrace{\left[\frac{-2}{K^0} \quad -2\frac{(I_p^0 - I_{ni}^{*,0})}{(K^0)^2}\nabla_{\sigma_\parallel}K \quad -2\frac{(I_p^0 - I_{ni}^{*,0})}{(K^0)^2}(D_{k,c}^Q)_{c_{in}}\right]}_{D_{I_{ni}^*,\sigma_\parallel,c_{in}}^Q}\begin{bmatrix}\delta I_{ni}^* \\ \delta\sigma_\parallel \\ \delta c_{in}\end{bmatrix} + Q^0 \tag{4.42}
$$

where we have defined $D_{I_p}^Q, D_{I_e}^Q, D_{I_{ni}^*,\sigma_\parallel,c_{in}}^Q$ accordingly. We can now express $\frac{d\psi_{AB}}{dt}$ in terms of the state variables $\{I_e, I_p\}$. We remember that $\psi_{AB} = \psi_{AB}(I_y, I_e)$, hence we perform a Taylor expansion and replace in the RHS of the Ohm's law,

95

$$\frac{d\psi_{AB}}{dt} = \nabla_{I_e}\psi_{AB}\frac{dI_e}{dt} + \nabla_{I_y}\psi_{AB}\frac{dI_y}{dt}. \tag{4.43}$$

We make use of eq. (4.33) to replace the expression for δI_y in terms of $\{I_e, c\}$ to get

$$\frac{d\psi_{AB}}{dt} = (\nabla_{I_e}\psi_{AB} + \nabla_{I_y}\psi_{AB}D_{I_e}^{I_y})\frac{dI_e}{dt} + (\nabla_{I_y}\psi_{AB}D_c^{I_y})_{I_p}\frac{dI_p}{dt} + (\nabla_{I_y}\psi_{AB}D_c^{I_y})_{c_{in}}\frac{dc_{in}}{dt}. \tag{4.44}$$

We can finally combine eq. (4.44), eq. (4.38) together to get the state space representation. We define,

$$M_1 = \begin{bmatrix} (M_{ee} + M_{ey}D_{I_e}^{I_y}) & (M_{ey}D_c^{I_y})_{I_p} \\ (\nabla_{I_e}\psi_{AB} + \nabla_{I_y}\psi_{AB}D_{I_e}^{I_y}) & (\nabla_{I_y}\psi_{AB}D_c^{I_y})_{I_p} \end{bmatrix} \tag{4.45}$$

$$M_2 = \begin{bmatrix} -R_e & 0 \\ D_{I_e}^Q & D_{I_p}^Q \end{bmatrix} \tag{4.46}$$

$$M_3 = \begin{bmatrix} -(M_{ey}D_c^{I_y})_{c_{in}} \\ -(\nabla_{I_y}\psi_{AB}D_c^{I_y})_{c_{in}} \end{bmatrix} \tag{4.47}$$

$$M_4 = \begin{bmatrix} 0 \\ D_{I_{ni}^*,\sigma_\parallel,c_{in}}^Q \end{bmatrix} \tag{4.48}$$

So that we can write,

$$M_1 \begin{bmatrix} \frac{dI_e}{dt} \\ \frac{dI_p}{dt} \end{bmatrix} = M_2 \begin{bmatrix} I_e \\ I_p \end{bmatrix} + M_3 \cdot \frac{dc_{in}}{dt} + M_4 \begin{bmatrix} \delta I_{ni}^* \\ \delta\sigma_\parallel \\ \delta c_{in} \end{bmatrix} + \begin{bmatrix} V \\ Q^0 - D_{I_p}^Q I_p^0 - D_{I_e}^Q I_e^0. \end{bmatrix} \tag{4.49}$$

Finally, inverting M_1, one gets the state-space representation of the system. In particular $A = (M_1)^{-1}M_2$ is the matrix which regulates the free dynamics of the system. The eigenvalue of A are the one to be compared to RZIP to compute the growth rate of the VDE instability in its initial phase.

We would like to make some remarks,

- The formulation has been derived in terms of derivative of the operator F. One can therefore replace the operator for the force balance equation for example with a rigid displacement of the plasma or an analytic solution of the GS equation. However, since
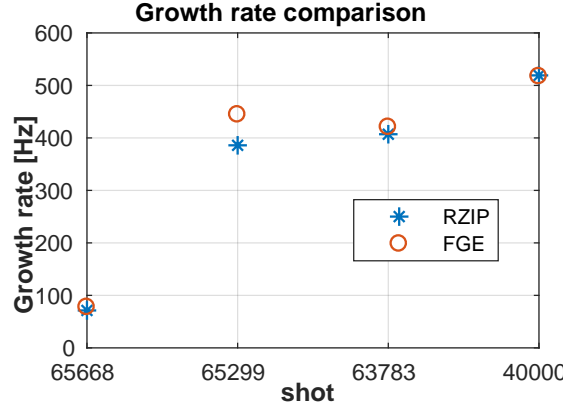
Figure 4.2 – Growth rate comparison of free evolution during vertical displacement events between RZIP and linearized FGE. 65665 limited plasma. 65299 diverted plasma. 63783 Negative triangularity limited plasma. 40000 Snowflake plasma.

during the derivation we exploited some a priori known dependencies of the operator F, one needs to be careful to reconsider them for a different operator.

4.4   Time evolutive free boundary code FGE validation

In this section we present a preliminary validation of the quasi-static evolutionary code FGE against TCV experiment. First we will present a benchmark of the linearized version of the code against an RZIP model often used to design vertical stability controllers in TCV, in order to validate the dynamics of VDE instability implemented in FGE. Then we will check the performance of the code when coupled to the real r_A, z_A, I_p control system of TCV, called "hybrid" controller [Lister et al. 1997], re-simulating an actual discharge and comparing the results with the experimental data.

We compare in fig 4.2 the growth rates of the most unstable eigenmode for the free-dynamic evolution (constant inputs) of the linearized FGE, computed from $A = M_1^{-1} M_2$ matrix eq. (4.49), and RZIP. The same equilibrium reconstruction computed with LIUQE is used to compute both matrices for the linearized FGE and for the RZIP model. Very different shapes and with different stability properties are considered. We find an excellent agreement between the two codes for all cases providing confidence on the time dynamics of the physics implemented in FGE.

To further validate FGE we couple it to a digital emulation of the TCV Hybrid control system. The goal is first to check that the controller stabilizes the system and to validate the current diffusion equation model implemented. Starting from an equilibrium reconstruction solution, we simulate 0.3s, equivalent to $2 - 3$ current diffusion time during an almost stationary phase of plasma operation, for the shot 65668. The simulation used a time step of $5 \times 10^{-5} [s]$, with a controller sampling time of $1 \times 10^{-4} [s]$ as during TCV operation. The forward inputs provided to FGE are $q_A(t)$ and β_p, shown in fig. 4.3a, obtained from the LIUQE magnetic equilibrium

reconstruction of the real discharge. The state is almost stationary because a slow evolution of q_A is still present. We used only three basis functions to represent the p' and TT' profiles, two constraints are given by the forward inputs and the third comes directly from the 0D current diffusion eq. (4.13). The feedforward commands for the voltages and references for coils current, position and total plasma current r_A, z_A, I_p are taken directly from the ones provided in the experiment. In fig. 4.3b,4.3c,4.3d we compare the simulation of FGE (blue) with the equilibrium reconstruction performed by LIUQE from the magnetic measurements of the experiment (red). The "hybrid" controller stabilizes the FGE simulation as it was the case for the real experiment. Since we started the simulation directly from a stationary phase of the plasma current, the integral part of the controller in the real-experiment had accumulated the error from the previous time instants while the FGE simulation started from a null initial state. This explains the initial oscillation of FGE simulation. Moreover what seems to appear as a high frequency numerical noise in FGE is in reality the result of the noisy $q_A(t)$ and β_p inputs obtained from the equilibrium reconstruction. We could have smoothed the inputs before providing to FGE, but it is interesting to keep it as an indication of the typical noise in the equilibrium reconstruction in inputs and the corresponding sensitivity of FGE simulation.

During a stationary state phase of constant plasma current I_p, the current diffusion equation relaxes to a state of constant $V = \frac{\partial \psi}{\partial t}$, in particular $V = \frac{\partial \psi_A}{\partial t} = \frac{\partial \psi_B}{\partial t}$, over the radius. This is shown in fig. 4.3f with an excellent agreement between the simulation and the experiment. The $\sigma_\parallel$ was estimated with the ICDBSEVAL routine described in Appendix B, which from the stationary state integral current diffusion equation, given the Thomson profiles for T_e and n_e, looks for the Z_{eff} to best matches the I_p and the measured V_{loop} in a given time interval of the experiment. The otherwise natural resistive decay of the plasma current requires that, in order to sustain a constant plasma current, the constant emf V at the plasma edge is maintained by an almost constant $\frac{dI_{OH}}{dt}$ of the dedicated OH coils as shown in fig. 4.3e. This is an indirect validation of the current diffusion model implemented in FGE. The same controller applied to the real tokamak and to FGE requires the same $\frac{dI_p}{dt}$ in a stationary phase in order to control and keep the same I_p.

In the future, the code will be benchmarked with similar codes such as CREATE [Albanese et al. 2015] and NICE [Faugeras 2020]. The dynamics of the code will be validated more extensively against VDEs in TCV, and also during transient phases such as ramp-up, ramp-down, limited to diverted and L-H transition phases. The code has started to be used to develop vertical position and shape controllers in TCV.

4.5   Magnetic equilibrium reconstruction with FGS

In this section we will show the application of the free-boundary static equilibrium code FGS to perform magnetic equilibrium reconstruction, extending in particular some limitations of the equilibrium reconstruction code LIUQE and making a comparison between the frequentist and Bayesian approaches to perform MER. The second will also show how to perform
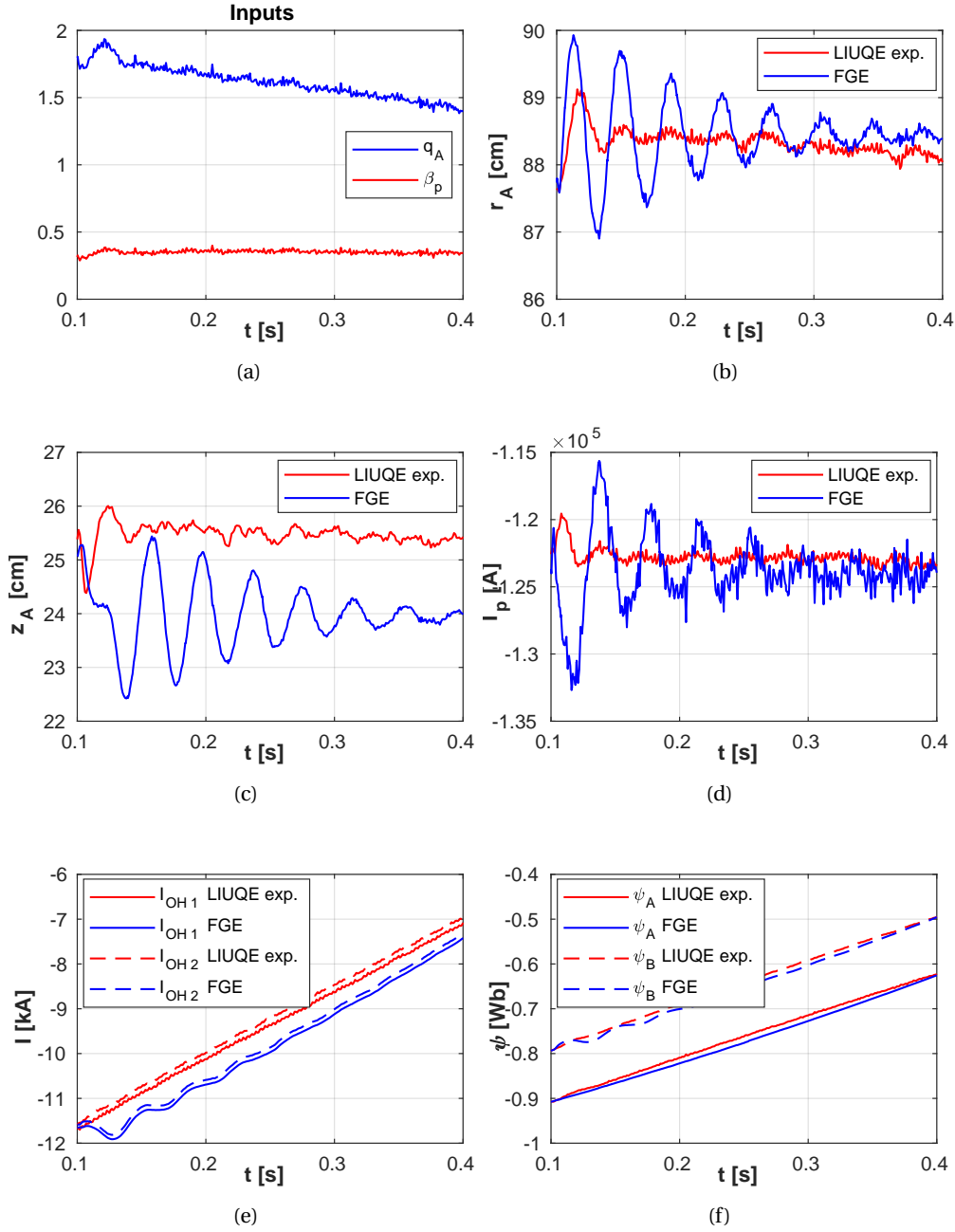
Figure 4.3 – Comparison between FGE re-simulation of shot 65668 and the magnetic equilibrium reconstruction with LIUQE from experimental data.

uncertainty propagation for the magnetic equilibrium reconstruction problem. The examples presented have the dual purpose of showing potential applications of FGS code and validate its numerical implementation. We remark that they have to be considered as preliminary analyses and proof-of-principle applications of the code.

4.5.1 Investigate limitations of LIUQE "quasi-linear" least-squares optimization

LIUQE has become in the latest years a potential candidate to perform real-time equilibrium reconstruction in ITER. An extensive benchmark with EFIT against synthetic free-boundary equilibrium data generated by the forward equilibrium code CREATE-NL [Albanese et al. 2015] for relevant plasma condition is ongoing with this purpose. It is important therefore to address any possible source of errors and limitations of the code and, in case of simplifying hypotheses, to test their impact on the final reconstruction.

Thanks to the contribution of this thesis with FGS, we can now solve the forward free-boundary equilibrium problem in the same code framework as LIUQE. Hence we can revise the equilibrium reconstruction performed by LIUQE and remove the following simplification hypothesis.

1. Solve the equilibrium reconstruction problem without the numerical vertical stabilization used in LIUQE, based on a vertical shift of the flux map which provides solutions that (slightly) violate the Grad-Shafranov equation. This is achieved thanks to the Newton-like solver developed.

2. Correctly solve the least-squares constrained optimization problem MER which, due to the algorithm simplification in LIUQE, did not allow to find the proper minimum for the cost function χ^2 in case of noisy measurements. This is detailed in the following.

3. Extend the capability of including measurements and constraints non-linearly dependent on the free parameters of the reconstruction problem.

We would like to explain better the second point.

Summary of difference between the simplified assumption in solving the "quasi-linear" least-squares problem in LIUQE compared to the correct solution of the problem

The problem is explained in general terms in Appendices E and F. We invite the reader to read first the Appendices since we will report here only the summary of the most important steps.

The equilibrium reconstruction problem aims to solve the non-linear least-squares optimization problem eq. (3.9), that we copy here for convenience, where $x = \psi(R, Z)$ and $\boldsymbol{\theta}$ are the free parameters for the equilibrium reconstruction problem. In LIUQE case $\boldsymbol{\theta} = \{\boldsymbol{I}_a, \boldsymbol{I}_v, \boldsymbol{a}, dz\}$ where we notice that the shifted stabilization parameter dz is one of the free parameters to be inferred from the optimization. All the external magnetic measurements are contained in $\tilde{\boldsymbol{M}}$.

We call with θ^* and x^* the solutions of the problem.

$$\{x^*, \boldsymbol{\theta}^*\} = \underset{x, \boldsymbol{\theta}}{\operatorname{argmin}} ||\tilde{\boldsymbol{M}} - \mathbb{A}(x)\boldsymbol{\theta}||_w^2$$

such that

$$\begin{cases} \Delta^*\psi = -2\pi\mu_0(j_{pl} + j_e) & \text{in} \quad \Omega_c \\ \psi(R, Z) = \sum_{i=[pl,a,s]} \int_{\Omega_i} G_i(R, Z; R', Z') j_{\varphi,i}(R', Z') dR' dZ' & \text{in} \quad \partial\Omega_c \\ j_{pl} = \sum_{i=1}^{N_g} a_i R^{\nu_i} g_i(\hat{\psi}(R, Z)) & \text{in} \quad \Omega_{pl} \\ j_{pl} = 0 & \text{in} \quad (\Omega_{pl} \cap \Omega_c)^c \end{cases} \tag{4.50}$$

The problem is a non-linear least-squares optimization problem with non-linear equality constraint represented by the Grad-Shafranov equation. However the forward model $\mathbb{A}(x)\boldsymbol{\theta}$ for the simulated measurements, meaning the relation that from the knowledge of the state x and parameters $\boldsymbol{\theta}$ allows to compute the synthetic estimation of the measurements, is represented by "quasi-linear" relation $\mathbb{A}(x)\theta$. This means that the relation with the free-parameters $\boldsymbol{\theta}$ is linear while the non linearity with respect to x is contained only in the dependency of the matrix $A(x)$.

To solve the problem one needs to consider variations with respect to the free parameters $\boldsymbol{\theta}$ and $\boldsymbol{x}$, making use of Lagrange's multipliers to take into consideration the equality constraint as explained in appendix F. However, if one allows only variation of the parameters $\boldsymbol{\theta}$, forgetting the variation of $A(x)$ with respect to x, an explicit solution of the optimization problem can be found $\theta^* = (\mathbb{A}^T(x)\mathbb{A}(x))^{-1}\mathbb{A}^T(x)\tilde{\boldsymbol{M}}$. This is explained in appendix F. With this assumption, which is adopted in LIUQE, the optimization problem turns into the following root-finding type problem.

$$\begin{cases} \theta^* = (\mathbb{A}^T(x)\mathbb{A}^{-1}(x)\mathbb{A}^T(x)\tilde{\boldsymbol{M}} \\ \Delta^*\psi = -2\pi\mu_0(j_{pl} + j_e) & \text{in} \quad \Omega_c \\ \psi(R, Z) = \sum_{i=[pl,a,s]} \int_{\Omega_i} G_i(R, Z; R', Z') j_{\varphi,i}(R', Z') dR' dZ' & \text{in} \quad \partial\Omega_c \\ j_{pl} = \sum_{i=1}^{N_g} a_i R^{\nu_i} g_i(\hat{\psi}(R, Z)) & \text{in} \quad \Omega_{pl} \\ j_{pl} = 0 & \text{in} \quad (\Omega_{pl} \cap \Omega_c)^c \end{cases} \tag{4.51}$$

LIUQE solves eq. (4.51) with Picard iterations where $\boldsymbol{\theta} = \{\boldsymbol{I}_a, \boldsymbol{I}_v, \boldsymbol{a}, dz\}$ and the flux map is vertically shifted by dz for numerical stabilization purposes. This strictly violates the GS equation at convergence [Moret et al. 2015]. With FGS and the JFNK we can solve it without the dz stabilization.

The static free-boundary equilibrium problem eq. (2.22), contained as an equality constraints in eq. (4.50), finds $x = \psi(R, Z)$ given θ. If we formally call $G(\theta)$ the operator which given θ solves the free-boundary equilibrium problem finding x, we can formally replace $x = G(\theta)$ in the $A(x)$ dependence of the cost function. The non-linear optimization problem eq. (4.50) becomes therefore an optimization problem only for the parameter θ.

$$\boldsymbol{\theta}^* = \underset{\boldsymbol{\theta}}{\operatorname{argmin}} ||\tilde{\boldsymbol{M}} - \mathbb{A}(G(\theta))\boldsymbol{\theta}||_w^2 = \underset{\boldsymbol{\theta}}{\operatorname{argmin}} \chi_w^2 \tag{4.52}$$

This problem eq. (4.52) is fully equivalent to eq. (4.50). The equality constraint is hidden in finding the solution by computing $G(\theta)$, which provides solutions of the Grad-Shafranov equation. $G(\theta)$ is exactly the problem solved by the code FGS.

We can therefore solve eq. (4.52) by looking for stable point of the cost function, finding θ such that $\nabla_\theta \chi_w^2 = 0$. We use the subscript w in the cost χ_w^2 to indicate that the different measurements in the cost function can be weighted independently, e.g. by their noise level content. Differently to what is performed in LIUQE, which leads to eq. (4.51), we will now properly consider the dependencies $\nabla_\theta \mathbb{A}$.

In order to solve eq. (4.52), we implemented a steepest descendent-like algorithm called Levenberg-Marquardt [Van Tol 1963]. We are aware of the fact that the algorithm is not the most robust algorithm nor the numerically cheapest one to solve the problem, also because it requires the estimation of the gradient of $G(\theta)$, meaning the gradient of the solutions of the Grad-Shafranov equation, which we perform brute force with second order finite differences. Sequential quadratic programming [Nocedal and Wright 2006] can be used more effectively for this purpose and also Jacobian free algorithms [Xu et al. 2016] are available for this scope. However, the purpose of the results that we present in the following is just to show a proof of principle of our findings, meaning the difference in the solution between eq. (4.52) and eq. (4.50), without aiming yet to develop an efficient and robust implementation.

Without changing the algorithm, we can now easily include constraints on the cost functions which are non-linearly dependent on the free parameters $\boldsymbol{\theta}$, since the Levenberg-Marquardt algorithm, as well as any fully non-linear optimization algorithm, is able to deal with general non-linear forward models for the simulated measurements and not just "quasi-linear" ones as in eq. (4.52). This removes the 3rd limitation of the LIUQE code listed above.

In the following, with the label "LIU" we will refer to the solution of the LIUQE algorithm solving eq. (4.51) with Picard iterations and stabilization parameter dz. With "L" we will refer to the solution of eq. (4.51) but without the dz stabilization making use of the JFNK algorithm. We call it "L", because it is effectively solving the "quasi-linear" original optimization problem as if it was a linear one, forgetting the dependencies of the matrix $A(x)$. Finally with "NL" we will refer to the solution of the original non-linear optimization problem eq. (4.50), expressed as in eq. (4.51) and solved with Levenberg-Marquardt algorithm.

We want now to demonstrate numerically the following.

- Suppose that we take a given set of parameters $\theta^* = \{I_a, I_v, \boldsymbol{a}\}$. We compute the solution of the forward free-boundary problem $x = G(\theta^*)$. This is obtained for example with FGS with high convergence requirements or with an analytic solution. We consider as measurements $\tilde{\boldsymbol{M}}$ exactly the estimation of the forward model for the simulated measurements computed at the given parameters θ^* such that $\tilde{\boldsymbol{M}} = \mathbb{A}(G(\theta^*)\theta^*$. This way the solution of the forward problem clearly has $\chi_w^2 = 0$. This case represents the artificial situation when the forward model perfectly describes the physical reality and
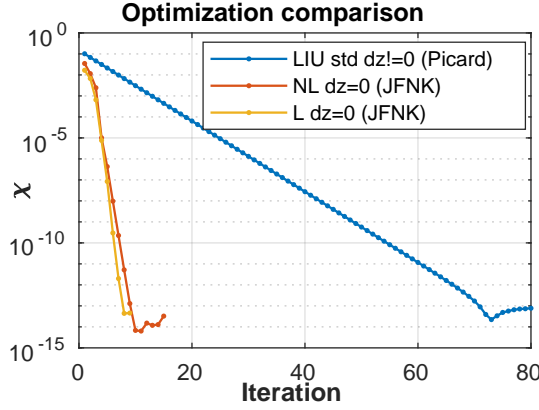
Figure 4.4 – Convergence comparison over iterations of magnetic equilibrium reconstruction codes for noise free synthetic data. LIUQE (blue, label "LIU") over Picard iterations. FGS with Levenberg-Marquardt (red, label "NL") over steepest descendent steps. FGS solving LIUQE like formulation but without dz stabilization and JFNK solver (yellow, label "L") over Newton iterations.

there is no noise in the measurements nor uncertainty in the model. What we want to show is that in this specific case, all the three solution "LIU", "L","NL" must converge to the same solution at $\chi_w^2 = 0$. This is demonstrated analytically at the end of the appendix E.

We compute a solution of the free boundary equilibrium with FGS and the related synthetic measurements $\tilde{M}$ in the same location as the physical diagnostics of TCV. We feed the three equilibrium reconstruction algorithms "LIU", "L", "NL" with this noise free perfect measurements and we check the convergence of the χ^2 to zero over iterations till machine double precision. This is shown in fig. 4.4. All the three algorithms converge until machine double precision 1×10^{-14} to the original solution generating the measurements.

The original equilibrium computed with FGS was obtained with exactly the same set of basis functions used in all the equilibrium reconstruction codes. This means that the original solution is contained among the set of solutions of the three codes spanned by the free parameters $\boldsymbol{\theta}$ to be estimated with the optimization.

The codes were initialized with the same plasma current distribution and free parameters I_a, I_v, a. The iteration index in the horizontal axis of the plot has different meaning for the three cases. For "LIU" it refers to the iteration of the Picard scheme. For "L" the iterations refer to the Newton steps of the JFNK algorithm to solve eq. (4.51), hence the LIUQE equivalent problem with $dz = 0$. For the "NL" case the iteration refers to the Levenberg-Marquardt updating step which is almost a steepest-descendent Newton step. The Newton algorithm has a faster convergence in terms of iterations than Picard, but every iteration step requires several evaluations of the FGS solution, hence it is overall much more expensive.

The results shown in fig. 4.4 have two important consequences. It demonstrates that LIUQE

103

would find the correct solution in case of completely noise free data and if the solution is contained in the space of solutions spanned by the free parameters of LIUQE. This is an important validation for the LIUQE code. This can happen only when the basis functions of LIUQE can perfectly represent the plasma profiles of the equilibrium which generated the measurements. The result is also an indirect benchmark for the FGS code. To reach the machine precision was expected since FGS shares all the low-level routines of LIUQE, for example for the search of the plasma boundary and the inversion of the Grad-Shafranov operator, but it is important to demonstrate it.

We will now perform a second numerical test:

- Suppose the measurements have noise or the true equilibrium generating the data is not contained in the set of equilibria spanned by the free parameters of the forward model. For example this is the case when the pressure profile shows a pedestal feature and the basis functions for the equilibrium reconstruction are composed of simple polynomials which cannot reproduce it. More generally this is the case whenever $\tilde{\boldsymbol{M}}$ cannot be simply computed from the solution of the forward model for the simulated measurements given a set of parameters $\theta^* = I_a^*, I_v^*, a^*$. This means more specifically $\tilde{\boldsymbol{M}} \neq \mathbb{A}(G(\theta^*))\theta^*$. This is the opposite to the previous numerical test and reproduces a simplified synthetic case of what happens when performing equilibrium reconstruction from real measured data. In these cases the three algorithms, "NL","L" and "LIU" will find different solutions. At the three solutions in general $\chi^2_{LIU} \neq \chi^2_L \neq \chi^2_{NL} \neq 0$. Moreover, since χ^2_L is not a proper solution of the original optimization problem eq. (4.50) but only has the "linear-like" simplification hypothesis eq. (4.51), we expect $\chi^2_L > \chi^2_{NL}$. Instead for χ^2_{LIU}, since LIUQE has an extra free parameter, dz, a priory one cannot establish the relation of χ^2_{LIU} with the other χ^2, and potentially it could be smaller than all the others.

We consider the case of a typical single null plasma in TCV. We compute a solution of the free boundary equilibrium problem with FGS in order to get noise-free synthetic data as in the previous numerical experiment. In this case however we add a constant offset of 2σ to one of the flux loop in the upper high field side, fig. 4.5. The σ is the standard deviation of the expected noise of the measurements which enter in the reconstruction problem as a weight for the χ^2_w. This is a very extreme case since a perturbation of this order, supposing that the noise of the measurements is well estimated by this σ, should be very unlikely to occur in a statistical sense. The σ used is the one estimated for TCV among a large number of discharges. We feed the three reconstruction algorithms, "LIU", "L", "NL" with this perturbed data and we look at the solutions at convergence.

The obtained flux surfaces for the different cases are shown in fig. 4.5, with a zoom in the region near by the noisy probe in fig. 4.5. The resulting total χ^2_w are shown in fig. 4.6. The $\chi_w = \sqrt{\sum_i (\tilde{M} - \mathbb{A}(x)\boldsymbol{\theta})_i / w_i}$ is computed with respect to the noisy data since that is the cost function that the several algorithms try to minimize.
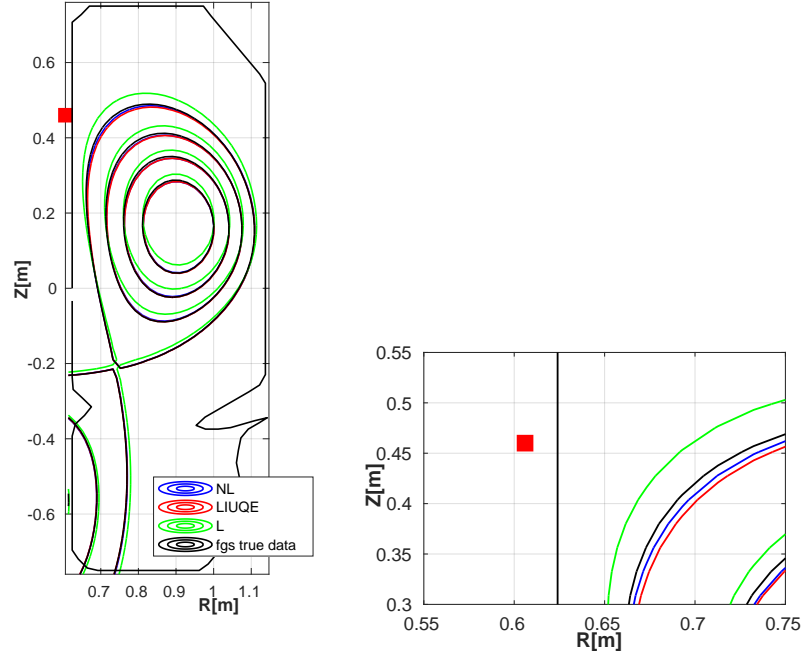
Figure 4.5 – Flux surfaces of magnetic equilibrium reconstruction codes with synthetic data with single flux loop (red square) noise. LIUQE (red). FGS with Levenberg-Marquardt (blue, label "NL"). FGS solving LIUQE like formulation but without dz stabilization and JFNK solver (green, label "L").
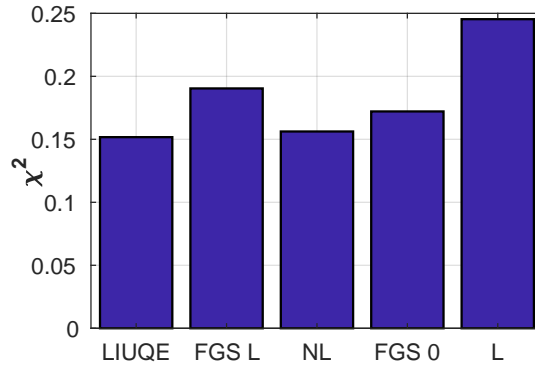

Figure 4.6 – Comparison of resulting χ^2 for magnetic equilibrium reconstruction with different algorithms for single flux loop noise synthetic data. "LIUQE" for LIUQE code. "FGS L" for the re-computation of the free-boundary equilibrium solution from the I_a, I_v and basis function coefficients obtained with LIUQE. "NL" for FGS magnetic equilibrium reconstruction with Levenberg-Marquardt algorithm. "FGS 0" for the original equilibrium generating the synthetic data before adding the noise to the probe. "L" for FGS solving the LIUQE problem without dz stabilization. $dz = 0.8mm$ from LIUQE

- LIUQE, with the stabilization $dz \neq 0$ (label "LIUQE"), finds the absolute minimum value of χ_w among all the other codes. This could not be predicted a priori but it is not surprising since "LIUQE" has an extra free-parameter, dz, to vary in order to find the minimum of χ_w. The resulting dz in this case is $dz = 0.8mm$.

- However, the solution of LIUQE is not a proper solution of the free-boundary equilibrium problem, because of the stabilization vertical shift which enters in the equation. Moreover, it is not true that if one takes the solution of LIUQE and shifts it back by dz the flux map obtained is a proper solution of the free boundary problem either with the same I_a, I_v, a of the reconstruction. It violates (slightly) the GS equation.

- In fact, if one takes $\{I_a, I_v, a\}$ computed from the LIUQE solution and solves the forward free-boundary equilibrium problem with FGS with these inputs one gets a different χ^2, shown in in fig. 4.6 with the label "FGS L".

- The solution of "FGS L" is now a proper solution of the forward free-boundary problem, nevertheless it is not the solution which minimizes the χ_w. Indeed, the non-linear optimization "NL" with Levenberg-Marquardt algorithm finds another solution which is at the same time both a solution of the forward Grad-Shafranov and a minimum for the χ_w. This of course could be a local minimum and not an absolute one. But at least it is a solution of the original magnetic equilibrium reconstruction problem eq. (4.50). Differently stated a solution with $\nabla_\theta \chi = 0$ where all the non linear dependencies of χ_w, including $\nabla_x A(x)$ neglected by LIUQE, have been considered.

- The linear optimization problem "L" finds a bigger χ than the "NL" as expected. This is true for all the cases we investigated, and it must be the case since "L" is not properly solving the original optimization problem eq. (4.50).

- It is instructive to compare the previous χ_w for the several codes, with the one computed from the original FGS solution which generate the noise free data. The χ_w^2 for this original FGS is equal to the perturbation added artificially scaled by the weight. This is called $FGS0$ in fig. 4.4. It is interesting to notice that both LIUQE and the NL optimization finds a χ_w^2 which is smaller than the one of the original FGS. This should have been expected since both LIUQE and the NL algorithm try to minimize the χ_w^2 computed from the noisy measurements. Hence they can find a proper solution of the optimization problem eq. (4.50) and eq. (4.51), which overfits potentially the noise in the measurements resulting in a lower χ while still respecting the equality constraint represented by the free-boundary equilibrium. This teaches a very important point when comparing different equilibrium reconstruction solutions. In presence of noisy data one cannot judge two different reconstructions, in terms of how close they get to the real noise free solution originating the data, only based on the resulting value of χ^2. If one finds a very big χ for a given solution, much higher than the σ, and believe that the σ well describes the noise content of the measurements, in that case one can doubt that the reconstruction solution is accurate. But two different solutions with a difference in χ within σ cannot be compared based only on the χ^2.

- If we take the NL flux map solution, and use it to compute the $\mathbb{A}(x)$ matrix for the "quasi-linear" problem eq. (4.51) and we solve the "quasi-linear" optimization with the normal equation $\theta^* = (\mathbb{A}^T \mathbb{A})^{-1} \mathbb{A}^T \tilde{\boldsymbol{M}}$, we do not get the same basis function coefficients as for the NL solution. This means that in case of noisy data, the solution of the NL eq. (4.50), is not a solution of the L problem eq. (4.51) and vice-versa.

In summary in this section we explored some applications of the forward equilibrium reconstruction code FGS to perform magnetic equilibrium reconstruction. The aim was first to remove some of the limitations of the equilibrium reconstruction code LIUQE, in particular: eliminating the artificial vertically shifted solution introduced for numerical stability reason, which violates the Grad-Shafranov equation at convergence; check the difference between the "quasi-linear" optimization with respect to the full non-linear optimization problem; potentially extend the capability of handling measurements non-linearly dependent on the flux map and the free-parameters for the problem I_e, I_v, a, without considering only "quasi-linear" problems.

The results presented in this chapter have to be considered as preliminary analyses which aim first of all to show the potential of the new suite codes developed to address many different reconstruction problem, rather than making conclusive statement on quantitative differences between the different optimization techniques. However, from our preliminary analyses we find that the simplifications adopted in the code LIUQE do not affect strongly the final reconstruction solution. A broader validation towards many different plasma shapes and different noise content is undergoing to identify potential pathological cases when the simplification hypothesis in LIUQE is no longer valid.

4.5.2 Bayesian vs frequentist magnetic equilibrium reconstruction

In this section we would like to complete the understanding of the magnetic equilibrium reconstruction problem making a comparison between the frequentist approach, which leads to the least-squares optimization problem presented in the previous section, and exploiting FGS to address the Bayesian approach. The Bayesian approach has the important application to perform the uncertainty propagation of the magnetic equilibrium reconstruction problem.

In the introduction section 3.1 we discussed how to derive the formulation of an inverse problem which we summarize here both for reading convenience and to explain the analysis performed in this section.

1. *Start from a forward model.* For the MER problem this is the free-boundary equilibrium problem solved by FGS eq. (3.9), where the input parameters are $\boldsymbol{\theta} = \{\boldsymbol{I}_a, \boldsymbol{I}_v, \boldsymbol{a}\}$, with $\boldsymbol{a}$ the coefficients for the basis function expansion.

2. *Make assumptions on the type of errors and model uncertainties.* For example one can consider that the measurements are only affected by additive white noise, described by

the likelihood probability distribution function,

$$p(\tilde{y}|\boldsymbol{\theta}) \propto \prod_{i=1}^{N} exp\left(-\frac{(\tilde{y}_i - g_i(\boldsymbol{\theta}))^2}{2\sigma_i^2}\right) \tag{4.53}$$

where $\tilde{y}$ are the magnetic measurements table 3.2, σ_i describes the noise level of the measurement i provided as an assumption, and $g_i(\boldsymbol{\theta})$ is the estimate of the measurement i given the parameter $\boldsymbol{\theta}$. To compute $g_i(\boldsymbol{\theta})$ one needs to solve the free boundary equilibrium problem with FGS eq. (2.22) and eq. (4.8) for the parameters $\boldsymbol{\theta}$ and compute the relevant post processing.

3. *Adopt a statistical approach to estimate $\boldsymbol{\theta}$*. The frequentist approach estimates $\boldsymbol{\theta}$ looking for the values which maximize the likelihood which leads to the minimum least-squares problem eq. (3.9), solved with FGS with the Levenberg-Marquardt algorithm and with some approximations by LIUQE as shown in section 4.5.1. In the Bayesian approach one looks instead for the posterior distribution function $p(\boldsymbol{\theta}|\tilde{y})$ which from the Bayes theorem $p(\boldsymbol{\theta}|\tilde{y}) \propto p(\tilde{y}|\boldsymbol{\theta})p(\boldsymbol{\theta})$ where $p(\tilde{y}|\boldsymbol{\theta})$ is the likelihood and $p(\boldsymbol{\theta})$ the prior belief on the parameters.

When does the two approaches coincide when a point estimate of $\boldsymbol{\theta}$ is sought?
To provide a single estimate of the parameter $\boldsymbol{\theta}$ from the posterior $p(\boldsymbol{\theta}|\tilde{y})$, one can compute the maximum a posterior (MAP) of the distribution function. If the prior $p(\boldsymbol{\theta})$ is assumed as a uniform distribution function with a wide range, than the $\boldsymbol{\theta}$ which maximizes the likelihood $p(\tilde{y}|\boldsymbol{\theta})$, hence the solution of the least-squares type problem solved in section 4.5.1, maximizes also the posterior $p(\boldsymbol{\theta}|\tilde{y})$. Wide in this context means wider than the support of the resulting posterior distribution for the parameters, which can be checked when the analysis is concluded.

To demonstrate the previous statement we perform the following analysis for the TCV shot 65561@1s. We take the definition of the likelihood for white noise eq. (4.53). We use as σ_i the standard values used in TCV for the magnetic measurements which enter as weights in the magnetic equilibrium reconstruction with minimum least-squares approach. We perform the magnetic equilibrium reconstruction with LIUQE and with FGS with the Levenberg-Marquardt algorithm as in section 4.5.1. We assume as prior for the coefficients of the basis function $\boldsymbol{a}$ a wide uniform distribution function. For $\boldsymbol{I}_a, \boldsymbol{I}_v$ we do not assume any prior since these quantities enter as measurements and compose part of the likelihood distribution. The posterior $p(\boldsymbol{\theta}|\tilde{y})$ is therefore in the form,

$$p(\boldsymbol{\theta}|\tilde{y}) \propto \prod_{i=1}^{N} exp\left(-\frac{(\tilde{y}_i - g_i(\boldsymbol{\theta}))^2}{2\sigma_i^2}\right) \prod_{i}^{N_a} U(a_i) \tag{4.54}$$

where with U we indicate a uniform distribution. Thanks to FGS, which can solve $g_i(\boldsymbol{\theta})$, we can perform a Monte Carlo sampling to estimate the posterior $p(\boldsymbol{\theta}|\tilde{y})$.

The settings for the simulations are the following. The free parameters are composed by 19 poloidal field currents $\boldsymbol{I}_a$, the 256 vessels filaments are grouped into 38 segments connected in parallel, sharing the same voltages, located around the location of the flux loops (fig. 2.1a). Three polynomial basis functions are considered, 1 linear in $\hat{\psi}$ for p' called a_1, 1 linear plus 1 quadratic for TT' called a_2 and a_3 in the following. This is the standard set of basis functions used to perform equilibrium reconstruction in TCV. In total the dimension of the free parameters is 60. To estimate the posterior we used a Markov Chain Monte Carlo (MCMC) technique based on the slice sampler algorithm [Neal 2003] provided by the statistical Matlab package. The algorithm allows to sample from a general non-normalized probability distribution function, as it is the case for eq. (4.54), since when performing Bayesian parameter estimation we are not interested in estimating the "evidence" (eq. (3.3) for reference). We computed 1×10^5 samples which, looking at the marginal traces of the parameter, was considered to be the more than enough for the algorithm to converge to a random realization from the target distribution, forgetting about the initial condition. There are cases in which the forward model FGS does not converge. This can be due both to physical reasons that an equilibrium solution for the set of trial parameters $\boldsymbol{\theta}$ does not exist or potentially from stability issues with the Newton algorithm in FGS. In case the FGS fails to find a solution, the sampled parameters are removed from the distribution, as if their prior probability was null. Only 90 failed cases were found out of 1×10^5 samples. The sampling is initialized from the solution parameters $\boldsymbol{\theta}$ obtained with LIUQE equilibrium reconstruction. A normal kernel smoothing function is then used to obtain a smooth representation of the posterior distribution from the samples obtained with MCMC.

The first finding that we wanted to check is that the solution of least-squares optimization problem solved with FGS and the Levenberg-Marquardt algorithm, labeled with "NL", which is supposed to correspond to the maximum of the likelihood, is also the maximum of the posterior (MAP) when defined as eq. (4.54). This is shown in fig. 4.7a,4.7b,4.7c for the 3 coefficients of the basis functions a_1, a_2, a_3 where the solution "NL" (yellow vertical line) is indeed found at the maximum of the marginal posterior (blue line). The LIUQE solution is also shown with the red vertical line and, as already discussed in section 4.5.1, since it is not a proper minimum of the least-squares problem due to the simplifications adopted in the algorithm, it cannot correspond to the MAP in this analysis.

All the marginal distribution functions have been normalized to their maximum value. We decided to show the cases only for the coefficients of the basis function, rather than for the other free parameters represented by the conductor currents, since these are the main parameters that the magnetic equilibrium reconstruction, in whatever formulation, aims to infer from the measurements since for the conductor currents the measurements are already well constraining a small range of possible solutions. Moreover, the chosen uniform prior is not influencing the final distribution for the marginal posterior of the basis function coefficients since we chose a very broad uniform distribution where the resulting posterior (blue line) is well contained inside.

It is also worth noticing that the previous analysis can also be considered as another benchmark for the "NL" algorithm. Indeed the estimated posterior (blue) and the solution of the "NL" (yellow) has been obtained with two completely independent algorithms. One by sampling with Monte Carlo technique and the other by solving a non-linear least-squares optimization problem.

The previous analysis can be considered an academic example, even if applied to an unusual forward model. However one of the most useful application of Bayesian approach is to not just provide a point estimation for the inferred parameters $\boldsymbol{\theta}$ but to estimate full posterior distribution function which allows to then compute the uncertainty quantification of the parameters and, more importantly I_y and all the quantities that can be computed as a post processing from the parameters. As an example, from fig. 4.7d to 4.7h, we show the marginal posterior for some of the main global quantities of interest when performing the equilibrium reconstruction problem in order, the internal inductance l_i, the total stored energy W_k, the total plasma current I_p, the radial and vertical position of the magnetic axis r_A,z_A, but could be extended to 1D profiles. Since I_p enters as a direct measurement, we also displayed the likelihood distribution with violet line.

The Bayesian approach is finding increasing interests and applications for many reconstruction problem in fusion, and since the equilibrium reconstruction is an ubiquitous input for many forward diagnostic models, the free-boundary equilibrium should be treated at the same level to perform a consistent Bayesian inference, in the same direction as [Hole et al. 2010b; Fischer et al. 2010]. However performing MCMC on a relatively large parameter space as for the case of MER is computationally demanding, that is why frequentist approach is still the essential tool for post-discharge and real-time analyses.

4.6 Limitation of MER for realistic ITER kinetic profiles

The main limitation of magnetic equilibrium reconstruction is due the low sensitivity of the external magnetic measurements to internal plasma profile features. The result, well known in the fusion community, is that magnetic equilibrium reconstruction provides accurate results to reconstruct the external plasma shape. However providing additional information to internal plasma profiles, hence performing kinetic equilibrium reconstruction as described in 3.3, is necessary to obtain a good knowledge of the shape of the internal flux surfaces. This is especially true when the plasma profiles have local features given from both external actuators (heating/fueling/current drive) and plasma transport physics (H-mode pressure pedestal profile, advanced scenarios with reversed shear, transport barriers...). This is of particular interest for high performance discharges in particular for ITER where these profile features will be present "by-design", meaning they are necessary components of the scenario to achieve the performances sought by the experiment. It is important therefore to be able to identify these features and their contribution in the final reconstruction, potentially also in real-time during the experiment in order to be able to control them.
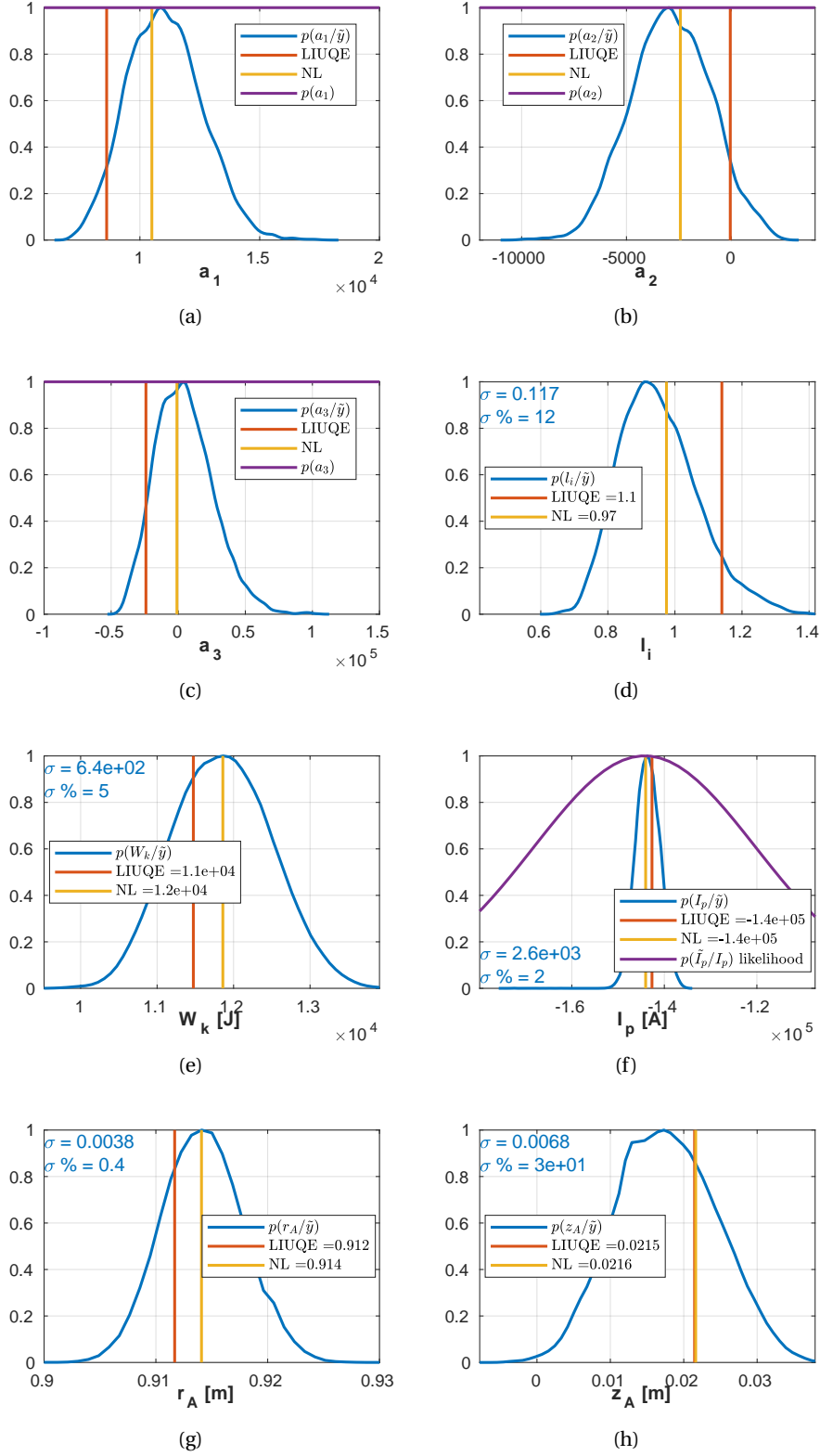
Figure 4.7 – Comparison between posterior distribution function (blue) computed with FGS with MCMC, the maximum likelihood estimate (standard MER with minimum least-squares) computed with FGS and Levenberg-Marquardt algorithm (yellow) and with LIUQE (red). Shot 65561@1s

We consider a realistic ITER H-mode base scenario of 15 MA during stationary state operation. We take the internal plasma profiles and coils currents from a transport simulation of JETTO [Romanelli et al. 2014] code. These profiles present the characteristic pedestal pressure profiles of H-mode plasmas, including the bootstrap contribution to the current density profile in particular at the plasma edge.

We first compute a solution of the forward free-boundary equilibrium with FGS. This provides a synthetic data for the magnetic measurements which are clean from measurement noise. We use the full set of magnetic diagnostics designed for ITER. We consider the case of no currents in the passive structures surrounding the plasma. It is only during transient phases that they play an important role. During the stationary phase, instead, they would provide a small contribution with respect to the active conductor currents. To estimate them one would need a full dynamic simulation, for example with FGE, CREATE-NL or DINA-CH which is not yet considered in this analysis.

Given this noise-free data, we perform the magnetic equilibrium reconstruction. The final aim is to recover at best the original equilibrium which generated the data. To perform the equilibrium reconstruction we use the best settings of LIUQE estimated during the benchmark with EFIT. In particular a set of 6 polynomial basis functions is used together with a penalization in the cost function to avoid high current density at the plasma edge. Using these settings with the described synthetic data provides the important information of what would be so far the "best" magnetic equilibrium reconstruction that could be achieved with LIUQE. As a continuation of the investigation computed in the previous section, the magnetic equilibrium reconstruction with the LIUQE equivalent code without stabilization solved with the JFNK algorithm and the non-linear optimization computed with the Levenberg-Marquardt algorithm. All of the reconstruction codes share the same settings for the basis functions and measurements weights.

The main difference in this analysis with respect to the numerical investigation performed in the section 4.5.1 is that the set of basis functions used to perform the equilibrium reconstruction cannot recover perfectly the features of the equilibrium which originated the synthetic data. In particular they do not allow for a pedestal "knee". In other words, the real solution of the problem is not within the space of solutions spanned by all the possible solutions of the reconstruction codes with the chosen set of basis functions. This feature emulates a realistic situation in which magnetic equilibrium reconstruction is performed in tokamaks during this type of scenarios. Before entering in the analysis of the results one can understand quickly this point by having a glance to the original $\frac{\partial p}{\partial \psi}$ from JETTO (black line in fig. 4.10b and the reconstruction ones which shapes come mainly from the basis function choice.

The important point to understand is that it is not just an arbitrary choice to limit the basis functions to this reduced set of few polynomial and to not allow pedestal features. It is an intrinsic limitation of the magnetic equilibrium reconstruction problem. Even if we were to use more basis functions, the external magnetic measurements are not sufficiently sensitive to
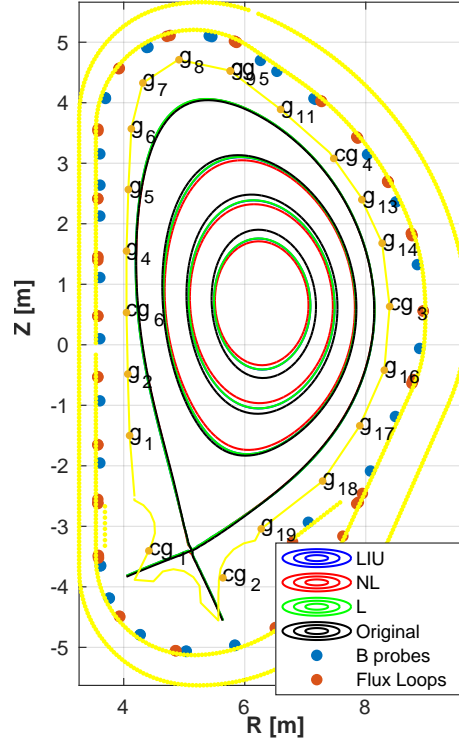
Figure 4.8 – Comparison of flux surfaces between magnetic equilibrium reconstruction performed with LIUQE (blue, label "LIU"), FGS with Levenberg-Marquardt (red, label "NL"), FGS solving LIUQE-like formulation but without dz stabilization (green, label "L"), original data (black, label "Original").

internal profile features to be able to distinguish among their contributions. Hence, we could not obtain much better results than the current settings in any case. As in the previous section we call with the label "LIU" (blue) the solution of the LIUQE equilibrium reconstruction, with "L" (green) the solution of the LIUQE equivalent "quasi-linear" optimization problem without the artificial "dz" stabilization and with "NL" (red) the solution of the full non-linear optimization problem with Levenberg-Marquardt algorithm. The original equilibrium from which the synthetic data have been generated, labeled "Original", are shown with the black lines. The black lines are therefore the reference target that all the reconstruction algorithms aim to reproduce at best.

First in fig. 4.8 we present the result for the flux surfaces. We show with the blue red bullets the location of the magnetic field probes and flux loops respectively which are inside the vessel but outside obviously of the limiter. The first expected result is that there is a very good agreement between all the reconstructions on the last closed flux surface as expected. The magnetic equilibrium reconstruction provides accurate enough information of the plasma shape to

prevent the plasma touching the wall and indeed plasma shape controllers are designed receiving the real-time magnetic equilibrium reconstruction as an observable input.

This can be measured quantitatively by measuring the spatial gaps between the plasma last-closed flux surface and the few points distributed on the wall around poloidal direction, indicated with the names g_x and cg_x in fig. 4.8. In fig. 4.9a we call with Δ gaps the difference between the gaps of the original solution and the different reconstructions with the same color convention as in the other plots. We also show in fig. 4.9b the percentage difference of the gaps with respect to the gaps of the original solution. All the reconstructions perform better in absolute terms in the poloidal region where the LCFS is close to the actual measurements, which are the two sides of the tokamak corresponding to the diagnostic g_1 to g_5 and g_{13} to g_{16}, but equally well in relative terms for all the diagnostics. All the reconstructions achieve few percent differences with respect to the original gap. The non-linear optimization performed slightly better than the other reconstructions in terms of the gaps, but this is not a general finding. Hence, the only meaningful expected result in the previous plot is to confirm that magnetic equilibrium reconstruction can well identify the shape of the LCFS as already stated. The magnetic equilibrium does not provide the same accuracy in reconstruction of the shape of the internal flux surfaces and plasma profiles. In fig. 4.10c, 4.10b, 4.10a, 4.10d we show in order the pressure profile, the $\frac{\partial p}{\partial \psi}$ and $T\frac{\partial T}{\partial \psi}$ profiles resulting from the basis functions expansion, the coefficients obtained by solving the least-squares optimization problem and the T profile. All the reconstructions provide as a result a significantly different pressure profiles, not only because they cannot reproduce the pedestal feature, but also because they have a different dependency towards the axis with a decreasing derivative. This results in a difference of the total stored energy with respect to the equilibrium data of the order of 10%. This is even more clear in the $\frac{\partial p}{\partial \psi}$ profile in fig. 4.10b. The small pedestal feature cannot be recovered by the simple basis representation used for the equilibrium reconstruction.

Overall the difference in the profiles result in a noticeable difference in the shape of the internal flux surfaces location within $\rho < 0.4$. Moreover, features like the flat j_{tor} profile in the center (fig. 4.10e) or the bootstrap component of the current density at the pedestal cannot be recovered precisely. In fig. 4.10e one can see that the MER reconstruction provides only a qualitative correct estimate of the edge current. All these limitations result in a significantly different q profile towards the axis, fig. 4.10f. It is interesting to note that for this specific case, since the surfaces at $q = 1.5$ and $q = 2$, where the NTMs instability might appear and will have to be controlled with the use of electron cyclotron current drive, are fairly outside the plasma all the reconstructions perform relatively well in identifying them for this particular case of investigation.

The final comment, for an accurate identification of the shape of the internal flux surfaces and plasma profiles in presence of plasma profile features, the external magnetic measurements are not sufficient and direct information on the profiles should be provided. This would be useful for example when the magnetic reconstruction is used as starting analysis for stability calculations, transport analysis with gyrokinetic codes, mapping of plasma diagnostics into 1D
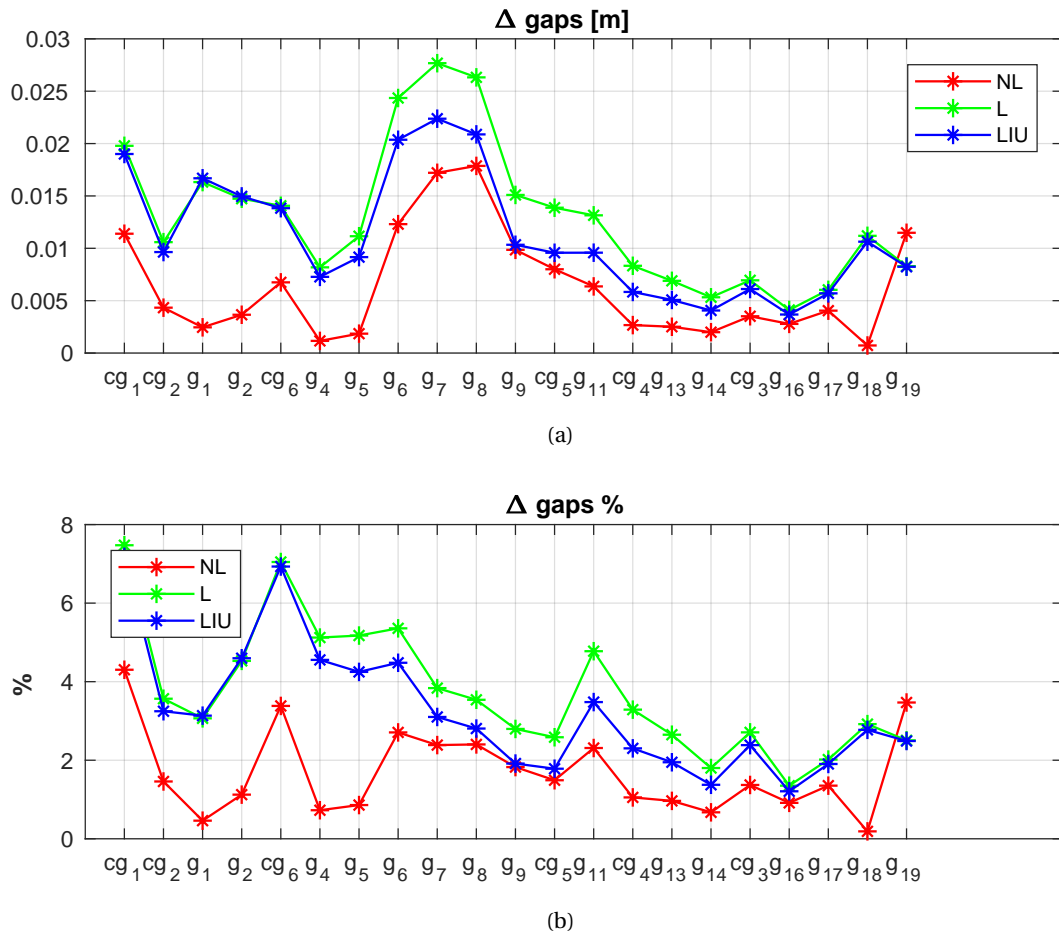
(a)

(b)

Figure 4.9 – Differences original solution and different reconstruction algorithm plasma-wall gaps.
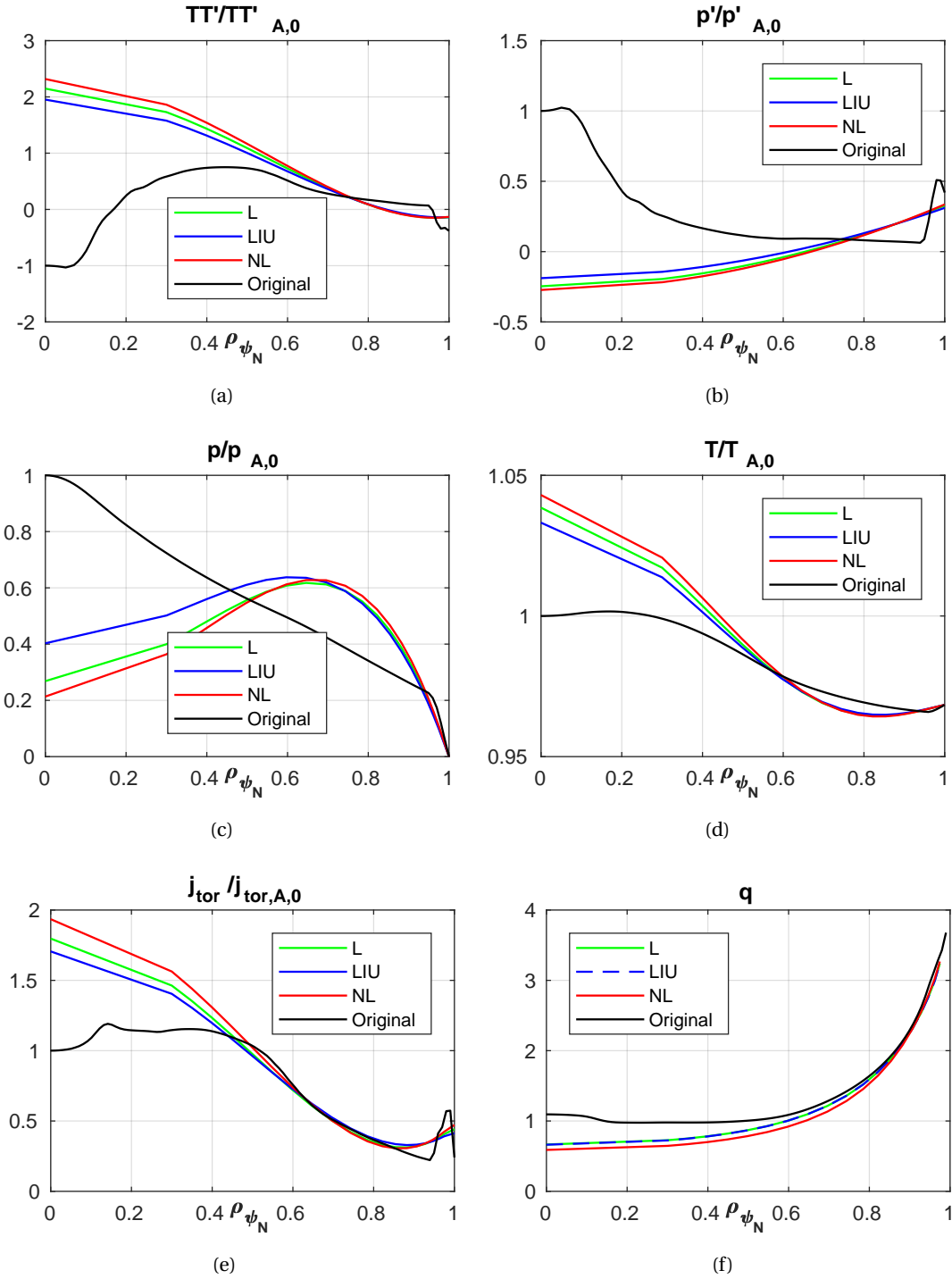
Figure 4.10 – Comparison of reconstructed profiles. LIUQE (blue, label "LIU"), FGS with Levenberg-Marquardt (red, label "NL"), FGS solving LIUQE-like formulation but without dz stabilization (green, label "L"), original data (black, label "Original"). With the subscript $A, 0$ we indicate the absolute value of the original profile (black) at plasma axis.

radial profiles, to perform core profile control in real time. With this aim in the next chapters we will investigate different techniques to perform kinetic equilibrium reconstruction which we will be applied to TCV both for the post-discharge analysis and in real-time during plasma experiments.

The analysis performed in this section considered a very ideal case and had the aim to show how in the best conditions the magnetic equilibrium reconstruction would perform in presence of realistic plasma profiles. There are two important missing features in our analysis. The first is investigating the results in presence of measurements noise. We only started to perform some preliminary sensitivity analysis on the reconstruction codes with white noise. However to make conclusive statements one should consider all the potential sources of error with realistic importance such as electronic errors, calibration and thermal errors, cross-talk and absolute measurements errors during ramps as explained in [Peruzzo 2012].

The second missing aspect is the introduction of the current in the passive structure during transient phases such as current ramp-up/ramp-down, L-H transition and limited to diverted shape transition. An agreed strategy to measure them and to take them into account when performing magnetic equilibrium reconstruction has not been achieved yet. We will discuss about this topic in some more details in the outlook section.

4.7 Summary

In this chapter we presented the new suite of codes developed in this thesis to solve forward and inverse problems related to the free-boundary equilibrium in tokamaks. In particular we developed a forward free-boundary static equilibrium code called FGS and a dynamic code FGE based on the evolution of the free-boundary equilibrium coupled with the evolution of the currents in the active and passive conductors. The dynamic solver includes a 0D Ohm's law for the resistive dissipation of the total plasma current. We presented also a linearized version of the dynamic code which includes a linearized free-boundary equilibrium coupled to the current diffusion equation. Moreover we presented some first applications of this suite of codes for the solution of both forward and inverse problems summarized in the following.

The original idea was to re-use the optimized low level routines developed for the equilibrium reconstruction code LIUQE [Moret et al. 2015] to address a larger set of problems. The main issue was to resolve the numerical instability of the Picard type iterations previously used when solving the free-boundary Grad-Shafranov equation by replacing the numerical scheme with a Newton like scheme. The scheme, called Jacobian Free Newton Krylov (JFNK) and explained in Appendix D, while retaining the stability properties of a Newton scheme, does not require to explicitly form the Jacobian of the problem. Thanks to its flexibility, it allowed us to quickly test many different applications.

The main novelty of our code stands in the way the 0D current diffusion equation is coupled to the equilibrium and currents evolution, in a monolithic system of equations without

iterative approaches. They are eventually needed only to compute the post-processing of some quantities.

FGE is already coupled to the real-time control system of TCV and is currently being exploited to develop the shape and vertical stability control system of our tokamak. Among the preliminary validations of the code presented, we showed in particular how the implemented current diffusion equation in our simulator makes the TCV hybrid control system to require currents in the Ohmic coils closely comparable to the experimental one, in order to maintain a fixed plasma current.

We presented a linearized version of the FGE code.

- Our formulation is based on the linearization of the time evolutive system on approximate solutions of the free-boundary equilibrium problem as in [Walker and Humphreys 2006]. This constraint of considering only approximate solutions of free boundary problem is given by a normal equation for the operator representing the force balance, hence the Grad-Shafranov equation in our case. The advantage of considering the linearization only in terms of derivative of the force balance operator is that the same linearization approach can be applied easily to different force balance models like for example considering rigid displacements of the plasma or analytic solution of the Grad-Shafranov.

- We provided also a state-space representation of the linearized system, using as states the current in the conductors and the total plasma current, to conform at most to the RZIP model, which has been widely used to design vertical stability controller in TCV [Sharma et al. 2005]. As a validation of our model, we compared the growth rates for the most unstable mode of the free dynamics of the system for plasma of different shapes. We found an excellent agreement between linearized FGE and RZIP, giving us confidence that our code well represents the physical dynamics of the system for the early phases of vertical displacement events.

In this chapter we also exploited the new forward free-boundary equilibrium static code FGS to address the magnetic equilibrium reconstruction problem with some proof of principle applications which have a potential general interest for the fusion community. The first application aimed to remove some of the limitations of the equilibrium reconstruction code LIUQE and investigate the importance of its simplification hypothesis. With FGS we implemented a Levenberg-Marquardt optimization algorithm to solve the least-squares non-linear optimization problem with non-linear equality constraints represented by the Grad-Shafanov equation. We summarize the main findings in the following.

- We can remove the numerical stabilization of the Picard iterations scheme in LIUQE, which is common to EFIT [Ferron et al. 1998] and the fast version of CLISTE [McCarthy et al. 1999], thanks to the stability of the Newton like scheme implemented. The previous

stabilization scheme indeed was based on solving a vertically shifted Grad-Shafranov equation where the amplitude of the vertical shift was part of the free parameters to be estimated in the least-squares problem. From our preliminary investigation we found that the difference of the solution removing this non-physical stabilization is small but still measurable.

- LIUQE code allowed to consider only measurements and constraints in the cost function whereas the forward model between the free-parameters to be estimated by the reconstruction problem and the estimation of the measurements must be a "quasi-linear" relation. The parameters θ are in general the coefficients for the basis function expansion of the plasma profiles and the currents in the conductors. Thanks to the Levenberg-Marquardt algorithm implemented, we can now handle any non-linear relations.

- We found that LIUQE, due to the simplification adopted in solving the MER problem represented by a non-linear least squares optimization problem with equality constraints, was not converging to the proper minimum of the cost function in presence of noisy measurements or features in the profiles that cannot be represented by the chosen basis functions. We discuss this analytically in Appendices E and F and demonstrated this numerically applying FGS with the Levenberg-Marquardt algorithm.

From the investigations conducted, the impact of all these limitations have been found small when comparing to the final reconstruction, however further investigations are undergoing to discover potential pathological cases.

As a second application of FGS, we addressed the magnetic equilibrium reconstruction problem comparing the Bayesian approach to the frequentist one, which leads to the least-square optimization problem solved by LIUQE, and with FGS with the Levenberg-Marquardt algorithm. The goal was twofold: to show when these approaches coincide and benchmark the different solvers developed; to show how, with the Bayesian approach, the uncertainty quantification of the magnetic equilibrium reconstructed quantities is obtained.

As a last investigation presented in this chapter, we investigated the intrinsic limitations of performing magnetic equilibrium reconstruction due to the low sensitivity of external magnetic measurements to internal plasma profile features. We considered an ITER H-mode 15 MA standard scenario with pressure and current profiles taken from a transport code JETTO. This scenario includes the standard pedestal feature and the consequent edge bootstrap current. With our suite of codes we computed noise-free synthetic measurements. We considered a single stationary state time-slice and we neglected the contribution of the current in the vessel which is supposed to be small during this phase. We then performed magnetic equilibrium reconstruction with LIUQE and the other techniques developed in this thesis. The results showed that the magnetic equilibrium reconstruction can accurately reconstruct the external plasma boundary. However to accurately identify the internal flux surfaces shape and internal plasma profiles, extra internal measurements are needed. Since these features

will be present by design during ITER operation in order to achieve the desired performances, this advocates to move from magnetic equilibrium reconstruction to kinetic equilibrium reconstruction. In the next chapters therefore we will discuss techniques to perform kinetic equilibrium reconstruction applied to TCV tokamaks both in the post-discharge and in the real-time analysis.

In conclusion, thanks to the codes developed in this thesis, we extended the **LIUQE-suite** to address free-boundary equilibrium problems ranging from predictive forward static and dynamic problems to inverse/reconstruction problems applied to several devices. The FGS and FGE are still in their infancy and will need further developments to make them robust and speed up the computation as described in Appendix D.

4.8 Outlook

We would like to list in the following some of the future developments and analyses that would be a natural prosecution of the work developed in this thesis.

- While being very flexible, the computational cost of the JFNK algorithm implemented is still demanding compared to other existing codes such as CREATE-NL [[Albanese et al. 2015]], or NICE [[Faugeras and Orsitto 2019]]. Improvements will move in two directions. One will be investigating different algorithms for the solution of the root-finding problem, or at least finding numerically cheap solutions to precondition it. These are briefly described in appendix D. The other will be to adopt hardware solutions by parallelizing the most expensive parts of the code.

- Within the present framework, we can easily extend the system of equations to take into account different transport models. One of the first foreseen attempt will be to add a 1D version of the current diffusion equation in order to be able to simulate both the magnetic control and the current density profile control. Eventually the addition of the halo currents will be investigated, as done in DINA code, for a better description of the VDE events.

- During this thesis work, the porting of the equilibrium code LIUQE to be able to read the IMAS/IDS data structure has been developed. This allows the code to be able to run for many different devices providing data in that format, which is also the format chosen by ITER. Since the new suite of codes have been developed sharing most of the LIUQE low level routines, it will be easy to extend our suite of codes to address different devices.

- A proper study of the sensitivity of the magnetic equilibrium reconstruction in presence of noisy measurements will be conducted, especially for the ITER case with a realistic noise content of the measurements. This will provide important information to the reliability of the equilibrium reconstruction and the need for kinetic equilibrium reconstruction. This study could be first tested on TCV where many real data are available from different experiments.

- A robust observer for the evolution of the current in the passive structures during transient phases to improve the equilibrium reconstruction. These include in particular the ramp-up/ramp-down phases, the L-H transition, the limited to diverted transition and during vertical displacement events. The study could start by simulating these events with our forward time evolutive solver FGE. Test the reliability during these events of the linear model. Develop a state and parameter estimation, hence an inverse problem for the time evolving model, based on the forward model and the unscented or extended Kalman filter technique to take into account process and measurements noise. These approaches are suited to perform inverse problem of dynamic system in a recursive fashion (see Appendix A). Test this observer in simulations with artificial noise. Analyse what are the limitations of the static equilibrium reconstruction when considering different estimators for the vessel currents during these events. Test the observer against real data during these events. The currents in the passive structure might significantly impact the shape of the plasma during these transient events also in ITER. Developing a robust estimation of these currents during these events will be beneficial during plasma operation to improve the plasma control and avoid the ITER plasma to approach too closely the limiter during transient phases.

5 Kinetic Equilibrium Reconstruction in TCV (post experiment)

In the last part of the previous chapter we showed how magnetic equilibrium reconstruction performs well on the task of identifying the external shape of the plasma but fails on accurate identification of the internal plasma profiles and internal distribution of the flux surfaces. To improve the reconstruction, direct information from the plasma inside the last closed flux surface is needed. To this end, in this chapter, we present the implementation of kinetic equilibrium reconstruction for TCV tokamak for the post discharge analysis based on the formulation of the problem described in sec. 3.3.

Kinetic Equilibrium Reconstruction (KER) aims to identify the poloidal flux distribution $\psi(R, Z)$ and the internal plasma profiles to obtain a solution of the plasma equilibrium force balance consistent with the magnetic and kinetic measurements and/or transport modelling. In this chapter we will first in sec. 5.1 provide an overview of the different implementation of KER available in literature. Then in sec. 5.2, we will discuss the implementation of KER with the set of codes used for TCV post-shot analysis, based on the simplified formulation derived in sec. 3.3.2. In presenting the result of the developed tools we will first focus on a sensitivity analysis of magnetic equilibrium reconstruction using realistic plasma profiles from kinetic measurements and modelling on a TCV database in sec. 5.4.1. We will then compare in sec. 5.4.2 the difference between KER and MER for few discharges with internal profile features, such as H-mode pedestal and reverse shear, coming from both external heating and current drive and/or plasma transport. Finally we will list in details the critical aspects of the present implementation and provide outlooks for future development.

5.1 Literature investigation

The magnetic equilibrium reconstruction MER became a widely used analysis in the tokamak operation starting from [Lao et al. 1985; Blum et al. 1981] when the code EFIT, in particular, was developed and after that used in many different tokamaks and later followed by its first real-time implementation [Ferron et al. 1998]. Many different codes were developed in the same period to perform magnetic equilibrium reconstruction [Brusati et al. 1984],[Blum and

Thooris 1985], [McCarthy et al. 1999] including the first version of the code LIUQE [Hofmann and Tonetti 1988].

Kinetic equilibrium reconstruction started by adding progressively more information from internal measurements principally to constrain the current density profile with MSE and polarimetry and the pressure profile from kinetic measurements in the free-boundary equilibrium problem. Examples for EFIT are found in [Lao et al. 2005, 2016; Burrell et al. 2018]. Many other groups developed similar techniques [Giannone et al. 2016; McCarthy et al. 1999; Faugeras 2020; Jiang et al. 2019; Li et al. 2013] or more developed integrated data analysis techniques including Bayesian approach [Fischer et al. 2010], [Fischer et al. 2019]. Kinetic equilibrium reconstruction was performed at the beginning mainly after the experiment rather than during the operation since some of the diagnostics, especially for the reconstruction of the internal plasma current, are difficult to calibrate or require human intervention and the computational requirements are significant.

Kinetic Equilibrium Reconstruction has become one of the standard analyses performed after the experiment in many devices. It is the starting point to provide the geometrical description to map the internal diagnostic into 1D profiles, to run gyrokinetic transport analysis [White 2019] and MHD stability analysis.

At the same time progressively more complex modelling were added, including time evolving models to better estimate the evolution of the plasma profiles. Two main frameworks have emerged and used in different tokamaks. The "Integrated Data analysis Equilibrium" (IDE) [Fischer et al. 2016], developed at IPP-Garching, couples the free-boundary equilibrium with the current diffusion equation. Magnetic measurements and constraints to internal plasma profiles are provided to the cost function of the equilibrium reconstruction problem which is in the form of a weighted least-squares type as we discussed in eq. (3.9). One interesting feature is the use of a Bayesian framework to perform what is called "Integrated Data Analysis" (IDA) [Fischer et al. 2010] to combine internal kinetic measurements from several diagnostics while propagating measurements uncertainties. This combined information is then used to provide constraints to the internal plasma profiles p and j in the free-boundary equilibrium problem. This approach is a hybrid between the frequentist interpretation, for the free-boundary inverse problem, and the Bayesian one described in sec. 3.1 for the kinetic measurements handling. A Bayesian analysis for the free boundary equilibrium problem has been obtained in [Von Nessi et al. 2013], however due to the high dimensionality of the state to be reconstructed, the $\psi(R, Z)$ map, it is computationally expensive for routine use. The IDA approach at present is the one treating different diagnostics and their uncertainties in the most consistent way, providing also their uncertainty propagation. Similar Bayesian approaches have been developed for the framework Minerva [Hole et al. 2010a] used in JET and W7-X to combine the information of several diagnostics. Bayesian analysis is typically computational demanding, however a real-time application framework has been achieved recently in the Minerva framework using Neural-Networks [Pavone et al. 2019].

A second popular approach is performed with the integrated modeling tool called "One Modeling Framework for Integrated Tasks" (OMFIT) [Meneghini et al. 2015; Lao et al. 2005]. This performs in a loop the magnetic equilibrium reconstruction, the fitting of the kinetic measurements in a $\psi(R, Z)$ map, runs a transport code (TRANSP [Hawryluk 1981], ONETWO [Owen et al. 2010]) to estimate the fast ions contribution to the total plasma pressure and density and finally performs equilibrium reconstruction with pressure constraints and current constraints from MSE measurements and neoclassical contribution. The loop is eventually repeated till convergence. This analysis process is mostly known with the name of "kinetic-EFIT". It allows to make a scan on unknown parameters and estimate the sensitivity of the obtained reconstructed quantities via Monte-Carlo sampling. The "kinetic-EFIT" [Huang et al. 2020] is very similar to the kinetic equilibrium reconstruction problem formulated in the previous chapter. The main difference is that the current density profile is directly constrained from measurements, since good quality MSE is available in DIII-D and most other tokamaks where this tool is used. The strength of OMFIT tool stands in its high flexibility which allows to easily couple different analysis codes and provides tools for I/O handling. Using the OMFIT environment, starting from Kinetic-Efit, KER has progressively been automatize resulting in the package CAKE [Roelofs et al. 2017], used to provide a database of KER for stability analysis.

The tool that will be presented in the following to perform kinetic equilibrium reconstruction in TCV is very similar to the "Kinetic-EFIT" one. The main difference is that, since no current profile diagnostics are available in TCV at present, a flux surface averaged current diffusion equation will be used to compute and provide that constraint.

5.2   Historical background of integrated data analysis in TCV

Among the motivation to perform a kinetic equilibrium reconstruction described in sec. 3.3.2 there were two specific needs for TCV before this thesis work started which were considered to impact significantly the reconstruction of the plasma states.

The first was the lack of direct measurements of current density profile in TCV. The second was the installation of a neutral beam [Fasoli et al. 2015], [Vallar et al. 2019]. The beam allowed to reach higher performance discharges were the internal plasma profiles features play a significant role for both the global performance of the experiment and the stability of the plasma.

In order to address these needs, a standard post discharge analysis, that we will call integrated data analysis in this section, was conducted by running in order the steps listed in the following where the name of the relative codes solving each individual problem is provided. The formulation of the forward problem solved for each of them was already explained in part I of this thesis.

1. LIUQE [Moret et al. 2015]: Free boundary Magnetic Equilibrium Reconstruction (MER)

problem as explained in sec.3.2, in particular eq. (3.9) under the linear optimization assumption described in sec. 3.2.1. The result is the $\psi(R, Z)$ map and all the related geometrical quantities.

2. ANAPROF (Container for a set of routines):

   - PROFFIT: Automatic mapping of the $\{\tilde{T}_e(R_i, Z_i)\}$, $\{\tilde{n}_e(R_i, Z_i)\}$ Thomson's scattering measurements [Arnichand et al. 2019] to the $\rho(R, Z)$ from LIUQE MER. Fitting of the resulting $\{\tilde{T}_e(\rho_i, t)\}$, $\{\tilde{n}_e(\rho_i, t)\}$ with a cubic spline representation to obtain 1D profiles.

   - CHIE_TCV: Computing $n_i(\rho, t)$ from $n_e(\rho, t)$ quasi-neutrality hypothesis given the Z_{eff} eq. (3.12). In case $T_i(\rho, t)$ is not solved with ion energy transport equation (option 2 eq. (2.64)), it estimates T_i by matching the W_{MHD} of MER from LIUQE. It also computes the heat diffusion coefficients from the experimental profiles of TCV to be used eventually for heat diffusion modeling.

   - ICDBSeval: Estimating $Z_{eff}(t)$ from current diffusion equation and stationary state assumption. Details are provided in Appendix B.

   - Toray-GA [Matsuda 1989]: Compute the current density j_{cd} and heat deposited into the plasma by gyrotron beams. It needs the electron density $n_e(\rho, t)$ and temperature $T_e(\rho, t)$ from PROFFIT, $Z_{eff}(t)$ from ICDBSeval and the flux map $\psi(R, Z)$ from LIUQE.

$$\text{ANAPROF}\begin{cases} T_e(\hat{\rho}, t) = Fit(\boldsymbol{T_e}, \psi(R, Z)) \\ n_e(\hat{\rho}, t) = Fit(\boldsymbol{n_e}, \psi(R, Z)) \end{cases}\Bigg\} \text{PROFFIT} \\ n_i(\rho) = n_e(\rho) \frac{Z_c - Z_{eff}}{Z_c - 1} \Big\} \text{CHIE\_TCV} \\ j_{cd}(\hat{\rho}, t) = \text{Toray}(T_e, n_e, \psi(R, Z)) \Big\} \text{Toray-GA} \\ I_{pl} = <V_{loop}>_t \Omega(Z_{eff}) + I_{ni}(Z_{eff}) \frac{\partial \psi}{\partial \hat{\rho}}\big|_{\hat{\rho}=0} = 0 \quad \text{in\_few\_}t^* \Big\} \text{ICDBSeval}$$

$$(5.1)$$

3. ASTRA [Pereverzev and Yushmanov 2002]: Generic 1.5D transport solver. In this thesis it is used to solve primarily the current diffusion equation eq. (2.56) to estimate $j_{\parallel}$. It is also used to solve the T_i heat diffusion equation particularly when neutral beam heating and current drive is used during the experiment. The current density and heat deposited by the beam are computed by internal dedicated routines [Polevoi et al. 1997], referenced as "Polevoi" in the following. In case the predictive T_i equation is solved, a diffusion coefficient χ_i is used based on neoclassical estimation with a correction factor tuned on CXRS data from TCV discharges when this diagnostic is available. This takes into account different transport level for L-mode and H-mode discharges. Otherwise T_i is provided externally. In the version of ASTRA code used in this work, two different fixed boundary eq. (2.23) equilibrium solvers are coupled to the 1D transport equations. The geometrical coefficients $g_{1,2,3}$ needed for 1D transport are

provided by the internal equilibrium solver which receives from the LIUQE magnetic equilibrium reconstruction (MER) the description of the plasma last closed flux surface. The internal plasma profiles to be used in the magnetic internal equilibrium solver are computed directly from the p and j coming from the transport equations. This means that the internal equilibrium solver already has a well constrained internal profile description from transport modelling and measurements. A summary of the equations solved by the code ASTRA is provided here for convenience. The inputs are, $\chi_i(\rho, t)$, j_{cd} from Toray-GA and the neutral beam contribution, n_e and T_e from Thomson PROFFIT, Z_{eff} from ICDBSeval, n_i from quasi-neutrality assumption, $I_p(t)$ and LCFS description from LIUQE magnetic equilibrium reconstruction.

$$
\text{ASTRA}\begin{cases}
\text{Fix boundary eq}: \psi(R,Z), g_2, g_3 \text{ From LIUQE LCFS} \left.\right\} \textcolor{red}{\text{3M/SPIDER}} \\[4pt]
\sigma_{\parallel}\left(\frac{\partial \psi}{\partial t} - \frac{\hat{\rho}\dot{\Phi}_B}{2\Phi_B}\frac{\partial \psi}{\partial \hat{\rho}}\right) = \frac{T^2}{16\pi^2\mu_0\Phi_B^2\hat{\rho}}\frac{\partial}{\partial \hat{\rho}}\left(\frac{g_2 g_3}{\hat{\rho}}\frac{\partial \psi}{\partial \hat{\rho}}\right) - \frac{B_0}{2\Phi_B\hat{\rho}}V'_{\hat{\rho}}(j_{bs}+j_{cd}+j_{NB,cd}) \\
\left(\frac{g_2}{4\pi^2\mu_0}\frac{1}{V'_{\hat{\rho}}}\frac{\partial \psi}{\partial \hat{\rho}}\right)\big|_{\hat{\rho}_B} = I_{pl}(t), \qquad \frac{\partial \psi}{\partial \hat{\rho}}\big|_{\hat{\rho}=0} = 0, \qquad \psi(\rho, t=0) = \psi_0
\end{cases} \left.\right\} \textcolor{red}{\text{CDE}}
$$

$$
\begin{cases}
\frac{3}{2}(V')^{-5/3}\left(\frac{\partial}{\partial t} - \frac{\dot{B}_0}{2B_0}\frac{\partial}{\partial \rho}\right)\left[(V')^{5/3}n_i T_i\right] + \frac{1}{V'}\frac{\partial}{\partial \rho}q_i = P_i \\
\frac{\partial T_i}{\partial \rho}\big|_{\hat{\rho}_A} = 0 \qquad T_i(\hat{\rho}_B) = 0
\end{cases} \left.\right\} \textcolor{red}{T_i}
$$

$$
j_{tor}(\hat{\rho}, t) = 2\pi R_0 \frac{1}{16\pi^3\mu_0\Phi_b}\frac{1}{V'_{\hat{\rho}}}\frac{\partial}{\partial \hat{\rho}}\left(T\frac{g_2 g_3}{\hat{\rho}}\frac{\partial \psi}{\partial \hat{\rho}}\right)
$$

$$
TT'(\hat{\rho}, t) = \frac{\mu_0}{g_3}\left(\frac{1}{R_0\pi}j_{tor} - p'\right)
$$

$$
p(\hat{\rho}, t) = n_e T_e + n_i T_i + \frac{p_{B,\parallel}+p_{B,\perp}}{2} + p_{fast}
$$

$$
\{p_{\parallel}, p_{\perp}, j_{NB,cd}\} = NU(\psi(R,Z), T_e, n_e, T_i) \left.\right\} \textcolor{red}{\textit{Polevoi}}
$$

(5.2)

The two codes used for the internal fixed boundary solver within ASTRA are the SPIDER [Ivanov A A and Yu 2006] code which solves the Grad-Shafranov equation and the so called "3 moments" (referred here as 3M) which solves a Fourier expansion in the poloidal direction of the Grad-Shafranov equation, and provides a simplified faster solution of the problem. We would like to anticipate at this point that the fact that ASTRA uses an internal fixed boundary equilibrium solver will limit the choice of which kinetic equilibrium reconstruction formulation we will implement in TCV and investigate in this chapter. This limitation could be however easily removed by providing the necessary geometrical information to the transport equations directly from LIUQE.

4. CHEASE [Lütjens et al. 1996]: Fixed boundary equilibrium code used to compute a more refined equilibrium solution as input to Toray-GA, taking the description of the LCFS and the internal plasma profiles from LIUQE.

5.2.1 Steps from historical integrated data analysis towards KER

In the previous section we described the set of available tools run sequentially, which constituted the standard post-shot analysis at the time of start of this work. We would like now to

make the link between the previous standard procedure and the formulation of the kinetic equilibrium reconstruction presented in sec. 3.3.2, and investigated in this chapter. More specifically we refer to the first reduced formulation derived in eq. (3.17), reported in eq. (5.3) for reading convenience which will be the one implemented and analyzed in the next section. We will then comment on the possibility of implementing the second reduced formulation eq. (3.19).

$$
\begin{cases}
\{\boldsymbol{I}_a, \boldsymbol{I}_v\} = (\mathbb{A}^T \mathbb{A})^{-1} \mathbb{A}^T \tilde{\boldsymbol{M}}_m \\
\Delta^* \psi = -4\pi^2 \left(\mu_0 R^2 p' + T T' \right)
\end{cases} \text{LIUQE} \\[2ex]
\left. \begin{array}{l}
\{T_e(\rho, t), n_e(\rho, t)\} = (\mathbb{B}^T \mathbb{B})^{-1} \mathbb{B}^T \tilde{\boldsymbol{M}}_k \ \text{PROFFIT} \\
Z_{eff} = \text{ICDBSEVAL} \\
n_i(\rho) = n_e(\rho) \frac{Z_c - Z_{eff}}{Z_c - 1} \ \text{chie\_tcv\_to\_nodes} \\
j_{cd} = j_{cd}(\psi(R, Z), n_e(\rho, t), T_e(\rho, t)) \ \text{TORAY}
\end{array} \right\} \text{ANAPROF} \\[2ex]
\left. \begin{array}{l}
\{g_1, g_2\} = \text{SPIDER/3M from LIUQE LCFS)} \\
\{p_{fast}, p_\parallel, p_\perp\} = \text{NUBEAM} \\
\frac{3}{2}(V')^{-5/3} \left(\frac{\partial}{\partial t} - \frac{\dot{B}_0}{2B_0} \frac{\partial}{\partial \rho} \right) \left[(V')^{5/3} n_i T_i \right] + \frac{1}{V'} \frac{\partial}{\partial \rho} q_i = P_i \\
q_i(\rho) = -V' G_1 n_i \chi_i \left[1 + 2 \left(\frac{\rho}{\rho_B} \right)^2 \right] \frac{\partial T_i}{\partial \rho} \\
p(\hat{\rho}, t) = n_e T_e + n_i T_i + \frac{p_{B,\parallel} + p_{B,\perp}}{2} + p_{fast} \\
\sigma_\parallel \left(\frac{\partial \psi}{\partial t} - \frac{\hat{\rho} \dot{\Phi}_B}{2\Phi_B} \frac{\partial \psi}{\partial \hat{\rho}} \right) = \frac{T^2}{16\pi^2 \mu_0 \Phi_B^2 \hat{\rho}} \frac{\partial}{\partial \hat{\rho}} \left(\frac{g_2 g_3}{\hat{\rho}} \frac{\partial \psi}{\partial \hat{\rho}} \right) - \frac{B_0}{2\Phi_B \hat{\rho}} V'_{\hat{\rho}} (j_{bs} + j_{cd}) \\
j_{tor}(\hat{\rho}, t) = 2\pi R_0 \frac{1}{16\pi^3 \mu_0 \Phi_b} \frac{1}{V'_{\hat{\rho}}} \frac{\partial}{\partial \hat{\rho}} \left(T \frac{g_2 g_3}{\hat{\rho}} \frac{\partial \psi}{\partial \hat{\rho}} \right) \\
T T'(\hat{\rho}, t) = \frac{\mu_0}{g_3} \left(\frac{1}{R_0 \pi} j_{tor} - p' \right)
\end{array} \right\} \text{ASTRA}
\end{cases} \tag{5.3}
$$

In eq. (5.3) we dropped the boundary conditions for readability. We also recall that the set of measurements are composed by $\tilde{\boldsymbol{M}}_{\boldsymbol{m}} = \{\tilde{\boldsymbol{B}}_m, \tilde{\boldsymbol{F}}_f, \tilde{I}_p, \tilde{\Phi}_t, \tilde{\boldsymbol{I}}_v, \tilde{\boldsymbol{I}}_a\}$ and $\tilde{\boldsymbol{M}}_{\boldsymbol{k}} = \{\tilde{\boldsymbol{T}}_e, \tilde{\boldsymbol{n}}_e\}$, with $\tilde{\boldsymbol{T}}_i$ including available.

Comparing the equations of each code independently used in the standard post discharge analysis (eq. (2), eq. (5.2)) to the formulation of KER in eq. (3.17), eq. (5.3) one can notice that the tools to solve every sub-part of the problem were already available before this thesis. In eq. (5.3) we labeled every part of the problem with the code dedicated to solve it.

What was missing in the standard post processing analysis was to feedback the plasma profiles p' and $T T'$, obtained with the kinetic measurements and transport modelling in ANAPROF and ASTRA, to compute a new equilibrium reconstruction with constraints on the internal profiles, and finally re-use this new equilibrium solution in the measurements fitting and the transport modelling. In other words what was missing was to consider the system of equations in eq. (5.3) as a "proper system of equations", meaning trivially that a solution of the system requires that a given quantity appearing in different places of the system must have the same value. This could be called also consistency between the different codes or self-consistency of the kinetic equilibrium reconstruction problem in eq. (5.3). It is important to repeat that the

ASTRA internal fixed boundary equilibrium solver (SPIDER/3M) is already computed with essentially self-consistent profiles of p and j_{tor}, or equivalently p' and TT', coming from the kinetic measurements n_e, T_e, the transport modelling for T_i and j_{tor} from the current diffusion equation within ASTRA, except for the remapping of the diagnostics on the new equilibrium. It only receives the description of the LCFS information from the free boundary equilibrium code LIUQE.

We will see in the result section 5.4 that solution of eq. (5.3) will produce a LCFS almost identical to the one obtained with the magnetic equilibrium reconstruction, at least for TCV case. Hence solving the eq. (5.3) mainly means making LIUQE to match the SPIDER solution of the equilibrium equation inside the plasma volume and use this solution in ANAPROF to map the kinetic measurements into 1D profiles and compute the current deposited by the ECCD. This enables the next step which was also missing, to analyze if the diagnostics and models are consistent, that is integrated data analysis.

We would like now to comment on the possibility to implement the 2nd reduced formulation presented in eq. (3.19) which aimed to restore some of the non-linear relations between the equilibrium problem and kinetic modelling neglected when passing from the general formulation of KER eq. (3.14) to the simplified one eq. (5.3) described previously in this section and implemented in the following. The main difference between the first reduced formulation eq. (3.14) and the second, eq. (3.19), is to extend the set of free parameters in the equilibrium reconstruction problem to include $p'(\rho)$ and $TT'(\rho)$. Moreover, the estimate of $\tilde{p}'(\rho)$ and $\tilde{T}T'(\rho)$ provided by the kinetic measurements and transport modeling, affected by the uncertainties coming from the uncertainties of the inputs to the transport modelling, are added as extra measurements to the equilibrium reconstruction problem at the same level as the magnetic measurements. To implement eq. (3.19) from the available tools one would first require that the equilibrium reconstruction code includes $\tilde{p}'(\rho)$ and $\tilde{T}T'(\rho)$ as extra measurements, which is a trivial extension for the actual state of the code. The second requirement could be considered as an issue to the present I/O handling of the version of ASTRA code used in this thesis. The geometrical coefficients $g_{1,2,3}, T, \Phi_b$. are computed inside ASTRA by the fixed boundary equilibrium code (SPIDER/3M). In order to solve the fixed boundary equilibrium problem one needs the description of the LCFS and the definition of the functional form $p'(\rho)$ and $TT'(\rho)$. In ASTRA these last two profiles are provided self-consistently from $p(\rho)$ and $j_{tor}(\rho)$ computed from current diffusion equation and transport modelling. We can consider therefore formally that all the quantities computed from the equilibrium problem needed in the transport modelling are non-linear functions of $p'(\rho)$, $TT'(\rho)$ and the set of pair of coordinates $\{R_i, Z_i\}_{LCFS}$ describing the plasma boundary. Hence for example $g_2(p'(\rho), TT'(\rho), \{R_i, Z_i\}_{LCFS})$. Let us assume one would like to use ASTRA and SPIDER/3M, together with the other codes, to solve eq. (3.19). The description of the LCFS would be provided by LIUQE, which solves the equilibrium reconstruction problem with $p'(\rho)$ and $TT'(\rho)$ coming from the equilibrium reconstruction optimization problem. However SPIDER/3M would solve the fixed boundary problem with $\tilde{p}'(\rho)$ and $\tilde{T}T'(\rho)$ profiles and not $p'(\rho)$ and $TT'(\rho)$. This would mean that all the geometrical related quantities in ASTRA would not be consistent with the ones of LIUQE.

This violates the basic requirement for the solution to be a solution of the system of equation eq. (3.19), meaning the same quantity appearing in different places of the system must have the same value. For example $g_2(p'(\rho), TT'(\rho), \{R_i, Z_i\}_{LCFS}) \neq g_2(\tilde{p}'(\rho), \tilde{T}T'(\rho), \{R_i, Z_i\}_{LCFS})$. Indeed, we would effectively have in the system of equation two times the same equation, the Grad-Shafranov equation, with two slightly different solutions.

We would like to stress that the issue for the non-consistency of the geometrical quantities within the same system of equation does not apply to the difference between p', TT' and $\tilde{p}', \tilde{T}T'$. We already discussed during the formulation of eq. (3.19) the different meaning of these 2 quantities. In short, $\tilde{p}', \tilde{T}T'$ are estimates affected by the uncertainties of the inputs of the kinetic measurements, while p', TT' are the reconstructed states solution of the KER problem.

In order to be able to use ASTRA to solve eq. (3.19) one would therefore need to remove the internal fixed boundary equilibrium solved and provide the geometrical information directly from LIUQE, or use the LIUQE p', TT' in SPIDER/3M. This was not attempted during this work for the off-line kinetic equilibrium reconstruction.

5.3 Implementation details

In this section we would like to explain the approach adopted during this thesis to solve the kinetic equilibrium reconstruction problem as formulated in eq. (5.3).

In the previous sections we discussed extensively the formulation of the problem with its simplification assumptions (sec. 3.3.4) and provided the list of codes available in our institution to solve sub-parts of the problem (sec. 5.2). What we obtained is a non-linear root-finding type of problem eq. (5.3). Having already dedicated codes to solve sub-parts of the problem, the most straightforward numerical scheme to implement is a Picard fixed point iteration method [Hoffman and Frankel 2018]. This means solving recursively each sub-part of the problem providing the I/O and checking the convergence from one iteration to the next. To help the numerical convergence successive over-relaxation (SOR [Hadjidimos 2000]) is used between iterations.

To help visualizing the algorithm we provide a schematic picture of the loop in fig. 5.1. Moreover in table 5.1 a summary of some of the main inputs and outputs of the different codes is given, distinguishing in particular the quantities that are iterated between codes (labeled "iterated") to the ones which are provided as input only once (labeled "fixed"). The color in the second column of the input is related to the code that compute and provide the output to the other module. Interfacing heterogeneous codes requires flexibility in checking the results of the sub-parts, detect faults and provide recovery strategies. To obtain this flexibility the decision was to exploit Object Oriented programming with Matlab. For each of the codes, at each iteration, a dedicated object is specified, called "runner". Each "runner" once initialized is completely independent of the others and in particular provides methods to run the code,
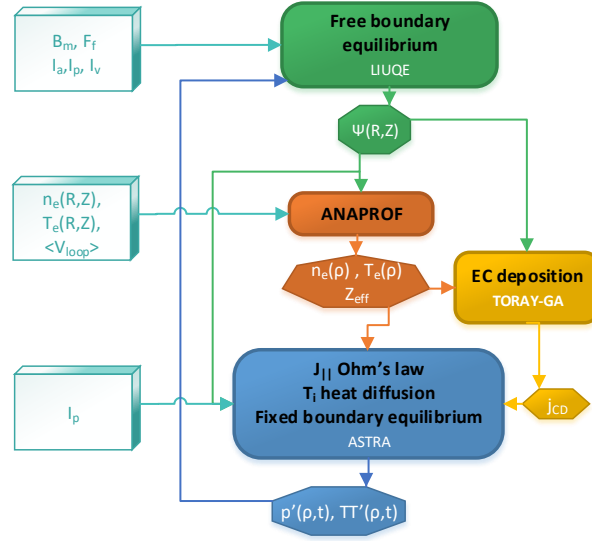
Figure 5.1 – Kinetic Equilibrium Reconstruction implementation: fixed point iteration scheme. All the quantities have to be considered as function of time.

check the results and take actions in case of failure. Incrementally more checks and recovery actions can be implemented by the users and developer. Moreover this strategy allows to easily change the order of the loop chain for example avoiding to recompute some of the sub-modules when computationally expensive and not very sensitive to small inputs variation.

5.4 Analysis of results

In this section we will discuss the analysis performed with the implemented kinetic equilibrium reconstruction in TCV described in sec. 5. We will first investigate the sensitivity of the equilibrium solution to the plasma profiles, by taking an existing database of previous integrated data analysis performed for TCV discharges. After having checked the numerical properties of the scheme, we will investigate a comparison between KER and MER for two shots where the internal profile features are expected to contribute significantly to the equilibrium solution.

5.4.1 Sensitivity analysis of MER to plasma profiles for TCV

One of the main reasons to move from magnetic equilibrium reconstruction to kinetic equilibrium reconstruction was to improve the equilibrium solution by providing constraints in particular to the pressure profile $p(\rho, t)$ and current density profile $j(\rho, t)$, which are reflected in $p'(\rho, t)$ and $TT'(\rho, t)$ constraints, making use of kinetic measurements and transport modelling. In this section we want to quantify the sensitivity of the magnetic equilibrium reconstruction when these profiles are provided as constraints.

Table 5.1 – I/O for Kinetic Equilibrium' Reconstruction

Measurements	$\tilde{\boldsymbol{B}}_m\ \tilde{\boldsymbol{F}}_f\ \tilde{\boldsymbol{I}}_a\ \tilde{\boldsymbol{I}}_v$ $\tilde{I}_p\ \tilde{\boldsymbol{n}}_e\ \tilde{\boldsymbol{T}}_e < V_{loop} >_t$	
	INPUTS	
LIUQE	fixed	$\tilde{\boldsymbol{B}}_M\ \tilde{\boldsymbol{F}}_f\ \tilde{\boldsymbol{I}}_a\ \tilde{\boldsymbol{I}}_v\ \tilde{I}_p$
	iterated	$p'\ TT'$
ANAPROF	fixed	$\tilde{\boldsymbol{n}}_e\ \tilde{\boldsymbol{T}}_e < V_{loop} >_t$
	iterated	$\psi(R,Z)\ V'_\rho$
ASTRA	fixed	$\tilde{I}_p$
	iterated	$N_e(\rho)\ T_e(\rho)\ Z_{eff}$ LCFS description

In TCV, the magnetic equilibrium reconstruction is performed for all the shots as a standard post-discharge analysis with LIUQE. This is true also for the Thomson scattering profile fitting and current deposition evaluation performed by ANAPROF. Moreover a database of solutions of the ASTRA transport code is available and constantly increasing and it is composed currently of roughly 600 discharges with different physics content and heating and current drive mix.

It is therefore relevant to investigate the sensitivity of the equilibrium solution performed by LIUQE with respect to the p' and TT' profiles when these are provided from ASTRA interpretative solutions in the database. This is indeed one of the steps in the iteration loop to solve eq. (5.3). The analysis performed in this section corresponds to the first iteration of the loop to solve eq. (5.3) when no relaxation is applied and p' and TT' are directly fed to LIUQE from ASTRA.

It is important to recall that there is a significant difference between the equilibrium reconstruction problem in MER eq. (3.9) and the equilibrium reconstruction problem in KER eq. (5.3). In the first, together with $\boldsymbol{I}_a$ and $\boldsymbol{I}_v$, the set of parameters which are allowed to vary includes also the coefficients of the basis functions for the p' and TT' representation. The basis functions set, a polynomial representation, is very limited in MER to keep the problem well conditioned, and the choice of these basis functions ultimately decide the functional form of the internal plasma profiles. In KER p' and TT' are imposed and considered instead as part of the "given" parameters for the equilibrium problem. Because of this choice and the simplification hypothesis that led to a linear optimization formulation of the problem, the measurement of Φ_t cannot be included in the equilibrium reconstruction problem in KER, since it has a null linear variation on the only remaining free parameters $\boldsymbol{I}_a$ and $\boldsymbol{I}_v$. Moreover, Φ_t is crucial in MER to disentangle the contribution of p' and TT' to the j_ϕ since it depends only on T, hence on one of the two. The final estimate of p and related quantities such as W_k are therefore strongly affected by this measurement in MER. In the kinetic equilibrium reconstruction presented, the separation between p' and TT' is instead provided by the kinetic measurements and transport modeling, hence making the DML measurement less

fundamental for the analysis. However, this means relying more on the transport modelling and kinetic measurements which might not be accurate either.

We anticipate here that performing the full converged KER iteration with this particular formulation eq. (5.3) for typical TCV discharges gives only a small difference to the poloidal flux distribution. In particular no significant differences are found in the LCFS which is the only input from LIUQE to ASTRA internal equilibrium solver (tab. 5.1). This will be demonstrated in the following. This means that the solution of the internal ASTRA equilibrium solver, where the profiles are not taken from LIUQE, will remain almost unchanged. As a consequence, performing a full converged KER almost reduces to make LIUQE matching the equilibrium solution of the ASTRA internal equilibrium solver. Therefore, performing the analysis proposed, meaning imposing the p' and TT' directly from ASTRA in LIUQE, gives meaningful indication of what the result would be of a full converged KER with specific formulation used in this chapter.

The following statistical analysis is computed on a basis of 1000 independent time-slices sorted randomly from 100 different discharges with different physical performances out of the 500 available in the ASTRA database. We chose to not considered the first 200 discharges in the database because related to old experiments during which TCV was in a different state and hence not relevant for this investigation.

Since the main purpose is to provide physical constraints on $p(\rho, t)$ and $j(\rho, t)$ we will focus first on investigating quantities closely related to these profiles. In fig. 5.2 we compare the total stored energy, $W_k = 3/2 \int p \, dV$, computed from the standard MER $W_{k,MER}$ and computed with LIUQE as in eq. (5.3) where the p' and TT' are taken from ASTRA $W_{k,L-ASTRA}$. We considered in fig. 5.2 only cases when the $T_i(\rho, t)$ was computed by solving the transport equation eq. (2.64) within ASTRA, which corresponds to case 2. It is interesting to notice that there is a non-negligible difference between the two W_k estimates: the MER is on average 13% larger than the one estimated using ASTRA. The transport equation which solves for T_i in ASTRA, hence relying on the given parameter χ_i, is essentially systematically underestimating the total stored energy with respect to the MER in the available database. On top of that, a relatively large standard deviation of 30% is found, although standard in transport analyses. One cannot state a priori which of the two estimates is more correct, but the analysis gives a warning that the choice of χ_i might lead to pressure profiles not consistent with the magnetic measurements. This will be one of the issue for the KER formulation adopted as already explained.

We focus in fig.5.3 on quantities related to the j profiles which are constrained by the current density diffusion equation. In fig. 5.3a we compare the minimum value reached by the safety factor profile q_{min} reconstructed with the standard MER performed with LIUQE (blue) and the one obtained by using the ASTRA profiles (orange). We notice that the ASTRA profiles produce on average a minimum value of the safety factor below 0.8, a condition that it is physically hardly reached because of the onset of the sawtooth like instability, which relaxes
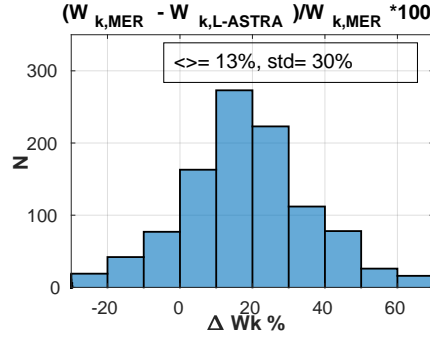
Figure 5.2 – Statistical investigation of percentage different between total stored energy compute with standard MER $W_{k,MER}$ and equilibrium reconstruction imposing p' and TT' from ASTRA modelling and kinetic measurements $W_{k,L-ASTRA}$. Only the case where ASTRA is solving the diffusion equation for T_i are considered.

the current profile, and brings periodically q_A above 1. To describe this phenomenon a model for the sawtooth physics should be included in the forward models [Kadomtsev 1987] used and this requires a finer temporal resolution. This model is available in ASTRA and we will show an application later in this section. In fig. 5.3b the percentage difference of the internal inductance between the two reconstructions is compared. In summary, most of the Ohmic plasma discharges in TCV, which constitute the majority of the database, present a peaked current at the plasma axis leading to sawtooth behavior hence when precise reconstruction of the q profile up to the plasma axis is sought, the dedicated physics should be included in the analysis, at least on average, to avoid for unrealistic $q_A < 0.8$ eventually synchronizing the crashes with the information from fast diagnostics.

A good localization of the $\rho_{\hat{\psi}}$ and $\rho_{\hat{\Phi}}$ at the $q = 1.5/2$ location is important to target the deposition location of $ECCD$ during suppression and prevention of 2/1 and 3/2 NTMs. With this purpose we compare in fig. 5.3c and fig. 5.3d the absolute value of the difference of this location between the standard MER and the equilibrium solution using ASTRA profiles $\delta\rho_{\hat{\Phi}}$ or $\delta\rho_{\hat{\psi}}$. The average difference of $\rho \sim 0.1/0.2$ is of the same order as the current density deposition by ECCD. To show this in fig. 5.4a,5.4b,5.4c we compare the q profile of MER (red) to the LIUQE solution with the p' and TT' profiles of ASTRA (blue), for cases where off-axis current drive at the $q = 1.5$ surface was applied. The current density deposited by the ECCD is computed by Toray-GA (yellow) and an interpolated Gaussian normalized in order to have the same height as the maximum q is shown in violet. We consider the full width at half maximum of the interpolated Gaussian (2.35σ) as a measure of the width called w_{dep} in the figures. With the green and light blue vertical dashed lines we show the location of the $q = 1.5$ surface for the recomputed LIUQE with ASTRA profiles and the standard MER respectively. The absolute value of this difference, corresponding to what is computed in fig. 5.3c, is called in the figures $|\Delta\rho|$. The deposition width at a given q can vary substantially, on a typical range of $0.02 - 0.15$, depending on many factors such as the injection angle of the gyrotron and the local density of the plasma. This is clear looking at fig. 5.4a with respect to fig. 5.4c. In all cases the difference in ρ is of the same order as the width. For instance in fig. 5.4b, even
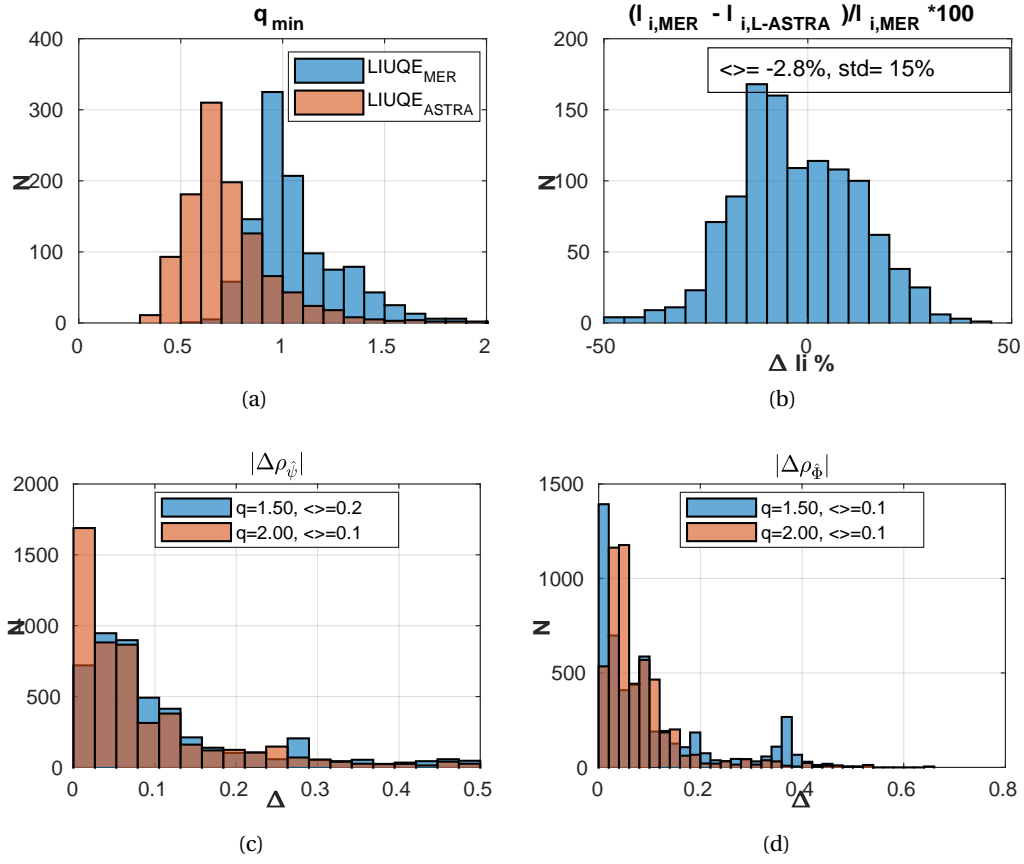
Figure 5.3 – Difference between j related quantities between MER and equilibrium reconstruction imposing p' and TT' from transport modelling and kinetic measurements from ASTRA.

thought the two q have the same value at the plasma axis and at q_{95}, and the gyrotron was aiming to the $\rho(q = 1.5)$ as computed by the MER the location of this surface provided by the current diffusion model in ASTRA was completely outside the deposition width of the gyrotrons. This means that, if the profile from ASTRA was the real one, aiming the beam based on the MER would have failed in stabilizing the NTM, since it needs to be within half the deposition width [Kong et al. 2019]. Moreover cases of non-monotonic q profile, such as in fig. 5.4c, cannot be reconstructed by MER with the standard set of basis functions. In summary, the reconstruction of the location of $\rho(q = 1.5)$ and $\rho(q = 2)$ can change significantly, with respect to the width of the deposition of the gyrotrons current density, when passing from the MER to a profile constrained by kinetic measurements and current diffusion modelling. The question is therefore whether the kinetic measurements and current diffusion modelling can reach a level of accuracy on the order of fraction of w_{dep}. Unfortunately with the present set of diagnostics and modelling, the uncertainties associated to a poor knowledge of Z_{eff} and T_i can provide variation of q of the same order of w_{dep} as shown also in Lucas Marietan's master thesis [Marietan]. This will be even worse in real-time KER presented in the next chapter where a limited set of diagnostic is available. Performing KER therefore will be good in general to recover more macroscopic features such as non monotonic q profiles or local features of the plasma current density like the bootstrap contribution, but would fail in providing q profiles with accuracy of fraction of w_{dep} as it would be needed for NTM control in real-time. Probably in TCV only with a dedicated diagnostic for the current density profile and a proper uncertainty analysis one could achieve information to that level of precision. On the other hand the MER has no physical constraints for the q profile and is not sufficient when the q profile is important.

After having considered the sensitivity of the quantities directly related to p and j profiles in the equilibrium, we would like to address now the differences to the shape of the plasma in particular the LCFS which is the only geometrical input provided in the KER formulation addressed in this chapter eq. (5.3) from LIUQE to the transport modelling. In fig. 5.5a we compare the percentage variation of the minor radius between the LIUQE solutions with standard basis functions and with imposed profiles, at the mid plasma height. In fig. 5.5b we compare the percentage difference of plasma elongation κ. In fig. 5.5c we compare the percentage difference of the triangularity. For the definition of these quantities we refer to [Sauter and Medvedev 2013]. The percentage difference of all these plasma shape moments are significantly below 10%. From the database analysis also the plasma volume was found to have a variation < 10%. We remind that for typical TCV plasma triangularity can be ∼ 0, hence the standard deviation of the percentage difference of this quantities, which is still < 10% but larger than the other geometrical quantities could be enhanced by that.

From the previous investigation we conclude that, since the plasma shape is not much influenced by the internal plasma profiles when they are provided by ASTRA results, the main part of performing KER as formulated in eq. (5.3) will consist in making LIUQE solution consistent with the internal solver of ASTRA, meaning in particular having the same internal profiles. This also allows other diagnostics to be mapped on an equilibrium consistent with the kinetic
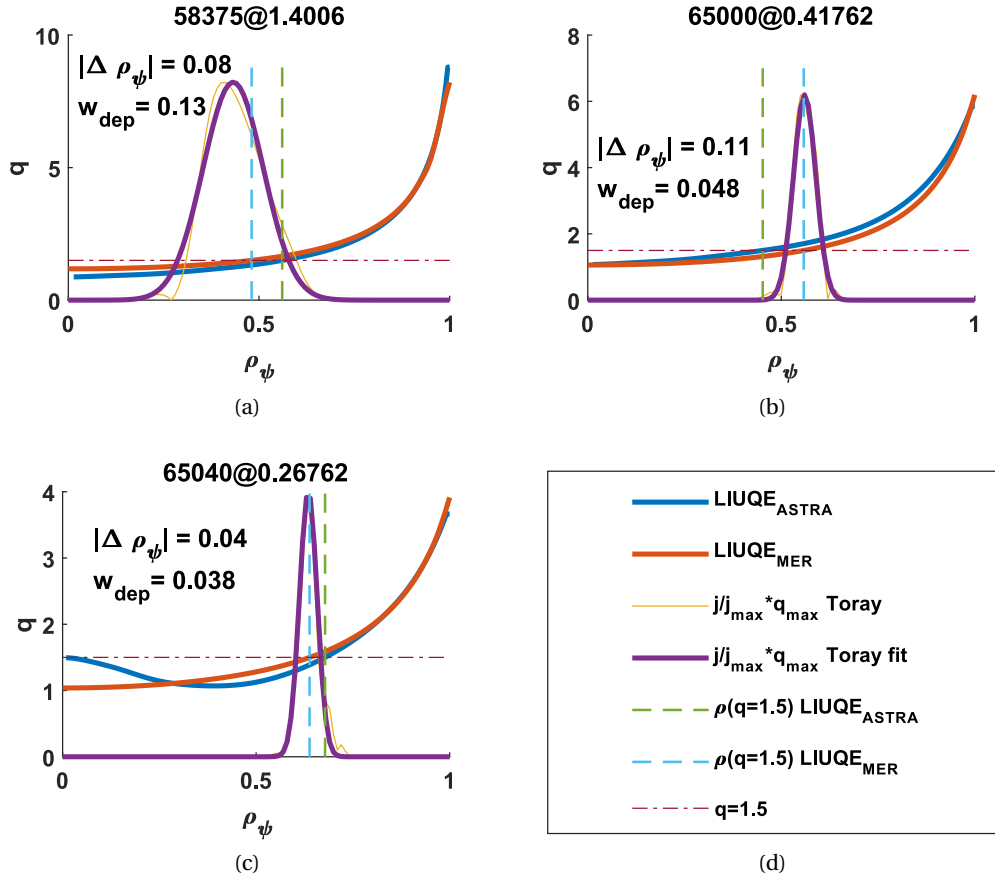
Figure 5.4 – Comparison between ECCD deposition profile (yellow original Toray-GA evaluation, violet Gaussian interpolation) and location of $q = 1.5$ surface computed with LIUQE with standard polynomial basis functions ("LIUQE$_{MER}$" vertical dashed light blue line) and LIUQE with p' and TT' profiles from ASTRA ("LIUQE$_{ASTRA}$" vertical dashed green line). The difference of the location between "LIUQE$_{MER}$" and "LIUQE$_{ASTRA}$" is called $\delta\rho_\psi$. Deposition width w_{dep} is computed as the full width at half maximum of interpolated Gaussian (violet).

(a)

(b)

(c)
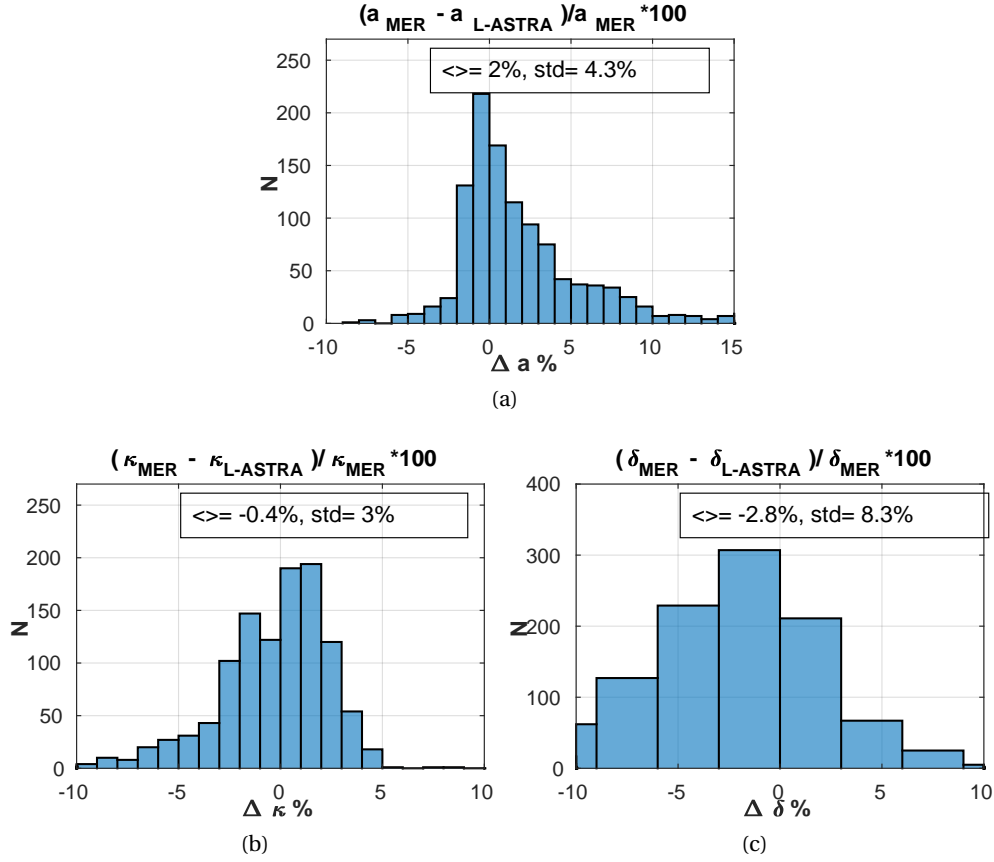
Figure 5.5 – Statistical investigation of differences for LCFS shape parameters (minor radius a, elongation κ, triangularity δ) LIUQE with standard polynomial basis functions ("MER") and with LIUQE with p' and TT' from ASTRA ("L-ASTRA") over the set of ASTRA databases

measurements, which is a necessary condition for integrated data analyses. Moreover the analysis provided in this chapter on the available database of ASTRA run provides meaningful information on the expected sensitivity of the full KER.

We can now summarize our findings from the database of TCV ASTRA runs.

- A systematic difference on the total stored energy W_k warns about consistency between parameters choice for the T_i modelling and magnetic measurements in integrated data analysis performed in TCV so far. This is also one of the expected issues of the formulation of KER adopted as a consequence of breaking non-linearities between the magnetic and kinetic part of the reconstruction. It confirms the need to perform systematic integrated data analysis and compare various diagnostics and modeling results in a same framework.

- The need to add in the forward modelling the models to describe sawteeth crash when present in the discharge for accurate reconstruction of q near the axis.

- The impact on the localization of the $\rho(q = 1.5)$ and $\rho(q = 2)$, important for NTM

stabilization, can be of the same order as the ECCD deposition width or even larger. However, the accuracy of the current density modelling to resolve fraction of w_{dep} is a concern due to uncertainty associated with other quantities such as Z_{eff} and T_i.

- The impact on the shape of the LCFS will be very small. It is well known that the external shape of the plasma is well identified already with the MER, as was shown also for the ITER cases in previous chapter.

We would like to remark that the results discussed here are valid only for TCV standard scenarios. Internal profile features, which are at the basis of some of the advanced tokamak operating modes were not present in the database as they are more difficult to obtain experimentally [Piron et al. 2019] and out of the scope of this thesis. Therefore, most part of the plasma discharges analyzed in the presented database are low performances discharges. Thus the statistical comparison performed here is biased by this fact. We will therefore now investigate the difference between MER and KER for cases where more significant internal plasma profile features are present due to either external actuators or plasma physics features. Performing the database analysis was nevertheless instructive to provide the expected order of magnitude of differences passing from MER to KER.

5.4.2   KER vs MER comparison in TCV

In this section we will compare the Magnetic Equilibrium Reconstruction to the Kinetic Equilibrium reconstruction for a TCV H-mode and a reversed shear case. These are representative of some of the most extreme cases of physical interest, in terms of internal plasma profile features, achieved in TCV as opposed to the low performance discharges mostly seen in the database of the previous section.

We will consider shot 64770 and adopt the simplified formulation eq. (3.17), where the p' and TT' are fed directly from the kinetic measurements and transport modelling to the equilibrium reconstruction. In particular Z_{eff} is estimated with the stationary state option for the current diffusion described in B. $T_i(\rho, t)$ is computed by solving the diffusion equation eq. (2.64). The shot was characterized by electron cyclotron heating but no current drive. There was instead heating and current drive from neutral beam injection. The fast particle contribution to the total pressure is estimated as in [Polevoi et al. 1997] within ASTRA. The simulation was carried out in the interval $t = [1.15s, 1.5s]$ during ELMy H-mode phase.

When performing Kinetic Equilibrium Reconstruction the first step is assessing the numerical convergence of the Picard iteration scheme summarized in 5.1. We usually add a small sub-relaxation between iterations for the different I/O listed in 5.1 provided between codes. For each run we analyze the convergence at different levels of the loop. However, since we are mostly interested in the effect of the equilibrium solution, we present here only the convergence of the flux map and of profiles input to LIUQE. In fig. 5.6b we show the convergence of the flux map $\psi(R, Z)$ computing the sum over all times of the two norm in space of the incre-
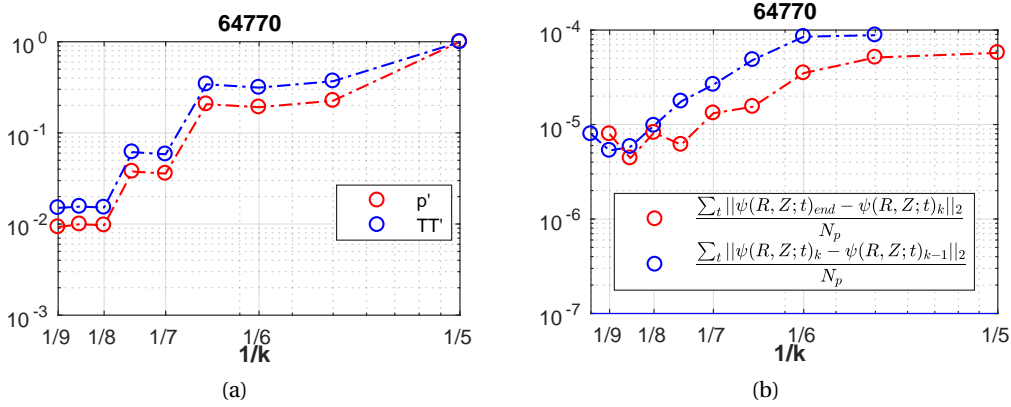
Figure 5.6 – Converge of Picard iterations in KER implementation

ment between iterations (blue) and the difference between given iteration and last iteration (red), normalized to the number of iterations. After few iterations, the flux map is converged to its minimum considering the spatial and temporal resolution of the simulation. From other investigation we found that already after one iteration with low relaxation the flux map of the equilibrium was close to the converged solution. In fig. 5.6a the same analysis is carried out for the sum over all times of the two norm over the ρ grid of the $p'(\rho, t)$ and $TT'(\rho, t)$ provided as inputs to the equilibrium reconstruction code.

We focus on the time instant 1.4s, during the ELMy H-mode phase. In fig. 5.7a with the red dots and error-bars the Thomson data for T_e are provided while with the continuous line, one can see the spline fit performed by PROFFIT routine. Similarly in fig. 5.7b the n_e and n_i are shown. In particular we stress the presence of the pedestal feature in the profile typical to H-mode discharges. In larger tokamaks these feature might be relatively more prominent. With the blue line the estimation of T_i from the diffusion equation is provided remembering that the fast particle from the beam provides the source term for the ion energy transport equation.

The $Z_{eff}(t = 1.4s) = 1.6$ was estimated with ICDBSEVAL routine. We recall that Z_{eff} contributes to different parts of the transport modelling. It is used to estimate n_i with the quasi-neutrality assumption eq. (3.12) but enters also in the current diffusion equation to estimate the neoclassical conductivity and the non-inductive contribution. Affecting n_i, it also affects the T_i diffusion equation in its energy flux term $n_i T_i$. It also affects the computation of the deposited power by the neutral beam. Overall therefore it contributes to both the p' and TT'.

In fig. 5.8b the resulting total pressure profile is shown. The functional form of MER profile (blue) is given by the choice of basis functions adopted for p'. A usual choice for TCV is a linear term in ψ_N, hence quadratic in ρ_{ψ_N} shown in fig. 5.8c (blue). The obtained profile computed with eq. (3.11) is shown in green taking into account also the contribution of the fast ions pressure (violet). In the same fig. 5.8b we show also the pressure profile resulting from equilibrium reconstruction part of KER computed by LIUQE at convergence of the iteration
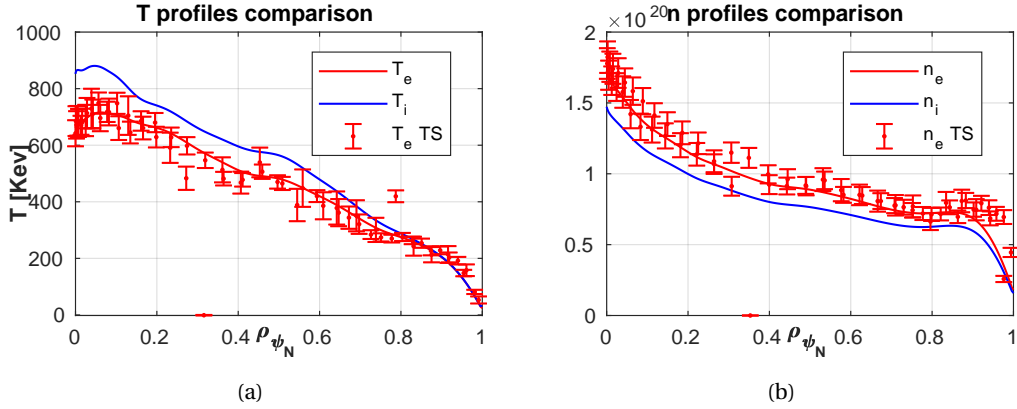
Figure 5.7 – Comparison of kinetic profiles shot 64770 at $1.4s$. Thomson scattering T_e, n_e measurements (red dot with error bars, "TS") and interpolation of Thomson scattering data (red line), n_i computed from quasi-neutrality given $Z_{eff} = 1.6$ and T_i from the heat diffusion equation.

loop (red dots label with KER) which matches the ASTRA one as expected. We remark that the violet line is only the contribution of the fast ions from the beam to the total pressure while the part of the fast ions which thermalized provided their contribution to the source of the energy diffusion equation for the ion. We can notice also in the pressure profiles the small pedestal feature which is indeed the improved information that KER provides with respect to MER thanks ultimately to including the Thomson scattering measurements.

The other contribution in KER is the improvements in the reconstruction of the plasma current density profile, in particular for TCV where no direct measurements are available. The $j_\parallel$ current density profile resulting from ASTRA modelling is shown in fig. 5.8e. In blue the current density profile for the MER is shown computed with eq. (2.40). We stress that its functional form is strongly affected by the choice of basis function for p' and TT'. In the same figure we see in green the profile obtained by the current diffusion modeling with ASTRA composed by the Ohmic component (violet), the bootstrap component (light green) and the current drive by the neutral beam in yellow. We notice that the current drive from the beam provides a very small contribution while instead the bootstrap (light green) contribution has a larger influence. The bootstrap contribution in particular presents features coming from the dependency of the neo-classical coefficients to the n_e and $T_e(\rho)$ measured by Thomson. We notice in particular the contribution of the bootstrap current due to the pedestal feature typical of H-mode discharges. This would be even larger before en ELM-crash, but it is out of the scope of the present study. With the red-line we show the $j_\parallel$ profile resulting from the equilibrium reconstruction at convergence of the KER loop.

From p and $j_\parallel$, p' and TT' can be computed. In fig. 5.8c and 5.8d we show the original profiles of the MER (blue), the profiles obtained from the kinetic measurements and the transport modelling (green) and the profiles used in the equilibrium reconstruction at convergence of the iteration loop (red).
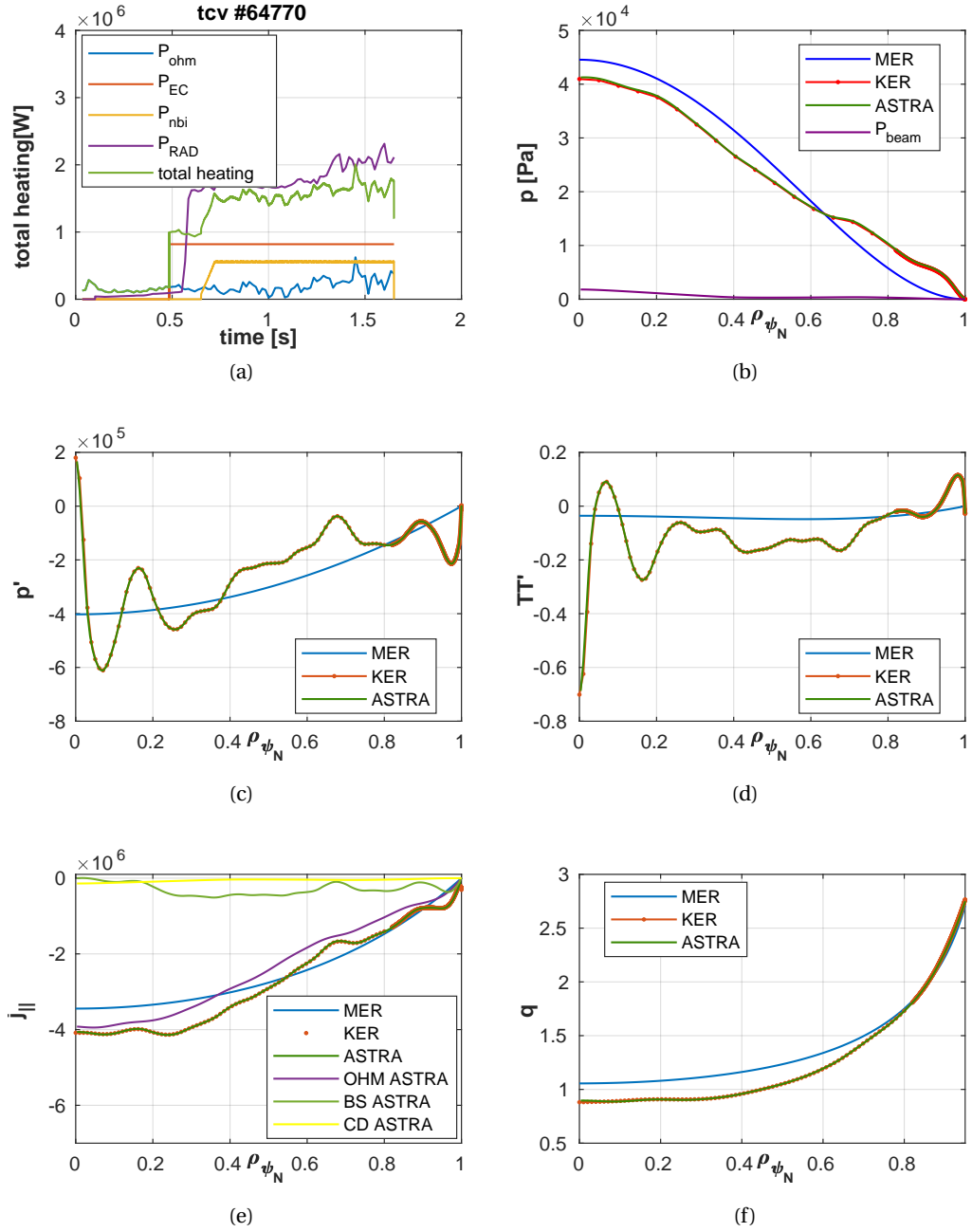
(a)

(b)

(c)

(d)

(e)

(f)

Figure 5.8 – Comparison of several kinetic profiles between MER, KER and ASTRA 64770@1.4s

(a) 64770 at 1.4s H-mode

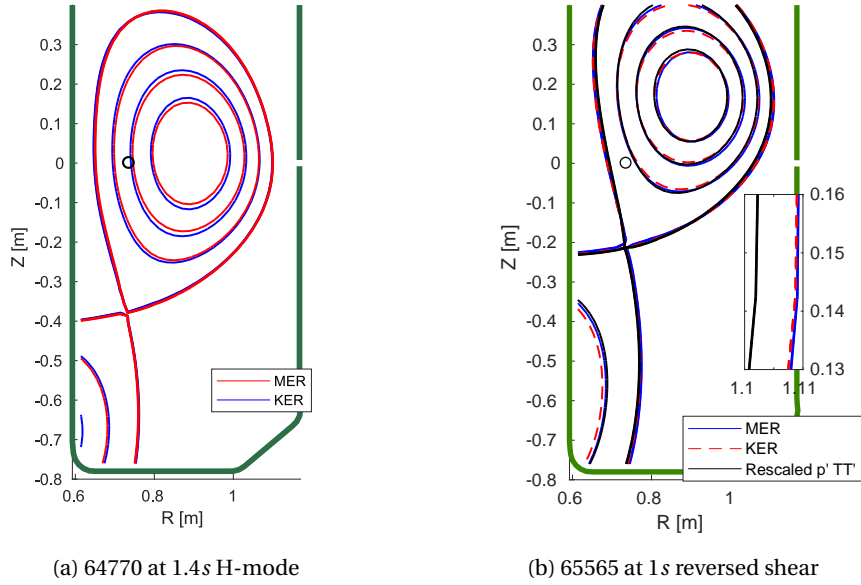(b) 65565 at 1s reversed shear

Figure 5.9 – Comparison of flux surfaces shape between "MER" and "KER". "Rescaled" indicates the case when $p'_{LIUQE} = \alpha p'_{ASTRA}$ and $TT'_{LIUQE} = \beta TT'_{ASTRA}$, where α, and β are found minimizing the least-squares differences with magnetic measurements.

We now investigate the effects of these new features in p' and TT', to the free-boundary equilibrium solution. The difference of the flux map between the two reconstructions is shown in fig. 5.9a. In blue the flux surfaces from MER and in red the flux surfaces from KER are shown. With the black bullet we indicate the tangent point of the injection line of the neutral beam which is slightly shifted to the high field side. Also for this H-mode case the difference of the flux surfaces is quite small as observed during the database analysis performed in previous section. This is in agreement with the comparison of the p and $j_\parallel$ profiles between MER and KER which have globally the same scaling and only higher order features. The LCFS in particular is basically not affected by these features as expected.

As a last analysis in fig. 5.10 we compare the difference between the reconstructed synthetic magnetic diagnostics and the measurements scaled by their uncertainties for the MER (blue) and the KER (red). The sum of the squares of these signals (adding the I_p) composes the χ^2_m cost function which is minimized by the equilibrium reconstruction in the KER problem (LIUQE part of eq. (5.3)). We notice in particular that the magnetic probes and the flux loops are distributed in the poloidal plane starting from the mid-plane high-field and circulating clockwise. Hence in the first plot in fig. 5.10, the first (1) and last (38) signal, corresponds to probes and flux loops close to the high field side mid-plane, while the 20th to the mid-plane low-field side. We would like clarify the interpretation of fig. 5.10 which might be easily misunderstood. In particular one cannot judge on the quality of the solution by only comparing the χ^2_m. First of all, if the measurements were perfect, hence without noise, and the free-boundary equilibrium problem would represent perfectly the reality then one would have

$\chi_m^2 = 0$. In that case the quality of two different equilibrium reconstructions could be compared based on χ_m^2 directly. However this is not the case when performing the reconstruction on a real experiment. This means that an equilibrium solution which obtains a lower $\chi_m^2 \sim 0$ by increasing the number of free parameters would just be over-fitting the data, by fitting also the noise in the measurements. Secondly, the MER formulated in eq. (3.9) with respect to the equilibrium reconstruction in the KER formulation used in this section eq. (3.17) has a different number of free parameters, in particular KER does not allow freedom in p' and TT'. This means that most of the time MER will have a lower χ_m^2 than KER. It is just a matter of coincidence that for the specific shot and time slice shown KER has a slightly smaller χ_m^2 than MER but it is often the opposite due to the more freedom of MER. This point was already made clear during the formulation of the problem in particular when discussing the simplification hypothesis which led to eq. (5.3), and an in-depth discussion was presented for synthetic data with noise in the previous chapter. Braking the non-linearities in the optimization problem, between the equilibrium and the kinetic modeling, means that there might exist solutions which have a smaller χ_m^2, but are not a minimum for the total $\chi_m^2 + \chi_k^2$. This is the case for the MER that can match better the magnetic measurements but do not have the pedestal feature in the pressure which are measured by the Thomson scattering. Therefore as long as the χ_m of two different reconstructions is within the error-bars and similar to one another, it makes no sense to judge on the quality of one or the other based only on χ_m. If instead when providing the constraints for p and $j_{\parallel}$ one results in a huge discrepancy between the magnetic measurements and synthetic signals one can doubt on the kinetic modelling, meaning that the kinetic modelling is not consistent with the magnetic measurements. All these difficulties in interpretation arise from having broken the non-linearity between the equilibrium and transport or for having considered wrong assumptions for the transport modelling for χ_i. For the case presented in 5.10, the χ_m^2 from KER is similar to MER and well within the error-bars hence providing us confidence that the kinetic modelling is consistent with measurements for this case. Note that this is remarkable, since the p' and TT' are fully fixed by the modelling, thus providing confidence in our models.

We consider now a second discharge 65565 at 1s, where a reversed shear in the current density profile is obtained with off-axis heating and current drive from both NBH and ECH. The shot was performed in order to study advanced steady state scenarios.

A peaked T_e profile is obtained as shown in fig. 5.11a due to the ECH contribution and most probably the improved core confinement. However the discharge at the selected time-slice was not operating in H mode, as one can see from the absence of a pedestal feature in the kinetic profiles as well as in the total pressure profile 5.11b.

In fig. 5.11c, the off-axis current drive (yellow), together with the bootstrap (light green) contribute to obtaining an off-axis maximum (in absolute amplitude) of the total current profile (dark green) computed from the current diffusion equation and well matched at convergence by the Kinetic Equilibrium Reconstruction (dashed red line). This leads to an off-axis minimum of the q profile as shown in fig. 5.11c, with a region of reversed shear (a
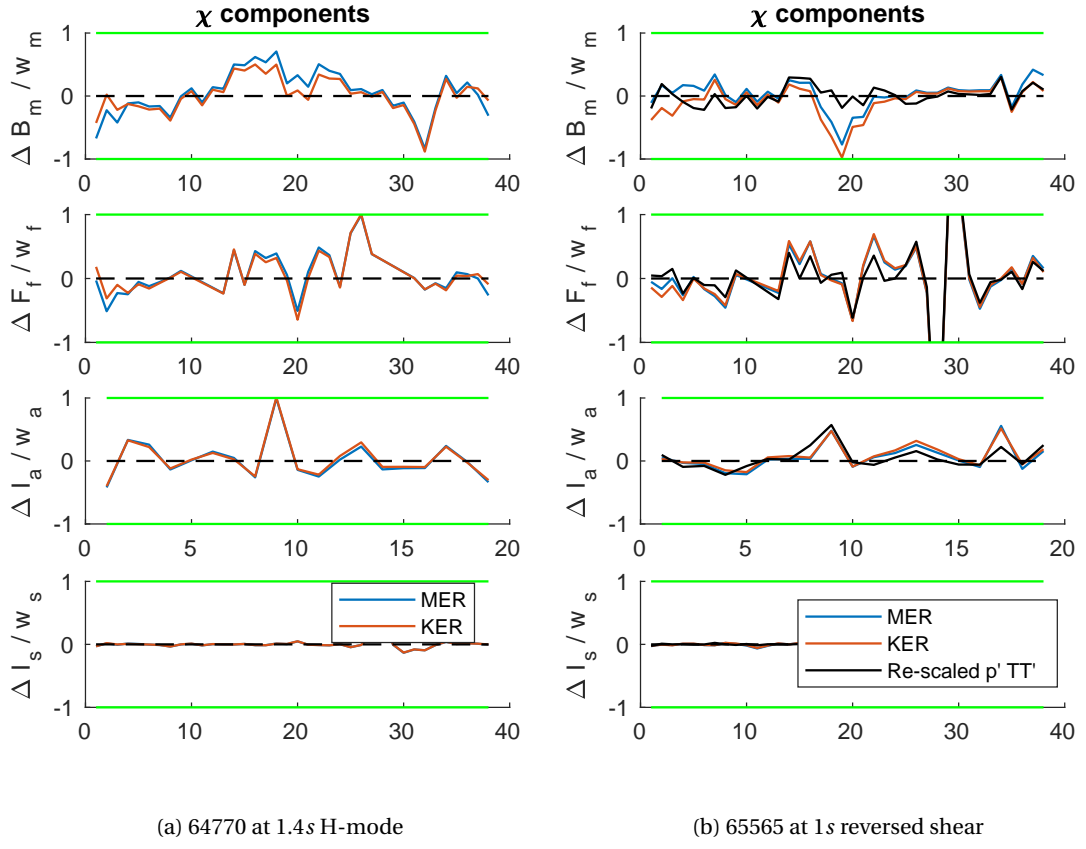
(a) 64770 at 1.4s H-mode

(b) 65565 at 1s reversed shear

Figure 5.10 – χ^2 component comparison between MER and KER reconstruction. "Rescaled" indicates the case when $p'_{LIUQE} = \alpha p'_{ASTRA}$ and $TT'_{LIUQE} = \beta TT'_{ASTRA}$, where α, and β are found minimizing the least-squares differences with magnetic measurements $\alpha = \beta = 1$
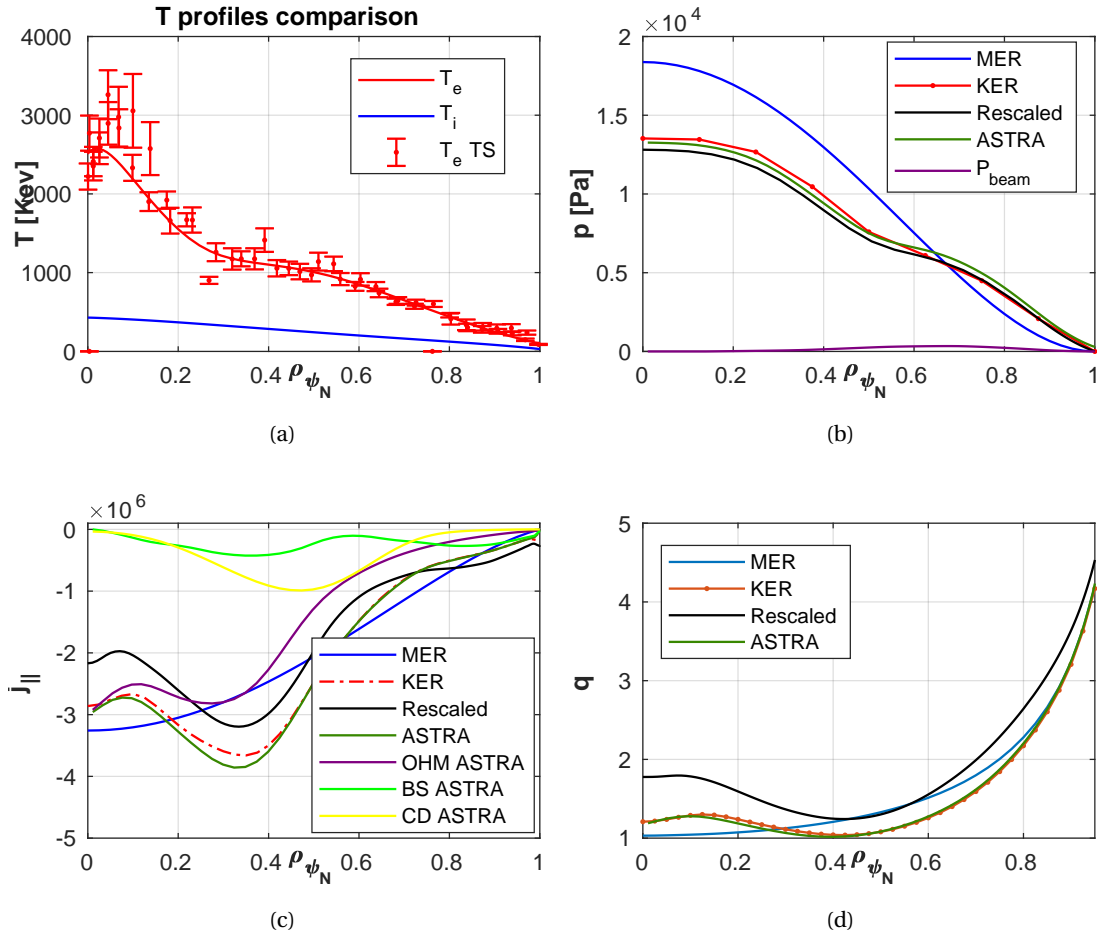
Figure 5.11 – MER vs KER 65565 at 1s. "Rescaled" indicates the case when $p'_{LIUQE} = \alpha p'_{ASTRA}$ and $TT'_{LIUQE} = \beta TT'_{ASTRA}$, where α, and β are found minimizing the least-squares differences with magnetic measurements while in "KER" $\alpha = \beta = 1$
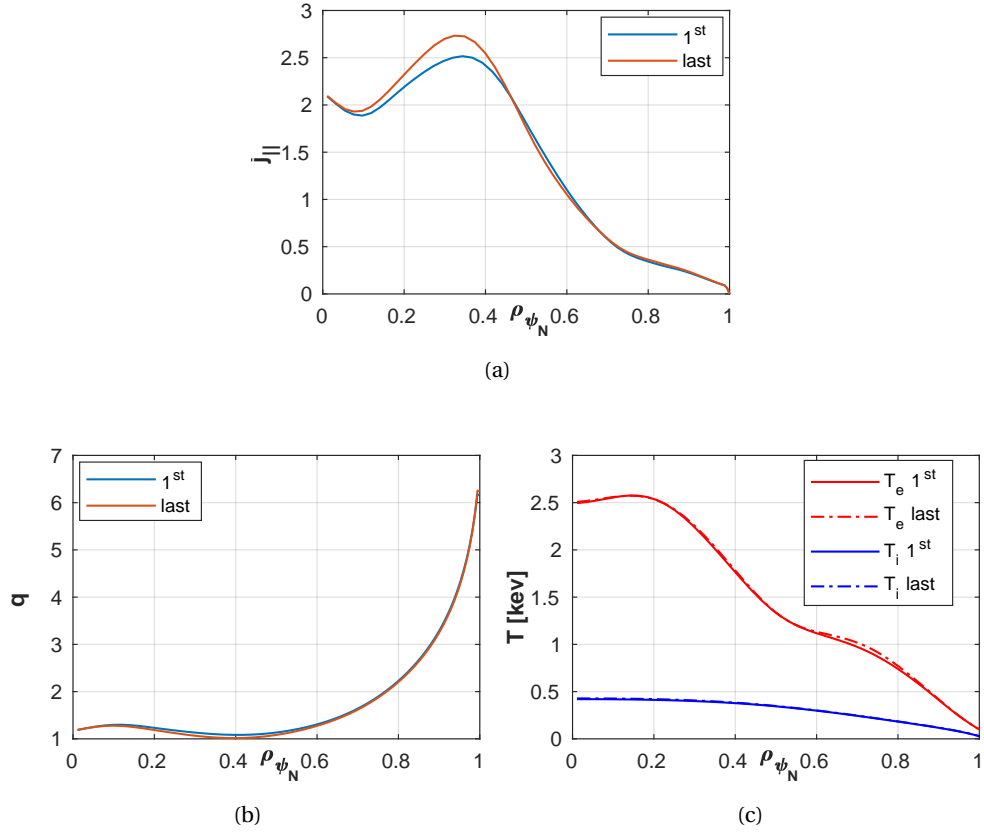
Figure 5.12 – Comparison between first and last Picard iteration in KER loop.

change of sign of the q profile derivative) within $\rho_{\psi_N} < 0.4$. Looking at χ^2_m we found a similar results for both MER (blue) and KER (red), meaning that the resulting p and j KER profiles are consistent with magnetic measurements. We will discuss later the meaning of the black line labeled with "rescaled".

The internal profile features slightly affect the shape of the flux surfaces inside the plasma, while the LCFS remains unchanged as shown in the zoom in fig. 5.9b. Since the flux surfaces shape was only slightly affected by the modification of the profiles, we do not expect that neither the mapping of the kinetic profiles nor the results of the transport solver have significant modifications. This is shown in figs. 5.12a, and 5.12c comparing the T_e, T_i, $J_\parallel$, and q profiles between the first and the last iteration. This demonstrate the statement that was anticipated at the beginning of this chapter, i.e. that performing KER with the formulation and tools as implemented in this section and summarized in fig. 5.1 means mainly making LIUQE to match the internal equilibrium solver of ASTRA while all the non-linear relation of the remapping of the diagnostics and the change to LCFS for the internal equilibrium solver of ASTRA do not make significant differences.

We show now an example of KER for shot 58499 in presence of sawtooth instability. The analysis for this shot was performed by M. Vallar [Vallar]. In the previous examples we considered

to perform kinetic equilibrium reconstruction only on resistive time scales. Considering the typical heat and current diffusion time in TCV ranging from $5 - 200 ms$, in order to follow the evolution of the profiles we could perform KER with a time sampling of $5 ms$. The information for the Thomson profiles are available every $17 ms$. However in most discharges, unless off-axis heating is used, a peaked central current density profile leads to the triggering of sawtooth instability, which causes periodical sudden relaxations of the current density profiles in the center, called "sawtooth crashes", bringing the safety factor on axis to $q \sim 1$. The typical period of these events is in the ms order in TCV but depends on several plasma parameters. The Kadomstev model [Kadomtsev 1975] can be used in ASTRA to describe this physics, and was found to well describe the Δq_0 during a sawtooth event [Fischer et al. 2019]. Performing KER, the local effects to the current density profile provided by this instability will be consistently included in the equilibrium reconstruction. We consider the shot 58499 in the interval $0.9 - 1.1 s$, where this instability was present with a crash period of 6 ms as shown in fig.5.13b. The experimental period is measured from the central channel of soft-X ray diagnostic which provides enough time resolution to resolve the instability. The Kadomtsev's model triggers a crash when a given threshold on the shear $s = \frac{\rho}{q} \frac{\partial q}{\partial \rho}$ is reached during the evolution of the current density profile [Porcelli et al. 1996],[Sauter et al. 1999a]. Tuning the threshold value one can match the experimental sawtooth period. A better way would be to synchronize the crashes in the model with the soft-X ray measurements directly. We show in fig. 5.13a the evolution of the q profile on axis using the sawtooth module in ASTRA (red), without using the sawtooth module (black) end estimated by the MER (blue). The resulting q profile immediately after a crash is shown in fig. 5.13c with the same color code. Without including the sawtooth physics the current diffusion equation provides an unrealistic $q_A \sim 0.6$. The MER, due to no significant features in the plasma profiles, was providing a q_A close to the minimum value reached by the current diffusion modelling before the crash, though this finding is specific to this shot and cannot be generalized since sometimes MER provides $q_A > 1$ even when sawteeth are present. A benchmark of the solution was conducted with the code TRANSP (green lines) by M.Vallar [Vallar]. To follow the evolution of the current density profiles during the sawtooth event, ASTRA needs to be run at a faster sampling ($0.5 ms$), hence a longer time is required to perform KER. Moreover in order for the instant of the crash to converge more iterations are required between the equilibrium and transport. This is shown in 5.13d, where the convergence of the p' profile over Picard iteration is given with color from blue to red, and the jump of the crash from one time instant to the next causes the oscillation in the initial iterations. This problem would be mitigated by imposing directly the crash instant from diagnostic. As a last analysis, we come back to the shot 65565 and we take again a look to fig. 5.10b to elaborate further on the meaning of matching the magnetic χ^2 and the relation with the kinetic profiles. We notice that both the MER and the KER seem to have a worse match of the magnetic probes in the low-field side mid-plane (B_m around 20). Since this could be an indication of internal profiles not consistent with the magnetic measurements for both of the cases, we recompute only the equilibrium reconstruction by letting the possibility to re-scale the p' and TT' profiles coming from the last converged iteration of ASTRA in order to better match the magnetic signals. This case is in the same direction as the 2nd proposed
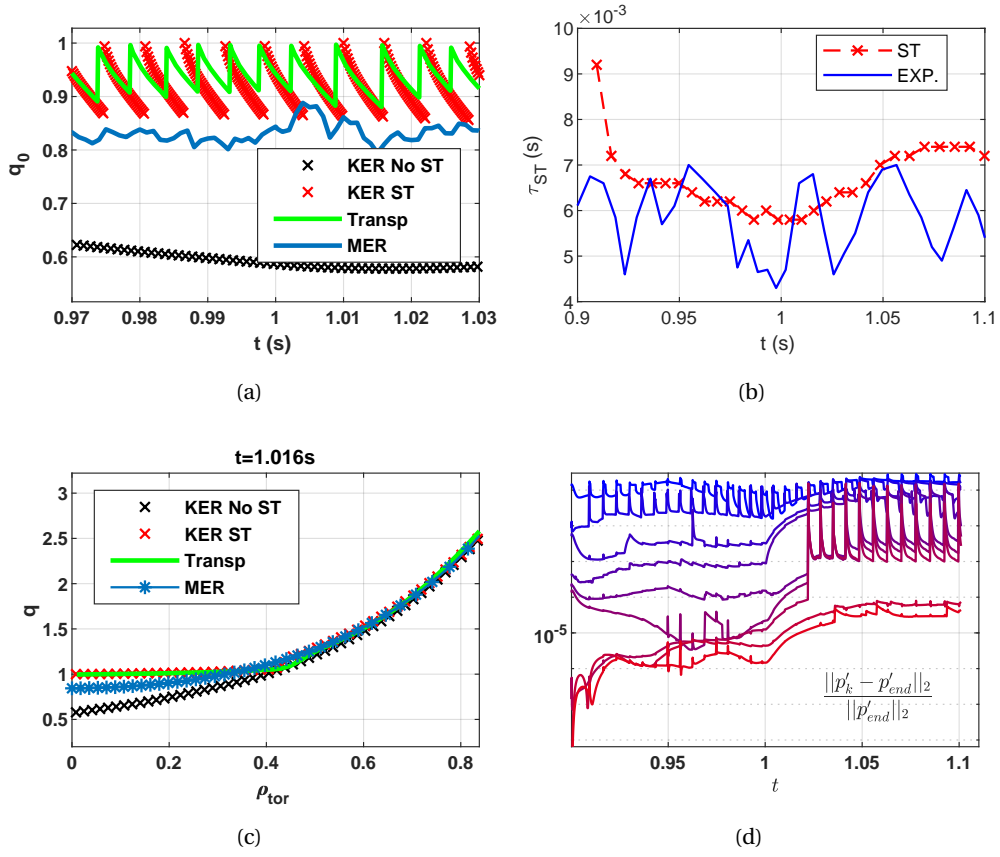
Figure 5.13 – Comparison between KER including sawtooth module ("KER ST"), KER without the sawtooth module ("KER No ST") and MER. Courtesy of M.Vallar [Vallar]. TRANSP simulation benchmark in green

simplified formulation of KER presented in section 3.3.4, that aims to try to recover part of the non-linearities between the reconstruction of the equilibrium and transport model, broken by the simplification assumptions to the numerical implementation. To be more precise, we only recompute the equilibrium reconstruction and not the KER Picard iterations. The result of the re-scaled equilibrium reconstruction is shown with the black line in all the plots related to 65565 reversed shear shot fig. 5.9b, 5.10b, 5.11b and 5.11d. Letting more freedom, the magnetic measurements are better matched 5.10b in particular in the low field side mid-plane resulting in a displacement of $\sim 1cm$ of the LCFS in this region as shown by the zoom. While the poloidal flux distribution is slightly affected, a bigger impact is found on the profile of q fig.5.11c and the profile of $j_{\parallel}$ fig. 5.11c. It is important to notice that also the opposite might be happening. Meaning that the kinetic profiles from the modelling are correct and the magnetic probes around the low field side mid-plane are affected by systematic error since they are close to one another..

A natural question arises: which of the two q profiles is more realistic? Unfortunately, the answer cannot be given within the formulation of KER implemented in this chapter. The analysis therefore shows just another example of ambiguity which arises when neglecting some non-linear relations between the magnetic and kinetic reconstruction. At the same time, it also shows that the q profile is a sensitive quantity to reconstruct compared to geometrical quantities for instance. The implemented KER while providing global improvements such as being able to include reversed shear features in the equilibrium, cannot provide localization of the surfaces with accuracy of fraction of the current deposition for instance. Since many applications can be sensitive to small modification of q profiles, such as transport analysis with gyrokinetic code, more developments are needed: to move to a different formulation as discussed in section 3.3.4 which at least would solves some ambiguities; to estimate the sensitivity of the solution to the most uncertain parameters like Z_{eff} and the assumption for T_i and n_i transport; to develop uncertainty quantification to provide information on the accuracy of the reconstructed profiles. Overall we remind that a dedicated diagnostic could provide a major improvement in the reconstruction of this quantity for TCV.

Why did we make the choice of imposing p' and TT' from the transport modelling? In the derivation of the formulation we made the hypothesis of no errors in the forward model, putting all freedom in the variation of the parameters χ_m and Z_{eff} that we imposed. We stick then with this assumption at least in the post-discharge reconstruction in TCV, considering also that in the off-line analysis the estimate of the temperature profile is very well resolved by the Thomson scattering and in any case we do not have extra measurement of j to rely on at the moment in TCV, hence there are no better information than the current diffusion model in any case. We chose to use the best estimate for each diagnostic also because there is not much of redundancy in the TCV set. Moreover we could not implement the second simplified formulation in section 3.3.4 due to the constraints in the available codes as explained in the formulation section, in particular for the internal solver of ASTRA. This is a relatively simple development that will be implemented in the near future.

5.5   Critical aspects of formulation and implementation in TCV

We would like to comment and summarize the critical aspects of the formulation and implementation of Kinetic Equilibrium Reconstruction adopted and presented in this chapter. Most of them are specific to TCV case and the suite of codes we have been using in the implementation at the current date of this thesis, hence they do not have to be considered as critiques to KER in general.

- No diagnostics available to measure the plasma internal current density and test the current diffusion modelling.

- None of the adopted strategies provide an accurate estimate of T_i, when good CXRS measurements are not available (which is the case at present in H-modes). Solving the diffusion equation with ASTRA requires to provide $\chi_i(\rho, t)$. One could leave this as a free-parameter to be optimized with a further external optimization loop procedure. The easiest implementation would require a scan of different solution for the value of the parameter. Another option is to consider $T_i = \alpha T_e$, in this case again α needs to be considered as one of the free parameter. If α is taken to match the total stored energy of the MER, this implicitly means relying mostly on the measurement of the diamagnetic flux loop (DML) which is known to be difficult to calibrate and prone to systematic errors. Note that this is a generic difficulty when transport models are an important input to KER, as is expected in real-time in particular in most machines.

- No direct measurements of Z_{eff} is available. This is also the case in most tokamaks in real-time in particular. It is a usual practice to estimate it from the current diffusion equation under stationary state assumption as explained in section B even though this is not fully consistent with the rest of the formulation, which may lead to inaccuracies in particular during transient phases.

- An important issue is the uncertainty of χ_i and Z_{eff} combined with the sensitivity of some of the results on these values, in particular the estimation of T_i and q. They can be of the same order of magnitude as the improvements obtained with a consistent modelling as a result of KER. This shows also the non-linearities involved and the need for an integrated analysis.

- Another important shortcoming in the implemented procedure is the lack of a proper error propagation analysis.

There are then specific limitations to the formulation of the simplified problem that we already explained in details in sec 3.3.4, and we recall a few here for convenience.

- Using the single best diagnostic for each quantity might be limiting. In devices with higher number of diagnostics this is not desirable. To combine the different information we refer to sec. 3.1.

- The formulation adopted where p' and TT' are directly imposed from kinetic modelling provides a low usage of the information content of the magnetic data and relies heavily on the kinetic modelling. The second simplified formulation should be implemented.

5.6 Summary and outlook

Kinetic equilibrium reconstruction (KER) is an inverse problem to infer the plasma poloidal flux distribution and internal kinetic profiles from available magnetic and kinetic measurements, which combines in its forward model a free-boundary equilibrium solution and kinetic transport modelling.

It started as an improvement of magnetic equilibrium reconstruction, providing constraints to internal profiles, and progressed towards more integrated data analysis where many different diagnostics and models, including dynamical models, are coupled together to provide the best estimate of plasma state. Its application is nowadays ubiquitous in post discharge experimental analysis for tokamaks, ranging from the mapping of diagnostics into 1D profiles, computation of MHD stability limits and transport investigation with gyrokinetic codes [White 2019]. The worldwide effort in developing the multiple aspects of this integrated data analysis approach were summarized in [Mazon et al. 2020], with the focus in particular of bringing together the knowledge and tools in view of ITER operation.

In this chapter we revised the main approaches available in the literature to perform kinetic equilibrium reconstruction and the historical integrated data analysis performed in TCV before this thesis. After having discussed in the previous chapters a formulation of the problem suited for the TCV diagnostic set, including several hypothesis to simplify its numerical solution, we presented its implementation and application to TCV post-discharge analysis.

We focused on comparing KER with the standard magnetic equilibrium reconstruction MER specifically for TCV. First we investigated the sensitivity of the equilibrium solution to internal profiles, to gain intuition on the effect to physical quantities related to pressure profile, current density profile and plasma shape. To do that we took a database of previous integrated data analysis performed in TCV. We used the profiles obtained from kinetic measurements and modelling to re-compute the equilibrium free-boundary problem. Small difference in the magnetic topology was found, in particular negligible changes to the last close flux surface. This confirms the previous results in the community that the magnetic measurements alone provide good information to reconstruct the external plasma shape. We also showed how between the magnetic equilibrium reconstruction and the current diffusion modelling a difference of localization of $\rho(q=1.5)$ and $\rho(q=2)$ surfaces of the same order as the width of the current deposition is found, which can be relevant in real-time for NTM control.

Most of the available database however was composed by low performance discharges with no significant internal profile features, hence we focused on performing the full converged KER developed in this chapter for an H-mode shot and a reversed shear plasma. We discussed

in particular the meaning of the χ^2 and the matching of the magnetic measurements when comparing MER against KER, and presented an example of reconstruction during the sawtooth crash.

For most of TCV discharges in the database, which are low performance discharges, full converging KER does not provide any relevant modification to the poloidal flux map, hence to the mapping and to the solution of the transport equations. Differently stated the previous "one pass through" integrated data analysis performed before this thesis was already almost equivalent to what is achieved in this thesis. Internal changes of the magnetic topology, which in any case are small for TCV discharges analyzed, can be appreciated for high external current drive scenario or internal transport barrier features. Also in these cases however the LCFS is barely modified. These small modifications can still be relevant when using the poloidal flux map and plasma profiles for stability analysis or gyrokinetic studies. We stress that with the current formulation the solution of the internal ASTRA equilibrium solver is already close to the consistent solution found with KER without the need to perform any iteration in the loop. The main gain is therefore in a reconstructed equilibrium consistent with kinetic measurements, which is necessary for comparing different diagnostics and modelling results. In addition, it provides the constraint of the current diffusion equation, not available in MER.

We identified several critical aspects for the implemented KER for TCV, which are shared also by the previous integrated data analysis performed before this thesis. They have been explained in details in this chapter and are related to both the simplifications adopted in the problem, the restricted set of diagnostics available and tools themselves that have been used. In particular having broken non-linearities between the different models with the purpose of simplifying the numerical implementation could lead to significant mismatch between kinetic measurements/modelling and the magnetic measurements. Although the main source of discrepancy is usually due to diagnostics mismatch, for example between W_{mhd} and ion transport predictions. We proposed a different formulation of the problem which is very close to Kinetic-EFIT, but it was not yet implemented in this work. The main source of uncertainty is found on the reconstruction of T_i and Z_{eff}, which can have an impact in the final solution of KER, for example in the localization of internal surfaces, and should be analyzed further.

All these aspects make us conclude that the present KER implemented in TCV, while providing improvements to the free-boundary equilibrium solution, such as providing a reconstructed equilibrium consistent with kinetic profiles and current diffusion equation in particular, including reversed shear and pedestal features, is not conclusive yet and overall it would largely benefit from an improvement of the diagnostic set.

The next steps should include a proper sensitivity analysis of all the components, starting from synthetic predictive data, including an uncertainty estimation analysis. Knowing the original solution which generated the data allows to disentangle the discrepancy in the reconstruction associated to the formulation of the reconstruction problem, to its numerical solution and to

eventual synthetic noise contribution. Since the forward predictive models are the same which enter in the reconstruction problem, we are always in favour of this end-to-end validation approach. This could be: first investigate the static equilibrium reconstruction problem; try different solution to pass information on the internal profiles and investigate the most sensitive quantities also in presence of measurement noise; move to the reconstruction on resistive time scales; investigate sensitivity of the transport solution; investigate the sensitivity of the measurement mapping; consider different formulation of the kinetic equilibrium reconstruction problem; investigate the uncertainty propagation with Monte Carlo sampling, Bayesian analysis or recursive Bayesian analysis for dynamic systems. This plan should be the preferred direction to check systematically the accuracy of kinetic equilibrium reconstruction and integrated data analysis in general.

Developing integrated kinetic equilibrium reconstruction tools, having to integrate many different aspects, is a complex problem. There exist proper ways to take into account consistently all the different measurements and uncertainties, both in the frequentist and Bayesian approach as explained in the introduction to the inverse problem. Steps in this direction are for example described in [Faugeras and Orsitto 2019], where all the non-linearities of the several models are considered consistently in the same properly stated optimization problem in the mean least-squares formulation. Full Bayesian approach such as IDA [Fischer et al. 2019] and Minerva [Svensson et al. 2010] are exploited in tokamaks such as AUG and JET to combine consistently different diagnostics with their uncertainties.

It is a fact that the forward models involved in kinetic equilibrium reconstruction are now well established and are composed by relatively simple diffusion equations at least for the models discussed in this thesis. Estimation of transport from gyrokinetic codes are improving in precision to recover big uncertainty of transport coefficients. Fast transport solvers are available (RAPTOR) and Neural Network have become in the last years a solid reality and, if properly trained, can speed up any computational problem including the most expensive computation part of the forward model involved in KER. A brilliant example in this sense is [Boyer et al. 2019; Kremers 2020] where a Neural Network was trained to provide real-time capable estimation of NUBEAM [Pankin et al. 2004] solution for fast ion transport, with high fidelity of the results. This is then used as a Kalman filter observer for Z_{eff} and ion anomalous transport diffusion coefficients. Another example is [Pavone et al. 2019] where a neural-network was trained on the results of the Minerva framework to approximate a full model Bayesian inference of plasma profile from x-ray imaging diagnostic system for W7-X. We can imagine in the near future to have them trained the forward coupled model and build a Bayesian estimator based on this. This would allow then to have both between shot analysis and real-time estimation including error on the reconstructed state and parameters.

Stressing on the importance of the original formulation of the problem will be helpful for the community to reflect on which direction the integrated data analysis is going to focus to take into account error propagation analysis and to provide meaningful information to the reconstructed parameters for example.

6 Kinetic Equilibrium Reconstruction in TCV (real-time)

In the previous chapters we implemented a tool to perform kinetic equilibrium reconstruction during post discharge analysis in TCV based on the available set of diagnostics and modeling. In this chapter we present a real-time implementation of kinetic equilibrium reconstruction and test it during TCV experiment.

First in section 6.1 we discuss the motivation to perform kinetic equilibrium reconstruction in real-time. Then in section 6.2 we present the real-time implementation for the TCV tokamak. After describing the codes RAPTOR [Felici et al. 2014] and RAPDENS [Blanken et al. 2019] to reconstruct the $T_e(\rho, t)$, $n_e(\rho, t)$ and $j_\parallel(\rho, t)$ combining dynamic modelling with available real-time measurements, we provide a novel approach suited for real-time application, to couple them with the magnetic equilibrium reconstruction performed by LIUQE [Moret et al. 2015]. In section 6.3 we present the result of real-time kinetic equilibrium reconstruction performed during a TCV experiment which presented different profile dynamics due to both external sources and plasma events. We also compare real-time KER with the standard real-time magnetic equilibrium reconstruction performed routinely during TCV operation. In section 6.4 we discuss in details the limitations and future developments of the current approach. Finally in section 6.5 we summarize our findings.

The goals of this chapter is not to compare extensively KER with MER in its real-time implementation, rather to develop a technique suited for real-time implementation and demonstrate its application to TCV operation. What is demonstrated for TCV in this chapter can be directly applied to other present and future tokamaks.

PAPER

First demonstration of real-time kinetic equilibrium reconstruction on TCV by coupling LIUQE and RAPTOR

Recent citations

View the article online for updates and enhancements.

6.1 Motivation and challenges for real-time application

Kinetic equilibrium reconstruction is becoming a standard post-shot analysis in many toka-maks as the basic post-discharge analysis to interpret experimental results and also as a starting point for MHD stability investigation and microscopic transport simulation with gyrokinetic codes [White 2019].

In order to reliably achieve and maintain the performances required for future tokamaks such as ITER, real-time control of the kinetic and current density profiles, together with the plasma equilibrium, will be needed [Humphreys et al. 2015]. Not only control algorithms but also supervisory control functionalities, such as real-time plasma monitoring for disruption avoidance, rely on the quality of the reconstruction of the plasma state [Blanken et al. 2019; Vu et al. 2019]. Therefore, improving both the real-time reconstruction of internal profiles and plasma equilibrium with consistent profiles will be useful for plasma operation especially during high performance scenarios. A better identification of the internal flux surfaces during the experiment would also allow to better aim the gyrotrons for NTM suppression.

Implementing a real-time kinetic equilibrium reconstruction presents additional challenges with respect to post-discharge analysis.

- Diagnostics might fail or degrade during the operation

- Fewer diagnostics can be used in real-time because of availability or computationally expensive post processing or need for human intervention.

- The measurements might be available at several different time rates and spatial resolutions.

- The computational time to perform the analysis must be smaller than the characteristic time of the phenomena of interest in order to allow the possibility to react and control the plasma state.

The first objective of kinetic equilibrium reconstruction is to identify the internal plasma profiles, in particular p and j, hence the time scales of interest for being real-time are set by the heat and particle transport time scales and the current diffusion time scale. Control-oriented codes that are 'faster-than-real-time' have been developed for this purpose. They present a departure from traditional aims of physics-oriented codes in terms of accuracy and completeness in order to achieve the real-time computational target. Grad-Shafranov solvers aimed at real-time implementation satisfy the computational time requirements via optimized algorithms as in LIUQE [Moret et al. 2015] or hardware solutions like parallelization and GPUs [Huang et al. 2017; Rampp et al. 2016]. For the transport models efforts are made to reduce the complexity of the modeling while retaining the most relevant features [Felici et al. 2011; Teplukhina et al. 2017; Barton et al. 2015], as well as using machine learning techniques to emulate the solutions of the most computational expensive part of the model [Meneghini

et al. 2017; Citrin et al. 2015; Felici et al. 2018; Boyer et al. 2019]. Another approach is to entirely substitute physics-based models with data driven models trained on databases of previous experiments [Moreau et al. 2013], which is receiving increasing attention in the last years with the gain of popularity of neural networks and machine learning.

One of the main requirement for developing real-time reconstruction tools, which are then used as observers for controllers, must be the robustness, to be used reliably during the experiment without causing failure of the experiment. For this reason we will not directly feed the equilibrium reconstruction with additional information from the available internal measurements, which in real-time suffers from the limitation listed above. Instead it is preferable in general to always have a forward predictive model, meaning in these cases a 1D transport code, and combine the information from the transport model and the measurements before using this information for the equilibrium reconstruction. This was achieved by the transport code RAPTOR [Felici et al. 2018] and RAPDENS [Blanken et al. 2018], in real-time making use of the Extended Kalman-Filter (EKF) [Särkkä 2013] technique, which we also make use of in this thesis. In this way we have the double advantage to always have an estimation of the internal profiles with arbitrary spatial and time resolution, which is correct within the assumption of the transport model, and also to correct the modelling whenever measurements are available.

6.2 Real-time implementation in TCV

A detailed description of the kinetic equilibrium reconstruction problem specific for the set of diagnostics of TCV has been derived and implemented in the previous chapter for the post-discharge analysis. However, some additional constraints need to be considered when approaching the real-time implementation in TCV.

A reduced set of diagnostics is available in real-time, in particular for the kinetic measurements. These include at present only an estimation of the central T_e from soft X-ray diagnostics and a measure of the n_e integrated profiles from far infrared interferometer FIR [S.Barry 1999]. The full set of the external magnetic measurements are also available with high time resolution. Inclusion of more diagnostics will be discussed in the outlook section.

There are stringent computational time requirements to achieve the real-time target. This is particularly true for TCV since, due to its relatively small size, the heat diffusion time scale (2-50ms) and current diffusion time scales (100-200ms) are much shorter than in larger devices such as ITER. Before this thesis, the magnetic equilibrium reconstruction code LIUQE and the transport code RAPTOR were already available, both capable of real-time performances with 1ms computational time to compute independently their solution at a given time instant, which made possible the coupling in real-time between the two codes presented in this chapter.

As for the case of the formulation of the kinetic equilibrium reconstruction problem presented

in the post-discharge analysis, the steps to derive the one implemented in real-time are:

- Start from the complete kinetic equilibrium reconstruction problem eq. (3.14), where the free-boundary equilibrium problem is coupled to the profile transport problem, all the unknowns quantities enter as free parameters to be found by minimizing the least-squares error which includes both the magnetic and kinetic measurements.

- Split the magnetic equilibrium reconstruction part (LIUQE), where only external magnetic measurements are used, from the kinetic reconstruction part (RAPTOR) where only the real time kinetic measurements are used.

- Coupling the two reconstruction problems, which together define the kinetic equilibrium reconstruction, in order to achieve a certain degree of consistency for the internal plasma profiles. This was explained for example in eq. (3.17) for the post-discharge analysis.

In this thesis, we developed a simple and efficient two way coupling technique suited for real-time application in particular, described in the following, which does not deteriorate the $\sim 1ms$ performances of the LIUQE and RAPTOR codes. This coupling technique was proposed to take into account both the computational requirements and the low accuracy of kinetic profile estimation due to the reduced set of measurements available in real-time. The resulting formulation of the problem is similar to eq. (3.19) presented in section 3.3.4.

In the following we start by describing the reconstruction problem solved by RAPTOR. We then provide the formulation of the problem for the real-time kinetic equilibrium reconstruction developed and tested during TCV operation in this thesis.

6.2.1 Kinetic profiles reconstruction: RAPTOR and RAPDENS

The target for the transport part of the reconstruction is to estimate $p(\rho, t)$ and $j(\rho, t)$, combining the real-time kinetic measurements with first principle modelling to be then used as additional information in the equilibrium reconstruction part. This is obtained by making use of RAPTOR [Felici et al. 2018] and RAPDENS [Blanken et al. 2018].

The current profile $j(\rho, t)$ is obtained directly from forward modeling by solving the current diffusion equation with RAPTOR, since no direct measurements of this quantity are available in TCV at the moment. The current diffusion equation has been explained already in section 2.4. In the real-time implementation the non-inductive contribution j_{ni} is composed of the bootstrap contribution j_{bs} from Sauter's formula [Sauter et al. 1999b, 2002] and the current driven by Electron Cyclotron Current Drive (ECCD) j_{cd} given by a parametrized Gaussian-like model [Felici et al. 2011],

$$j_{cd}(\hat{\rho}) = c_{cd} e^{\hat{\rho}^2/0.5^2} \frac{T_e}{n_e} e^{-4(\hat{\rho}-\hat{\rho}_{dep})^2/w_{dep}^2} P_g(t), \tag{6.1}$$

where the central deposition location ρ_{dep} and width w_{dep} are prescribed, $P_g(t)$ is the power of each source of ECCD obtained in real-time, n_e is computed from its transport equation and c_{cd} is a machine-dependent proportionality factor. The neutral beam current drive is neglected in the current implementation.

The total pressure $p(\rho, t)$ is considered as given by,

$$p = n_e T_e + n_i T_i. \tag{6.2}$$

The electron temperature T_e and density n_e are reconstructed by RAPTOR and RAPDENS respectively combining the prediction from a 1D transport model with the estimation of the central T_e from XTe (for RAPTOR) and the n_e profile measurements from far infrared interferometer FIR [S.Barry 1999] (for RAPDENS), making use of the Extended Kalman filter technique. The ion temperature T_i and density n_i profiles are assumed proportional to the electron ones. In the present work for the real-time implementation, we will not consider the contribution of fast ions hence in the analysis we will consider only discharges without NBH.

The electron temperature T_e is estimated by RAPTOR from the thermal energy diffusion equation,

$$\frac{3}{2(V'_{\hat{\rho}})^{5/3}} \frac{\partial}{\partial t} \left[(V'_{\hat{\rho}})^{5/3} n_e T_e \right] = \frac{1}{V'_{\hat{\rho}}} \frac{\partial}{\partial \hat{\rho}} \left[\frac{g_1}{V'_{\hat{\rho}}} n_e \chi_e \frac{\partial T_e}{\partial \hat{\rho}} \right] + P_e, \tag{6.3}$$

The electron particle flux Γ_e to the heat diffusion equation (eq. (6.3)) is assumed negligible [Teplukhina et al. 2017] and $n_e(\hat{\rho}, t)$ is given by the electron density diffusion equation specified later. In this work, for simplicity, an ad-hoc diffusivity coefficient χ_e, tuned for TCV discharges has been used [Felici et al. 2011]. The total power density for electrons is written as $P_e = P_{OH} + P_{e,aux} - P_{ei} - P_{e,rad}$, where P_{OH} is the Ohmic heating, P_{ei} the power exchanged between electrons and ions and $P_{e,rad}$ the radiated power. In this work $P_{e,aux}$ is composed only by ECRH modeled with a Gaussian deposition of prescribed width and location. The merge of transport model prediction and central T_e measurements from XTe is obtained with EKF [Felici et al. 2014].

The electron density n_e is estimated in RAPDENS [Blanken et al. 2018] with the particle diffusion equation,

$$\frac{\partial}{\partial t} [V'_{\hat{\rho}} n_e] = -\frac{\partial \Gamma_e}{\partial \hat{\rho}} + V'_{\hat{\rho}} S_e \tag{6.4}$$

where the electron particle flux Γ_e is given by,

$$\Gamma_e = -\frac{g_1}{V'_{\hat{\rho}}} D_e \frac{\partial n_e}{\partial \hat{\rho}} + g_0 V_e n_e, \tag{6.5}$$

with $g_0 = \langle \nabla V \rangle$, and the diffusion coefficient D_e and pitch velocity V_e are estimated to represent empirical system behavior. The model includes empirical expressions for thermal ionization of other neutral species, thermal recombination of ions, the particle sink in the scrape-off layer due to wall impact of particles exiting the plasma through the scrape-off layer.

Details on the diffusion coefficient and particle sources are found in [Blanken et al. 2018]. The merge of transport model prediction and far infrared interferometer FIR measurements [S.Barry 1999] is obtained with EKF [Blanken et al. 2018].

Given a forward dynamic model (the transport heat and particle equations), assuming Gaussian additive noise on the model and measurements, the EKF finds recursively an estimate of the state ($\hat{T}_e$ and $\hat{n}_e$) which maximizes the condition probability of $\hat{T}_e$ and $\hat{n}_e$ given the measurements and the state at previous time instants.

The ion temperature T_i in this work is considered to be proportional to T_e. The ratio is either provided as given input, or estimated in real time by matching the total stored energy computed from the p estimated with RAPTOR with the one estimated from the equilibrium reconstruction with a Proportional Integral (PI) controller (more details later in sec. 6.3.4).

The ion density n_i is computed in order to match the quasi-neutrality hypothesis $n_i(\rho) = n_e(\rho)\frac{Z_c - Z_{eff}}{Z_c - 1}$ assuming for TCV carbon as the main impurity. The effective charge Z_{eff} is provided as an input to the system.

In conclusion, the transport codes RAPTOR and RAPDENS receive I_p from the magnetic measurements, the geometric information $g_{0,...,3}$, $V'_{\hat{\rho}}$ and Φ_b from the equilibrium reconstruction given by LIUQE, and source terms for the transport equations. They evolve the current diffusion equation, the electron heat and the particle diffusion equations combining the modeling with available measurements $\tilde{T}_e(0, t)$ and $\tilde{n}_e(\rho, t)$. From the solution of RAPTOR and RAPDENS the total plasma pressure $p = n_e T_e + n_i T_i$ and

$$j_{\parallel} = \frac{1}{8\pi^2 B_0} \frac{1}{\mu_0 \Phi_B} \frac{T^2}{V'_{\hat{\rho}}} \frac{\partial}{\partial \hat{\rho}} \left[\frac{g_2 g_3}{\hat{\rho}} \frac{\partial \psi}{\partial \hat{\rho}} \right],$$

are computed. From these profiles an estimate for $p'_{RAP} = \frac{dp}{d\psi}$ and $T\frac{dT}{d\psi}_{RAP}$ is obtained using the relation:

$$TT'_{RAP} = \left(\mu_0 p'_{RAP} - j_{\parallel,RAP} \frac{\mu_0 B_0}{2\pi T} \right) \left[g_3 + \frac{g_2}{4\pi^2 T^2 (V'_{\hat{\rho}})^2} \left(\frac{d\psi}{d\hat{\rho}} \right)^2 \right]^{-1}. \tag{6.6}$$

6.2.2 Equilibrium and transport coupling methodology

In the real-time implementation we needed to make a compromise due to both a reduced set of diagnostics and the strict computational time requirements. As a consequence p'_{RAP} and TT'_{RAP} will be less accurate than the post discharge analysis, since they will rely more on the simplification hypothesis for the transport coefficients. For this reason, we prefer to not impose them directly as fixed profiles for the free boundary equilibrium.

We already proposed a solution in eq. (3.19) section 3.3.4, which is similar to what is performed in Kinetic EFIT [Li et al. 2013] and IDE [Fischer et al. 2016]. The idea was to include the estimate of the internal profiles coming from the transport as additional measurements for the magnetic

equilibrium reconstruction part, considering them at the same level as the other magnetic measurements. The profiles for the computation of the free boundary equilibrium p'_{LIU} and TT'_{LIU}, which we call with the subscript "LIU" to indicate that they are used in LIUQE as RHS of the Grad-Shafranov equation, will be expanded into a set of basis functions. As usual in magnetic equilibrium reconstruction the coefficients for this basis function expansion will be computed minimizing the least-squares error with the measurements that in this case will include also p'_{RAP} and TT'_{RAP}. The intuition behind is that the magnetic measurements, though not sensitive to small internal profiles features, are aware of global scaling at least of the total pressure profile. However, in order to be able to represent the features contained in p'_{RAP} and TT'_{RAP} a larger number of basis functions would be needed for p'_{LIU} and TT'_{LIU} but this would affect the computational time requirements to achieve real-time performances.

We propose therefore the following coupling scheme suited for real-time application in particular. $p'_{RAP}(\psi_N)$, $TT'_{RAP}(\psi_N)$ are used as directly unique basis functions for p'_{LIU} and TT'_{LIU} respectively such that,

$$p'_{LIU} = \alpha p'_{RAP},$$
$$TT'_{LIU} = \beta TT'_{RAP},$$

where α and β are scalar coefficients to be found by matching the magnetic measurements in least-squares sense.

We can finally state the kinetic equilibrium reconstruction problem implemented in real-time, which is very similar to eq. (3.19) in section 3.3.4 except for the handling of p'_{LIU} and TT'_{LIU}.
Given: The magnetic measurements $\tilde{\boldsymbol{M}}_m = \{\tilde{\boldsymbol{B}}_m, \tilde{\boldsymbol{F}}_f, \tilde{I}_p, \tilde{\Phi}_t, \tilde{\boldsymbol{I}}_v, \tilde{\boldsymbol{I}}_a\}$, kinetic measurements $\tilde{\boldsymbol{M}}_k = \{\tilde{\boldsymbol{T}}_e(0, t), \tilde{\boldsymbol{n}}_e(\rho, t)\}$, the transport heat and particle models, the sources j_{cd} and P_e, and the forward inputs Z_{eff} and T_e/T_i ratio.
Find: $\boldsymbol{I}_a, \boldsymbol{I}_v, \alpha(t), \beta(t)$ and all the quantities related to the free-boundary equilibrium in particular and kinetic transport, in particular $\psi(R, Z; t), T_e(\rho, t), n_e(\rho, t), n_i(\rho, t), T_i(\rho, t), j_{\parallel}(\rho, t)$ such that

$$\begin{cases} \{\boldsymbol{I}_a, \boldsymbol{I}_v, \alpha, \beta\} = (\mathbb{A}(\psi)^T \mathbb{A}(\psi))^{-1} \mathbb{A}(\psi)^T \tilde{\boldsymbol{M}}_m \\ \Delta^* \psi = 2\pi \left[R(\alpha p'_{RAP}) + \frac{1}{\mu_0 R}(\beta TT'_{RAP}) \right] \\ \{p'_{RAP}, TT'_{RAP}\} = RAPTOR(g_{0,...,3}, \mathbb{M}_k, I_p, \text{sources}) \end{cases} \qquad (6.7)$$

In real-time, the problem is solved with a Picard iteration scheme between LIUQE, RAPTOR and RAPDENS, summarized in figure (6.1). At every computational time step, one equilibrium solution (with p'_{RAP}, TT'_{RAP} from the previous time step) and one transport solution (with the new equilibrium geometry) are performed. We will show that achieving a cycle time to compute a single iteration faster than the characteristic timescales of the transport evolution allows to obtain a good level of consistency between codes, measured in terms of how the kinetic profiles in the equilibrium reconstruction matches the information coming from the

transport one. Convergence is therefore achieved also during time-evolving events of $j_\parallel, T_e, n_e$ as long as these changes follow the diffusive time scales. We recall that the current diffusion time in TCV is 100-200ms, the energy confinement time τ_e ranges from 2ms to 50 ms, the particle confinement time from $5\tau_e$ to $10\tau_e$. Larger devices like ITER will have much longer time scales allowing eventually for multiple Picard iterations for a single time step and/or a more refined spatial grid. A relaxation procedure, which in time acts as a low pass filter, is used to help the convergence of the algorithm.
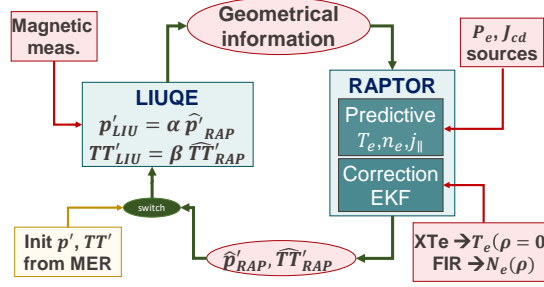

Figure 6.1 – Iterative LIUQE/RAPTOR coupling scheme. Closed iteration loop indicated with green arrows. Inputs indicated with red arrows (color online). Initialization from MER in yellow.

We would like to comment the coupling technique proposed. The least-squares minimization problem in the magnetic equilibrium reconstruction needs to find only two scaling coefficients α and β to describe p'_{LIU} and TT'_{LIU}. This heuristic solution mimics the intuition that while the modeling and the measurements provide good knowledge of the profile features, the magnetic measurements better represent their global scaling. This assumption could be proven now with the suite of codes developed in this thesis in sec. 4 to solve the forward free-boundary equilibrium, though this was not addressed yet extensively. We expect to obtain $\alpha, \beta \approx 1$ whenever p'_{RAP}, TT'_{RAP} profiles are consistent with the magnetic measurements and vice versa. This will be investigated in detail in section 6.3.2 and the implication of this choice discussed further in this section. We will show in sec. 6.3 that this coupling is sufficient to achieve a good matching of $j_\parallel$ and p profiles between LIUQE and RAPTOR/RAPDENS, which is the end goal of kinetic equilibrium reconstruction.

There are several numerical advantages for the proposed coupling technique: the codes LIUQE, RAPTOR and RAPDENS required very little I/O modifications keeping them separated and allowing for their independent developments; with only two coefficients α and β to be found, the least-squares problem is linear and did not increase the computational cost with respect to the independent solution of the two codes; since only two basis functions are used, the solution avoids the ill-posed problem of magnetic equilibrium reconstruction, which requires to either reduce the number of basis functions or to introduce regularization techniques. In addition, the spatial details of the shape of the internal kinetic profiles depend only on the spatial resolution of the transport solver, without requiring a large number of basis function coefficients for the Grad-Shafranov equilibrium reconstruction. For example, reverse shear q

profiles can be represented in this way as well as steep pressure gradients and highly localized edge bootstrap current density in H-modes.

We would like to stress the fact that the coupling technique adopted was mainly used to achieve the real-time computational target. However both for the real-time, if the computational time would allow that, and off-line we would prefer to provide p'_{RAP} and TT'_{RAP} as extra measurements for the magnetic equilibrium reconstruction extending the number of basis functions used to represent p'_{LIU} and TT'_{LIU}, or using p'_{RAP} and TT'_{RAP} as basis function or within the basis function set. This would make it consistent with the formulation eq. (6.7) in section 3.3.4 and allow to provide weights for p'_{RAP} and TT'_{RAP}, and considering eventually, when available, extra measurements on the χ cost function. With the approach used in this chapter instead we only check a posteriori whether $\alpha, \beta \approx 1$ as a test whether kinetic estimations are consistent with magnetic data.

We also stress the fact that the Kalman Filter technique used in RAPTOR and RAPDENS could provide directly not just p'_{RAP} and TT'_{RAP}, but also the propagation of the measurements and model uncertainties, assuming additive Gaussian noise to the measurements and the process, which could be used directly as weights for p'_{RAP} and TT'_{RAP} in the cost function of the equilibrium reconstruction.

6.2.3 Differences between real-time and post-discharge kinetic equilibrium reconstruction in TCV

To help understanding the relation between the different parts of this thesis we would like to summarize here the differences between the real-time and off-line implementation of kinetic equilibrium reconstruction in TCV. In particular the different sources for the kinetic quantities appearing in the reconstruction of the kinetic profiles. The usual settings are summarized in table 6.1.

	Post-discharge	Real-time
p	$n_e T_e + n_i T_i + P_{fast}$	$n_e T_e + n_i T_i$
n_e	Thomson	RAPDENS transport + FIR
T_e	Thomson	RAPTOR transport + XTe
n_i	$n_i(\rho) = n_e(\rho)\frac{Z_c - Z_{eff}}{Z_c - 1}$	$n_i(\rho) = n_e(\rho)\frac{Z_c - Z_{eff}}{Z_c - 1}$
T_i	$\propto T_e$/transport model/CXRS	$\propto T_e$ given/ W_k matching
j_{eccd}	Toray-GA	Gaussian deposition
P_{fast}	ASTRA	To be implemented
j_{NBCD}	ASTRA	To be implemented
Z_{eff}	Imposed/ICDBSEVAL	Imposed

Table 6.1 – Comparison between assumption for real-time and post-discharge KER

The differences at present are justified by either lack of availability in real-time of the diag-

nostics or numerical expensive requirement to compute the modelling or simply ongoing development. More details on the present limitation of the real-time implementation are provided in the outlook section of this chapter.

6.3 Results of real-time KER in TCV

The results of the real-time KER performed in TCV during the discharge 62958 are presented in this section. The discharge, summarized in figure (6.2), was selected because several interesting physical events involving internal plasma profile evolution occurred (figure 6.3).

First, the initialization methodology and the computational cycle time achieved will be reported (sec. 6.3.1), then the effectiveness of the coupling methodology to provide the desired constraints to the equilibrium will be shown (sec. 6.3.2) and finally the results of the real-time KER will be compared to MER in presence of ECCD and during the formation and locking of an NTM (sec. 6.3.3).
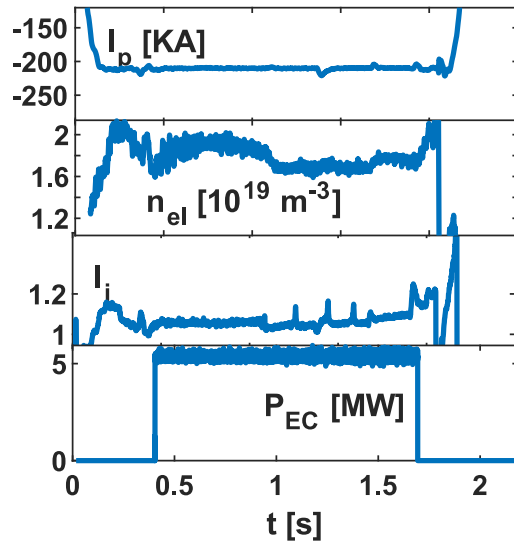

Figure 6.2 – TCV discharge 62958 main physical parameters using standard off-line magnetic equilibrium reconstruction.
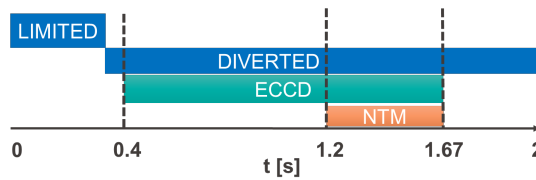

Figure 6.3 – TCV discharge 62958 event intervals.

6.3.1 Initialization and computational cycle time

In previous work, the LIUQE, RAPTOR and RAPDENS codes were implemented in Simulink and integrated in a node of the TCV plasma control system based on a i7-5930K 3.5 GHz processor [Maljaars et al. 2017]. On this node, four threads are active, each running a different part of the algorithm. Thread 1 runs the density model with the EKF filter (RAPDENS) and two instances of LIUQE, the first performing the magnetic equilibrium reconstruction (MER) with standard basis functions and the second computing the KER with p'_{RAP} and TT'_{RAP} as basis functions. Both instances evaluate also the geometrical quantities (flux surface integrals) needed for the transport code. Thread 2 is dedicated to solve Ohm's law and the electron heat diffusion equation with RAPTOR. The remaining threads were not used in this paper. LIUQE solves the GS based on a finite difference approximation, it uses a spatial (R,Z) grid of 28x65 points to match the TCV elongated aspect ratio and 17 points on ρ_ψ for the flux surface averaged integrals $g_{0,...,3}$, $T(\rho_\psi)$ and $V'_{\hat\rho}$ computed using 32 values of the poloidal angle. The linear minimization problem includes all 133 available measurements and ~ 60 free parameters including the vessel and active coil currents together with the two basis function coefficients α, β. In RAPTOR, which solves the equations based on a finite element approximation, the n_e equation is solved by the RAPDENS module using cubic splines with 4 knots packed at the edge [Blanken et al. 2018], while T_e and $\psi(\rho)$ are represented by cubic splines with 11 knots [Felici et al. 2011].
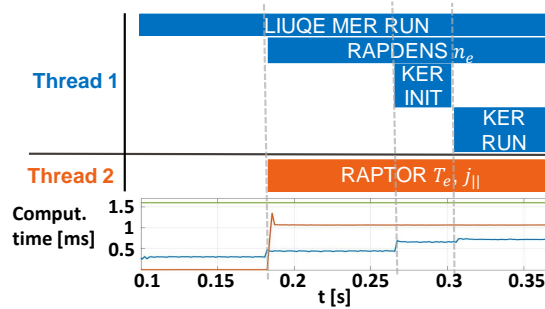

Figure 6.4 – Shot 62958. Start-up of the coupling scheme up to closed loop convergence. Computational time of thread 1 (blue) and thread 2 (orange) during different tasks and sampling period communication between threads 1.6ms (green).

The initialization procedure for the scheme (sec. 6.2.2) is shown in figure (6.4).

- The first instance of LIUQE, performing the standard MER, is initialized in thread 1.

- After waiting some time steps, to let the computation of the geometrical coefficients converge, RAPTOR starts running in thread 2 ($\sim 0.18s$) using the geometrical coefficients from LIUQE MER; when RAPTOR has relaxed from the initial conditions, the second instance of LIUQE, performing KER using p'_{RAP} and TT'_{RAP} as basis functions, is initialized ($\sim 0.27s$) from the last available solution of the MER.

- As for the MER also the KER instance of LIUQE requires some time steps for the geometrical coefficients to converge. Note that here we chose to let LIUQE evolve for

approximately 18 iterations over $\sim 30 ms$. A smaller number of iterations would probably have sufficed however in this work we wanted to be sure to have a well converged geometrical coefficients before switching to the full coupling without investigating how early in the discharge we could have achieved it.

- At $\sim 0.31 s$ the loop is closed and the convergence is obtained after few iterations, i.e. RAPTOR uses geometrical information from the LIUQE KER, while providing p'_{RAP} and TT'_{RAP} for the next time step of LIUQE KER.

- Meanwhile, the standard LIUQE MER continues to run in background for comparison and as a restarting point in case of a failure of the coupling scheme.

The computational times are displayed in figure (6.4) (bottom). The communication period between threads was set to $\sim$1.6ms, thread 1 runs during the full coupling phase in $\sim$0.75ms including two instances of LIUQE ($\sim$0.25 ms each) and the density observer ($\sim$ 0.15ms) while thread 2 runs in $\sim$1.1ms. Summing up all the computational times, considering only 1 LIUQE instance, the consistent KER could in principle run in a single thread in less than 1.6ms. Similar performances have been obtained in other discharges not reported in this work. Nevertheless, the converged coupling is achieved before the transition from limited to diverted configuration at $\sim$0.31s and before the ECCD and NTM phases (see figure 6.3), and continues to work without failures till the end of the ECCD phase ($\sim$1.67s) and of the plasma discharge.

During the analysis of the results, some erroneous settings of the real-time KER set-up were discovered due to earlier application of the code for other purposes, in particular the temperature ratio T_e / T_i was set to 4. This value is not the typically observed one TCV, as checked with the charge exchange radiation spectroscopy diagnostic to measure T_i unless strong ECRH power is applied which is not the case for the discharges analyzed in this paper. Moreover the ECCD source in the current diffusion equation was turned off. Since these discharges were obtained at the end of the then running TCV experimental campaign 2018, these shots could not be rerun immediately after. The quantitative results shown in the next section are therefore based on a re-simulation with the same real-time measurements, grid resolution and computer hardware but corrected transport model settings. In particular the T_e / T_i was set to 1.42 during the ECCD phase and 1.2 otherwise, values that are within the typical bounds observed for this type of discharges. This modification does not affect the performance of the code, reproduces exactly how the code would have performed during the discharge and therefore does not invalidate the findings of this chapter. We could have chosen to present the results of other experiments, however the erroneous settings were there during the full campaign and the physical content of the selected one was the most relevant to compare with MER.
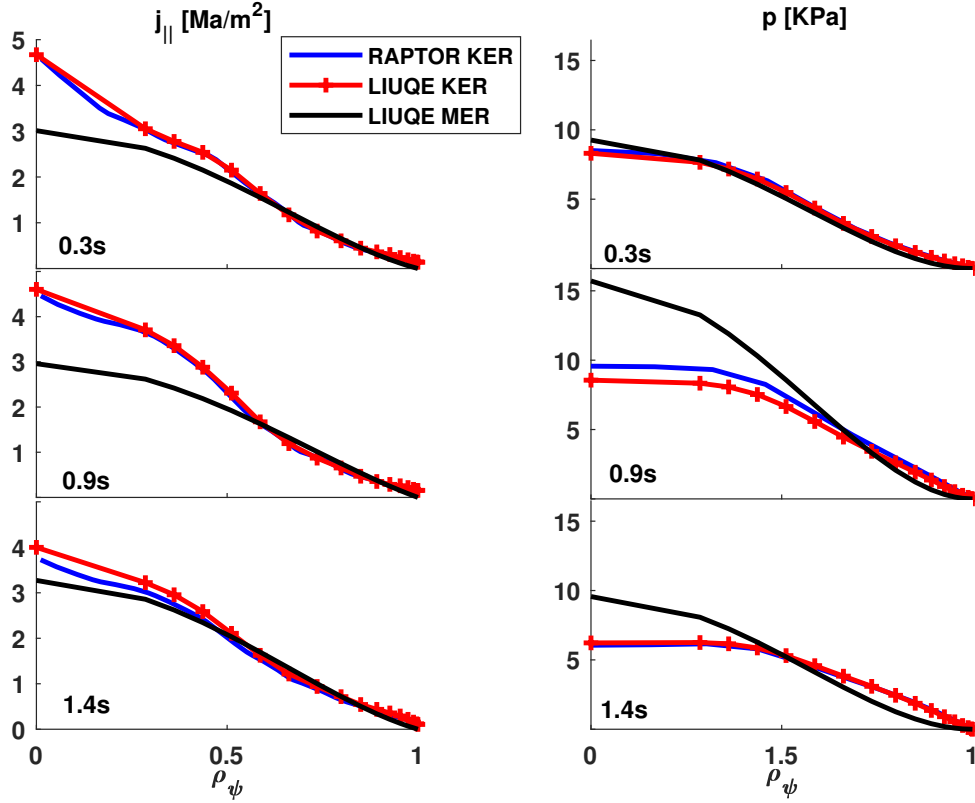
Figure 6.5 – Shot 62958. Comparison of $j_\parallel$ profile (left) and p profile (right) between RAPTOR KER(blue), LIUQE KER(red) and LIUQE MER(black) during three plasma phases: Ohmic diverted (0.3s), off-axis current drive (0.9s) and off-axis current drive in presence of NTM (1.4s).

6.3.2 Investigating the coupling methodology results

As a first result, we will prove that the coupling methodology detailed in section 6.2.2 is effective in providing $p(\rho, t)$ and $j_\parallel(\rho, t)$ constraints from measurements and modeling to the equilibrium solver. In figure (6.5) we compare the profiles reconstructed by RAPTOR KER (blue), with the ones computed by LIUQE KER (red) when p'_{RAP} and TT'_{RAP} are used as basis functions during three different experimental phases: at the beginning of the transition from limited to diverted shape (0.3s), during the ECCD phase (0.8s) and finally when the NTM is fully developed (1.4s). We find a good match for the quantities of interest, namely $p(\rho, t)$ and $j_\parallel(\rho, t)$ demonstrating consistent profiles in the equilibrium and transport codes. In particular, when the profiles from RAPTOR are consistent with the magnetic measurements, we expect that $\alpha, \beta \approx 1$ as is indeed the case in figure (6.6). Figure (6.5) aims only to show that the shape and amplitude of the profiles are coherent while a quantitative measure of them this is given directly by the coefficients in figure (6.6). We notice from figure (6.6) that a larger discrepancy is found during the limited and NTM phases, indicating that the transport modeling is less accurate in these phases. Note also that with α, β about 20% away from the ideal value of

one, the pressure and $j_\parallel$ profiles shown in Fig. 6.5 are relatively consistent. We will elaborate further on these topics in section 6.4.
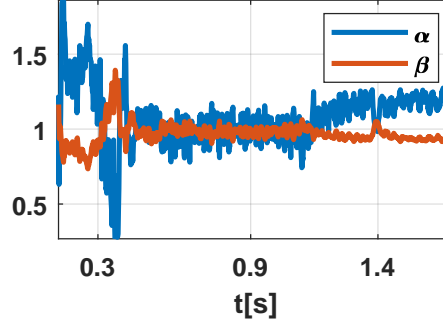

Figure 6.6 – Shot 62958. α, β basis function coefficients

6.3.3 Comparison between real-time MER and KER

In this section we will show how the implemented KER, achieving real-time performances, is able to reconstruct well the expected internal profile features and profile dynamics due to particular physical events during the plasma discharges. Every time we will refer to MER in this section we will intend the standard real-time MER routinely computed during TCV operation. In the standard MER the set of basis functions has been chosen ([Moret et al. 2015] and references therein) in order to find a compromise between having a low error of the reconstruction with respect to the magnetic measurements and keeping the least squares minimization problem well-conditioned, while avoiding under-fitting for a large range of experimental conditions. The KER, having constraints on the internal profiles coming from measurements/modeling, needs less a priori assumptions on the profiles. As expected, this allows the KER to better represent the true physical profiles. It is instructive to compare in this section the KER with the standard MER which was the only equilibrium reconstruction available in real-time so far for TCV.

We address first the contribution provided by the internal kinetic measurements to the reconstructed solution. In figure (6.5) the p and $j_\parallel$ profiles from KER (red cross) are compared to the MER (black). The central flattening of the pressure profile in KER at 0.9s is due to the broad central density profile as shown in figure (6.7) and computed by RAPDENS (red) constrained in real-time by the FIR measurements. The flattening is confirmed by the post-shot Thomson scattering data in fig.6.7 (black) [Arnichand et al. 2019] . This flat feature is propagated to the equilibrium through p'_{RAP}. The MER pressure profile instead has the dependence $p \propto (\rho^2 - 1)^2$, imposed by the basis functions adopted, hence it cannot reproduce the flattening. Given the consistency between the RAPTOR-KER and LIUQE-KER profiles provided, by the coupling and demonstrated in the previous section, we will no longer make the distinction between them as in figure (6.5) (blue and red line) . We will consider from now on the LIUQE-KER to be representative of the reconstruction, calling it simply with the label "KER".
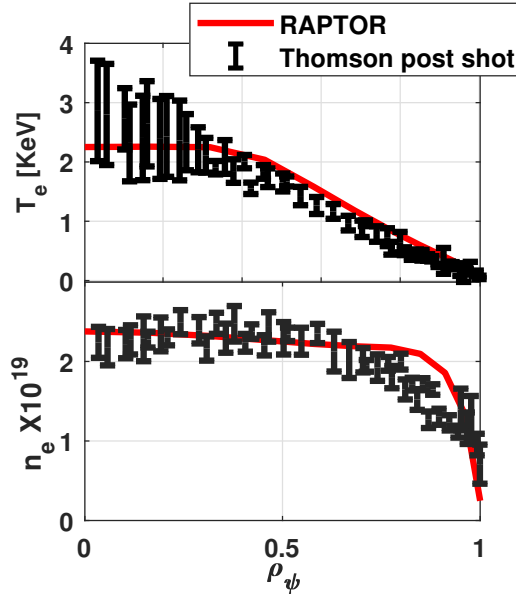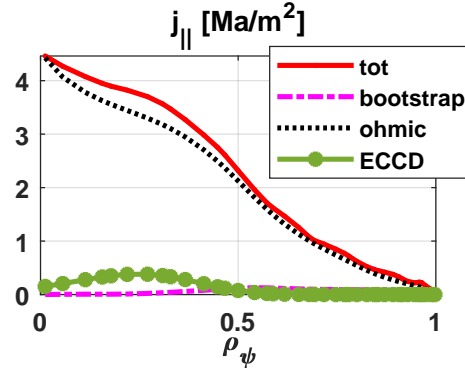
Figure 6.7 – Shot 62958@0.9s. Comparison between T_e and n_e profiles reconstructed in real-time by RAPTOR/RAPDENS and the Thomson scattering measurements available after the experiment.

We consider now the contribution provided by the $j_\parallel$ constraint. A small off-axis external current drive contribution from ECCD with constant power and deposition location is added at 0.4s while the total current is kept constant through feedback control of the central solenoid current. At 0.9s, when the current profiles are relaxed and in stationary condition, the different components of $j_\parallel$ computed in real-time by RAPTOR are shown in figure (6.8). The small contribution from ECCD (green) produces a broadening of the total current density profile (red) while the contribution of the bootstrap current (violet) is very small. In figure (6.9) we compare the $j_\parallel$ profile from KER and MER before the gyrotron is turned on (0.3s, dashed lines) and after when the current profile reaches a new stationary state (0.9s, continuous lines). The profiles from KER (red and magenta) reproduce the expected broadening highlighted with the green zone between the arrows. The MER instead seems to be little affected by this contribution as a result of both the limited choice of basis functions and the low sensitivity of external magnetic measurements to small internal profile features. In this experiment the very small amount of externally driven current provided a small difference between MER and KER results localized only in the plasma center as found in figure (6.10) where the relative difference in percentage of the flux map $\Delta\psi(R,Z) = 100 * (\psi_{MER} - \psi_{KER})/\psi_{MER}$ is displayed. A difference of 8% is found within the $\rho_{\psi_N} = 0.5$ flux surface (blue line) and less than 1% everywhere else. This is comparable with the findings of the post-discharge kinetic equilibrium reconstruction presented in the previous chapter.

The last result addresses the importance of including dynamical models together with the measurement constraints in order to reconstruct the time evolution of internal plasma profiles

Figure 6.8 – Shot 62958@0.9s. $j_\parallel$ components computed by RAPTOR
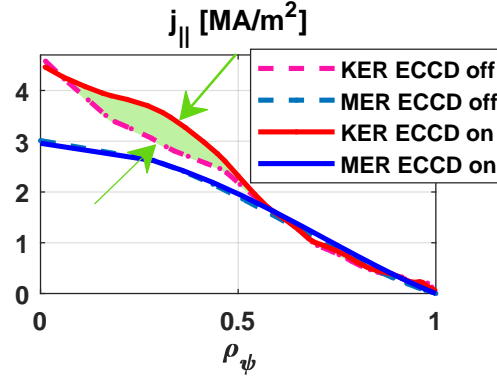
Figure 6.9 – Shot 62958. Comparison of $j_\parallel$ profiles between MER (blue, light blue) and KER (magenta,red) before (dashed lines, 0.3s) and during (continuous lines, 0.9s) the applied external ECCD.

in their correct time-scales caused by physical events during the experiment. Thanks to the closed loop introduced (figure 6.1), the KER provides improvements to the reconstruction of single time instants, as shown above, but also to the full dynamic evolution as discussed in the remaining part of this section. From $t \sim 1.2$s an NTM develops causing the central temperature to slowly drop in ~ 100ms (figure 6.11). This evolution is detected in real-time by the XTe measurement of the central T_e (green) and followed by the RAPTOR observer (red) in the correct time scale thanks to the EKF. As a direct consequence, the neoclassical conductivity $\sigma_\parallel$ in the Ohm's law, which scales as $\propto T_e^{3/2}$, drops in the central region $\rho_{\psi_N} < 0.5$ (lines from red to yellow). The $j_\parallel$ profile reconstructed by the KER follows this expected evolution. Indirectly this is also an example of a dynamical model, the current diffusion equation, that supplements the missing diagnostic for the internal plasma current density profile. The evolution of standard MER profiles (lines from blue to teal) are also shown for comparison.
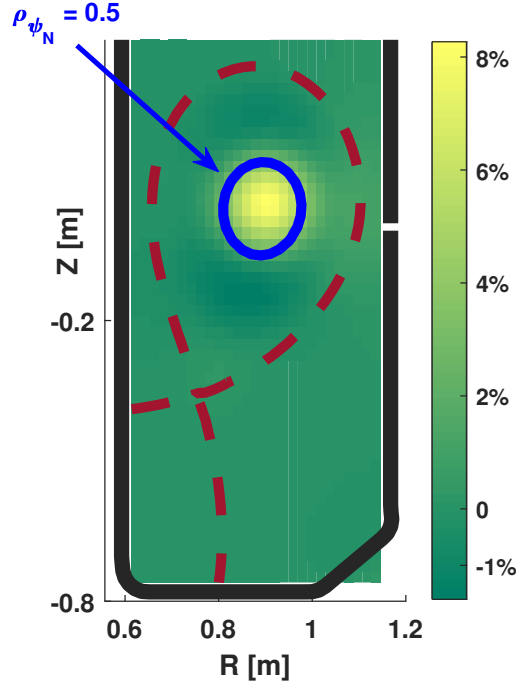
Figure 6.10 – Shot 62958@0.9s. Relative poloidal flux map difference $\Delta\psi(R,Z) = 100 * (\psi_{KER} - \psi_{MER})/\psi_{MER}$ in percentage (green to yellow colormap), with $\rho_{\psi_N} = 0.5$ surface (blue) and last close flux surface (red).
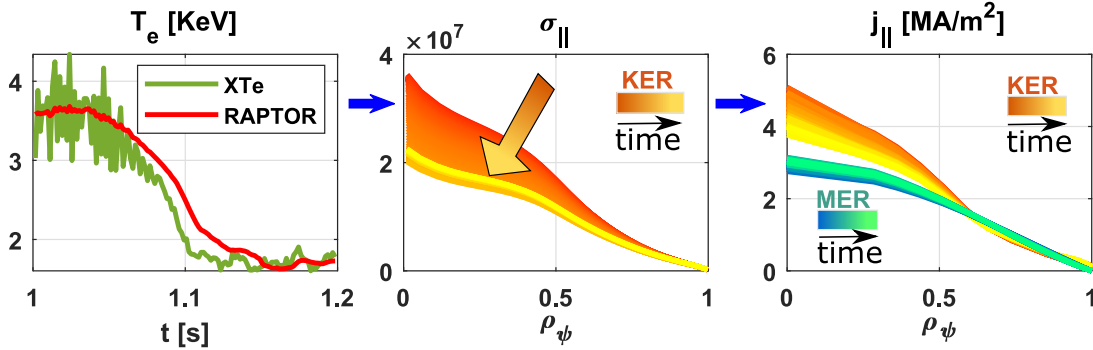
Figure 6.11 – Shot 62958. From left to right: comparison of the evolution of central T_e form real-time XTe and RAPTOR estimation during NTM formation and locking; evolution of neoclassical conductivity $\sigma_\parallel$ during the event (from red to yellow); reconstructed evolution of $j_\parallel$ from KER (red to yellow) and MER (blue to teal).

6.3.4 Estimate T_e/T_i ratio from matching the total kinetic energy between equilibrium reconstruction and transport solution

In the absence of real-time T_i measurements and reliable transport modeling for this quantity, we propose in this section an approach to estimate the T_e/T_i ratio within the implemented real-time KER, avoiding in this way to provide it as an given fixed input. This is based on the heuristic assumption that the magnetic measurements all together retain reliable information

on global plasma parameters such as the total kinetic energy W_k, i.e. the volume integral of the total plasma pressure profile p. Moreover, among the free parameters to be imposed in the transport modelling (Z_{eff}, transport coefficients, ...), T_e/T_i influences the most the estimate of the total pressure of the transport code, T_e and n_e are constrained by the available real-time measurements in our implementation.

As discussed in this chapter, we consider $p'_{LIU} = \alpha p'_{RAP}$, $T T'_{LIU} = \beta T T'_{RAP}$. Again we let α, β be found in order for the equilibrium solution to best match the magnetic measurements. From the total plasma pressure of the equilibrium reconstruction p_{LIU}, we compute the total stored energy $W_{k,LIU}$. In this approach, differently to section 6.2.2, we add a PI (proportional integral) [Ogata and Yang 2010] controller that changes the T_e/T_i input of the transport code such that $W_{k,RAP}$ matches $W_{k,LIU}$. In this way the magnetic measurements are used to constrain $W_{k,LIU}$ which is then used to estimate T_e/T_i and ensure consistency of the total stored energy between the equilibrium and the transport codes.

In figure (6.12) we compare the results obtained with $T_e/T_i = 4$, as used during the experiments, and an offline re-simulation using a PI controller. The top figure compares the total stored energy W_k for the case of $T_e/T_i = 4$ (black line LIUQE, blue line RAPTOR) and the estimation with the PI controller technique (green line LIUQE, red line RAPTOR). The middle figure shows the obtained α and β coefficients, dark/light green for the case of $T_e/T_i = 4$ and dark/light blue for the estimate with the technique explained in this section. The bottom figure shows the T_e/T_i ratio obtained from the PI controller.

As a result, the PI controller is effectively changing the T_e/T_i ratio in order to make RAPTOR W_k (red line top figure) match the LIUQE one (green line figure). This results in α, β coefficients of the simulation using this technique (dark/light blue middle figure) closer to 1 with respect to the case $T_e/T_i = 4$ (dark/light green middle figure). This confirms that the value $T_e/T_i = 4$ used during the TCV discharge provided pressure profiles not consistent with magnetic measurements.

The controller is forced to provide T_e/T_i between 1 and 4, the typical values found in TCV, at least for cases without direct ion heating as for the discharge presented in this paper. In particular we do not allow $T_e < T_i$ since in this discharge we expect dominant electron heating. During the first 0.3s, the controller would request a ratio lower than the minimum bound, explaining the poor matching of W_k during this time interval.

In previous sections we chose to fix T_e/T_i ratio equal to 1.2 during the ECCD phase and 1.4 otherwise (from comparison with offline simulations) which provided results similar to the ones obtained with the technique proposed in this section.

As a last caveat, we would like to point out that magnetic measurements are sensitive to the total plasma pressure including supra-thermal components and thus $W_{k,LIU}$ can contain a supra-thermal contribution as well. Without a proper description of those components in the transport model, this method could still be used yielding an effective ion temperature
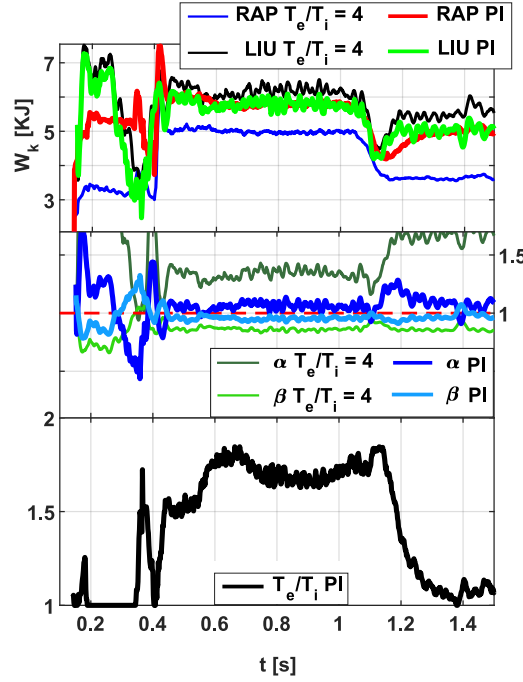
Figure 6.12 – Shot 62958. Comparison between KER with constant $T_e/T_i = 4$ and with T_e/T_i controlled by PI controller aiming at W_k consistency between LIUQE and RAPTOR as explained in section 6.3.4. Top figure: W_k comparison between $T_e/T_i = 4$ (blue RAPTOR , black LIUQE) and with PI controller (red RAPTOR, green LIUQE). Middle figure: α, β comparison between $T_e/T_i = 4$ case (dark/light green) and re-simulation with PI controller (dark/light blue). Bottom figure: T_e/T_i estimate from PI controller case.

but at the cost of a reduced fidelity in particular when computing quantities depending on T_i such as the energy transfer between ions and electrons or the bootstrap current. Additionally these supra-thermal pressure components could be anisotropic whereas LIUQE assumes an isotropic pressure. No significant supra-thermal pressure nor anisotropy are present in the discharge presented here. Modelling for fast ions should be included in the transport code as done in ASTRA in the off-line reconstruction.

6.4 Limitations of current approach and outlook

We have shown that the formulated KER in 6.2.2 can be implemented in real-time with very little modifications to both the equilibrium reconstruction and transport codes. The present technique has several limitations in part due to practical constraints in TCV. We summarize them and propose improvements since they are typical of what is needed in present and future machines.

The electron density n_e profile in the current implementation is computed by solving the diffusion equation constrained by the FIR measurement and fringe jumps can be avoided

thanks to the model-based approach included in RAPDENS [Blanken et al. 2018]. However using the FIR diagnostic is less precise than using Thomson scattering [Arnichand et al. 2019]. As an example in shot 62958 at 0.9s, the FIR measurements provides an edge steep gradient feature (figure 6.7 bottom) which is not confirmed by the Thomson scattering measurements.

The electron temperature T_e profile in the current implementation is computed by solving the electron heat diffusion equation. Only the central value of the temperature is constrained by the real-time XTe estimation. Therefore, localized features (H-mode pedestal or flattening due to an internal mode) cannot be captured unless included somehow in the predictive modeling (which is the case for RAPTOR but this was not tested here).

Both T_e and n_e real-time reconstruction will benefit from the real-time Thomson scattering system, and such a system is planned to be commissioned in the coming campaign on TCV. Eventually an EKF technique will be implemented to combine the 1D diffusion modeling with the real-time Thomson measurements as done for the FIR in the current approach. In parallel, the predictive capability should be improved as well, in particular regarding the transport coefficients. RAPTOR can already include transport coefficients obtained from neural networks trained on gyrokinetic simulation results [Citrin et al. 2015] and this should be included in our approach as well which will help applying it to other machines.

The parallel current density ($j_\parallel$) is obtained by solving the current diffusion equation (eq. (2.56)). Unfortunately no internal measurements (MSE, polarimetry) are available at present in TCV neither to constrain the modeling nor to confirm it. In other tokamaks these diagnostics are used to constrain the equilibrium solution directly, also in real-time as in [Lao et al. 2005; Brix et al. 2008; Qian et al. 2016; Li et al. 2011; Coelho et al. 2009; Holcomb et al. 2006]. In principle, real-time MSE measurements can also be included in RAPTOR with the EKF technique as described in [Messmer et al. 2018]. We favour the EKF approach when eventually porting this tool to other tokamaks that have real-time MSE measurements, or other relevant diagnostics in general.

An improvement on the description of the current sources can be obtained making use of the real-time capable ray tracing code TORBEAM [Poli et al. 2018], instead of the Gaussian deposition model adopted in this chapter. This code has already been coupled in real-time to RAPTOR in AUG and TCV and provides the real-time deposition location and deposited power of the ECRH sources.

The lack of modelling for the fast-ions contribution from external sources is the main missing feature for the transport modelling with RAPTOR in the present implementation, with respect to the off-line analysis performed with ASTRA. A real-time capable code for simulating the effects of NBI sources (RABBIT, [Weiland et al. 2018]) will also be included in the near future.

Another important aspect that has not been considered in the current implementation is the internal profile crash due to the presence of sawtooth instabilities. This leads, in the present implementation, to non-physical central safety factor much below 1. In [Fischer et al. 2019] it

was shown that the CDE coupled to the equilibrium solution is able to reproduce the measured q-profile evolution associated to a sawtooth crash, when sawtooth-induced current relaxation is accounted for by reconnection models [Kadomtsev 1987], and the fast ions contribution is correctly modeled. These reconnection models are already implemented in RAPTOR [Piron et al. 2017] but were not used yet in this analysis.

The fast particle contribution to the current drive and the total pressure has not been considered in the current approach, however the previously mentioned RABBIT code [Weiland et al. 2018] includes these effects.

In the first results presented, T_i profile is assumed to be proportional to T_e and the proportionality constant is considered as a parameter to be specified a priori. A sensitivity analysis revealed that the j profile reconstructed by the transport solver is not very sensitive to this parameter, since mainly T_e is important for σ_{neo}, j_{eccd} and j_{bs}. However, a wrong choice of this parameter leads to a poor estimate of the total plasma pressure in the transport solver. To mitigate this problem we let p' free to be scaled in the equilibrium solver by the coefficient α in order to match the magnetic measurements in the least squares sense. Hence, α different than 1 indicates that the total plasma pressure of the transport solver is not consistent with the magnetic measurements. Another possible approach is to include the T_i evolution equation in case a reliable transport modeling is available and/or benefit directly from CXRS real-time measurements if available. In the absence of that, another solution is to adjust in real-time the T_e/T_i ratio in order to match the total stored kinetic energy W_k between the equilibrium solution and transport solution. This approach is detailed in section 6.3.4 and was found very promising but has limitation in presence of fast-ions contribution.

The n_i profile is presently considered to be proportional to n_e in order to respect the quasi-neutrality assumption given the knowledge of effective charge Z_{eff}. The lack of a reliable estimation of Z_{eff} is shared with the post-discharge implementation analysis. In other tokamaks more precise estimate from charge exchange diagnostic may be available, which can help in its identification. A possible solution in real-time could be estimating Z_{eff} to match the loop voltage between the current diffusion and the equilibrium reconstruction as in [Felici 2011]. In the off-line analysis, this was estimated from matching the loop voltage on an integral stationary state current diffusion equation as discussed in Appendix B. Models to study the radial impurity transport are under investigation but not yet sufficiently mature to consider their use in real-time. More consistent approach will be investigate for example to consider Z_{eff} as one of the many free-parameters to be estimated from the reconstruction problem as done in [Boyer et al. 2019]. This would however add non-linearities to the optimization problem making it more difficult to solve. The estimation of Z_{eff} is an active field of research so for the moment in the current implementation imposing a priori constant value based on results from post-discharge analysis is the best we can obtain at this stage.

To conclude this section we would like to comment on one of the most natural continuation of this work. In [Messmer et al. 2018] the LIUQE and RAPTOR codes, without a self-consistent

coupling, were used in TCV to develop a model predictive control technique to control ι profile and β. In the present paper we did not close the loop with the real-time controllers yet. However, the difference between the ι profile between LIUQE and RAPTOR observed in [Messmer et al. 2018] is now resolved thanks to the achieved KER. Moreover, the RAPTOR results depend on the geometrical coefficients given by LIUQE which non-linearly depend on the ι profile of the latter. Therefore, having consistent profiles in LIUQE removes one source of uncertainty for the ι estimation of RAPTOR which is the only estimate that the controllers rely on due to the lack of direct measurements of the current density profile in TCV. For this low plasma current discharge the difference is not expected to be significant, but we argue that it might become important in case of hybrid or reversed shear scenarios for example. A dedicated investigation will be carried out on the influence of KER to the performance of the real-time profile controllers in particular for advanced scenarios.

6.5 Conclusions

Whenever an accurate reconstruction of the internal flux surface shapes and plasma profiles is required, external magnetic measurements are not sufficient and kinetic equilibrium reconstruction should be addressed, as shown in section 4.6 especially when internal profile features are present due to both external control sources or plasma transport physics. This is particularly true for high performance scenario where these features are present "by design" as intrinsic component to achieve desired performance. For example turbulent transport depends on the safety factor and its derivative in advanced scenarios. With this aim in chapter 5 we showed the implementation of KER for post-discharge analysis in TCV.

However, to achieve and maintain the performances required for future tokamaks, such as ITER, a real-time control of the kinetic profiles but also supervisory control functionalities such as plasma monitoring for disruption avoidance will benefit from the improved quality of the reconstructed plasma state.

In this chapter we implemented and tested during TCV plasma operation a real-time kinetic equilibrium reconstruction. New challenges had to be faced compared to the post-discharge analysis, related mainly to the reduced number of measurements available and the requirement to achieve computational time faster than the diffusion time scales of the kinetic profiles, which is particularly stringent for the relatively small tokamak TCV.

We proposed a simple coupling suited in particular for real-time application to allow providing internal profile information to the equilibrium problem. This is based on using the estimation of the internal profiles from the transport modelling and real-time measurements as basis functions for p' and TT' to be used in the solution of the equilibrium. Only two coefficients for the basis function expansion, one for p' and one for TT', are then left free to be re-scaled to match the external magnetic measurements in the least squares sense.

The choice of the coupling technique proposed was based on the good results obtained with

the off-line KER (previous chapter) and aimed to meet the real-time computational target. When tested on the TCV real-time control system, it required negligible additional computational time with respect to running the equilibrium and transport codes independently. Nevertheless it enables the full freedom for functional dependence while keeping small number of free coefficients. Furthermore, our results show that a tight coupling between the codes is not strictly necessary for real-time purposes, allowing their independent development. The coupling technique proved to converge in few iterations and to provide globally correct p and $j_\parallel$ evolution for the equilibrium solution, while accurate reconstruction of local features depends more on the limitation of the diagnostic set.

We stress the importance to be able to obtain robust estimation of the plasma state, especially in real-time when the control algorithm and supervisory control rely on this reconstruction. For this reason we always prefer to perform the reconstruction of the kinetic profiles by merging the information of a forward transport model with the available real-time measurements, in order to always have at least an estimation, prevent non-physical behavior of potentially failing diagnostics but at the same time correct the error in modelling with the available measurements. This is achieved by the RAPTOR code (estimating T_e and $j_\parallel$) and RAPDENS code (estimating n_e) exploiting the extended Kalman filter technique.

For the first time, kinetic equilibrium reconstruction has been performed in real-time during tokamak operation, coupling consistently an equilibrium reconstruction code (LIUQE) with transport codes (RAPTOR and RAPDENS) used as state observer, thanks to the simple coupling technique developed. This technique is directly applicable to other devices and indeed its implementation in ITER Plasma Control System Simulation Platform has started.

We also compared the results of the KER with the real-time standard magnetic equilibrium reconstruction routinely performed in TCV, which considers external magnetic measurements only, for cases where we expected internal plasma profile modifications due to physical events. In all cases, contrary to MER, the implemented KER was able to reproduce these expected modifications, improving not only the reconstruction on a single time instant but also allowing the equilibrium solution to follow the time evolution of internal profiles driven by the transport modeling and real-time measurements. Moreover, the limitations of the approach together with the improvements expected in future developments have been discussed in details.

To conclude we would like to notice that, thanks also to the suite of forward codes developed in Chapter 2, we will aim to have the full pipeline from simulating the plasma behavior in many different conditions, both on static instant and during the most important transient phases, to generate synthetic data and eventually modelling the measurements and process noise, and then perform magnetic and kinetic equilibrium reconstruction both with the off-line approach and the real-time simplification hypothesis. A proof-test example of that was shown for a static free-boundary equilibrium case during standard H-mode scenario in ITER. This will allow us to study in depth the improvements provided by kinetic equilibrium reconstruction, knowing the real solution which generated the data, and most importantly to test the relevance of every

simplification hypothesis adopted in performing post-discharge and real-time reconstruction. This will be an extremely useful analysis to assess the accuracy and robustness of all our suite of codes in primis for TCV but also for other devices.

7 Conclusions

This thesis focuses on two topics directly relevant for tokamak operation: the development of a tokamak simulator and the consistent reconstruction of plasma equilibrium and kinetic profiles both in post-discharge analysis and in real-time.

"LIUQE-suite" for free-boundary static/evolutive and forward/inverse problems

A fully Matlab-based suite of routines called "LIUQE-suite", sharing the same optimized low level routines, has been developed at SPC-EPFL addressing multiple problems related to the free-boundary equilibrium. Before this thesis it included the computation of the coil currents for a sequence of desired plasma equilibria (FBT code), the MER from synthetic/experimental data both in post discharge analysis and in real-time (LIUQE code). In this thesis the optimized low level routines were exploited aiming to develop a fast control oriented simulator to test, design and verify the controllers for plasma shape, position and vertical stability control.

Free-boundary Grad-Shafranov Evolutive (FGE) code The FGE code developed in this thesis, and presented in chapter 4, solves the evolution of the current, through plasma state equilibria, coupling a 0D resistive evolution of the total plasma current obtained from the radial integration of the flux surface averaged current diffusion equation. The novelty, among the several other codes available in literature to perform similar analysis, stands in the numerical monolithic coupling of the current diffusion equation with the other equations of the system. A novel linearization of the system, on approximate free-boundary equilibrium solutions, is presented including the 0D current diffusion equation. This enables faster approximate simulations and the design of linear controllers. Previously, either the linearization of the free boundary without the CDE or with the CDE but for fixed plasma displacement were presented in literature. We validated FGE, comparing the linear growth rates of vertical displacement events, against the RZIP model which assumes rigid displacement of the plasma. The CDE model was further validated, after coupling FGE to the "hybrid" real-time control system used for position control in TCV, against the actuator requests of a re-simulation of TCV experiment, finding good agreement in all cases. Many potential uses are foreseen including adding

progressively more physics, addressing reconstruction problems with dynamic evolution of the current in conductors during transient plasma events and develop controllers for unusual plasma shapes such as doublets in TCV.

Free-boundary Grad-Shafranov Forward Static (FGS) code The FGS code developed in this thesis solves the free-boundary equilibrium forward static equilibrium problem given the currents in the external conductors and specification of the plasma profiles. The code was used as a starting point to investigate different formulations and aspects of the magnetic equilibrium equilibrium (MER) problem. A generic MER solver, for the related non-linear least-squares optimization problem, was developed starting from FGS to investigate the impact of some simplification hypotheses adopted by LIUQE, presented in section 4.5: the non-physical numerical stabilization strategy, which results in a vertically shifted solution that does not strictly respect the Grad-Shafranov equation; neglecting the variation of the synthetic diagnostics with respect to the plasma flux map when minimizing the least-squares errors relative to the measurements, which does not allow finding a proper minimum of the least-squares problem. All these contributions when tested on noise-free and real experimental data provided small modifications to the final reconstruction of the plasma shape and profiles. We notice that the purpose of the project was not to develop another code solving MER for the LIUQE-suite, rather to test and confirm the robustness of the LIUQE one.

Uncertainty quantification for MER solution is useful since this analysis is ubiquitous as a starting point for many other analyses, for example for kinetic equilibrium reconstruction discussed later. The Bayesian approach provides a formal framework to propagate correctly the uncertainties of all measurements to the final reconstructed plasma state. However, due to the necessity of solving many times the free-boundary equilibrium problem in order to sample from the posterior distribution, few applications for the MER problem are found [Von Nessi et al. 2013, 2014]. A fast forward solver could enable to bring this analysis to a more routine use. We used FGS to implement, only as a proof-of-principles, a Bayesian approach and compute the uncertainty propagation of the magnetic equilibrium reconstruction. We confirmed in addition, as a benchmark, when this Bayesian approach coincides with the frequentist approach.

FGS and FGE base their numerical solutions on the Jacobian Free Newton Krylov (JFNK) solver, which combines the stability properties of Newton algorithm and does not need the explicit knowledge of the Jacobian of the problem. The latter is not known analytically for the free-boundary equilibrium problem in continuous space representation, due to the non-linearity of finding the plasma boundary. Thanks to the flexibility of the JFNK, all the forward and reconstruction problems developed in this thesis, once formulated as monolithic root finding problem, could be solved with the same solver. Another novel contribution of this thesis is also the derivation of the analytic Jacobian in Appendix C for the free-boundary problem, specific to the finite differences discretization, which can enable the use of a standard Newton method. This was inspired by [Heumann et al. 2015] where the Jacobian was obtained for the finite elements discretization. The implementation was not attempted in this work, but could

potentially speed up FGS and FGE.

Kinetic equilibrium reconstruction (KER)

Post-discharge KER. Kinetic Equilibrium Reconstruction is the consistent reconstruction of the plasma shape and kinetic profile making use of free-boundary equilibrium, external magnetic measurements, internal kinetic measurements and modeling.

Starting from the integrated data analysis tools available before this thesis, which did not consider using internal profile information to constrain the equilibrium reconstruction, we formulated the KER problem suited for the diagnostic set of TCV for post-discharge analysis, carefully highlighting the simplification hypotheses and criticisms. What is implemented for TCV is very similar to the Kinetic-EFIT approach [Meneghini et al. 2015].

The implementation is then based on a simple loop performing in order: the equilibrium reconstruction code with LIUQE, map the Thomson scattering and CXRS (when available) measurements into 1D profiles, compute the current and heat deposited by gyrotrons with the TORAY-GA, compute diffusion equation and neutral beam deposition with ASTRA, provide the plasma profiles information to the equilibrium reconstruction.

We compared in chapter 5 MER against KER, finding that for most of the TCV experiment analyzed in this thesis, which are low performance discharges, KER does not provide important modifications to the internal flux surface shape, hence to the diagnostic mapping and to the solution of the transport equations. Internal changes of the flux surfaces can be appreciated for external current drive scenarios or internal transport barrier features. These can still be relevant when KER is used for stability analysis or gyrokinetic studies. However several sources of uncertainties due to the limited set of diagnostics, simplification hypothesis and model uncertainties such as in particular large uncertainty on T_i and Z_{eff}, have effects on the final solution potentially at the same order as the improvements obtained by having a consistent equilibrium. This indicates that KER implemented in TCV, while globally improving MER by providing physically expected features to the pressure and current density profiles of the equilibrium solution, is not conclusive, still has significant uncertainties, and would largely benefit from an improvement of the diagnostic set and/or physical models as well as a proper sensitivity and uncertainty propagation analysis, as for example performed in the integrated data analysis IDA [Fischer et al. 2010]. On the other hand, the possibility for routine use of KER analysis developed in this thesis provides insights on which diagnostics and physics models need first to be improved and/or verified.

Real-time KER. Internal plasma profile features, a natural characteristic of high performance operation, need to be maintained in real-time during the plasma experiment in order to achieve the desired performances. Moreover they are associated to the trigger of plasma instabilities which degrade the plasma performances and might damage the tokamak. KER is therefore useful also in real-time to improve the reconstruction of the plasma state in order to

inform the real-time controllers for profile shaping and plasma supervision. However the real-time implementation requires to solve additional challenges due to the tight computational time requirements, the reduce set of diagnostic availability and their potential degradation during experiment.

In this thesis, for the first time, KER was performed in real-time during tokamak operation [Carpanese et al. 2020], coupling a free-boundary equilibrium code with a flux surface averaged transport code. The results were presented in chapter 6. The equilibrium reconstruction code LIUQE receives the current density and pressure profiles from the transport code RAPTOR [Felici et al. 2011] and from RAPDENS [Blanken et al. 2018]. These combine the evolution of the flux surface averaged current density equation, the electron temperature and electron density diffusion equations with the available kinetic measurements, making use of the extended Kalman filter technique.

We developed a simple technique to couple the free-boundary equilibrium solution with the transport code, suited for real-time application, and applied KER during TCV operation showing how the plasma profiles in LIUQE follows the dynamics of the internal profile features better than MER. We stated already for off-line KER that many source of uncertainties are still present in the current implementation, which for the real-time cases are enhanced by the smaller set of diagnostics available. What is shown in this thesis has to be intended therefore as a demonstration that KER can be performed in real-time, especially in bigger tokamaks such as ITER where resistive time scales are much longer than in TCV. The accuracy will be progressively improved including more and more diagnostics and better physics models in the formulation.

In conclusion, this thesis provides significant improvements to both the kinetic equilibrium reconstruction for the post-discharge and real-time analyses, developing techniques which could be of direct use for future reactor relevant experiments, where internal profiles feature is a necessary requirements to achieve and control the desired performances. Moreover, the predictive solver developed will be the basis for many new applications in TCV, where highly shaped plasmas can be obtained and need to be controlled accurately.

A (Extended) Kalman Filter for parameter and state estimation

The Kalman Filter (KF) [Kalman 1960] is an algorithm to estimate the state x and parameter θ of a dynamical system combining a forward model with the available measurements. It is part of the so called Bayesian filters family, which are techniques to estimate recursively the posterior distribution $p(x_k|y_{1:k})$ for the state, at the time instant k, given the measurements $y_{1:k}$ up to k. The parameter θ estimation can be included by considering them as extra states. In this thesis it was used in the implementation of the real-time KER [Carpanese et al. 2020] by RAPTOR [Felici et al. 2011] and RAPDENS [Blanken et al. 2019], to estimate the $T_e(\rho, t)$ and $n_e(\rho, t)$ from the XTe and FIR diagnostics. However it is not only suited for real-time application but it can be exploited in every reconstruction problem that involves a dynamic forward model, such as KER or the estimation of Z_{eff} as in Appendix B. We provide in this section a simple, not complete, explanation to help the reader in understanding the corresponding part of the thesis and the connection with the Bayesian inverse problem described in section 3.1.2. The content of this Appendix is largely taken from [Särkkä 2013].

To perform Bayesian inversion for a dynamic model, one could in principle use the Bayes' rule to compute the joint posterior distribution given all the states and all the measurements at all the time slices.

$$p(x_{0:T}|y_{1:T}) = \frac{p(y_{1:T}|x_{0:T})p(x_{0,T})}{p(y_{1:T})} \qquad (A.1)$$

where $x_{0:T} = \{x_0, ..., x_T\}$ is the estimate of the state and $y_{1:T} = \{y_1, ..., y_T\}$ the observed measurements. As in section 3.1.2 the likelihood $p(y_{1:T}|x_{0:T})$ is the probability of experiencing the measurement $y_{1:T}$ given the knowledge of the state $x_{0:T}$, the prior $p(x_{0,T})$, describes our prior belief on the state, and the evidence is defined as $p(y_{1:T}) = \int p(y_{1:T}|x_{0:T})p(x_{0:T})dx_{0:T}$. Unfortunately when the number of time steps increases the dimensionality of the posterior increases as well, making the computational problem intractable, particularly when the forward model contained in the likelihood is numerically expensive to compute.

First of all, one needs to reduce the correlation between time steps. This is achieved by assuming Markovian processes, where the state x_k depends only on the previous time step

Appendix A. (Extended) Kalman Filter for parameter and state estimation

x_{k-1}, defined in terms of transition probability distribution $p(x_k|x_{k-1})$. Suppose to have a forward deterministic model such that $x_k = F(x_{k-1}, v_{k-1})$ and assuming that the model has no error, then $p(x_k|x_{k-1}) = \delta(x_k - F(x_{k-1}))$, where δ is the Dirac distribution. If the model is assumed to have errors, for example some of the parameters present white noise, then $p(x_k|x_{k-1})$ would be the corresponding distribution function. In case of RAPTOR for the real-time KER for example, $F(x_{k-1}, v_{k-1})$ is the temperature diffusion equation. An additive white noise is assumed, hence $p(x_k|x_{k-1}) \propto N(F(x_{k-1}), \sigma)$ and σ is a given input which describes the process uncertainty.

Secondly the purpose of the Bayesian filter is not to estimate the full distribution eq. (A.1), but only the **marginal posterior distribution** recursively,

$$p(x_k|y_{1:k}) \quad k = 1,.., T \tag{A.2}$$

where we notice that x_k, differently then eq. (A.1), is only considered at the instant k and depending on all the previous measurements up to k. The idea behind is to use as a prior the posterior computed at $k-1$, in order to compute the marginal posterior at the instant k. The recursive steps, which we will refer to as Bayesian filter equation, are given by

1. Initialization: Initialize a prior distribution $p(x_0)$.

2. Prediction: Compute the predictive distribution of the state x_k

$$p(x_k|y_{1:k-1}) = \int p(x_k|x_{k-1}) p(x_{k+1}|y_{1:k-1}) dx_{k-1} \tag{A.3}$$

3. Update step: Given the new measurement y_k, use the Bayes's rule

$$p(x_k|y_{1:k}) \propto p(y_k|x_k) p(x_k|y_{1:k-1}) \tag{A.4}$$

The Kalman Filter (KF) is a particular closed form solution of the Bayesian filter, when the forward model governing the state evolution $F(x_{k-1}, v_{k-1})$ is a linear function of the previous state and inputs. A Gaussian noise is assumed both for the measurements and the process. The Extended Kalman Filter, as the name suggests, is the extension of the KF to non-linear models, which is based on local linearization of $F(x_{k-1}, v_{k-1})$.

To clarify it, we make the example of the estimation of T_e with RAPTOR. In order to use the EKF one needs:

- A forward dynamic model $x_k = F(x_{k-1}, v_{k-1})$, the T_e diffusion equation, able to predict the evolution of the state $x_k = T_e(\rho, t_k)$, given the state at $k-1$, the inputs v_{k-1}, represented by the transport coefficients, the heat sources and boundary condition.

- A model for the simulated measurements $y_k = H(x_k)$, which provides the synthetic diagnostic from the knowledge of the state x_k. For the case of the T_e this is the value of

the central temperature to be compared in real-time to the estimation from XTe soft X-ray measurements.

- Assume additive Gaussian type of noise both for the measurements and the process noise. This defines the likelihood $p(y_k|x_k)$ and the state transition probability $p(x_k|x_{k-1})$ as a Normal distribution. The covariance matrices Q,R, which potentially can be time dependent, describe respectively the noise content of the process, hence of the T_e diffusion equation, and of the measurements. The matrices Q,R are given inputs to the Kalman Filter. They correspond to provide assumptions of the type of error. In the frequentist interpretation this correspond to providing the weights for the χ^2. Indeed most of the time the covariance matrix is assumed simply as a diagonal matrix with the standard deviation of the different measurements in the diagonal.

- The EKF assumes a marginal posterior distribution $p(x_k|y_{1:k}) = N(x_k|m_k, P_k)$, where x_k is the prediction for the forward model F. The goal of the EKF is therefore to compute the mean m_k and the covariance matrix P_k of the marginal posterior, in order to respect the Bayes filter equations eq. (A.3),eq. (A.4). This means to compute an estimate $\hat{T}_e(\rho, t)$ including its uncertainty estimation.

The EKF update rule for the computation of m_k can be expressed as,

$$m_k = x_k + K_k * (y_k - \tilde{y}_k) \tag{A.5}$$

$$\tag{A.6}$$

where K_k is called the Kalman Filter Gain, which depends on the previous state mean m_{k-1}, the covariance matrices Q, P and all the previous measurements, and guarantees that $p(x_k|y_{1:k}) = N(x_k|m_k, P_k)$. A similar equation can be written for the state covariance P_k. We refer to [Särkkä 2013] for the actual definition of the Kalman filter gain.

In summary, to perform parameter and state reconstruction with a Bayesian approach, when the model involved is a dynamic model, Bayesian filters, such as EKF, allow to obtain a recursive estimation of the posterior distribution function. This provides at the same time an estimate of the parameters and the state which combines the information from the forward models and the measurements, providing also an estimate of the uncertainty propagation. The EKF was implemented in the code RAPTOR and RAPDENS before this thesis to estimate T_e and n_e in real-time. We are planning to apply this to FGE to estimate the evolution of the current in passive structures during transient events, and potentially also to perform KER.

B Estimate Z_{eff} using the current diffusion equation

In most general cases, as discussed in eq. (3.14), Z_{eff} is considered as one of the free-parameters to be estimated from kinetic equilibrium reconstruction in order to minimize the least-squares error composed by both magnetic and kinetic measurements constrained by the several transport and equilibrium modelling. However one can estimate Z_{eff} from an inverse problem starting only from the current diffusion equation, possibly under the assumption of stationary-state. We discuss here this approach since it is at the basis of the SPC-ICDBSeval [O.Sauter 2016-2020] routine often used in the KER implemented in TCV (section 3.3).

As always, when deriving an inverse problem, we start from the forward model for the current diffusion equation [Hinton and Hazeltine 1976].

$$\begin{cases} \sigma_{\parallel}(Z_{eff})\left(\frac{\partial \psi}{\partial t} - \frac{\hat{\rho}\dot{\Phi}_B}{2\Phi_B}\frac{\partial \psi}{\partial \hat{\rho}}\right) = \frac{T^2}{16\pi^2\mu_0\Phi_B^2\hat{\rho}}\frac{\partial}{\partial \hat{\rho}}\left(\frac{g_2 g_3}{\hat{\rho}}\frac{\partial \psi}{\partial \hat{\rho}}\right) - \frac{B_0}{2\Phi_B\hat{\rho}}V'_{\hat{\rho}}[j_{bs}(Z_{eff}) + j_{cd}] \\ \left(\frac{g_2}{4\pi^2\mu_0}\frac{1}{V'_{\hat{\rho}}}\frac{\partial \psi}{\partial \hat{\rho}}\right)\Big|_{\hat{\rho}=1} = I_{pl}(t), \qquad \frac{\partial \psi}{\partial \hat{\rho}}\Big|_{\hat{\rho}=0} = 0 \end{cases} \tag{B.1}$$

We consider that $\Phi_b(t)$, $T(\rho,t)$, $g_2(\rho,t)$, $g_3(\rho,t)$, $B_0(t)$, $V'_{\hat{\rho}}$ are known, for example provided by the magnetic equilibrium reconstruction with LIUQE. Also $I_p(t)$ is given either directly from the measurements or from the MER with LIUQE. The external current drive $j_{cd}(\rho,t)$ is assumed to be known including both the contribution of the gyrotrons and the neutral beam when used.

The previous eq. (B.1) contains the parameter Z_{eff}, which enters both in the $\sigma_{\parallel}$ and the bootstrap current contribution j_{bs}, and with a smaller dependency to j_{cd} which we neglect in this derivation. We consider here $Z_{eff}(t)$ is constant over the radius. The inverse problem aims therefore to reconstruct the unknown free-parameter $Z_{eff}(t)$ given a set of measurements. We consider only one measurement $\langle\frac{\partial \tilde{\psi}_B}{\partial t}\rangle_t$, which is the time derivative of the $\tilde{\psi}_B$ obtained from the equilibrium reconstruction where with $<>_t$ we indicate a time average to remove high frequency oscillation (equivalent to applying a non-causal low pass filter to the signal). We use the symbol ~ to indicate that it is considered as measurement for the system. $\langle\frac{\partial \tilde{\psi}_B}{\partial t}\rangle_t$ is typically close to the time derivative of the flux loop measurements, hence sometimes this

measurement is directly used.

As discussed several times starting from section 3, there are several ways to combine the forward model and measurements to estimate Z_{eff}. Being a dynamic forward model, the Extended Kalman Filter technique, explained in appendix A, can be applied as performed for this specific problem in [Boyer et al. 2019]. Another option is to use the frequentist approach leading to non-linear least-squares problem,

$$
\begin{cases}
\sigma_{\parallel}\left(\frac{\partial\psi}{\partial t} - \frac{\hat{\rho}\dot{\Phi}_B}{2\Phi_B}\frac{\partial\psi}{\partial\hat{\rho}}\right) = \frac{T^2}{16\pi^2\mu_0\Phi_B^2\hat{\rho}}\frac{\partial}{\partial\hat{\rho}}\left(\frac{g_2 g_3}{\hat{\rho}}\frac{\partial\psi}{\partial\hat{\rho}}\right) - \frac{B_0}{2\Phi_B\hat{\rho}}V'_{\hat{\rho}}j_{ni} \\
\left(\frac{g_2}{4\pi^2\mu_0}\frac{1}{V'_{\hat{\rho}}}\frac{\partial\psi}{\partial\hat{\rho}}\right)\Big|_{\hat{\rho}=1} = I_{pl}(t), \qquad \frac{\partial\psi}{\partial\hat{\rho}}\Big|_{\hat{\rho}=0} = 0 \\
Z_{eff} = \operatorname{argmin}(<\frac{\partial\tilde{\psi}_B}{\partial t}>_t - \frac{\partial\psi}{\partial t}\big|_{\hat{\rho}_B})^2
\end{cases}
\tag{B.2}
$$

where $\frac{\partial\psi}{\partial t}\big|_{\hat{\rho}_B}$ is computed from the solution of the CDE equation. Many different measurements dependent on the state could eventually be added.

We discuss here the particular case of eq. (B.2) under stationary state assumptions. We recall the distinction between the steady-state $\frac{\partial\psi}{\partial t} = 0$ and the stationary state where $\frac{\partial\psi}{\partial t}(\hat{\rho}) \neq 0$ and $\frac{\partial\psi}{\partial t}(\hat{\rho})$ is constant over the radius $\hat{\rho}$, i.e. $\frac{\partial}{\partial\hat{\rho}}\left[\frac{\partial\psi}{\partial t}(\hat{\rho})\right] = 0$. We call $\frac{\partial\psi}{\partial t}$ as V_{loop}, hence $V_{loop} \equiv \frac{\partial\psi_B}{\partial t}$. We consider $\dot{\Phi}_B = 0$. We recall the definition of $j_{tor} \equiv R_0\langle\frac{j_\varphi}{R}\rangle$,

$$
j_{tor} = 2\pi R_0 \frac{1}{16\pi^3\mu_0\Phi_b}\frac{1}{V'_{\hat{\rho}}}\frac{\partial}{\partial\hat{\rho}}\left(T\frac{g_2 g_3}{\hat{\rho}}\frac{\partial\psi}{\partial\hat{\rho}}\right)
\tag{B.3}
$$

One can show that $j_{tor} = 2\pi R_0 \frac{dI_p}{dV}$, and $I_p(\hat{\rho}) \equiv \int_0^{V(\hat{\rho})} j_\varphi dA_\varphi$ can be expressed as,

$$
I_p(\hat{\rho}) = T\frac{1}{16\pi^3\mu_0\Phi_b}\frac{g_2 g_3}{\hat{\rho}}\frac{\partial\psi}{\partial\hat{\rho}}.
\tag{B.4}
$$

We recall that $j_{\parallel} \equiv <\frac{\boldsymbol{j}\cdot\boldsymbol{B}}{B_0}>$, can be expressed as in eq. (2.38),

$$
j_{\parallel} = \frac{2\pi T^2}{B_0}\frac{1}{16\pi^3\mu_0\Phi_b}\frac{1}{V'_{\hat{\rho}}}\frac{\partial}{\partial\hat{\rho}}\left(\frac{g_2 g_3}{\hat{\rho}}\frac{\partial\psi}{\partial\hat{\rho}}\right)
\tag{B.5}
$$

If we want now to compute the total plasma current $I_p = I_p(\hat{\rho}_B)$, from eq. (B.5) and eq. (B.4) we obtain,

$$
I_p = I_p(\hat{\rho}_B) = T(\hat{\rho}_B)\frac{B_0}{2\pi}\int_{\hat{\rho}_A}^{\hat{\rho}_B}\frac{V'_{\hat{\rho}}}{T^2}j_{\parallel}d\hat{\rho}
\tag{B.6}
$$

where $\hat{\rho}_B = 1$ and $\hat{\rho}_A = 0$. We consider only the stationary state condition $\frac{\partial\psi}{\partial\hat{\rho}}\big|_{\hat{\rho}_A} = 0$, and assume $\dot{\Phi}_B = 0$. For a given quantity $A(\hat{\rho})$ we define formally the functional $\Gamma(A) = \frac{T_B B_0}{2\pi}\int_0^1\frac{1}{T^2}V'_{\hat{\rho}}Ad\hat{\rho}$, where inside the integration signal $T = T(\hat{\rho})$, and $T_B = T(\hat{\rho}_B)$. This operator is the same as what will be used in Appendix eq. (G.1) to derive the 0D current diffusion equation without

the stationary state assumption. The CDE equation eq. (B.2) is written in terms of $j_\parallel$ and j_{ni} as,

$$j_\parallel = \sigma_\parallel \frac{\partial \psi}{\partial t} + j_{bs} + j_{cd} \tag{B.7}$$

We apply the operator Γ to all terms in eq. (B.7) obtaining,

$$I_p = V_{loop}\Omega(Z_{eff}) + I^*_{ni}(Z_{eff}) \tag{B.8}$$

where in particular $I^*_{ni} = \Gamma(j_{bs}(Z_{eff}) + j_{cd})$, and $\Omega = \Gamma(\sigma_\parallel)$. The I^*_{ni} is not exactly equal to the total toroidal current of the non inductive sources, that is why we introduce here the $*$. Providing I_p and $\tilde{V}_{loop} = \frac{d\tilde{\psi}_B}{dt}$, for example from the equilibrium reconstruction with LIUQE, eq. (B.8) becomes a non-linear root finding problem for $Z_{eff}(t)$. This is solved by the ICDBSeval routine and used to estimate Z_{eff} in KER performed in TCV and presented in previous chapters.

The hypotheses considered to obtain eq. (B.8) are sufficient to find the stationary solution for $\frac{\partial \psi}{\partial \hat{\rho}}(\hat{\rho})$. Indeed calling $K(\hat{\rho}) = \frac{2\pi T^2}{B_0} \frac{1}{16\pi^3 \mu_0 \Phi_b} \frac{1}{V'_{\hat{\rho}}}$, replacing eq. (B.1) into eq. (B.7) one obtains,

$$\frac{\partial}{\partial \hat{\rho}}\left(\frac{g_2 g_3}{\hat{\rho}} \frac{\partial \psi}{\partial \hat{\rho}} \right) = \frac{1}{K}\left(\sigma_\parallel V_{loop} + j_{bs} + j_{cd} \right) \tag{B.9}$$

that can be easily integrated using eq. (B.4) evaluated at ρ_B as boundary condition.

In summary, under the stationary and $\dot{\Phi}_B = 0$ assumptions, provided I_{pl}, V_{loop}, the conductivity $\sigma_\parallel$, all the geometrical quantities, the external current drive sources j_{cd} and the formula for the bootstrap current j_{bs}, ICDBSeval estimates the Z_{eff} from an integral Ohm's law and computes the corresponding stationary state $\frac{\partial \psi}{\partial \hat{\rho}}$, $j_\parallel$ and j_{tor}. The I_p is taken from the equilibrium reconstruction. The V_{loop} is either estimated from equilibrium reconstruction as well or taken from the V_{loop} measurements of one of the flux loops close to the plasma boundary.

We would like to comment on the approach adopted by ICDBSeval.

- No reliable measurements of Z_{eff} are available at TCV at the moment of this thesis.
- The assumption of constant Z_{eff} over the plasma radius is a strong assumption to be confirmed.
- The Z_{eff} dependence enters in many equations of the 1.5D equilibrium and transport model as seen in section 3.3 and not just in the current diffusion equation. For example it enters in the quasi-neutrality equation for the estimation of the n_i, which affects p. Choosing to infer Z_{eff} from the CDE exclusively means implicitly trusting the Z_{eff} dependence in this model more than the other.
- Using the approach of ICDBSeval and the stationary state assumption provides a computationally very cheap estimation of $Z_{eff}(t)$. However, using it in KER to run the current diffusion equation is ASTRA is formally incorrect. Indeed, from the stationary assumption one can obtain directly $j_\parallel$ from eq. (B.9), which would not be consistent with the

time evolving equation. In other words, if the state is truly stationary one could simply perform KER on a single time slice using $j_\parallel$ from eq. (B.9) without running the ASTRA time evolution, if it is not stationary instead a source of inconsistency is introduced.

In conclusion the estimation Z_{eff}, as already stated in previous chapters, is affected by large uncertainties, due primarily to the lack of a direct measurement in TCV. Estimating it with the stationary state assumption as in ICSBSeval provides a reasonable estimate during stationary state phases and though it is a source of inconsistency when using in the current diffusion model in ASTRA performing KER at TCV, we use it for its simplicity. A better option would be to consider instead Z_{eff} as a free parameter of the global KER problem, making use therefore of both magnetic and kinetic measurements to estimate with EKF technique or with least-squares type problem. This however was not attempted during this work.

C Analytic Jacobian for free boundary Grad-Shafranov finite differences discretization

The non-linear problem of finding the plasma boundary in the free-boundary equilibrium solvers leads to the fact that an analytic Jacobian in continuous space representation has not been found yet in presence of diverted plasma. However, it is possible to find an analytic expression gradient for specific spatial discretization as show in [Heumann et al. 2015]. Inspired by that work, we present here the formulation of the analytic gradient specific to the finite differences discretization used in the LIUQE suite of code discussed in [Moret et al. 2015]. The Jacobian obtained is valid everywhere except exactly at the plasma boundary. The implementation has not been attempted yet.

We recall first of all the Newton algorithm to find the root x such that $F(x) = 0$ for a generic non-linear operator $F(x)$

$$(\nabla_x F)\Big|_{x^k} \Delta x = -F(x^k) \tag{C.1}$$

$$x^{k+1} = x^k + \Delta x \tag{C.2}$$

In eq. (C.1) with $|_{x^k}$ we indicate that the Jacobian $\nabla_x F$ is evaluated at the iterative solution x^k. To use the Newton algorithm one needs to be able to evaluate the operator F and to know its Jacobian $\nabla_x F$. When implementing the codes FGS and FGE, we avoided this problem by making use of the JFNK algorithm explained in Appendix D. However the JFNK requires several evaluations of F for a given Newton step k in order to approximate the application of the Jacobian on $\Delta^k x$, which is the expensive part of the algorithm. If the analytic $\nabla_x F$ was known, the Newton algorithm would require only 1 evaluation of F per Newton step.

We state the free boundary equilibrium problem in its discrete form, making use of a slightly different formulation to eq. (4.7), which will simplify the derivation of the Newton algorithm in the following. We use the same notation for the spatially discretized problem as in section

Appendix C. Analytic Jacobian for free boundary Grad-Shafranov finite differences discretization

4.2. Given $\{\boldsymbol{I_a}, \boldsymbol{I_e}, \boldsymbol{a}\}$, find $x = \{\psi_y, \psi_o, \psi_A, \psi_B\}$ such that $F(x) = 0$ where $F(x)$ is defined as,

$$F(x) = \begin{cases} D\psi_x + 2\pi \frac{\mu_0 R_y}{\Delta R \Delta Z} \boldsymbol{I}_y + 2\pi \mu_0 R_y \boldsymbol{I}_e & \text{in } Y \\ \psi_o - \mathbb{M}_{boe} I_e - \mathbb{M}_{boy} I_y & \text{in } O \\ \psi_A - F_{bo}^{\psi_A}(\psi_x) \\ \psi_B - F_{bo}^{\psi_B}(\psi_x) \end{cases} \tag{C.3}$$

With $F_{bo}(\psi_x)$ we indicate the operator that extracts the ψ_A and ψ_B from the discrete map ψ_x. This operator, which will be described in details in the following, is the same one used to extract R_A, Z_A, R_X, Z_X. As opposed to eq. (4.7) we included ψ_A and ψ_B as explicit unknowns, adding two equations to the system. This is convenient only to understand and simplify the derivation but can be removed in the implementation by replacing the R_A, Z_A, R_X, Z_X dependencies in eq. (C.8) directly with the operator $F_{bo}(\psi_x)$. We recall that ψ_x is not the flux at the X point but the flux in the X grid, which is $X = Y \cup O$, hence the full discretized computational grid including points at the boundary. In eq. (C.3) we do not invert D as in eq. (4.8). The formulation in eq. (C.3), without inverting the D, was the first tested for the code FGS. We moved to eq. (4.8) because has the advantages of having only currents as unknowns, and was found to be better conditioned numerically. However, using D^{-1} would also complicate the formulation of the analytic Jacobian and we do not discuss the case in this section.

The goal is to be able to compute analytically $\nabla_x F(x)$, for $x = \{\psi_y, \psi_o, \psi_A, \psi_B\}$. In the following we show this for I_y, the application of D to ψ_x, hence $D\psi_x$, and F_{bo}, which are the most complicated part of F. We start by recasting the I_y into a more convenient form. We recall its definition,

$$I_y \equiv I_y(R_i, Z_i) \, \forall (R_i, Z_i) \in Y = \begin{cases} \sum_{g=1}^{N_g} a_g R^{\nu_g} g_g(\hat{\psi}(R_i, Z_i)) \Delta R \Delta Z & \forall \{R_i, Z_i\} \in P \\ 0 & \forall \{R_i, Z_i\} \in (P)^c \end{cases} \tag{C.4}$$

where Y is the discrete computational grid without the boundary points contained in O. P is the discrete region where the plasma current $I_y \neq 0$ and $(P)^c$ its complement in Y. We refer to fig. 4.1 for details. Moreover g_g and a_g with $g = [1, .., N_g]$ are the basis functions for p' and TT', and their coefficients, respectively. We will specify later some functional forms for g_g, for the moment we consider them to be C^1 functions in $0 < \hat{\psi} < 1$. The exponent ν_g is either 1 or -1 depending whether a given basis function refers to p' or TT' respectively.

Looking at fig.C.1a showing an example LCFS in presence of an X point, which is a saddle point for the flux map. In this there exist a region in Y, called the private flux region (see fig. C.1a), which is a region without plasma current, i.e. $I_y = 0$, but where $0 < \hat{\psi}(R_i, Z_i) < 1$ due to the saddle point nature of the X point. To remove these points from P, we separate the Y domain with a line perpendicular to the segment $(R_A, Z_A)(R_X, Z_X)$ where (R_A, Z_A) is the location of the plasma axis and (R_X, Z_X) the location of the X point (which is not necessarily one of the point of the Y grid), and passing through the X point. This is the same approach used also in LIUQE, FGS, and FGE, where also the case for more X points is considered, [Moret

et al. 2015]. This can be formally written as,

$$P = \{R_i, Z_i\} \, \forall (R_i, Z_i) \in Y \text{ such that} \tag{C.5}$$

$$\begin{cases} 0 < \hat{\psi}(R_i, Z_i) < 1 \\ (R_i - R_X)(R_A - R_X) + (Z_i - Z_X)(Z_A - Z_X) > 0. \end{cases} \tag{C.6}$$

We consider the Heaviside function,

$$H(x) = \begin{cases} 0 & x < 0 \\ 1 & x \geq 0 \end{cases} \tag{C.7}$$

which is a piece-wise continuous function with $\frac{dH}{dx} = 0$ everywhere except exactly at $x = 0$ where the derivative is not defined (at least not as a function but only as a distribution). We can use H to embed the relations which defines P and recast the I_y into a more convenient form.

$$I_y(R_i, Z_i) = \sum_{g=1}^{N_g} a_g R^{\nu_g} g_g \left[\hat{\psi}(R_i, Z_i) \right] H \left[1 - \hat{\psi}(R_i, Z_i) \right] H \left[\hat{\psi}(R_i, Z_i) \right] \times$$

$$\times H \left[(R_i - R_X)(R_A - R_X) + (Z_i - Z_X)(Z_A - Z_X) \right] \tag{C.8}$$

valid $\forall (R_i, Z_i) \in Y$. If we define $\psi_{y,i} = \psi_y(R_i, Z_i)$, $I_{y,i} = I_y(R_i, Z_i)$ with $(R_i, Z_i) \in Y$, we can see explicitly the following dependencies,

$$I_{y,i} = I_{y,i}(\psi_{y,i}, \psi_A, \psi_B, R_A, Z_A, R_X, Z_X). \tag{C.9}$$

We would like to make some remarks, recalling that the final goal will be to evaluate the gradient of $I_{y,i}$ with respect to all its inputs to form the Jacobian of the free-boundary equilibrium problem.

- We consider in this section that the coefficients of the basis functions are given, hence they do not enter in the set of inputs for which the gradient will be computed. This hypothesis can easily be relaxed.

- The eq. (C.9) is C^1 with respect to its inputs everywhere except exactly at the plasma boundary $\hat{\psi} = 1$, at the plasma axis $\hat{\psi} = 0$ and on the line separating the private flux region. Since we will consider the plasma current I_y evaluated only in a set of discrete points $(R_i, Z_i) \in Y$, and Y is not a flux aligned mesh, all the points of Y will be infinitesimally close to the non differentiable region, but very unlikely on top of them. This could happen due to numerical finite precision. In those cases one could consider the value of the gradient to be in one of the to side of the Heaviside function, but we have not yet test this solution.

- If we were considering the presence of scrape of layer current we could have used, instead of a Heaviside function, a C^0 smooth function from the plasma region to the 0

Appendix C. Analytic Jacobian for free boundary Grad-Shafranov finite differences discretization

current region. This was not considered in this work.

- $I_Y = 0$ outside P and moreover $\frac{\partial H}{\partial k} = 0$ outside the plasma for any input k due to the properties of Heaviside function H, and in particular $\frac{\partial I_y(R_i, Z_i)}{\partial k} = 0$ everywhere outside P.

- Since $s = \{R_A, Z_A, R_X, Z_X\}$ only enters in the Heaviside function H, and $\frac{\partial H}{\partial s} = 0$ except exactly at the points where the argument of H is null, then $\frac{\partial I_{y,i}}{\partial s} = 0$ everywhere in Y and not just inside P.

The goal is to compute the Jacobian $\frac{\partial I_{y,i}}{\partial k}$ for all its inputs everywhere in Y. We have already seen that this is null in all the grid points for $\{R_A, Z_A, R_X, Z_X\}$, hence we only need to compute $\frac{\partial I_{y,i}}{\partial \psi_{y,i}}, \frac{\partial I_{y,i}}{\partial \psi_A}$ and $\frac{\partial I_{y,i}}{\partial \psi_B}$. Looking at eq. (C.8), since the derivative of the Heaviside function are null in all grid points, we are left with computing only the contribution of the $g_g(\hat{\psi}_{y,i})$. Hence,

$$
\frac{\partial I_y}{\partial \{\psi_{y,i}, \psi_A, \psi_B\}} = \sum_{g=1}^{N_g} a_g R^{\nu_g} \frac{\partial g_g(\hat{\psi}_i)}{\partial \{\psi_{y,i}, \psi_A, \psi_B\}} \prod_k H_k, \tag{C.10}
$$

where we indicate with $\prod_k H_k$ the product of all the Heaviside functions which defines the plasma region.

We provide as an example the case of the most used basis functions in the LIUQE, FGS, FGE codes, but this can be easily generalized to any set of C^1 basis functions in $\hat{\psi} \in (0, 1)$.

$$
g_{1,i} = g_1(\hat{\psi}_y(R_i, Z_i)) = g_1(\hat{\psi}_{y,i}) \equiv \hat{\psi}_{y,i} - 1 = \frac{\psi_{y,i} - \psi_A}{\psi_B - \psi_A} - 1 \tag{C.11}
$$

$$
\frac{\partial g_{1,i}}{\partial \psi_{y,j}} = \frac{\delta_{i,j}}{\psi_B - \psi_A} \tag{C.12}
$$

$$
\frac{\partial g_{1,i}}{\partial \psi_A} = -\frac{\psi_B - \psi_{y,i}}{(\psi_A - \psi_B)^2} \tag{C.13}
$$

$$
\frac{\partial g_{1,i}}{\partial \psi_B} = \frac{\psi_A - \psi_{y,i}}{(\psi_A - \psi_B)^2} \tag{C.14}
$$

and

$$
g_{2,i} = g_2(\hat{\psi}_y(R_i, Z_i)) = g_2(\hat{\psi}_{y,i}) \equiv (\hat{\psi}_{y,i} - 1)\hat{\psi}_{y,i} = g_{1,i}\hat{\psi}_{y,i} \tag{C.15}
$$

$$
\frac{\partial g_{2,i}}{\partial \psi_{y,j}} = -\frac{\psi_A + \psi_B - 2\psi_{y,i}}{(\psi_A - \psi_B)^2} \tag{C.16}
$$

$$
\frac{\partial g_{2,i}}{\partial \psi_A} = -\frac{(\psi_B - \psi_{y,i})(\psi_A + \psi_B - 2\psi_{y,i})}{(\psi_A - \psi_B)^3} \tag{C.17}
$$

$$
\frac{\partial g_{2,i}}{\partial \psi_B} = \frac{(\psi_A - \psi_{y,i})(\psi_A + \psi_B - 2\psi_{y,i})}{(\psi_A - \psi_B)^3} \tag{C.18}
$$

$$
\tag{C.19}
$$

Typically g_1 is used as unique basis function for p' and g_1 and g_2 for TT'. We are now able to compute $\frac{\partial I_{y,i}}{\partial \psi_{y,i}}, \frac{\partial I_{y,i}}{\partial \psi_A}$ and $\frac{\partial I_{y,i}}{\partial \psi_B}$. We note that there is no need to evaluate nor even to define
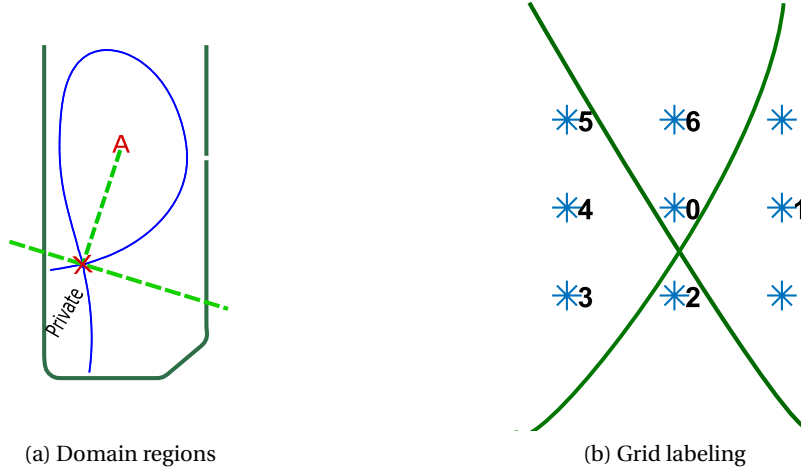
(a) Domain regions (b) Grid labeling

Figure C.1

the basis functions outside P since the Heaviside functions in eq. (C.10) will make that contribution zero.

The operator D is an operator mapping from $X \rightarrow Y$ grid and represents the Grad-Shafranov operator discretized with 2nd order finite differences. It was defined in eq. (4.4) and reported here below for reading convenience,

$$(D\psi_x)\bigg|_{(R_i,Z_j)} \equiv (D\psi_x)_{i,j} = (\Delta z)^{-2}(\psi_{R_i,Z_{j+1}} + \psi_{R_i,Z_{j-1}} + a_i\psi_{R_{i+1},Z_j} + b_i\psi_{R_{i-1},Z_j} - c_i\psi_{R_i,Z_j})$$

(C.20)

The value of $(D\psi_x)|_{(R_i,Z_j)}$ depends on the value of the four neighboring points of R_i, Z_j in the 2D map of ψ_x. Note that we use two distinct indices for the R and Z coordinate to properly represent proximity in the poloidal plane of the grid points, while before we were considering the ψ_x as a straight vector evaluated at (R_i, Z_i) pairs of coordinates. It is straightforward from eq. (C.20) to compute $\frac{\partial (D\psi_x)_{i,j}}{\partial \psi_{x,l,m}}$ with (R_i, Z_j), $(R_l, Z_m) \in Y$, which will result in a combination of the coefficients a, b, c, d for a given point in the grid and the value of the fluxes $\psi_{x,l,m}$. Note that $(D\psi_x)|_{(R_i,Z_j)}$ does not depend on ψ_A, ψ_B. We stress that we are not looking at the gradient of the operator, which is not well defined, but to the gradient of the application of the operator to the flux map ψ_x.

In order to complete all the terms missing and to obtain the Jacobian, we need to define F_{bo} and its derivatives with respect to the unknowns $x = \{\psi_y, \psi_o, \psi_A, \psi_B\}$. This is the most less intuitive part of the derivation, which analytically in continuous space representation cannot be handled exactly. The plasma axis is a maximum/minimum (depending on the I_p sign) of the ψ_y map while the X point is a saddle point of the map. From the rectangular grid Y we select a subset of points, contained in a square box, and we number the 7 points from 0 to 6 (see fig. C.1b). In order to identify the boxes containing the critical points of a 2D discrete map (points where the spatial derivatives are zero, hence saddles points and extrema), an algorithm

Appendix C. Analytic Jacobian for free boundary Grad-Shafranov finite differences discretization

[Kuijper 2004] taken from computer vision is used. It scans the ψ_x map identifying the boxes, all the combinations of 9 adjacent points on the ψ_x map, selecting the relevant subset of 7 points, and identifies those that contain an critical points. To compute the (R_c, Z_c) location of the critical point, both minimum or saddle point type, and the value of its flux ψ_c, a six points quadratic interpolation is used. If we define $x = \frac{R-R_0}{\Delta R}, y = \frac{Z-Z_0}{\Delta Z}$, the functional form of the quadratic interpolation is given by,

$$\psi(x, y) = \psi_0 + ax + by + cx^2 + dy^2 + exy. \tag{C.21}$$

Interpolating on the $1, 2, 3, 4, 6$ points we can compute the coefficients obtaining,

$$a = \frac{\psi_1}{2} - \frac{\psi_4}{2} \tag{C.22}$$

$$b = \frac{\psi_6}{2} - \frac{\psi_2}{2} \tag{C.23}$$

$$c = \frac{\psi_1}{2} - \psi_0 + \frac{\psi_4}{2} \tag{C.24}$$

$$d = \frac{\psi_2}{2} - \psi_0 + \frac{\psi_6}{2} \tag{C.25}$$

$$e = \psi_0 - \psi_2 + \psi_3 - \psi_4 \tag{C.26}$$

$$\tag{C.27}$$

It is easy to look for critical point (x_c, y_c) such that $(\nabla \psi)|_{x_c, y_c} = 0$,

$$x_c = \frac{\psi_0\psi_2 - 2\psi_0\psi_1 + \psi_1\psi_2 + 2\psi_0\psi_4 + \psi_2\psi_3 - \psi_0\psi_6 - 2\psi_2\psi_4 + \psi_1\psi_6 + \psi_2\psi_6 - \psi_3\psi_6 - \psi_2^2}{2\left(2\psi_0\psi_1 + 2\psi_0\psi_3 - \psi_1\psi_2 - 2\psi_2\psi_3 + 2\psi_0\psi_6 + \psi_2\psi_4 - \psi_1\psi_6 - 2\psi_3\psi_4 - \psi_4\psi_6 - 3\psi_0^2 + \psi_2^2 + \psi_3^2 + \psi_4^2\right)} \tag{C.28}$$

$$y_c = \frac{2\psi_0\psi_2 - \psi_0\psi_1 + \psi_0\psi_4 - \psi_1\psi_3 + \psi_1\psi_4 - 2\psi_0\psi_6 - 2\psi_2\psi_4 + \psi_1\psi_6 + \psi_3\psi_4 + \psi_4\psi_6 - \psi_4^2}{2\left(2\psi_0\psi_1 + 2\psi_0\psi_3 - \psi_1\psi_2 - 2\psi_2\psi_3 + 2\psi_0\psi_6 + \psi_2\psi_4 - \psi_1\psi_6 - 2\psi_3\psi_4 - \psi_4\psi_6 - 3\psi_0^2 + \psi_2^2 + \psi_3^2 + \psi_4^2\right)} \tag{C.29}$$

We have therefore an expression for the location of the extremum (x_c, y_c) in a box as a function of the fluxes $\psi_{\{0,1,2,3,4,6\}}$ which can be substituted in the quadratic expression to obtain the value of the flux at the extremum $\psi(x_c, y_c) \equiv \psi_c$ as a function of $\psi_{\{0,1,2,3,4,6\}}$. This way we can compute $\frac{\partial \psi_c}{\partial \psi_{\{0,1,2,3,4,6\}}}$. We obtained the final result with Matlab symbolic operation package. Since the final expression is very long, we rather prefer to provide the Matlab script to generate it, which we think could be more useful for a potential user.

```
1  syms  f0 f1 f2 f3 f4 f5 f6 x y r0 z0   % Define symbolic variables
2  xi = [  1;  0; -1; -1; -1;  0]; % Quadrature x points
3  yi = [  0; -1; -1;  0;  1;  1]; % Quadrature y points
4  A = [xi yi xi.^2 yi.^2 xi.*yi];
5  tmp  = A([1 2 3 4 6],:)\[f1-f0;f2-f0;f3-f0;f4-f0;f6-f0]; % Interpolate
6  % Get coefficients
7  a = tmp(1); b = tmp(2);  c = tmp(3); d = tmp(4); e = tmp(5);
```

```
8   % Get psi quadratic expression with interpolated coefficients
9   psi = f0 + a*x + b*y +c*x^2 + d*y^2 + e*x*y;
10  % Find critical points
11  [xc,yc] = solve( [diff(psi,x);diff(psi,y)]==0  ,x,y);
12  % Compute flux at extremum
13  psie = f0 + a*xc + b*yc +c*xc^2 + d*yc^2 + e*xc*yc;
14  % Compute derivative of the flux at extremum
15  dpsicdf0 =diff(psic,f0);
16  ...
```

The Matlab script gives the expression to compute $\frac{\partial F_{bo}}{\partial \psi_{y,i}}$, provided to know in which cells the critical points are found. The derivation of $\frac{\partial F_{bo}}{\partial \psi_{y,i}}$ done for the Y map extends directly to the X grid, hence allowing to include the computational boundaries.

We completed therefore how to compute the Jacobian with respect to the unknowns $x = \{\psi_y, \psi_o, \psi_A, \psi_B\}$ for all the terms appearing in eq. (C.3).

Some additional remarks:

- In order to perform one step of the Newton algorithm given $x^k = \{\psi_y^k, \psi_o^k, \psi_A^k, \psi_B^k\}$, one needs first to evaluate $F(x^k)$. This requires first to search for the extremum points of ψ_x, in particular obtaining $\psi_A^k, \psi_B^k, R_A^k, Z_A^k, R_B^k, Z_A^k$. Then to compute $(\nabla_x F)|_{x^k}$. In particular, to evaluate $\frac{\partial I_{y,i}}{\partial \psi_{y,i}}, \frac{\partial I_{y,i}}{\partial \psi_A}$ and $\frac{\partial I_{y,i}}{\partial \psi_B}$ at x^k requires to know $\psi_A^k, \psi_B^k, R_A^k, Z_A^k, R_B^k, Z_A^k$ which enter in the Heaviside definition eq. (C.8). At the same time from ψ_y^k one needs to extract the cells containing the extrema, in order to compute the $\frac{\partial F_{bo}}{\partial \psi_y}$.

- We provided in this appendix the derivation of the analytic Jacobian only for the case where the basis function coefficients $\boldsymbol{a}$ are given. However it would be easy to extend to the cases where the basis function coefficients enter as additional unknowns, as in FGS and FGE eq. (4.8), and an adequate number of constraints are given, provided that is possible to compute an analytic gradient for the equations of the constraints.

- As we stated at the beginning, the Jacobian obtained is not valid exactly at the plasma boundary due to the Heaviside function. Since the grid used is not flux aligned, the point on the grid could be eventually infinitesimally close but never exactly on top of this region, unless for very unluckily cases due to finite machine precision. It still needs to be proven that this does not cause numerical problem for the implementation of Newton algorithm. However we notice that the Jacobian would be correct in all the other points of the grid, hence it could still be used as a preconditioner for example for the JFNK method.

- The derivation provided so far assumes the presence of only 1 X point. Extension to several X points is possible but requires a careful analysis on how to define the plasma region P, define the correct Heaviside functions to describe it and extend the unknowns to consider all the X points.

Appendix C. Analytic Jacobian for free boundary Grad-Shafranov finite differences discretization

- The sparsity pattern of the Jacobian is not fixed for subsequent Newton iterations, however is known a priori given x^k. Indeed the sparsity of $(D\psi_x)|_{(R_i, Z_j)}$ is fixed, but $\frac{\partial I_{y,i}}{\partial \psi_{y,i}}, \frac{\partial I_{y,i}}{\partial \psi_A}, \frac{\partial I_{y,i}}{\partial \psi_B}, \frac{\partial F_{bo}}{\partial \psi_y}$ depends on the location of the plasma boundary at x^k.

- We considered in this derivation ψ_A and ψ_B as independent unknowns only to simplify the derivation. However, one can directly embed F_{bo} into the expression for I_y, and exploit the chain rule while computing the Jacobian in order to reduce the number of unknowns only to ψ_y and ψ_o.

- Also in case of limited plasma it is possible to derive an analytic expression for the gradient. It is sufficient to interpolate the ψ_x with a quadratic interpolation as done for the diverted case. Then, instead of looking for the global critical point of the interpolation, one needs to search the critical point of the map constrained to stay on the location of the limiter.

- A different derivation of the Jacobian should be investigated to include the Lackner's [Lackner 1976] solution to compute ψ_o, and avoid the expensive computation of $\mathbb{M}_{boy} I_y$. However we have not investigated this option yet.

The proposed analytic Jacobian will be implemented and tested in future and compared against finite difference approximation. If working effectively, it could provide a significant improvement in the computational cost of FGS and FGE, since the operator $F(x) = 0$, and in particular the scan of the whole grid to find the extremum points, needs to be performed only once per Newton iteration.

D | Solving the root-finding problem with a Jacobian Free Newton Krylov algorithm

In this appendix, we will summarize how to solve a root-finding problem of the type "find x such that $F(x) = 0$" with the Jacobian Free Newton Krylov (JFNK) algorithm. This algorithm is used to solve most of the root-finding problems described in this thesis, in particular for the FGS and FGE code. We will discuss in the end of the section pros and cons of the algorithm, commenting in particular on the approaches to reduce its computational cost. The description in this section is mostly taken from [Knoll and Keyes 2004].

Every non-linear root-finding problem can be written as finding x such that $F(x) = 0$, with $F(x)$ a non-linear (vector) function of the unknown x. We stress the importance of formulating every problems in this form in the part I of the thesis in order to use the same solver for all of them. Most of the time the operator $F(x)$ can be re-written in the form $F(x) = x - h(x)$, for a properly defined non-linear operator $h(x)$. A usual approach to solve the problem is typically to apply Picard iteration scheme,

$$x^{k+1} = h(x^k) \tag{D.1}$$

where k is the iteration index. This is typically the first attempt for any code since it is very simple to implement and only needs to loop on the different subparts of the problem. However, Picard iterations for non-linear problems are often numerically unstable. Relaxation techniques are often used to recover this issue but they slow down the convergence rate of the algorithm.

The free-boundary equilibrium problem, is numerically unstable when Picard iterations are implemented also, even when including surrelaxation [Lackner 1976]. When performing the magnetic equilibrium reconstruction with LIUQE, the problem was stabilized by allowing the Grad-Shafranov solution to be computed in a shifted grid and using the magnetic measurements to find the appropriate shifting [Moret et al. 2015]. This approach is common to many equilibrium reconstruction codes, including EFIT [Ferron et al. 1998] and the fast version of CLISTE [McCarthy et al. 1999]. However, this stabilizing solution is not suitable when addressing the forward problems since no measurements can be used to infer the position of

Appendix D. Solving the root-finding problem with a Jacobian Free Newton Krylov algorithm

the plasma.

A possible solution is to adopt Newton algorithm, which is known to be more stable than Picard iterations. The Newton scheme is based on taking an iteration step Δx in the direction of the gradient of the operator $F(x)$. The Newton algorithm is given by

$$(\nabla_x F)_{x^k} \Delta x = -F(x^k) \tag{D.2}$$

$$x^{k+1} = x^k + \Delta x. \tag{D.3}$$

The algorithm is composed in two parts. The computation of the step Δx, solving eq. (D.2), and the update of the new guess of the solution x^{k+1}, from eq. (D.3). It requires at every iteration to compute the gradient of the operator $F(x)$, evaluate at its value at x^k and invert the linear problem eq. (D.2) to get Δx.

The algorithm relies on the possibility to compute $(\nabla F)_{x^k}$, which will be referred to in the following as Jacobian. Unfortunately, due to the non-linearity of finding the plasma boundary boundary from a $\psi(R, Z)$, which requires to find a saddle point of the map, an analytic expression for this gradient is not known for the formulation of the problem in continuous space. An analytic gradient has been obtained for a spatially discretized representation of the problem with finite element in [Heumann et al. 2015] and implemented in the codes CE-DRES++, FEEQS.M [Heumann et al. 2015] and now to NICE [Faugeras 2020]. Another option is to approximate numerically the Jacobian with finite differences, exploiting eventually the a priori knowledge of the sparsity of the matrix. This approach, together with a accurate use of parallelization has been adopted for the code CREATE-NL [Albanese et al. 2015].

In this thesis we adopted a different approach. The aim was to re-use most of the low-level routines from the equilibrium code LIUQE, which was based on finite difference spatial discretization as already explained in previous sections, hence we could not directly use the analytic formulation of the Jacobian for the discretized problem obtained in [Heumann et al. 2015]. In appendix C we derived the analytic gradient for the finite differences discretization suited for FGS and FGE code, but is was not tested yet. We decided initially to implement therefore the Jacobian Free Newton Krylov method, which is still based on a quasi-Newton step, hence it keeps the stability properties of the algorithm, but it does not need the explicit calculation of the Jacobian $(\nabla F)_{x^k}$. This is the reason why the algorithm is called "Jacobian Free". The main idea is that in eq. (D.2), one does not need to compute explicitly $(\nabla F)_{x^k}$ since what is needed is only the application of the Jacobian on a given direction $x + \delta x$, which can be approximated with finite differences,

$$\nabla_x F(x)\delta x \approx \frac{F(x + \delta x) - F(x)}{||\delta x||} \tag{D.4}$$

We will explain this with more detail, but we thought it was better to provide the intuition behind before discussing the details of the algorithm.

We focus now on the first operation in the Newton algorithm eq. (D.2), which we rewrite as the

standard notation for a linear problem in terms of the matrix A and known vector b to simplify the notation

$$(\nabla_x F)_{x^k} \Delta x = -F(x^k)$$
$$A(x^k)\Delta x = b(x^k)$$

From now on, we will discuss a single Newton step hence we will neglect the index k. The linear problem is solved with the Generalized Minimal RESidual (GMRES) method. In order to do that we express $\Delta x = \sum_i \mu_i U_i$ with a basis functions $\{U_i\}$ expansion and find the coefficient by solving the least-squares minimization problem,

$$\boldsymbol{\mu} = \text{argmin}||\sum_i \mu_i \underbrace{AU_i}_{K_i} - b||^2. \tag{D.5}$$

Collecting all the columns of K_i in a single matrix $\mathbb{K}$, the solution of the problem is given by $\boldsymbol{\mu} = (\mathbb{K}^T \mathbb{K})^{-1} \mathbb{K}^T b$. Recalling the definition of A, computing K_i means applying the Jacobian of F to the U_i direction, which can be approximated with finite differences, giving this way the Gradient Free Nature of the algorithm.

$$AU_i = \nabla F_x \cdot U_i \approx \frac{F(x + U_i) - F(x)}{||U||} \tag{D.6}$$

In order to make use of the GMRES algorithm, a particular set of basis functions U_i needs to be used to guarantee the convergence, the so-called Krylov space [Saad and Schultz 1986]. If we define $r_0 = -F(x_k)$, the initial residue for a given Newton step, then $\boldsymbol{U} = \{r_0, Ar_0, A^2 r_0...\}$, which means applying recursively the Jacobian in different directions to build the Krylov space. This part gives the "Krylov" name to the algorithm. Since the basis functions might become collinear, an Arnoldi orthonormalization technique is used while building the Krylov space [Björck 1967]. The advantage of this approach is in the dimension of the Krylov space N_K needed to solve the problem to a desired precision is typically much smaller than the dimension of the unknown x. This results in a significant saving of computational time with respect to computing the full Jacobian directly with finite differences.

The algorithm therefore is composed of two nested loops. We call with N_N the total number of Newton steps.

$U_0 = -F(x_0)$
$i = 1$
while $i < N_N$ and $||U_i|| <$ threshold Perform Newton step **do**
    for $j = 1 : N_k$ Construct the Krylov basis **do**
        $U_j = \frac{F(x^j + \epsilon U_{j-1}) - F(x^j)}{\epsilon}$ Evaluate the new basis function
        Ortho-normalize the new basis function (Arnoldi)
    end for
    $\Delta^i x = \boldsymbol{\mu} = (\mathbb{K}^T \mathbb{K})^{-1} \mathbb{K}^T b$ Solve leasr-squares problem

Appendix D. Solving the root-finding problem with a Jacobian Free Newton Krylov algorithm

$x^{i+1} = x^i + \Delta^i x$ Advance Newton step

$U_0 = -F(x^{i+1})$ Compute residual and new initial base function vector

$i = i + 1$

end while

This is a very basic outline of the algorithm. In the actual implementation the computation of the Krylov space would not be performed up to the maximum number of selected basis function but is stopped when the orthogonal component of the new basis with respect to the already computed space is smaller than a given threshold.

We would like to make some remarks about the procedure.

- The costly part of the algorithm is the evaluation of the non-linear operator $F(x)$, hence one is interested to reduce as much as possible the total number of evaluation, called N_F, to achieve a desired convergence, measured either as the norm of the residual or as the norm of the increment.

- The total number of evaluation of F is equal to $N_F = N_N \times N_K + 1$. The cost of the solution is therefore a trade-off between N_F and N_K. Reducing the number of Krylov basis provides a worse "estimate" of the Jacobian, hence more Newton iterations are needed and convergence issues might occur. To reduce the computational cost, preconditioning technique allows to reduce N_K to obtain the same precision in eq. (D.5). This allows to cluster the eigenvalues of the iterating matrix in GMRES. This means solving the problem $PA\delta u = Pb$, instead of the original one. The ideal preconditioner for each Newton iteration would be A^{-1}, which would require to compute the inverse of the Jacobian that we wanted to avoid by using the JFNK technique.

In FGE, where the problem to be solved is very similar from one time step to the next, we approximate the full Jacobian with finite differences for the first time step and use its inverse as a preconditioner for all the subsequent iterations. To provide an example the typical dimension of the unknowns x for the FGE problem is ~ 1600, hence to evaluate the Jacobian $\nabla F(x)$ with 2nd order finite differences requires ~ 3200 evaluations of the operator F. We simulate a VDE with a computational time step of $0.05[ms]$. The initial solution (black), from which the preconditioner is computed, and the final one (green) are shown in fig. D.1a. In fig. D.1b the total number of evaluations of the operator F to reach the same convergence threshold at a given time instant is shown along the simulation time. In red for the case when no preconditioner is used and in blue for the case with the preconditioner. Thanks to the preconditioner the dimension of the Krylov space is reduced substantially (from 50 to 6) which results in the need of only ~ 30 evaluation of F instead of 250. While is true that quality of the preconditioner progressively degrades when the plasma departs from the solution used for the linearization. However, as shown in fig. D.1b, the degradation is slow even for the very different shape (green) reached at the end of the simulation. The simulation was performed with high convergence threshold requirements, but when using FGE to perform simulation
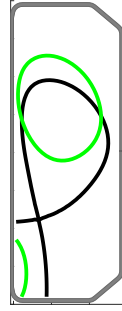
(a) Initial solution (black) and final displaced solution (green)
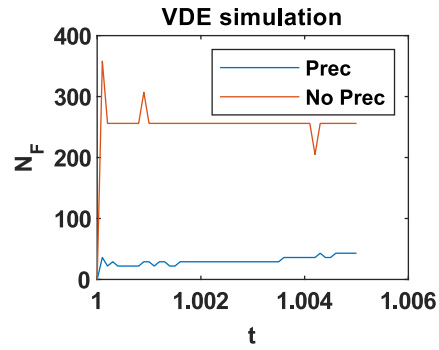
(b) Number of evaluation of F operator to reach convergence vs simulation time

Figure D.1 – VDE simulation for TCV

for TCV, we usually achieve $N_F \sim 7$ per time step with the code at the state of this thesis.

We are considering to test the following techniques to improve the computational cost: update the preconditioner while forming the Krylov space as proposed in [Chen and Shen 2006]; re-use the Krylov basis functions for multiple Newton iterations and time steps. This leads to the so called "deflation" technique to extract the Krylov basis functions during the JFNK algorithm [Al Daas et al. 2018]. In any case, we will explore also hardware solutions parallelizing the code. We will also test the analytic Jacobian derived in Appendix C either to directly implement a Newton method, which would solve the problem of finding a preconditioner, or as a preconditioner for the JFNK solver.

E Difference between linear and "quasi-linear" least-squares optimization problems

We discuss in this appendix the difference between the solution of the least-squares optimization problem when the forward model $\boldsymbol{y} = \boldsymbol{f}(\boldsymbol{\theta})$, which provides the estimate of the quantities $\boldsymbol{y} = \{y_i\}$ with $i = 1,..,N_y$ given the set of parameters $\boldsymbol{\theta} = \{\theta_i\}$ with $i = 1,..,N_\theta$, is represented by a linear model $\boldsymbol{f}_l = \mathbb{A}\boldsymbol{\theta}$, where $\mathbb{A} = \{A_{ij}\}$ with $i = 1,..,N_y$ and $j = 1,..,N_\theta$ is a constant matrix, and when the model is "quasi-linear" $\boldsymbol{f}_{ql} = \mathbb{B}(\boldsymbol{\theta})\boldsymbol{\theta}$, where $\mathbb{B}(\boldsymbol{\theta}) = \{B_{ij}(\boldsymbol{\theta})\}$ with $i = 1,..,N_y$ and $j = 1,..,N_\theta$ and all the elements of the matrix $\mathbb{B}(\boldsymbol{\theta})$ depend non-linearly on the parameters $\boldsymbol{\theta}$. This is relevant to the problem of performing magnetic equilibrium reconstruction, in particular when discussing the differences between LIUQE and FGS solutions in section 4.5.1.

In this appendix we will indicate with $\mathbb{A}\boldsymbol{\theta}$ the matrix vector product, hence $y_i = \sum_{j=1}^{N_\theta} A_{ij}\theta_j$ and in order to simplify the notation we will also make use of Einstein's notation to sum over repeated indices, such that $y_i = \sum_{j=1}^{N_\theta} A_{ij}\theta_j = A_{ij}\theta_j$.

The least squares optimization problem searches for the parameters $\boldsymbol{\theta}$ such that $\boldsymbol{y} = \boldsymbol{f}(\boldsymbol{\theta})$ best matches in the least squares sense a set of known measurements $\tilde{\boldsymbol{y}}$, where typically $N_y >> N_\theta$. Formally the problem can be stated as,
Given: The forward model functional form $\boldsymbol{f}(\boldsymbol{\theta})$ and a set of measurements $\tilde{\boldsymbol{y}}$
Find: The set of parameters $\boldsymbol{\theta}^*$
such that,

$$\boldsymbol{\theta}^* = \operatorname*{argmin}_{\boldsymbol{\theta}} \sum_{i=1}^{N_y} (\boldsymbol{f}_i(\boldsymbol{\theta}) - \tilde{\boldsymbol{y}}_i)^2 \tag{E.1}$$

In case of a linear forward function $\boldsymbol{f}_l = \mathbb{A}\boldsymbol{\theta}$ the explicit solution and is $\boldsymbol{\theta}^* = (\mathbb{A}^T\mathbb{A})^T\mathbb{A}^T\tilde{\boldsymbol{y}}$. This solution will be derived in the following. For the "quasi-linear" forward model $\boldsymbol{f}_{ql} = \mathbb{B}(\boldsymbol{\theta})\boldsymbol{\theta}$ instead, a close form of the solution is not available, but a set of N_θ non-linear equations can be found in terms of $\mathbb{B}$ and $\frac{\partial \mathbb{B}_{ij}}{\partial \theta_j}$. We will derive this set of equations and compare them with the linear case.

Appendix E. Difference between linear and "quasi-linear" least-squares optimization problems

We first define the least-squares cost function $\Gamma(\boldsymbol{\theta})$ in matrix like form using Einstein's notation.

$$\Gamma(\boldsymbol{\theta}) = \sum_{i=1}^{N_y} (\boldsymbol{f}_i(\boldsymbol{\theta}) - \tilde{\boldsymbol{y}}_i)^2 = (\mathbb{A}_{ij}\theta_j - \tilde{y}_i)(\mathbb{A}_{ij}\theta_j - \tilde{y}_i) \tag{E.2}$$

The solution $\boldsymbol{\theta}^*$ of eq. (E.1) must be found among the (possibly several) minima of $\Gamma(\boldsymbol{\theta})$, which respect $\frac{\partial \Gamma(\boldsymbol{\theta})}{\partial \theta_k} = 0$ for $k = 1, .., N_\theta$. We can write explicitly this set of equations $C_k = 0$ with $k = 1, .., N_\theta$

$$\begin{aligned} C_k = \frac{\partial \Gamma(\boldsymbol{\theta})}{\partial \theta_k} \quad &= 2\sum_{i=1}^{N_y} (\mathbb{A}_{ij}\theta_j - \tilde{y}_i)\frac{\partial}{\partial \theta_k}(A_{ij}\theta_j - \tilde{y}_i) \\ &= 2\sum_{i=1}^{N_y} (\mathbb{A}_{ij}\theta_j - \tilde{y}_i)\frac{\partial}{\partial \theta_k}(A_{ij}\theta_j) \\ &= 0 \end{aligned} \tag{E.3}$$

where we made use of the fact that $\frac{\partial \tilde{y}_i}{\partial \theta_k} = 0, \forall i, k$. The difference between the linear and the "quasi-linear" problem is found in the next step.

For the linear case,

$$\frac{\partial}{\partial \theta_k}(\mathbb{A}_{ij}\theta_j) = \mathbb{A}_{ij}\delta_{jk} = \mathbb{A}_{ik} \tag{E.4}$$

since the matrix components $\mathbb{A}_{ij}$ do not depend on any θ_k. In eq. (E.4) we made use of the Kroneker's δ_{jk} defined as

$$\delta_{ik} = \begin{cases} 1, & \text{if } i = k, \\ 0, & \text{if } i \neq k. \end{cases} \tag{E.5}$$

For the "quasi-linear" case instead

$$\frac{\partial}{\partial \theta_k}(\mathbb{B}(\boldsymbol{\theta})\theta_j) = \theta_j \frac{\partial \mathbb{B}_{ij}}{\partial \theta_k} + \mathbb{B}_{ij}\delta_{jk} = \theta_j \frac{\partial \mathbb{B}_{ij}}{\partial \theta_k} + \mathbb{B}_{ik} \tag{E.6}$$

We complete now the derivation of eq. (E.3) for the linear case and we will then discuss the difference with the "quasi-linear". We will use Einstein's notation to sum over repeated index to simplify the notation. We also drop the multiplication factor 2 since this does not change the location of the minimum hence the solution of the problem.

$$\begin{aligned} C_k \quad &= (\mathbb{A}_{ij}\theta_j - \tilde{y}_i)\mathbb{A}_{ik} \\ &= \mathbb{A}_{ik}(\mathbb{A}_{ij}\theta_j) - \mathbb{A}_{ik}\tilde{y}_i = 0 \end{aligned} \tag{E.7}$$

We remember now the definition of the transpose of a matrix,

$$(\mathbb{A})^T = (\mathbb{A}_{ij})^T = \mathbb{A}_{ji} \tag{E.8}$$

Hence we can write,

$$\mathbb{A}_{ki}^{T}\mathbb{A}_{ij}\theta_{j} = \mathbb{A}_{ki}^{T}\tilde{y}_{i} \tag{E.9}$$

which in standard matrix/vector product form becomes,

$$(\mathbb{A}^{T}\mathbb{A})\boldsymbol{\theta} = \mathbb{A}^{T}\tilde{\boldsymbol{y}}. \tag{E.10}$$

The solution $\boldsymbol{\theta}^{*}$ of problem eq. (E.1) for a linear forward model $\boldsymbol{f}_{l} = \mathbb{A}\boldsymbol{\theta}$ is therefore as anticipated,

$$\boldsymbol{\theta}^{*} = (\mathbb{A}^{T}\mathbb{A})^{-1}\mathbb{A}^{T}\tilde{\boldsymbol{y}}. \tag{E.11}$$

In case of the "quasi-linear" forward model $\boldsymbol{f}_{ql} = \mathbb{B}(\boldsymbol{\theta})\boldsymbol{\theta}$ instead, given eq. (E.6), we can provide the following N_{θ} set of non-linear equations Z_{k}, with $k = 1, .., N_{\theta}$, for the $\boldsymbol{\theta}^{*}$ unknowns, but not an explicit closed form solution as in eq. (E.11).

$$Z_{k} = \sum_{i=1}^{N_{y}}\left(\mathbb{B}_{ij}(\boldsymbol{\theta}^{*})\boldsymbol{\theta}^{*} - \tilde{y}_{i}\right)\left[\theta_{j}^{*}\left(\frac{\partial\mathbb{B}_{ij}(\boldsymbol{\theta})}{\partial\theta_{k}}\right)_{\boldsymbol{\theta}^{*}} + \mathbb{B}_{ik}(\boldsymbol{\theta}^{*})\right] = 0 \tag{E.12}$$

Ultimately the difference between the linear case and the "quasi-linear" case comes from the $\frac{\partial\mathbb{B}_{ij}}{\partial\theta_{k}}$ term when computing the gradient of the forward model, comparing eq. (E.6) and eq. (E.4). Nevertheless, looking at eq. (E.12) we notice that there exists a case when the solution θ^{*} of the linear and the "quasi-linear" problem coincide. This happens when $\tilde{y}_{i} = \mathbb{B}_{ij}(\boldsymbol{\theta}^{*})\boldsymbol{\theta}^{*}$, hence eq. (E.12) is respected anytime independently of the value assumed by $\frac{\partial\mathbb{B}_{ij}}{\partial\theta_{k}}$. This case is found when the measurements are exactly given by the forward model, hence the solution is found when the minimum of the least-squares error is exactly 0. Practically when performing reconstruction problem this corresponds to the ideal case when the model $f(\theta)$ has no uncertainties and the measurements $\tilde{y}$ have no noise. This is also the case when the measurements $\tilde{y}$ are obtained as synthetic measurements from the forward model. We showed this numerically in section 4.5.1 when performing magnetic equilibrium reconstruction comparing LIUQE, which uses a linear approach, with FGS which uses the "quasi-linear" one to minimize the least-squares problem, providing noise free synthetic data.

F Lagrange's multipliers solution of linear vs "quasi-linear" least-squares optimization with equality constraints

The aim of this appendix is to explain the differences between the simplification adopted in LIUQE to solve the "quasi-linear" least-squares optimization with equality constraints representing the magnetic equilibrium reconstruction eq. (3.9) and its correct solution implemented with FGS code. Numerical investigation have been shown in section 4.5.1. Here we will explain the difference analytically, making use of Lagrange multipliers to solve the MER "quasi-linear" least-squares with equality constraints.

We will use in the following a prototype problem equivalent to eq. (3.9) in order to focus only on the relevant aspect of LIUQE simplification, but having a simpler notation. As for the case presented in appendix E, we consider one single state ψ and one single parameter θ to be reconstructed with the inverse problem. We consider two forward models. The first $G = G(\theta)$ relates the parameter θ to the state ψ, $\psi = G(\theta)$ and could be in general a non-linear function of the parameter. The second $\mathbb{A}(\psi)$ relates the estimate of the measurements $\boldsymbol{y}$ to the state ψ with a linear relation $\boldsymbol{y} = \mathbb{A}(\psi)\theta$, which is often called the measurement model. The dimension of $\boldsymbol{y}$ is N_y, hence $\mathbb{A}\theta$ is a vector of dimension N_y. A set of N_y measurements $\tilde{\boldsymbol{y}}$ is considered and the following "quasi-linear" least squares problem with non-linear equality constraint is addressed.

Given: The set of measurements $\tilde{\boldsymbol{y}}$, the relation $\psi = G(\theta)$ and $y = \mathbb{A}(\psi)$.
Find: The parameter θ^* and the state ψ^*
such that

$$\{\theta^*, \psi^*\} = \operatorname*{argmin}_{\theta, \psi} ||\mathbb{A}(\psi)\theta - \tilde{\boldsymbol{y}}||_2^2$$
$$\text{such that}$$
$$\psi = G(\theta)$$

(F.1)

where $|| \cdot ||_2^2$ is the square of the 2 norm of the vector.

The analogy with the MER problem is given by considering ψ to be the solution of the free

Appendix F. Lagrange's multipliers solution of linear vs "quasi-linear" least-squares optimization with equality constraints

boundary equilibrium problem given the inputs $\{\boldsymbol{I}_a, \boldsymbol{I}_v, \boldsymbol{a}_g\}$ which are represented here by the single parameter θ, and $\mathbb{A}(\psi)$ the matrix connecting the parameters to the magnetic measurements, which depends on the Grad-Shafranov solution. Then eq. (F.1) can be seen as equivalent to eq. (3.9).

There are two possibilities to solve the problem eq. (F.1). The first is to replace $\psi = G(\theta)$ in the cost function. The problem becomes therefore finding the minimum for the functional $||A(G(\theta))\theta - \tilde{\boldsymbol{y}}||^2$ with respect to the single variable θ. This is the approach adopted in FGS discussed in section 4.5. The solution can be found by solving the system of equations eq. (E.12). However this approach requires to be able to evaluate the function $G(\theta)$ and its derivatives. In case of MER, evaluating $G(\theta)$ means solving the free-boundary equilibrium forward problem and both solving and estimating its derivative is expensive, in case of MER. In section 4.5 it was done numerically exploiting finite differences.

The second option to solve eq. (F.1) is applying the Lagrange's multipliers technique for constrained optimization. We consider a single Lagrange multiplier λ, since a unique constraint is present in eq. (F.1), and we define the cost function Γ as,

$$\Gamma(\theta, \psi, \lambda) = ||\mathbb{A}(\psi)\theta - \tilde{\boldsymbol{y}}||_2^2 + \lambda(\psi - G(\theta)). \tag{F.2}$$

To solve the problem one can look for a local minimum of $\Gamma(\theta, \psi, \lambda)$ by solving the set of normal equations obtained by setting $\nabla_{\theta, \psi, \lambda}\Gamma = 0$, hence

$$\begin{cases} \frac{\partial}{\partial\theta}||\mathbb{A}(\psi)\theta - \tilde{\boldsymbol{y}}||_2^2\Big|_\psi - \lambda\frac{\partial G}{\partial\theta}\Big|_\psi = 0 \\ \frac{\partial}{\partial\psi}||\mathbb{A}(\psi)\theta - \tilde{\boldsymbol{y}}||_2^2\Big|_\theta + \lambda = 0 \\ \psi = G(\theta) \end{cases} \tag{F.3}$$

The eq. (F.3) is a system of non-linear equations for the unknowns $\{\theta, \psi, \lambda\}$.

If and only if the matrix $\mathbb{A}$ does not depend on ψ, $\frac{\partial}{\partial\psi}||\mathbb{A}(\psi)\theta - \tilde{\boldsymbol{y}}||_2^2\Big|_\theta = 0$, hence $\lambda = 0$ from the second equation in eq. (F.3), and the solution θ^* of the first equation would be given by the normal equation $\boldsymbol{\theta}^* = (\mathbb{A}^T\mathbb{A})^{-1}\mathbb{A}^T\tilde{\boldsymbol{y}}$ as derived in eq. (E.11).

In conclusion, LIUQE solves a system of equation equivalent to,

$$\begin{cases} \boldsymbol{\theta} = (\mathbb{A}^T(\psi)\mathbb{A}(\psi))^{-1}\mathbb{A}^T(\psi)\tilde{\boldsymbol{y}} \\ \psi = G(\theta) \end{cases} \tag{F.4}$$

without checking that the condition $\frac{\partial}{\partial\psi}||\mathbb{A}(\psi)\theta - \tilde{\boldsymbol{y}}||_2^2\Big|_{\theta^*} = 0$ is satisfied which is not generally true as proved numerically in section 4.5. This provides a solution θ^* and ψ^* that respects the equality constraint $\psi = G(\theta)$, hence the free-boundary Grad-Shafranov, but is not generally a solution of the original problem eq. (3.9) equivalent to eq. (F.1), hence a minimum for

$||\mathbb{A}(\psi)\theta - \tilde{\boldsymbol{y}}||_2^2$. As discussed at the end of section E, the solution of LIUQE coincides with the real minimum only in the special case when $\tilde{\boldsymbol{y}} = \mathbb{A}(\psi)\theta$, hence only in case of noise free measurements and model with no uncertainty.

G Derivation of the integral OD current diffusion equation

We derive in this appendix the integral version of the current diffusion equation implemented in the FGE. The credits for most part of the derivation go to [A.Merle, private communication].

We recall here the current diffusion equation for reading convenience,

$$\underbrace{\sigma_{\parallel}\left(\frac{\hat{\rho}^2\dot{\Phi}_B}{V'_{\hat{\rho}}}\frac{\partial\psi}{\partial\hat{\rho}} - \frac{2\Phi_B}{V'_{\hat{\rho}}}\hat{\rho}\frac{\partial\psi}{\partial t}\bigg|_{\hat{\rho}}\right)}_{<\boldsymbol{j}_{\Omega}\cdot B>} = \underbrace{\frac{T^2}{8\pi\mu_0\Phi_B V'_{\hat{\rho}}}\frac{\partial}{\partial\hat{\rho}}\left(\frac{g_2 g_3}{\hat{\rho}}\frac{\partial\psi}{\partial\hat{\rho}}\right)}_{<\boldsymbol{j}\cdot B>} - <\boldsymbol{j}_{ni}\cdot B> \tag{G.1}$$

We define the integral operator,

$$\Gamma(A) = \frac{T_B}{2\pi}\int_0^1 \frac{V'_{\hat{\rho}}}{T^2}A\,d\hat{\rho} \tag{G.2}$$

and apply eq. (G.2) to eq. (G.1). The first term on the RHS of eq. (2.56) becomes directly I_p. Defining,

$$A_1 = \frac{T_B\Phi_B}{\pi}\int_0^1 \frac{\sigma_{\parallel}}{T^2}\hat{\rho}\frac{\partial\psi}{\partial t}\bigg|_{\hat{\rho}}\,d\hat{\rho} \tag{G.3}$$

$$A_2^* = -\frac{d\Phi_B}{dt}\frac{T_B(\psi_B - \psi_A)}{2\pi}\int_0^1 \frac{\sigma_{\parallel}}{T^2}\hat{\Phi}\,d\hat{\psi} \tag{G.4}$$

equation eq. (G.1) becomes,

$$-(A_1 + A_2^*) = I_p - \Gamma(<j_{ni}\cdot B>) \tag{G.5}$$

Since all the quantities computed from the equilibrium part of the FGE are expressed in a fixed in time $\hat{\psi}$ grid, we would like to express A_1 in the same terms, manipulating in particular $\frac{\partial\psi}{\partial t}\big|_{\hat{\rho}}$.

Appendix G. Derivation of the integral OD current diffusion equation

Starting form the definition,

$$\psi = \psi(\hat{\psi}, t) = \hat{\psi}(\psi_B(t) - \psi_A(t)) + \psi_A(t) \tag{G.6}$$

we can write,

$$\left.\frac{\partial \psi}{\partial t}\right|_{\hat{\psi}} = \hat{\psi}(\dot{\psi}_B - \dot{\psi}_A) + \dot{\psi}_A. \tag{G.7}$$

Moreover, from the definition

$$\Phi = \Phi(\psi) = \int_0^\psi \iota(\psi')d\psi' = \Phi(\psi(\hat{\psi}, t)) = \int_0^{\psi(\hat{\psi},t)} \iota(\psi')d\psi' \tag{G.8}$$

hence, since $\rho = \sqrt{\hat{\Phi}}$

$$\hat{\rho} = \frac{\rho}{\rho_B(t)} = \hat{\rho}(\psi, t) \tag{G.9}$$

and therefore,

$$\psi = \psi(\hat{\rho}(\hat{\psi}, t), t) \tag{G.10}$$

Performing the derivative of eq. (G.10) at fixed $\hat{\psi}$.

$$\left.\frac{\partial \psi}{\partial t}\right|_{\hat{\psi}} = \left.\frac{\partial \psi}{\partial \hat{\rho}}\right|_t \left.\frac{\partial \hat{\rho}}{\partial t}\right|_{\hat{\psi}} + \left.\frac{\partial \psi}{\partial t}\right|_{\hat{\rho}}. \tag{G.11}$$

We can now combine eq. (G.7) and eq. (G.11) to obtain an explicit expression for $\left.\frac{\partial \psi}{\partial t}\right|_{\hat{\rho}}$ to be used in eq. (G.3).

$$\left.\frac{\partial \psi}{\partial t}\right|_{\hat{\rho}} = \hat{\psi}(\dot{\psi}_B - \dot{\psi}_A) + \dot{\psi}_A - \left.\frac{\partial \psi}{\partial \hat{\rho}}\right|_t \left.\frac{\partial \hat{\rho}}{\partial t}\right|_{\hat{\psi}} \tag{G.12}$$

Remembering that $\hat{\psi}$ is a fixed coordinate in time, we now write,

$$\left.\frac{\partial \psi}{\partial \hat{\rho}}\right|_t = \left.\frac{\partial \psi(\hat{\psi}, t)}{\partial \hat{\rho}}\right|_t = \left.\frac{\partial \psi}{\partial \hat{\psi}}\right|_t \left.\frac{\partial \hat{\psi}}{\partial \hat{\rho}}\right|_t = (\psi_B - \psi_A)\left.\frac{\partial \hat{\psi}}{\partial \hat{\rho}}\right|_t \tag{G.13}$$

Finally we split the A_1 term in eq. (G.3) into the two following terms $A_{1,1}$ eq. (2.62) and $A_{1,2}$ eq. (G.15),

$$A_{1,1} = \frac{T_B \Phi_B}{\pi} \int_0^1 \frac{\sigma_\parallel}{T^2} \hat{\rho} \left[\hat{\psi}(\dot{\psi}_B - \dot{\psi}_A) + \dot{\psi}_A \right] d\hat{\rho} = \frac{T_B \Phi_B}{2\pi} \int_0^1 \frac{\sigma_\parallel}{T^2} \left[\hat{\psi}(\dot{\psi}_B - \dot{\psi}_A) + \dot{\psi}_A \right] d\hat{\Phi} \tag{G.14}$$

$$A_{1,2} = -(\psi_B - \psi_A)\frac{T_B \Phi_B}{\pi} \int_0^1 \frac{\sigma_\parallel}{T^2} \hat{\rho} \left.\frac{\partial \hat{\rho}}{\partial t}\right|_{\hat{\psi}} d\hat{\psi} = -(\psi_B - \psi_A)\frac{T_B \Phi_B}{2\pi} \int_0^1 \frac{\sigma_\parallel}{T^2} \left.\frac{\partial \hat{\Phi}}{\partial t}\right|_{\hat{\psi}} d\hat{\psi} \tag{G.15}$$

By making use of the chain rule and the definition of $\hat{\Phi}$,

$$\left.\frac{\partial \hat{\Phi}}{\partial t}\right|_{\hat{\psi}} = \frac{1}{\Phi_b}\left.\frac{\partial \Phi}{\partial t}\right|_{\hat{\psi}} - \frac{\Phi}{\Phi_b^2}\frac{d\Phi_b}{dt} \tag{G.16}$$

one can conveniently combine $A_{1,2}$ and A_2^* into a unique term,

$$A_2 = -\frac{T_B(\psi_B - \psi_A)}{2\pi}\int_0^1 \frac{\sigma_\parallel}{T^2}\left.\frac{\partial \Phi}{\partial t}\right|_{\hat{\psi}}d\hat{\psi}. \tag{G.17}$$

The A_2 and $A_{1,1}$ terms can be rewritten in a cleaner way as,

$$A_{1,1} = \frac{T_B}{2\pi}\int_0^{\Phi_B} \frac{\sigma_\parallel}{T^2}\left.\frac{\partial \psi}{\partial t}\right|_{\hat{\psi}}d\Phi \tag{G.18}$$

$$A_2 = -\frac{T_B}{2\pi}\int_{\psi_A}^{\psi_B} \frac{\sigma_\parallel}{T^2}\left.\frac{\partial \Phi}{\partial t}\right|_{\hat{\psi}}d\psi. \tag{G.19}$$

The additional information that has to be computed from the equilibrium solution is $\Phi(\hat{\psi},t)$ in the fixed grid $\hat{\psi}$ at each time t. The integral current diffusion equation eq. (2.56) becomes,

$$-(A_{1,1} + A_2) = I_p - \Gamma(<j_{ni}\cdot B>) \tag{G.20}$$

We remember that the sign convention is chosen in order to respect COCOS 17 [Sauter and Medvedev 2013]. The 1D CDE equation admits a stationary state solution where $\dot{\Phi}_B = 0$ and $\frac{\partial}{\partial\rho}\frac{\partial \psi}{\partial t} = 0$ meaning that the $\frac{\partial \psi}{\partial t}$ is constant over the radius ρ hence it can be extracted from the integration signal in the $A_{1,1}$ term. In particular $\frac{\partial \psi_A}{\partial t} = \frac{\partial \psi_B}{\partial t} \equiv V_{SS}$.

$$V_{SS} = \frac{\Gamma(<j_{ni}\cdot B>) - I_p}{\frac{T_B}{2\pi}\int_0^{\Phi_B}\frac{\sigma_\parallel}{T^2}d\Phi} \tag{G.21}$$

$$\tag{G.22}$$

We take inspiration from the Stationary State condition to derive an approximated current diffusion equation which is correct only in case a truly stationary state, but provides a good estimate during plasma phases which do not present rapid transient. We first define the following effective poloidal flux time derivative at constant $\hat{\rho}$,

$$V_{eff} = \frac{\int_0^1 \frac{\sigma_\parallel}{T^2}\hat{\rho}\left.\frac{\partial \psi}{\partial t}\right|_{\hat{\rho}}d\hat{\rho}}{\int_0^1 \frac{\sigma_\parallel}{T^2}\hat{\rho}d\hat{\rho}} \tag{G.23}$$

Given eq. (G.23) in case of a stationary-state $V_{eff} = V_{SS}$, that due to the $\frac{\partial}{\partial\hat{\rho}}\left(\left.\frac{\partial \psi}{\partial t}\right|_{\hat{\rho}}\right) = 0$, can be considered as $V_{SS} = \dot{\psi}_A = \dot{\psi}_B$, otherwise on can see V_{eff} is as an averaged $\left.\frac{\partial \psi}{\partial t}\right|_{\hat{\rho}}$ opportunely

Appendix G. Derivation of the integral OD current diffusion equation

weighted as defined in eq. (G.23). We assume the following heuristic estimate $V_{eff} = (\dot{\psi}_A + \dot{\psi}_B)/2$ of the average. The integral version of the current diffusion equation on stationary state condition eq. (G.5) takes the following form,

$$\frac{1}{2}\frac{d(\psi_B + \psi_A)}{dt} = \frac{\Gamma(< j_{ni} \cdot B >) - I_p}{\frac{T_B \Phi_B}{\pi} \int_0^1 \frac{\sigma_{\parallel}}{T^2} \hat{\rho} d\hat{\rho}} = \frac{I_{ni}^* - I_p}{\frac{T_B \Phi_B}{\pi} \int_0^1 \frac{\sigma_{\parallel}}{T^2} \hat{\rho} d\hat{\rho}} \tag{G.24}$$

We define in particular $I_{ni}^* = \Gamma(\langle j_{ni} \cdot B \rangle)$, where the symbol $*$ is used to indicate the fact that I_{ni}^* is not exactly equal to the total toroidal current of the non inductive current sources. The choice for V_{eff} and $\dot{\Phi}_B = 0$ is correct in the limit of stationary state. It suffers in particular for fast varying plasma shapes when the term $\dot{\Phi}_B$ cannot be considered small and during fast transient phases of current relaxation for example after a rapid change of non inductive sources.

Acknowledgements

Thanks to Olivier Sauter, for being at the same time a great physicist with incredible intuition and a great mentor, finding always the positive side of every situation. For sure he will not remember me as an easy student to handle. Yet, all the times, with a patience and commitment way beyond any believable limit he was teaching me what was the good way to take, by being an example at first. He demonstrated that to me till the very last hours of my thesis. From him I have learnt, and I am still learning, that human relations and personal attitude are as important as technical competencies, also when it is about to discussing an objective topic on how to solve an equation. You will be forever my example when I will think about a physicist who does his work for passion. Federico Felici, for being in constant search of perfection, eager to discover and try new things and new approaches. In my thesis I felt dragged by your constant momentum. From you I have learnt an incredible amount of technical skills and I shared the passion for clean coding and good practices, even though at the beginning I was not that practical. Antoine Merle, for his meticulous approach to every problem, and his attention to go down to the very details before accepting any statement. He was an invaluable colleague to work with and I apologize if sometimes I made him waste so much time with first year calculus question. Jean-Marc and Cristian for all the help with the implementation and the technical support. My work was just a tiny piece on top of the mountain they have built. Ivo, for his multiple discussions during lunch time which inspired me and let my mind free to think about practical world topics. My office-mates, for having tasted together the most amazing teas from all over the word and got addicted to them. I would like to thank all the PhD colleagues at SPC. MatNicoteo (I did not want to put an order hence I fused the names since in any case one of the two likes the acronym and the other has developed his own dictionary), Lorenzo, Federico e Riccardo who shared with me the fun of being a PHD outside the working hours. I must thank also the "older" colleagues Matteo, Fabio and Federico for having welcome me at SPC and been good friends for all the time spent. When I hear saying "SPC is a big family" I think there is a big part of truth underneath. A special thanks goes to my wife Elena. We have been together for long time without living together and being constantly in a different country. Eventually, due to the most unexpected reason of a pandemic, we have been sharing a very small house in Turin while writing my thesis. It is thanks to her if I lived this period with confidence and I owe her a lot. (Well, in this contest, I must say that also having an amazing Pizzeria Napoletana nearby was somehow helpful to survive the lockdown) To all the friends in Lausanne, Silvia, Ania, Gioia, Omar, Piotrek and Fabio (again) which made

219

Acknowledgements

me feel home. I hope to share with you still a lot of adventures. And finally to my family, which has been always far away in the last years, but supporting me all the times I needed.

Lausanne, October 31, 2020   F.C.

220

Bibliography

H. Al Daas, L. Grigori, P. Hénon, and P. Ricoux. Recycling krylov subspaces and reducing deflation subspaces for solving sequence of linear systems. 2018.

R. Albanese, R. Ambrosino, and M. Mattei. Create-nl+: A robust control-oriented free boundary dynamic plasma equilibrium solver. *Fusion Engineering and Design*, 96:664–667, 2015.

R. Ambrosino, R. Albanese, G. Calabrò, A. Castaldo, F. Crisanti, V. Loschiavo, M. de Magistris, S. Minucci, and G. Ramogida. The dtt device: Poloidal field coil assessment for alternative plasma configurations. *Fusion Engineering and Design*, 122:322–332, 2017.

C. Angioni and O. Sauter. Erratum: "neoclassical transport coefficients for general axisymmetric equilibria in the banana regime" [phys. plasmas 7, 1224 (2000)]. *Physics of Plasmas*, 7(7): 3122–3122, 2000a. doi: 10.1063/1.874172. URL https://doi.org/10.1063/1.874172.

C. Angioni and O. Sauter. Neoclassical transport coefficients for general axisymmetric equilibria in the banana regime. *Physics of Plasmas*, 7(4):1224–1234, 2000b. doi: 10.1063/1.873933. URL https://doi.org/10.1063/1.873933.

H. Arnichand, Y. Andrebe, P. Blanchard, S. Antonioni, S. Couturier, J. Decker, B. Duval, F. Felici, C. Galperti, P.-F. Isoz, et al. New capabilities of the incoherent thomson scattering diagnostics in the tcv tokamak: divertor and real-time measurements. *Journal of Instrumentation*, 14 (09):C09013, 2019.

F. J. Artola, P. Beyer, G. Huijsmans, A. Loarte, and M. Hoelzl. *Free-boundary simulations of MHD plasma instabilities in tokamaks*. PhD thesis, PhD thesis. Aix-Marseille Université, 2018.

M. E. Austin, A. Marinoni, M. Walker, M. Brookman, J. DeGrassie, A. Hyatt, G. McKee, C. Petty, T. Rhodes, S. Smith, et al. Achievement of reactor-relevant performance in negative triangularity shape in the diii-d tokamak. *Physical Review Letters*, 122(11):115001, 2019.

N.-n. Bao, Y. Huang, J. Barr, Z.-p. Luo, Y.-h. Wang, S.-l. Chen, B.-j. Xiao, and D. Humphreys. Tests of the real-time vertical growth rate calculation on east. *Chinese Physics B*, 2020.

S. Barry. The extension of the fir interferometer of tcv to a polarimeter and measurements of the faraday rotation caused by the poloidal magnetic field. Technical report, 1999.

Bibliography

J. E. Barton, M. D. Boyer, W. Shi, W. Wehner, E. Schuster, J. R. Ferron, M. L. Walker, D. A. Humphreys, T. C. Luce, F. Turco, et al. Physics-model-based nonlinear actuator trajectory optimization and safety factor profile feedback control for advanced scenario development in diii-d. *Nuclear Fusion*, 55(9):093005, 2015.

A. S. Bishop. Project sherwood: the us program in controlled fusion. 1958.

D. Biskamp and J. Drake. Dynamics of the sawtooth collapse in tokamak plasmas. *Physical review letters*, 73(7):971, 1994.

Å. Björck. Solving linear least squares problems by gram-schmidt orthogonalization. *BIT Numerical Mathematics*, 7(1):1–21, 1967.

T. Blanken, F. Felici, C. Rapson, M. de Baar, W. Heemels, et al. Control-oriented modeling of the plasma particle density in tokamaks and application to real-time density profile reconstruction. *Fusion Engineering and Design*, 126:87–103, 2018.

T. C. Blanken, F. Felici, C. Galperti, N. M. T. Vu, M. Kong, O. Sauter, M. de Baar, E. M. Team, T. Team, et al. Real-time plasma state monitoring and supervisory control on tcv. *Nuclear Fusion*, 59(2):026017, 2019.

J. Blum and J. Le Foll. Plasma equilibrium evolution at the resistive diffusion timescale. *Computer Physics Reports*, 1(7-8):465–494, 1984.

J. Blum and B. Thooris. Parametric identification of the plasma current density from the magnetic measurements and pressure profile rep. *JET contract JT3/9008 (Abingdon, Oxfordshire: JET Joint Undertaking)*, 1985.

J. Blum, J. Le Foll, and B. Thooris. The self-consistent equilibrium and diffusion code sced. *Computer Physics Communications*, 24(3-4):235–254, 1981.

J. Blum, C. Boulbe, and B. Faugeras. Reconstruction of the equilibrium of the plasma in a tokamak and identification of the current density profile in real time. *Journal of computational physics*, 231(3):960–980, 2012.

J. Blum, H. Heumann, E. Nardon, and X. Song. Automating the design of tokamak experiment scenarios. *Journal of Computational Physics*, 394:594–614, 2019.

S. Bo, Y. Jinhong, Y. Cheng, D. Cheng, W. Hui, H. Zhang, D. Haifei, Q. Junli, G. Xianzu, and W. Weihua. Double-null divertor configuration discharge and disruptive heat flux simulation using tsc on east. *Plasma Science and Technology*, 20(7):074006, 2018.

M. Bornatici, R. Cano, O. De Barbieri, and F. Engelmann. Electron cyclotron emission and absorption in fusion plasmas. *Nuclear Fusion*, 23(9):1153, 1983.

M. Boyer, S. Kaye, and K. Erickson. Real-time capable modeling of neutral beam injection on nstx-u using neural networks. *Nuclear Fusion*, 59(5):056008, 2019.

M. Brix, N. Hawkes, A. Boboc, V. Drozdov, S. Sharapov, and J.-E. Contributors. Accuracy of efit equilibrium reconstruction with internal diagnostic information at jet. *Review of Scientific Instruments*, 79(10):10F701, 2008.

M. Brusati, J. Christiansen, J. Cordey, K. Jarrett, E. Lazzaro, and R. Ross. Analysis of magnetic measurements in tokamaks. *Computer Physics Reports*, 1(7/8):345–372, 1984.

K. Burrell, L. Lao, and B. Grierson. Using motional stark splitting of d α emission to constrain mhd equilibrium analysis in diii-d plasmas. *Review of Scientific Instruments*, 89(10):10D111, 2018.

F. Carpanese, F. Felici, C. Galperti, A. Merle, J. Moret, O. Sauter, et al. First demonstration of real-time kinetic equilibrium reconstruction on tcv by coupling liuqe and raptor. *Nuclear Fusion*, 60(6):066020, 2020.

A. Castaldo, A. Mele, R. Albanese, R. Ambrosino, G. De Tommasi, Z. Luo, A. Pironti, B. Xiao, and Q. Yuan. Simulation suite for plasma magnetic control at east tokamak. *Fusion Engineering and Design*, 133:19–31, 2018.

A. J. Cerfon and J. P. Freidberg. "one size fits all" analytic solutions to the grad–shafranov equation. *Physics of Plasmas*, 17(3):032502, 2010.

I. Chapman. Controlling sawtooth oscillations in tokamak plasmas. *Plasma Physics and Controlled Fusion*, 53(1):013001, 2010.

Y. Chen and C. Shen. A jacobian-free newton-gmres (m) method with adaptive preconditioner and its application for power flow calculations. *IEEE Transactions on Power Systems*, 21(3): 1096–1103, 2006.

M.-S. Chu and M. Okabayashi. Stabilization of the external kink and the resistive wall mode. *Plasma Physics and Controlled Fusion*, 52(12):123001, 2010.

J. Citrin, S. Breton, F. Felici, F. Imbeaux, T. Aniel, J. Artaud, B. Baiocchi, C. Bourdelle, Y. Camenen, and J. Garcia. Real-time capable first principle based modelling of tokamak turbulent transport. *Nuclear Fusion*, 55(9):092001, 2015.

S. Coda, O. Sauter, M. Henderson, and T. Goodman. Full bootstrap discharge sustainment in steady state in the tcv tokamak. In *Proceedings of the 22nd IAEA Fusion Energy Conference*, number CONF, pages EX–2. IAEA, 2008.

S. Coda, J. Ahn, R. Albanese, S. Alberti, E. Alessi, S. Allan, H. Anand, G. Anastassiou, Y. Andrèbe, C. Angioni, et al. Overview of the tcv tokamak program: scientific progress and facility upgrades. *Nuclear Fusion*, 57(10):102011, 2017.

S. Coda, M. Agostini, R. Albanese, S. Alberti, E. Alessi, S. Allan, J. Allcock, R. Ambrosino, H. Anand, Y. Andrebe, et al. Physics research on the tcv tokamak facility: from conventional to alternative scenarios and beyond. *Nuclear Fusion*, 59(11):112023, 2019.

Bibliography

R. Coelho, D. Alves, N. Hawkes, M. Brix, and J. E. Contributors. Real-time data processing and magnetic field pitch angle estimation of the jet motional stark effect diagnostic based on kalman filtering. *Review of Scientific Instruments*, 80(6):063504, 2009.

A. Coutlis, I. Bandyopadhyay, J. Lister, P. Vyas, R. Albanese, D. Limebeer, F. Villone, and J. Wainwright. Measurement of the open loop plasma equilibrium response in tcv. *Nuclear Fusion*, 39(5):663, 1999.

L. Degtyarev and V. Drozdov. An inverse variable technique in the mhd-equilibrium problem. *Computer Physics Reports*, 2(7):341–387, 1985.

E. Fable, C. Angioni, F. Casson, D. Told, A. Ivanov, F. Jenko, R. McDermott, S. Y. Medvedev, G. Pereverzev, F. Ryter, et al. Novel free-boundary equilibrium and transport solver with theory-based models and its validation against asdex upgrade current ramp scenarios. *Plasma Physics and Controlled Fusion*, 55(12):124028, 2013a.

E. Fable, C. Angioni, A. Ivanov, K. Lackner, O. Maj, S. Yu, G. Pautasso, G. Pereverzev, et al. A stable scheme for computation of coupled transport and equilibrium equations in tokamaks. *Nuclear Fusion*, 53(3):033002, 2013b.

A. Fasoli, T. Team, et al. Tcv heating and in-vessel upgrades for addressing demo physics issues. *Nuclear Fusion*, 55(4):043006, 2015.

A. Fasoli, S. Brunner, W. Cooper, J. Graves, P. Ricci, O. Sauter, and L. Villard. Computational challenges in magnetic-confinement fusion physics. *Nature Physics*, 12(5):411–423, 2016.

B. Faugeras. An overview of the numerical methods for tokamak plasma equilibrium computation implemented in the nice code. 2020.

B. Faugeras and F. Orsitto. On the identification of the electron temperature profile from polarimetry stokes vector measurements in tokamak free-boundary equilibrium reconstruction. *Plasma Physics and Controlled Fusion*, 61(11):115002, 2019.

B. Faugeras, J. Blum, C. Boulbe, P. Moreau, and E. Nardon. 2d interpolation and extrapolation of discrete magnetic measurements with toroidal harmonics for equilibrium reconstruction in a tokamak. *Plasma Physics and Controlled Fusion*, 56(11):114010, 2014.

J. F.Carpanese, O.Sauter. Benchmark of liuqe code against efit for iter synthetic data. 2017.

F. Felici. Real-time control of tokamak plasmas: from control of physics to physics-based control. *PhD thesis No 5203, 2011, EPFL, Switzerland, DOI:10.5075/epfl-thesis-5203*, 2011.

F. Felici, O. Sauter, S. Coda, B. Duval, T. Goodman, J. Moret, J. Paley, T. Team, et al. Real-time physics-model-based simulation of the current density profile in tokamak plasmas. *Nuclear Fusion*, 51(8):083052, 2011.

F. Felici, M. de Baar, and M. Steinbuch. A dynamic state observer for real-time reconstruction of the tokamak plasma profile state and disturbances. *2014 American Control Conference*, pages 4816–4823, 2014.

F. Felici, J. Citrin, A. Teplukhina, J. Redondo, C. Bourdelle, F. Imbeaux, O. Sauter, J. Contributors, E. M. Team, et al. Real-time-capable prediction of temperature and density profiles in a tokamak using raptor and a first-principle-based transport model. *Nuclear Fusion*, 58(9): 096006, 2018.

J. Ferron, M. Walker, L. Lao, H. S. John, D. Humphreys, and J. Leuer. Real time equilibrium reconstruction for tokamak discharge control. *Nuclear fusion*, 38(7):1055, 1998.

R. Fischer, C. Fuchs, B. Kurzan, W. Suttrop, E. Wolfrum, and A. U. Team. Integrated data analysis of profile diagnostics at asdex upgrade. *Fusion science and technology*, 58(2):675–684, 2010.

R. Fischer, A. Bock, M. Dunne, J. Fuchs, L. Giannone, K. Lackner, P. McCarthy, E. Poli, R. Preuss, M. Rampp, et al. Coupling of the flux diffusion equation with the equilibrium reconstruction at ASDEX upgrade. *Fusion Science and Technology*, 69(2):526–536, 2016.

R. Fischer, A. Bock, A. Burckhart, O. P. Ford, L. Giannone, V. Igochine, M. Weiland, and M. Willensdorfer. Sawtooth induced q-profile evolution at ASDEX upgrade. *Nuclear Fusion*, 59(5): 056010, 2019.

J. P. Freidberg. *ideal MHD*. Cambridge University Press, 2014.

D. Gamerman and H. F. Lopes. *Markov chain Monte Carlo: stochastic simulation for Bayesian inference*. CRC Press, 2006.

L. Giannone, B. Geiger, R. Bilato, M. Maraschek, T. Odstrčil, R. Fischer, J. Fuchs, P. J. McCarthy, V. Mertens, and K. Schuhbeck. Real-time diamagnetic flux measurements on asdex upgrade. *Review of Scientific Instruments*, 87(5):053509, 2016.

H. Grad and H. Rubin. Hydromagnetic equilibria and force-free fields. *Journal of Nuclear Energy (1954)*, 7(3-4):284–285, 1958.

L. Guazzotto and J. P. Freidberg. A family of analytic equilibrium solutions for the grad–shafranov equation. *Physics of Plasmas*, 14(11):112508, 2007.

A. Hadjidimos. Successive overrelaxation (sor) and related methods. *Journal of Computational and Applied Mathematics*, 123(1-2):177–199, 2000.

R. Hawryluk. An empirical approach to tokamak transport. pages 19–46. Elsevier, 1981.

T. Hender, J. Wesley, J. Bialek, A. Bondeson, A. Boozer, R. Buttery, A. Garofalo, T. Goodman, R. Granetz, Y. Gribov, et al. Mhd stability, operational limits and disruptions. *Nuclear fusion*, 47(6):S128, 2007.

H. Heumann, J. Blum, C. Boulbe, B. Faugeras, G. Selig, J.-M. Ané, S. Brémond, V. Grandgirard, P. Hertout, and E. Nardon. Quasi-static free-boundary equilibrium of toroidal plasma with CEDRES++: Computational methods and applications. *Journal of Plasma Physics*, 81(3), 2015.

F. Hinton and R. D. Hazeltine. Theory of plasma transport in toroidal confinement systems. *Reviews of Modern Physics*, 48(2):239, 1976.

J. D. Hoffman and S. Frankel. *Numerical methods for engineers and scientists*. CRC press, 2018.

F. Hofmann. Fbt-a free-boundary tokamak equilibrium code for highly elongated and shaped plasmas. *Computer physics communications*, 48(2):207–221, 1988.

F. Hofmann and G. Tonetti. Tokamak equilibrium reconstruction using faraday rotation measurements. *Nuclear Fusion*, 28(10):1871, 1988.

R. V. Hogg, J. McKean, and A. T. Craig. *Introduction to mathematical statistics*. Pearson Education, 2005.

C. Holcomb, M. Makowski, R. Jayakumar, S. Allen, R. Ellis, R. Geer, D. Behne, K. Morris, L. Seppala, and J. Moller. Motional stark effect diagnostic expansion on diii-d for enhanced current and e r profile measurements. *Review of scientific instruments*, 77(10):10E506, 2006.

M. Hole, G. Von Nessi, J. Bertram, J. Svensson, L. C. Appel, B. Blackwell, R. Dewar, and J. Howard. Model data fusion: developing bayesian inversion to constrain equilibrium and mode structure. *arXiv preprint arXiv:1002.3189*, 2010a.

M. Hole, G. Von Nessi, J. Bertram, J. Svensson, L. C. Appel, B. Blackwell, R. Dewar, and J. Howard. Model data fusion: developing bayesian inversion to constrain equilibrium and mode structure. *arXiv preprint arXiv:1002.3189*, 2010b.

Y. Huang, B.-J. Xiao, and Z.-P. Luo. Fast parallel grad–shafranov solver for real-time equilibrium reconstruction in east tokamak using graphic processing unit. *Chinese Physics B*, 26(8): 085204, 2017.

Y. Huang, Z. Luo, B. Xiao, L. Lao, A. Mele, A. Pironti, M. Mattei, G. Ambrosino, Q. Yuan, Y. Wang, et al. Gpu-optimized fast plasma equilibrium reconstruction in fine grids for real-time control and data analysis. *Nuclear Fusion*, 2020.

D. Humphreys, J. Ferron, M. Bakhtiari, J. Blair, Y. In, G. Jackson, H. Jhang, R. Johnson, J. Kim, R. LaHaye, et al. Development of iter-relevant plasma control solutions at diii-d. *Nuclear Fusion*, 47(8):943, 2007.

D. Humphreys, G. Ambrosino, P. de Vries, F. Felici, S. H. Kim, G. Jackson, A. Kallenbach, E. Kolemen, J. Lister, D. Moreau, et al. Novel aspects of plasma control in iter. *Physics of Plasmas*, 22(2):021806, 2015.

R. Isler. An overview of charge-exchange spectroscopy as a plasma diagnostic. *Plasma Physics and Controlled Fusion*, 36(2):171, 1994.

A. Ivanov, R. Khayrutdinov, S. Y. Medvedev, Y. Y. Poshekhonov, et al. New adaptive grid plasma evolution code spider. In *32nd EPS Conference on Plasma Phys., June*, volume 27, pages 5–063. Citeseer, 2005.

M. S. Y. Ivanov A A, Khayrutdinov R R and P. Y. Yu. The spider code-axisymmetric fixed boundary plasma equilibrium solver. *Preprint KIAM-7, M. http://www.keldysh.ru/papers/2006/prep07/prep2006_07.html*, (0):7–25, 2006.

F. Janky, E. Fable, W. Treutterer, I. G. Ortiz, O. Kudlacek, et al. Asdex upgrade flight simulator development. *Fusion Engineering and Design*, 146:1926–1929, 2019.

S. Jardin. *Computational methods in plasma physics*. CRC Press, 2010.

S. Jardin, S. Kaye, J. Menard, C. Kessel, and A. Glasser. Tokamak simulation code modeling of nstx. Technical report, Princeton Plasma Physics Lab., NJ (US), 2000.

S. C. Jardin, N. Pomphrey, and J. Delucia. Dynamic modeling of transport and positional control of tokamaks. *Journal of computational Physics*, 66(2):481–507, 1986.

Y. Jiang, S. Sabbagh, Y. S. Park, J. Berkery, J. H. Ahn, J. Riquezes, J. Ko, J. Lee, S. Yoon, A. Glasser, et al. Kinetic equilibrium reconstruction validation and stability analysis of kstar plasmas supporting disruption event characterization and forecasting. *APS*, 2019:PP10–049, 2019.

B. Kadomtsev. Magnetic field line reconnection. *Reports on Progress in Physics*, 50(2):115, 1987.

B. B. Kadomtsev. Disruptive instability in tokamaks. *FizPl*, 1:710–715, 1975.

R. E. Kalman. A new approach to linear filtering and prediction problems. *Journal of basic Engineering*, 82(1):35–45, 1960.

M. Keilhacker, J. Team, et al. Fusion physics progress on the joint european torus (jet). *Plasma Physics and Controlled Fusion*, 41(12B):B1, 1999.

R. Khayrutdinov and V. Lukash. Studies of plasma equilibrium and transport in a tokamak fusion device with the inverse-variable technique. *Journal of Computational Physics*, 109(2): 193–201, 1993.

R. Khayrutdinov, J. Lister, V. Lukash, and J. Wainwright. Comparing dina code simulations with tcv experimental plasma equilibrium responses. *Plasma Physics and Controlled Fusion*, 43(3):321, 2001.

S. Kim, J. Artaud, V. Basiuk, V. Dokuka, R. Khayrutdinov, J. Lister, and V. Lukash. Full tokamak discharge simulation of iter by combining dina-ch and cronos. *Plasma Physics and Controlled Fusion*, 51(10):105007, 2009.

Bibliography

D. A. Knoll and D. E. Keyes. Jacobian-free newton–krylov methods: a survey of approaches and applications. *Journal of Computational Physics*, 193(2):357–397, 2004.

T. Knudsen and J. Leth. A new continuous discrete unscented kalman filter. *IEEE Transactions on Automatic Control*, 64(5):2198–2205, 2018.

M. Kong, T. C. Blanken, F. Felici, C. Galperti, B. Maljaars, O. Sauter, T. Vu, F. Carpanese, A. Merle, J.-M. Moret, et al. Control of ntms and integrated multi-actuator plasma control on tcv. *Nuclear Fusion*, 2019.

B. Kremers. Neural network training data optimization for turbulence modeling. *Master Thesis, Tue*, 2020.

H. W. Kuhn and A. W. Tucker. Nonlinear programming, in (j. neyman, ed.) proceedings of the second berkeley symposium on mathematical statistics and probability. *University of California Press, Berkeley*, 1951.

A. Kuijper. On detecting all saddle points in 2d images. *Pattern Recognition Letters*, 25(15): 1665–1672, 2004.

K. Lackner. Computation of ideal mhd equilibria. *Computer Physics Communications*, 12(1): 33–44, 1976.

L. Lao, H. S. John, R. Stambaugh, A. Kellman, and W. Pfeiffer. Reconstruction of current profile parameters and plasma shapes in tokamaks. *Nuclear fusion*, 25(11):1611, 1985.

L. Lao, J. Ferron, R. Groebner, W. Howl, H. S. John, E. Strait, and T. Taylor. Equilibrium analysis of current profiles in tokamaks. *Nuclear Fusion*, 30(6):1035, 1990.

L. Lao, H. S. John, Q. Peng, J. Ferron, E. Strait, T. Taylor, W. Meyer, C. Zhang, and K. You. Mhd equilibrium reconstruction in the diii-d tokamak. *Fusion science and technology*, 48(2): 968–977, 2005.

L. Lao, B. Grierson, and K. Burrell. Tokamak equilibrium reconstruction with mse-ls data in diii-d. *Bulletin of the American Physical Society*, 61, 2016.

J. Lawson. Some criteria for a useful thermonuclear reactor. *Publication. Culham, United Kingdom: Atomic Energy Research Establishment*, 1955.

J. Leuer, R. Deranian, J. Perron, D. Humphreys, R. Johnson, E. Penaflor, M. Walker, A. Welander, R. Khayrutdinov, V. Dokouka, et al. Diii-d plasma control simulation environment. In *20th IEEE/NPSS Symposium onFusion Engineering, 2003.*, pages 397–400. IEEE, 2003.

G. Li, Q. Ren, J. Qian, L. Lao, S. Ding, Y. Chen, Z. Liu, B. Lu, and Q. Zang. Kinetic equilibrium reconstruction on east tokamak. *Plasma Physics and Controlled Fusion*, 55(12):125008, 2013.

Y. Li, P. Lotte, W. Zwingmann, C. Gil, and F. Imbeaux. EFIT equilibrium reconstruction including polarimetry measurements on tore supra. *Fusion Science and Technology*, 59(2):397–405, 2011.

J. Lister, V. Dokouka, R. Khayrutdinov, V. Lukash, B. Duval, J.-M. Moret, J.-F. Artaud, V. Baziuk, and M. Cavinato. Evolution of the dina-ch tokamak full discharge simulator. *Fusion Engineering and design*, 74(1-4):633–637, 2005.

J. B. Lister, F. Hofmann, J.-M. Moret, F. Bühlmann, M. J. Dutch, D. Fasel, A. Favre, P.-F. Isoz, B. Marletaz, P. Marmillod, Y. Martin, A. Perez, and D. J. Ward. The control of tokamak configuration variable plasmas. *Fusion {S}cience and {T}echnology*, 32(3):321–373, 1997.

V. Lukash, D. Raju, V. Dokouka, J.-Y. Favez, R. Khayrutdinov, and J. Lister. Dina simulations of tcv electron cyclotron heating discharges. *Fusion engineering and design*, 66:767–770, 2003.

H. Lütjens, A. Bondeson, and O. Sauter. The chease code for toroidal mhd equilibria. *Computer physics communications*, 97(3):219–260, 1996.

M. Makowski, M. Brix, and N. Hawkes. Semi-empirical calibration technique for the mse diagnostic on the jet and diii-d tokamaks. Technical report, Lawrence Livermore National Lab.(LLNL), Livermore, CA (United States), 2008.

E. Maljaars, F. Felici, T. C. Blanken, C. Galperti, O. Sauter, M. R. de Baar, F. Carpanese, T. P. Goodman, D. Kim, S.-H. Kim, et al. Profile control simulations and experiments on tcv: a controller test environment and results using a model-based predictive controller. *Nuclear Fusion*, 57(12):126063, 2017.

F. Marcus, S. Jardin, and F. Hofmann. Controlled evolution of highly elongated tokamak plasmas. *Physical review letters*, 55(21):2289, 1985.

L. Marietan. Quantitative analysis of tcv kinetic equilibrium reconstruction. *Master Thesis Applied Physics, EPFL 2019*.

C. Marini. Poloidal cx visible light plasma rotation diagnostics in tcv. Technical report, EPFL, 2017.

MATLAB. *R2017a*. The MathWorks Inc., Natick, Massachusetts, 2017.

K. Matsuda. Ray tracing study of the electron cyclotron current drive in diii-d using 60 ghz. *IEEE transactions on plasma science*, 17(1):6–11, 1989.

F. Maviglia, R. Albanese, R. Ambrosino, W. Arter, C. Bachmann, T. Barrett, G. Federici, M. Firdaous, J. Gerardin, M. Kovari, et al. Wall protection strategies for demo plasma transients. *Fusion Engineering and Design*, 136:410–414, 2018.

D. Mazon, S. M. G. de Vicente, R. M. Churchill, A. Dinklage, R. Fischer, M. Jakubowski, A. Murari, M. Romanelli, J. Vega, G. Verdoolaege, et al. Summary report of the 3rd iaea technical meeting on fusion data processing validation and analysis (fdpva). *Nuclear Fusion*, 2020.

P. J. McCarthy, P. Martin, and W. Schneider. The CLISTE interpretive equilibrium code. *Max-Planck-Institut für Plasmaphysik*, 1999.

Bibliography

O. Meneghini, S. Smith, L. Lao, O. Izacard, Q. Ren, J. Park, J. Candy, Z. Wang, C. Luna, V. Izzo, et al. Integrated modeling applications for tokamak experiments with omfit. *Nuclear Fusion*, 55(8):083008, 2015.

O. Meneghini, S. P. Smith, P. B. Snyder, G. M. Staebler, J. Candy, E. Belli, L. Lao, M. Kostuk, T. Luce, T. Luda, et al. Self-consistent core-pedestal transport simulations with neural network accelerated models. *Nuclear Fusion*, 57(8):086034, 2017.

M. C. Messmer, F. Felici, O. Sauter, A. A. Teplukhina, J. P. Loenen, M. Reich, R. Fischer, D. Rittich, and R. J. Jaspers. Optimal MSE polarisation angle and q-profile estimation using kalman filters and the plasma simulator RAPTOR. *Plasma Physics and Controlled Fusion*, 2018.

D. Moreau, M. L. Walker, J. R. Ferron, F. Liu, E. Schuster, J. E. Barton, M. D. Boyer, K. H. Burrell, S. Flanagan, P. Gohil, et al. Integrated magnetic and kinetic control of advanced tokamak plasmas on diii-d based on data-driven models. *Nuclear Fusion*, 53(6):063020, 2013.

J.-M. Moret, F. Buhlmann, D. Fasel, F. Hofmann, and G. Tonetti. Magnetic measurements on the tcv tokamak. *Review of scientific instruments*, 69(6):2333–2348, 1998.

J.-M. Moret, B. Duval, H. Le, S. Coda, F. Felici, and H. Reimerdes. Tokamak equilibrium reconstruction code liuqe and its real time implementation. *Fusion Engineering and Design*, 91:1–15, 2015.

Y. Nakamura, G. Pautasso, M. Sugihara, S. Miyamoto, S. Toshimitsu, and R. Yoshino. Tsc modelling approach to mimicking the halo current in asdex upgrade disruptive discharges. In *Proc. 37th EPS Conf. on Plasma Physics*, 2010.

R. M. Neal. Slice sampling. *Annals of statistics*, pages 705–741, 2003.

J. Nocedal and S. Wright. *Numerical optimization*. Springer Science & Business Media, 2006.

K. Ogata and Y. Yang. *Modern control engineering*, volume 5. Prentice hall Upper Saddle River, NJ, 2010.

a. a. O.Sauter. Icdbseval. *private communication*, 2016-2020.

L. Owen, J. Canik, R. Groebner, J. Callen, X. Bonnin, and T. Osborne. Comparing 1.5d ONETWO and 2d SOLPS analyses of inter-ELM h-mode plasma in DIII-d. *Nuclear Fusion*, 50(6):064017, may 2010. doi: 10.1088/0029-5515/50/6/064017.

A. Pankin, D. McCune, R. Andre, G. Bateman, and A. Kritz. The tokamak monte carlo fast ion module nubeam in the national transport code collaboration library. *Computer Physics Communications*, 159(3):157–184, 2004.

V. Parail, R. Albanese, R. Ambrosino, J.-F. Artaud, K. Besseghir, M. Cavinato, G. Corrigan, J. Garcia, L. Garzotti, Y. Gribov, et al. Self-consistent simulation of plasma scenarios for iter using a combination of 1.5 d transport codes and free-boundary equilibrium codes. *Nuclear Fusion*, 53(11):113002, 2013.

P. Patel, P. Springer, C. Weber, L. Jarrott, O. Hurricane, B. Bachmann, K. Baker, L. Berzak Hopkins, D. Callahan, D. Casey, et al. Hotspot conditions achieved in inertial confinement fusion experiments on the national ignition facility. *Physics of Plasmas*, 27(5):050901, 2020.

A. Pavone, J. Svensson, A. Langenberg, U. Höfel, S. Kwak, N. Pablant, R. Wolf, et al. Neural network approximation of bayesian models for the inference of ion and electron temperature profiles at w7-x. *Plasma Physics and Controlled Fusion*, 61(7):075012, 2019.

N. Peacock, D. Robinson, M. Forrest, P. Wilcock, and V. Sannikov. Measurement of the electron temperature by thomson scattering in tokamak t3. *Nature*, 224(5218):488–490, 1969.

G. V. Pereverzev and P. Yushmanov. Astra. automated system for transport analysis in a tokamak. *Max-Planck-Institut für Plasmaphysik report*, 2002.

S. Peruzzo. Review of the preliminary list of iter magnetic sensors and their positions. Annex 1 to GRT-047 deliverable D3.2-1 CREATE_047_R1.3-1_v_d01, 2012.

D. Pfefferlé, N. Ferraro, S. Jardin, I. Krebs, and A. Bhattacharjee. Modelling of nstx hot vertical displacement events using m 3 d-c 1. *Physics of Plasmas*, 25(5):056106, 2018.

S. Pinches, L. Abadie, L. Appel, J. Artaud, R. Castro, L. Van Dellen, D. Van Eester, J. Hollocombe, M. Hosokawa, F. Imbeaux, et al. Implementation of plasma simulators and plasma reconstruction workflows in iter's integrated modelling & analysis suite (imas). In *44th European Physical Society Conference on Plasma Physics, EPS 2017, 26 June 2017 through 30 June 2017*. European Physical Society (EPS), 2017.

S. Pinches, L. Abadie, H. Ancher, X. Bonnin, F. Carpanese, F. Casson, G. Corrigan, S. Dixon, L. Fleury, D. Harting, T. Hayward-Schneider, O. Hoenen, J. Hollocombe, M. Hosokawa, F. Imbeaux, A. Ivanov, T. Jonsson, L. Jung, R. Khayrutdinov, S. Kim, P. Knight, F. Köchl, S. Konovalov, P. Lauber, V. Lukash, S. Medvedev, A. Merle, V. Mitterauer, M. Owsiak, B. Palak, A. Popa, A. Polevoi, M. Romanelli, O. Sauter, M. Schneider, G. Tardini, and L. V. Dellen. Integrated modelling & analysis suite: Developments to address iter needs. *IAEA, fusion energy conference, expected from October 2020 and May 2021*, 2021.

C. Piron, G. Manduchi, P. Bettini, F. Felici, C. Finotti, P. Franz, O. Kudlacek, G. Marchiori, L. Marrelli, J.-M. Moret, et al. Integration of the state observer raptor in the real-time marte framework at rfx-mod. *Fusion Engineering and Design*, 123:616–619, 2017.

C. Piron, J. Garcia, M. Agostini, M. Fontana, G. Giruzzi, M. Gobbin, T. Goodman, A. Karpushov, M. Kong, A. Merle, et al. Extension of the operating space of high-b n fully non-inductive scenarios on tcv using neutral beam injection. *Nuclear Fusion*, 59(9):096012, 2019.

A. Polevoi, H. Shirai, and T. Takizuka. Benchmarking of the nbi block in astra code versus the ofmc calculations. 1997.

E. Poli, A. Peeters, and G. Pereverzev. Torbeam, a beam tracing code for electron-cyclotron waves in tokamak plasmas. *Computer Physics Communications*, 136(1-2):90–104, 2001.

Bibliography

E. Poli, A. Bock, M. Lochbrunner, O. Maj, M. Reich, A. Snicker, A. Stegmeir, F. Volpe, N. Bertelli, R. Bilato, et al. Torbeam 2.0, a paraxial beam tracing code for electron-cyclotron beams in fusion plasmas for extended physics applications. *Computer Physics Communications*, 225: 36–46, 2018.

F. Porcelli, D. Boucher, and M. Rosenbluth. Model for the sawtooth period and amplitude. *Plasma Physics and Controlled Fusion*, 38(12):2163, 1996.

J. Qian, L. Lao, H. Liu, W. Ding, L. Zeng, Z. Luo, Q. Ren, Y. Huang, J. Huang, D. Brower, et al. EAST equilibrium current profile reconstruction using polarimeter-interferometer internal measurement constraints. *Nuclear Fusion*, 57(3):036008, 2016.

M. Rampp, R. Preuss, R. Fischer, and A. U. Team. Gpec: A real-time–capable tokamak equilibrium code. *Fusion Science and Technology*, 70(1):1–13, 2016.

B. Rice, K. Burrell, L. Lao, and Y. Lin-Liu. Direct measurement of the radial electric field in tokamak plasmas using the stark effect. *Physical review letters*, 79(14):2694, 1997.

M. Roelofs, E. Kolemen, D. Eldon, A. Glasser, O. Meneghini, and S. P. Smith. Plasma stability analysis using consistent automatic kinetic equilibrium reconstruction (cake). *APS*, 2017: GP11–117, 2017.

M. Romanelli, G. Corrigan, V. Parail, S. Wiesen, R. Ambrosino, P. D. S. A. Belo, L. Garzotti, D. Harting, F. Köchl, T. Koskela, et al. Jintrac: a system of codes for integrated simulation of tokamak scenarios. *Plasma and Fusion research*, 9:3403023–3403023, 2014.

Y. Saad and M. H. Schultz. Gmres: A generalized minimal residual algorithm for solving nonsymmetric linear systems. *SIAM Journal on scientific and statistical computing*, 7(3): 856–869, 1986.

S. Särkkä. *Bayesian filtering and smoothing*, volume 3. Cambridge University Press, 2013.

O. Sauter and S. Y. Medvedev. Tokamak coordinate conventions: Cocos. *Computer Physics Communications*, 184(2):293–302, 2013.

O. Sauter, C. Angioni, D. Boucher, I. Furno, A. Pochelon, and F. Porcelli. Sawtooth period simulations of tcv discharges. In *Proc. Joint Varenna-Lausanne Int. Workshop on Theory of Fusion Plasmas*, number CONF, 1999a.

O. Sauter, C. Angioni, and Y. Lin-Liu. Neoclassical conductivity and bootstrap current formulas for general axisymmetric equilibria and arbitrary collisionality regime. *Physics of Plasmas*, 6 (7):2834–2839, 1999b.

O. Sauter, C. Angioni, S. Coda, P. Gomez, T. Goodman, M. Henderson, F. Hofmann, J.-P. Hogge, J.-M. Moret, P. Nikkola, et al. Steady-state fully noninductive operation with electron cyclotron current drive and current profile control in the tokamak à configuration variable (tcv). *Physics of Plasmas*, 8(5):2199–2207, 2001.

O. Sauter, C. Angioni, and Y. Lin-Liu. Erratum:neoclassical conductivity and bootstrap current formulas for general axisymmetric equilibria and arbitrary collisionality regime. *Physics of Plasmas*, 9:5140, 2002.

R. Sayer, Y.-K. Peng, S. Jardin, A. Kellman, and J. Wesley. Tsc plasma halo simulation of a diii-d vertical displacement episode. *Nuclear fusion*, 33(7):969, 1993.

S.Barry. The extension of the fir interferometer of tcv to a polarimeter and measurements of the faraday rotation caused by the poloidal magnetic field. *Univ. of Ireland, PhD thesis, EPFL-Lausanne report LRP 638/99*, 1999.

A. S. Sharma, D. J. Limebeer, I. M. Jaimoukha, and J. B. Lister. Modeling and control of tcv. *IEEE Transactions on Control Systems Technology*, 13(3):356–369, 2005.

C. R. Sovinec and K. Bunkers. Effects of asymmetries in computations of forced vertical displacement events. *Plasma Physics and Controlled Fusion*, 61(2):024003, 2019.

H. Strauss. Asymmetric wall force and toroidal rotation in tokamak disruptions. *Physics of Plasmas*, 22(8):082509, 2015.

H. Strauss. Reduction of asymmetric wall force in iter disruptions with fast current quench. *Physics of Plasmas*, 25(2):020702, 2018.

M. Sugihara, V. Lukash, R. Khayrutdinov, and Y. Neyatani. Edge safety factor at the onset of plasma disruption during vdes in jt-60u. *Plasma physics and controlled fusion*, 46(10):1581, 2004.

J. Svensson, O. Ford, A. Werner, G. Von Nessi, M. Hole, D. McDonald, L. Appel, M. Beurskens, A. Boboc, M. Brix, et al. Connecting physics models and diagnostic data using bayesian graphical models. In *37th EPS Conference on Plasma Physics*, volume 4, page 117. European Physical Society, 2010.

N. Takei, Y. Nakamura, H. Tsutsui, Y. Kawano, T. Ozeki, S. Konishi, S. Tsuji-Iio, R. Shimada, and S. Jardin. Tsc simulation of disruptive current termination on jt-60u reversed shear plasmas. In *Proc. 30th EPS Conf. on Controlled Fusion and Plasma Physics*, 2003.

A. Teplukhina. Realistic multi-machine tokamak profile simulations and numerical ramp-down optimization using the raptor code. *PhD thesis No 8478, EPFL, Switzerland, DOI: 10.5075/epfl-thesis-8478*, 2018.

A. Teplukhina, O. Sauter, F. Felici, A. Merle, D. Kim, T. Team, E. M. Team, et al. Simulation of profile evolution from ramp-up to ramp-down and optimization of tokamak plasma termination with the raptor code. *Plasma Physics and Controlled Fusion*, 59(12):124004, 2017.

A. Thorman, C. Michael, J. Howard, B. Victor, C. Holcomb, and S. Allen. Motional stark effect imaging first results on the diii-d tokamak. *Review of Scientific Instruments*, 89(10):10D124, 2018.

Bibliography

W. Treutterer, E. Fable, A. Gräter, F. Janky, O. Kudlacek, I. G. Ortiz, T. Maceina, G. Raupp, B. Sieglin, T. Zehetbauer, et al. Concepts of the new asdex upgrade flight simulator. *Fusion Engineering and Design*, 146:1073–1076, 2019.

F. Troyon, R. Gruber, H. Saurenmann, S. Semenzato, and S. Succi. Mhd-limits to plasma confinement. *Plasma physics and controlled fusion*, 26(1A):209, 1984.

A. Turnbull. Bifurcation of a free boundary equilibrium. *Journal of plasma physics*, 31(1):1–6, 1984.

J. J. Undertaking. Microwave reflectometry for fusion plasma diagnostics. 1992.

M. Vallar. Private comunication, 2020.

M. Vallar, A. Karpushov, M. Agostini, T. Bolzonella, S. Coda, B. Duval, A. Fasoli, C. Galperti, J. Garcia, B. Geiger, et al. Status, scientific results and technical improvements of the nbh on tcv tokamak. *Fusion Engineering and Design*, 146:773–777, 2019.

J. Van Tol. The programme simfit is a msdos compatible routine for non-linear regression analysis as described by marquardt in. *J. Soc. lndustr. Appl. Math*, 11, 1963.

S. von Goeler, W. Stodiek, and N. Sauthoff. Studies of internal disruptions and m= 1 oscillations in tokamak discharges with soft—x-ray tecniques. *Physical Review Letters*, 33(20):1201, 1974.

G. Von Nessi, M. Hole, M. team, et al. A unified method for inference of tokamak equilibria and validation of force-balance models based on bayesian analysis. *Journal of Physics A: Mathematical and Theoretical*, 46(18):185501, 2013.

G. Von Nessi, M. Hole, M. Team, et al. Recent developments in bayesian inference of tokamak plasma equilibria and high-dimensional stochastic quadratures. *Plasma Physics and Controlled Fusion*, 56(11):114011, 2014.

U. Von Toussaint. Bayesian inference in physics. *Reviews of Modern Physics*, 83(3):943, 2011.

N. T. Vu, T. C. Blanken, F. Felici, C. Galperti, M. Kong, E. Maljaars, O. Sauter, et al. Tokamak-agnostic actuator management for multi-task integrated control with application to tcv and iter. *Fusion Engineering and Design*, 147:111260, 2019.

J. Wainwright, D. Copsey, D. Limebeer, M. Haines, and A. Portone. Extensions to single filament modelling of a tokamak plasma. *Nuclear fusion*, 37(12):1679, 1997.

M. Walker and D. Humphreys. Valid coordinate systems for linearized plasma shape response models in tokamaks. *Fusion Science and Technology*, 50(4):473–489, 2006.

M. Walker, G. Ambrosino, G. De Tommasi, D. Humphreys, M. Mattei, G. Neu, G. Raupp, W. Treutterer, and A. Winter. A simulation environment for iter pcs development. *Fusion Engineering and Design*, 89(5):518–522, 2014.

M. Walker, D. Humphreys, B. Sammuli, A. Welander, A. Winter, J. Snipes, P. de Vries, G. Ambrosino, G. De Tommasi, M. Mattei, et al. Development environments for tokamak plasma control. In *2015 IEEE 26th Symposium on Fusion Engineering (SOFE)*, pages 1–8. IEEE, 2015.

M. Weiland, R. Bilato, R. Dux, B. Geiger, A. Lebschy, F. Felici, R. Fischer, D. Rittich, M. van Zeeland, E. M. Team, et al. Rabbit: Real-time simulation of the nbi fast-ion distribution. *Nuclear Fusion*, 58(8):082032, 2018.

M. Weiland, R. Bilato, C. Collins, W. Heidbrink, D. Liu, M. Van Zeeland, J. Contributors, et al. Simulation of neutron emission in neutral beam injection heated plasmas with the real-time code rabbit. *Nuclear Fusion*, 59(8):086002, 2019.

G. Welch, G. Bishop, et al. An introduction to the kalman filter, 1995.

B. Wendroff et al. Gi marchuk, methods of numerical mathematics. *Bulletin of the American Mathematical Society*, 82(6):864–865, 1976.

J. Wesson and D. J. Campbell. *Tokamaks*, volume 149. Oxford university press, 2011.

A. White. Validation of nonlinear gyrokinetic transport models using turbulence measurements. *Journal of Plasma Physics*, 85(1), 2019.

R. Wolf, A. Alonso, S. Äkäslompolo, J. Baldzuhn, M. Beurskens, C. Beidler, C. Biedermann, H.-S. Bosch, S. Bozhenkov, R. Brakel, et al. Performance of wendelstein 7-x stellarator plasmas during the first divertor operation phase. *Physics of Plasmas*, 26(8):082504, 2019.

W. Xu, N. Zheng, and K. Hayami. Jacobian-free implicit inner-iteration preconditioner for nonlinear least squares problems. *Journal of Scientific Computing*, 68(3):1055–1081, 2016.

L. Zakharov, E. Foley, F. Levinton, and H. Yuh. Reconstruction of the q and p profiles in iter from external and internal measurements. *Plasma physics reports*, 34(3):173–188, 2008.

H. Zohm, G. Gantenbein, G. Giruzzi, S. Günter, F. Leuterer, M. Maraschek, J. Meskat, A. Peeters, W. Suttrop, D. Wagner, et al. Experiments on neoclassical tearing mode stabilization by eccd in asdex upgrade. *Nuclear Fusion*, 39(5):577, 1999.

W. Zwingmann. Equilibrium analysis of steady state tokamak discharges. *Nuclear fusion*, 43 (9):842, 2003.

Francesco Carpanese

Chemin des avelines 5, 1004, Lausanne, Switzerland
in https://ch.linkedin.com/in/francesco-carpanese
✉ francescocarpanese@hotmail.it

Personal Data

Date/place of birth: 28/1/1990, *Monselice (PD), Italy 35043*.

Education

2016/2020   **PHD Plasma Physics**, Swiss Plasma Center, EPFL Lausanne, Switzerland
- Free-boundary equilibrium forward static/evolutive
- Kinetic equilibrium reconstruction off-line and real-time
Supervisors: O.Sauter, F.A.Felici, J.M.Moret

2-2020   **Machine Learning and NN** Coursera online courses, Stanford University

2015/2016   **PHD Plasma Physics** (unfinished), Max-Planck-Insitut, München, Germany
- FEM full-wave solver as syhtetic reflectometer diagnostic for turbulence studies with gyrokinetic simulations.
Supervisors: A.Biancalani, O.Maj, E.Poli

2014/2015   **Master Thesis** at DIII-D, General Atomics, San Diego (CA).
- Modeling plasma shape effects on ideal stability limits in steady state hybrid plasmas.
Supervisors: F. Turco, O.Meneghini, N.Ferraro

2012/2015   **MSc Nuclear Engineering**, Politecnico di Milano, Milan, Italy
<u>Final mark</u>: 110/110, *with honors*

2013   **Summer School for Plasma Physics and Fusion Research**, Max-Planck institute fur Plasmaphysik, *Greifswald, Germany*

2012/2015   **ASPRI** project for outstanding students, Politecnico di Milano, Milan, Italy
<u>Requirements:</u> GPA greater than 28/30, additional classes

2009/2012   **BSc** in **Energy Engineering**, Politecnico di Torino, Torino, Italy
<u>Final mark</u>: 110/110, *with honors*

Selected Publications

* **Carpanese, F.**, Felici, F., Galperti, C., Merle, A., Moret, J. M., & Sauter, O. (2020). First demonstration of real-time kinetic equilibrium reconstruction on TCV by coupling LIUQE and RAPTOR. Nuclear Fusion, 60(6), 066020.

* Kong, M., Blanken, T. C., Felici, F., Galperti, C., Maljaars, E., Sauter, O., ... & Carpanese, F. (2019). Control of neoclassical tearing modes and integrated multi-actuator plasma control on TCV. Nuclear Fusion, 59(7), 076035.

* **Carpanese, F.**, Sauter, O., Merle, A., Felici, F., & Moret, J. M. (2018). Kinetic equilibrium reconstruction on TCV: towards a self-consistent approach. In 45th EPS Conference on Plasma Physics.

* Maljaars, E., Felici, F., Blanken, T. C., Galperti, C., Sauter, O., De Baar, M. R., ... & Carpanese, F. (2017). Profile control simulations and experiments on TCV: a controller test environment and results using a model-based predictive controller. Nuclear Fusion, 57(12), 126063.

* Coelho, R., Zwingmann, W., Faugeras, B., Giovanozzi, E., Mc Carthy, P., Suchkov, E., ... & Carpanese, F. (2017, June). Equilibrium reconstruction analysis of TCV tokamak plasmas in the EU-IM platform.

* Turco, F., Petty, C. C., Luce, T. C., Carlstrom, T. N., Van Zeeland, M. A., Heidbrink, W., ...& Carpanese, F. (2015). The high-N hybrid scenario for ITER and FNSF steady-state missions. Physics of Plasmas, 22(5), 056113.

Selected conference presentation

* 24th MHD Workshop Carpanese, F., Felici, F., C,Galperti, Sauter, O. , "A forward solver for the Grad-Shafranov equation using the Jacobian Free Newton Krylov method", New York, Columbia University (Oral Presentation)

* 59th Annual Meeting of the APS Division of Plasma Physics Carpanese, F., Felici, F., C,Galperti, Sauter, O. , Moret, J. M. & TCV TEAM, "Kinetic equilibrium reconstruction in TCV with LIUQE/RAPTOR: first real-time demonstration during plasma operation", Fort-Lauderdale,Florida (Poster Presentation)

* 3rd IAEA TM meeting on fusion data processing Carpanese, F., Felici, F., C,Galperti, Sauter, O. , Moret, J. M. & TCV TEAM, "First demonstration of real-time kinetic equilibrium reconstruction on TCV using LIUQE-RAPTOR coupling", Wien, Austria, (Oral Presentation)

* 45th EPS Conference on Plasma Physics Carpanese, F., Sauter, O., Merle, A., Felici, F., Moret, J. M., "Kinetic equilibrium reconstruction on TCV: towards a self-consistent approach", Prague, Czech Republic (Poster presentation P2.1059)

Teaching experience

2016-2020 Teaching assistant for the 2nd year bachelor students EPFL: Computational Physics, exercise sessions.

Languages

Italian (Mother tongue), English (Full Professional), French (Intermediate)